



## **Terms and Conditions of Use of Digitised Theses from Trinity College Library Dublin**

### **Copyright statement**

All material supplied by Trinity College Library is protected by copyright (under the Copyright and Related Rights Act, 2000 as amended) and other relevant Intellectual Property Rights. By accessing and using a Digitised Thesis from Trinity College Library you acknowledge that all Intellectual Property Rights in any Works supplied are the sole and exclusive property of the copyright and/or other IPR holder. Specific copyright holders may not be explicitly identified. Use of materials from other sources within a thesis should not be construed as a claim over them.

A non-exclusive, non-transferable licence is hereby granted to those using or reproducing, in whole or in part, the material for valid purposes, providing the copyright owners are acknowledged using the normal conventions. Where specific permission to use material is required, this is identified and such permission must be sought from the copyright holder or agency cited.

### **Liability statement**

By using a Digitised Thesis, I accept that Trinity College Dublin bears no legal responsibility for the accuracy, legality or comprehensiveness of materials contained within the thesis, and that Trinity College Dublin accepts no liability for indirect, consequential, or incidental, damages or losses arising from use of the thesis for whatever reason. Information located in a thesis may be subject to specific use constraints, details of which may not be explicitly described. It is the responsibility of potential and actual users to be aware of such constraints and to abide by them. By making use of material from a digitised thesis, you accept these copyright and disclaimer provisions. Where it is brought to the attention of Trinity College Library that there may be a breach of copyright or other restraint, it is the policy to withdraw or take down access to a thesis while the issue is being resolved.

### **Access Agreement**

By using a Digitised Thesis from Trinity College Library you are bound by the following Terms & Conditions. Please read them carefully.

I have read and I understand the following statement: All material supplied via a Digitised Thesis from Trinity College Library is protected by copyright and other intellectual property rights, and duplication or sale of all or part of any of a thesis is not permitted, except that material may be duplicated by you for your research use or for educational purposes in electronic or print form providing the copyright owners are acknowledged using the normal conventions. You must obtain permission for any other use. Electronic or print copies may not be offered, whether for sale or otherwise to anyone. This copy has been supplied on the understanding that it is copyright material and that no quotation from the thesis may be published without proper acknowledgement.

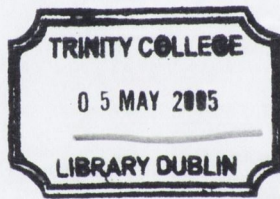
**FINITE ELEMENT & EXPERIMENTAL  
ANALYSIS  
OF  
DENTED AIRCRAFT PANELS**

**Kevin Lacey**

SUBMITTED IN FULFILLMENT OF THE REQUIREMENTS FOR THE  
DEGREE OF DOCTOR OF PHILOSOPHY AT UNIVERSITY OF DUBLIN,  
TRINITY COLLEGE DUBLIN, IRELAND, OCTOBER 2004.

Supervisor: **Professor John Monaghan**

The work presented in this thesis was conducted at the Department of Mechanical  
and Manufacturing Engineering, University of Dublin, Trinity College, Ireland.

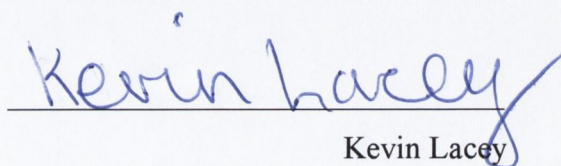


THESIS  
7670

## Declaration

I declare that the present work has not been submitted as an exercise for a degree at any other University. This thesis consists entirely of my own work except where references indicate otherwise.

I agree that the library of the University of Dublin, Trinity College, Dublin, may lend or copy this thesis upon request.

  
Kevin Lacey

## Acknowledgements

There are many people I would like to thank who have helped me in this research. Firstly, I would like to express my sincere gratitude to my supervisor Professor John Monaghan without whose guidance and advice this thesis would never have been completed. Thank you to my examiners, Professor Henry Rice (internal) and Professor Michael McCarthy (external), for managing to read the thesis so thoroughly and for a surprisingly enjoyable viva.

I would like to thank the academic and technical staff at the Department of Mechanical and Manufacturing Engineering Trinity College Dublin. In particular, I would like to thank the Materials Ireland staff Toman, Michael, Ray and JJ. A special word of thanks goes to Conor MacCormack for his support, technical input and friendship over the last few years.

I am also grateful to my colleagues from the IARCAS programme for their technical assistance in particular, Johannes Jochem of Airbus and Arjan Woerden at the Delft University of Technology.

I would like to thank the many friends I've made at Trinity College Dublin throughout the course of this research. Particularly my former office mates George, Mark, Alan, John and Brian.

I'd like to thank those closest to me who have shown me nothing but patience and encouragement in my endeavours to complete this thesis, my brothers Mark and Desmond and my mother Maureen, without their love and support this thesis could not have been completed.

To my girlfriend Kate, I cannot thank you enough for all the love and support you have shown me throughout the highs and lows of this research. Your confidence and belief in me were priceless. I am eternally grateful to you for proof reading this thesis with such painstaking attention to detail. Thank you for all the wonderful times; I love you Kate.

## Abstract

Aircraft fuselage panels are susceptible to low velocity impact damage in the form of “dents” from a variety of in-service sources, such as cargo and service trucks, dropped tools during servicing, walking on “no-step areas” and baggage handling mishaps. These dents result in a redistribution of load in the structure due to the change in shape and associated residual stresses.

Although the load carrying characteristics of the undamaged structure are well understood a knowledge gap exists regarding the effects of dents on the ultimate compressive strength of the fuselage panel.

It was this knowledge gap that the author sought to explore in investigating the compressive strength reduction characteristics of fuselage panels due to local denting. The effects of dent depth, diameter, shape and location were investigated in an experimental and numerical work programme. In addition the efficacy of current repair methods was studied and current modelling methods assessed.

The results display the inherent ability of the stiffened fuselage panel to maintain stability through load redistribution away from the damaged area. Numerical and experimental results are shown to be in close agreement showing the compressive strength of a panel with a dent of 10mm depth on a stringer to be 91% of the undamaged compressive strength. Parametric studies established the worst case location for a dent and the effects of increasing dent depth. The current repair procedure of dent dress back was shown to recover 80% of the load reduction due to the unrepaired dent.

# Table of Contents

DECLARATION .....	I
ACKNOWLEDGEMENTS .....	II
ABSTRACT .....	III
TABLE OF CONTENTS .....	IV
TABLE OF FIGURES .....	VII
NOMENCLATURE .....	XV
PART I .....	1
1 INTRODUCTION .....	1
1.1 OBJECTIVES .....	3
PART II .....	4
2 LITERATURE REVIEW .....	4
2.1 INTRODUCTION .....	4
2.2 FUSELAGE STRUCTURE .....	6
2.3 BUCKLING OF THIN-WALLED STRUCTURES .....	7
2.4 IMPACT DAMAGE .....	14
2.5 AIRCRAFT REPAIR .....	17
2.5.1 <i>Introduction</i> .....	17
2.5.2 <i>Inspection</i> .....	18
2.5.3 <i>Current Repair Procedures for Dents</i> .....	19
2.6 BUCKLING OF DAMAGED THIN-WALLED STRUCTURES .....	25
2.7 FINITE ELEMENT METHOD .....	28
2.7.1 <i>Historical Background</i> .....	28
2.7.2 <i>Finite Element Analysis Theory</i> .....	29
2.8 FINITE ELEMENT MODELLING OF DENTED STRUCTURES .....	31
PART III .....	34
3 EXPERIMENTAL METHODS .....	34
3.1 INTRODUCTION .....	34
3.2 COUPON DENTING TEST RIG .....	34
3.3 FULL SCALE DENTING RIG .....	37
3.4 FULL SCALE COMPRESSION RIG .....	42
PART IV .....	48

4	NUMERICAL METHODS .....	48
4.1	INTRODUCTION .....	48
4.2	FINITE ELEMENT ANALYSIS TYPE.....	49
4.3	ELEMENT CHOICE .....	49
4.4	MATERIAL MODELLING .....	54
4.5	PARAMETRIC MODELLING.....	55
4.6	GRAPHICAL USER INTERFACE.....	63
4.7	FINITE ELEMENT MESH .....	65
4.8	CONTACT ANALYSIS .....	67
4.9	BOUNDARY AND LOADING CONDITIONS .....	72
4.9.1	<i>Denting Boundary Conditions</i> .....	72
4.9.2	<i>Compression Loading</i> .....	75
	PART V.....	80
5	FINITE ELEMENT AND EXPERIMENTAL RESULTS .....	80
5.1	DENTING RESULTS: COUPON TEST RIG .....	80
5.2	DENTING RESULTS: A380 WELDED PANEL .....	83
5.2.1	<i>Experimental vs. FE Load-Displacement Results</i> .....	84
5.2.2	<i>Experimental Strains vs. FE Predicted Strains</i> .....	87
5.3	COMPRESSION RESPONSE: A380 WELDED PANEL.....	94
5.3.1	<i>Pristine Panel</i> .....	94
5.3.2	<i>Dented Panel</i> .....	100
5.4	DENT DEPTH INVESTIGATION .....	108
5.5	EFFECT OF DENT LOCATION .....	112
5.5.1	<i>Effects of Location on Bay Dents</i> .....	113
5.5.2	<i>Effects of Location on Stringer Dents</i> .....	117
5.6	EFFECT OF DENT SIZE .....	121
5.7	CYLINDRICAL DENTS .....	125
5.7.1	<i>Cylindrical Dent across Stringers</i> .....	125
5.7.2	<i>Cylindrical Dent along a Stringer</i> .....	128
5.8	EFFECT OF STRINGER PITCH .....	132
5.9	EFFICACY OF DENT DRESS BACK FROM A STATIC STRENGTH PERSPECTIVE.....	135
5.9.1	<i>Compression Response of a Repaired Dented Panel</i> .....	139
5.10	EFFECT OF INCLUDING RESIDUAL STRESSES.....	143
	PART VI .....	148
6	CONCLUSIONS.....	148
	PART VII .....	150
7	FUTURE WORK.....	150



REFERENCES ..... 151

## Table of Figures

FIGURE 1.1 DENTED FUSELAGE .....	2
FIGURE 2.1 BELUGA FUSELAGE, INTERNAL VIEW SHOWING SEMI-MONOCOQUE DESIGN .....	6
FIGURE 2.2 COLUMN BUCKLING .....	8
FIGURE 2.3 BUCKLING-STRESS RATIO AS A FUNCTION OF BUCKLE WAVE DEPTH FOR AXIALLY COMPRESSED COLUMNS, PLATES AND CYLINDERS [6].....	10
FIGURE 2.4 PLATE BUCKLING.....	10
FIGURE 2.5 EFFECTIVE WIDTHS: (A) TRUE STRESS DISTRIBUTION, (B) IDEALISED STRESS DISTRIBUTION .....	13
FIGURE 2.6 CARGO LOADING SYSTEM.....	14
FIGURE 2.7 RUBBER PADS TO SAFEGUARD AGAINST IMPACT .....	15
FIGURE 2.8 REPAIR OF IMPACT DAMAGE TO FRONT ENTRY DOOR OF AIRBUS A320 AT DUBLIN AIRPORT .....	15
FIGURE 2.9 DENT TO HAIL ON UPPER FUSELAGE OF EASYJET AIRBUS .....	16
FIGURE 2.10 DENTS ON RIGHT WING LEADING EDGE OF FINNAIR McDONNELL DOUGLAS DC- 9-81 [26] .....	17
FIGURE 2.11 DRESS OUT PROCEDURE [28].....	20
FIGURE 2.12 MEASUREMENT OF ALLOWABLE DENT IN SKIN [28] .....	21
FIGURE 2.13 ALLOWABLE DENT LIMITS IN SKIN SHEET FOR GIVEN FLIGHT CYCLES (FC) [28] .....	22
FIGURE 2.14 UNDAMAGED AND DAMAGED CLIP DUE TO DENT ON EXTERNAL SKIN .....	23
FIGURE 2.15 COMPLETE STRINGER REPAIR [28].....	24
FIGURE 3.1 ORIGINAL COUPON DENTING TEST RIG.....	35
FIGURE 3.2 SLIPPAGE OF ALUMINIUM .....	36
FIGURE 3.3 MODIFIED COUPON DENTING TEST RIG .....	36
FIGURE 3.4 FULL SCALE DENTING TEST RIG.....	38
FIGURE 3.5 DENTING RIG TEST SECTION CLOSE UP.....	39
FIGURE 3.6 FRAME INNER FLANGE WOODEN SUPPORT .....	40
FIGURE 3.7 EXTERNAL FRAME CLAMP REASONING .....	40
FIGURE 3.8 INDENTOR.....	41
FIGURE 3.9 INTERNAL STRAIN GAUGE LOCATIONS.....	42
FIGURE 3.10 TEST RIG I AND II [58].....	43
FIGURE 3.11 FULL SCALE TEST RIG, ISOMETRIC VIEW [58].....	44

FIGURE 3.12 PLAN VIEW OF CURVED PANEL AND HINGED SUPPORTS [58] .....	44
FIGURE 3.13 ELEVATION VIEW CURVED PANEL LOAD INTRODUCTION [58] .....	45
FIGURE 3.14 TEST PANEL DETAILING LONGITUDINAL CUT-OUT AND END CLAMPS.....	46
FIGURE 3.15 SECTION B-B CIRCUMFERENTIAL END CLAMPING.....	46
FIGURE 3.16 PANEL REINFORCEMENTS .....	47
FIGURE 4.1 FINITE ELEMENT REPRESENTATION OF GENERIC AIRCRAFT PANEL .....	48
FIGURE 4.2 PROBLEM OF SHEAR LOCKING FOR BEAM UNDER BENDING.....	50
FIGURE 4.3 PANEL SKIN SHOWING MAPPED SHELL 181 ELEMENT MESH .....	51
FIGURE 4.4 EARLY STIFFENER MODEL USING BEAM ELEMENTS .....	52
FIGURE 4.5 TRADITIONAL SHELL ELEMENT WITH THICKNESS OFFSET ABOUT THE MID-PLANE .....	53
FIGURE 4.6 ELEMENT PLOT SHOWING THE ELEMENT THICKNESS OFFSET TO THE TOP .....	53
FIGURE 4.7 MATERIAL DATA PLOTS .....	55
FIGURE 4.8 USER DEFINED PARAMETERS.....	56
FIGURE 4.9 POSSIBLE STRINGER CROSS SECTIONS.....	58
FIGURE 4.10 CIRCUMFERENTIAL PANEL CROSS SECTION .....	58
FIGURE 4.11 EXAMPLE OF CHANGE IN SKIN THICKNESS OR “POCKETING” DUE TO CHEMICAL MILLING .....	59
FIGURE 4.12 AS MANUFACTURED SKIN THICKNESS AREAS .....	59
FIGURE 4.13 CHEMICALLY MILLED SKIN THICKNESS AREAS.....	60
FIGURE 4.14 STRINGER SURFACES .....	61
FIGURE 4.15 CLIP SURFACE GENERATION.....	62
FIGURE 4.16 FRAME CROSS SECTION SHOWING CUT OUTS AND TRANSLUCENT SKIN AND STRINGER SURFACES.....	62
FIGURE 4.17 PANEL SURFACES WITH ASSIGNED THICKNESSES CORRESPONDING TO COLOURS .....	63
FIGURE 4.18 GUI ENTRY AND SKIN DATA ENTRY FORM.....	64
FIGURE 4.19 STRINGER DATA ENTRY FORM.....	64
FIGURE 4.20 FRAME DATA ENTRY FORM .....	65
FIGURE 4.21 FINITE ELEMENT MESHED PANEL.....	66
FIGURE 4.22 STRINGER MESH .....	67
FIGURE 4.23 SCHEMATIC REPRESENTATION OF PENALTY STIFFNESS [62].....	68
FIGURE 4.24 TARGET AND CONTACT SURFACES .....	70
FIGURE 4.25 DENTING BOUNDARY CONDITIONS .....	72

FIGURE 4.26 FORCE CONTROLLED CONTACT, CONSTRAINTS ON SPHERE ESTABLISHED WHEN IN CONTACT .....	73
FIGURE 4.27 INDENTOR LOADING .....	74
FIGURE 4.28 CONTROL FLOW RESIDUAL DENT DEPTH MACRO .....	75
FIGURE 4.29 NEWTON-RAPHSON SOLUTION- ONE ITERATION [62] .....	76
FIGURE 4.30 NEWTON-RAPHSON DEVELOPS SINGULARITY [71] .....	77
FIGURE 4.31 ARC-LENGTH METHODOLOGY [62].....	78
FIGURE 4.32 MULTI-POINT CONSTRAINT SET-UP, SHOWING ELEMENTS ON CIRCUMFERENTIAL END OF PANEL ONLY .....	79
FIGURE 5.1 FINITE ELEMENT OF COUPON DENTING TEST RIG .....	81
FIGURE 5.2 EXPERIMENTAL VS. FE INDENTATION LOAD CURVES .....	82
FIGURE 5.3 FE PREDICTED RESIDUAL DENT DUE TO 10MM INDENTATION .....	82
FIGURE 5.4 DENT LOCATION.....	83
FIGURE 5.5 DENTING LOAD VS. DENT DEPTH .....	84
FIGURE 5.6 RADIAL DISPLACEMENT AT MAXIMUM INDENTATION.....	85
FIGURE 5.7 INDUCTIVE DISPLACEMENT TRANSDUCER POSITION ON STRINGER FLANGE.....	85
FIGURE 5.8 VON MISES STRESS AT POINT A .....	86
FIGURE 5.9 VON MISES STRESS AT POINT B.....	87
FIGURE 5.10 VON MISES STRESS AT POINT C.....	87
FIGURE 5.11 EXTERNAL SKIN STAIN GAUGE LOCATIONS .....	87
FIGURE 5.12 EXPERIMENTAL VERSUS FINITE ELEMENT STRAIN AT POSITIONS 2, 4 AND L .....	89
FIGURE 5.13 EXPERIMENTAL VERSUS FINITE ELEMENT STRAINS AT POSITIONS 3 AND R.....	89
FIGURE 5.14 LONGITUDINAL STRAIN ON OUTER SKIN SURFACE AT 8MM INDENTATION .....	90
FIGURE 5.15 LONGITUDINAL STRAIN ON OUTER SKIN SURFACE AT 16MM INDENTATION.....	90
FIGURE 5.16 RESIDUAL LONGITUDINAL STRAIN OUTER SKIN.....	90
FIGURE 5.17 RESIDUAL LONGITUDINAL STRAIN INNER SKIN.....	90
FIGURE 5.18 STRAIN GAUGE LOCATIONS ON INNER PANEL SURFACE .....	91
FIGURE 5.19 FE VERSUS EXPERIMENTAL STRAIN IN STRINGER FLANGE .....	91
FIGURE 5.20 FE VERSUS EXPERIMENTAL STRAIN IN STRINGER FLANGE .....	93
FIGURE 5.21 MAXIMUM LONGITUDINAL STRAIN.....	93
FIGURE 5.22 RESIDUAL LONGITUDINAL STRAIN.....	93
FIGURE 5.23 EXPERIMENTAL & FINITE ELEMENT COMPRESSIVE LOAD VERSUS END SHORTENING CURVES .....	95
FIGURE 5.24 RADIAL DISPLACEMENT AT POINT A.....	96
FIGURE 5.25 RADIAL DISPLACEMENT AT POINT B .....	96

FIGURE 5.26 LONGITUDINAL MID-SURFACE STRESS IN TEST SECTION SKIN AT END SHORTENING OF 0.8MM.....	97
FIGURE 5.27 LONGITUDINAL MID-SURFACE STRESS IN TEST SECTION SKIN AT END SHORTENING OF 2.4MM.....	97
FIGURE 5.28 LONGITUDINAL MID-SURFACE STRESS ALONG PATH X-X.....	97
FIGURE 5.29 RADIAL DISPLACEMENT AT POINT C.....	98
FIGURE 5.30 RADIAL DISPLACEMENT AT POINT D.....	98
FIGURE 5.31 RADIAL DISPLACEMENT AT POINT E.....	99
FIGURE 5.32 RADIAL DISPLACEMENT AT POINT F.....	99
FIGURE 5.33 RADIAL DISPLACEMENT AT STRINGER-SKIN CONNECTION ALONG PATH Y-Y....	99
FIGURE 5.34 RADIAL DISPLACEMENT FOR CENTRAL NODE ON STRINGER-SKIN CONNECTION .....	100
FIGURE 5.35 LONGITUDINAL MID-SURFACE STRESS IN TEST SECTION SKIN AT END SHORTENING 5.53MM.....	100
FIGURE 5.36 LONGITUDINAL MID-SURFACE STRESS IN TEST SECTION SKIN AT END SHORTENING 8.0MM.....	100
FIGURE 5.37 EXPERIMENTAL & FINITE ELEMENT COMPRESSIVE LOAD VERSUS END SHORTENING CURVES.....	101
FIGURE 5.38 FINITE ELEMENT PREDICTED COMPRESSION RESPONSE FOR PRISTINE AND DENTED PANELS.....	102
FIGURE 5.39 RESIDUAL DENT FULL PANEL VIEW.....	102
FIGURE 5.40 RESIDUAL DENT STRINGER VIEW.....	102
FIGURE 5.41 DENTED PANEL RADIAL DISPLACEMENT AT POINT A.....	103
FIGURE 5.42 DENTED PANEL RADIAL DISPLACEMENT AT POINT B.....	103
FIGURE 5.43 DENTED PANEL LONGITUDINAL MID-SURFACE STRESS IN TEST SECTION SKIN AT AN END SHORTENING 0.8MM.....	104
FIGURE 5.44 DENTED PANEL LONGITUDINAL MID-SURFACE STRESS IN TEST SECTION SKIN AT AN END SHORTENING 2.4MM.....	104
FIGURE 5.45 LONGITUDINAL MID-SURFACE STRESS ALONG PATH X-X.....	104
FIGURE 5.46 LONGITUDINAL MID-SURFACE STRESS IN SECTION X-X AT END SHORTENING 2.4MM.....	105
FIGURE 5.47 DENTED PANEL RADIAL DISPLACEMENT AT POINT C.....	105
FIGURE 5.48 DENTED PANEL RADIAL DISPLACEMENT AT POINT D.....	105
FIGURE 5.49 DENTED PANEL RADIAL DISPLACEMENT AT POINT E.....	106
FIGURE 5.50 DENTED PANEL RADIAL DISPLACEMENT AT POINT F.....	106

FIGURE 5.51 LOAD AT STRINGER-SKIN CONNECTION IN PRISTINE PANEL..... 107

FIGURE 5.52 LOAD AT STRINGER-SKIN CONNECTION IN DENTED PANEL..... 108

FIGURE 5.53 COMPRESSIVE LOAD VERSUS END SHORTENING FOR INCREASING DENT DEPTHS  
..... 109

FIGURE 5.54 ULTIMATE STRENGTH REDUCTIONS AS A FUNCTION OF DENT DEPTH FOR  
STRINGER DENTS ..... 111

FIGURE 5.55 ULTIMATE STRENGTH REDUCTIONS AS A FUNCTION OF DENT DEPTH FOR  
STRINGER AND BAY DENTS..... 112

FIGURE 5.56 DENTED BAY AND STRINGER ON PANEL ..... 113

FIGURE 5.57 LOCATIONS OF DENTS ON STRINGER AND IN BAY ..... 113

FIGURE 5.58 COMPRESSION RESPONSE FOR 4MM DEPTH BAY DENTS AT LOCATIONS B0, B1  
AND B2..... 114

FIGURE 5.59 COMPRESSION RESPONSE FOR 8MM DEPTH BAY DENTS AT LOCATIONS B0, B1  
AND B2..... 114

FIGURE 5.60 COMPRESSION RESPONSE FOR 10MM DEPTH BAY DENTS AT LOCATIONS B0, B1  
AND B2..... 115

FIGURE 5.61 BAY DENT LOCATION "B2" ..... 117

FIGURE 5.62 BAY DENT LOCATION "B0" ..... 117

FIGURE 5.63 BUCKLING MODE AT ULTIMATE COMPRESSIVE STRENGTH FOR DENT AT  
LOCATION "B2" ..... 117

FIGURE 5.64 BUCKLING MODE AT ULTIMATE COMPRESSIVE STRENGTH FOR DENT AT  
LOCATION "B0" ..... 117

FIGURE 5.65 COMPRESSION RESPONSE FOR 4MM DEPTH STRINGER DENTS AT LOCATIONS S0,  
S1 AND S2 ..... 118

FIGURE 5.66 COMPRESSION RESPONSE FOR 8MM DEPTH STRINGER DENTS AT LOCATIONS S0,  
S1 AND S2 ..... 118

FIGURE 5.67 COMPRESSION RESPONSE FOR 10MM DEPTH STRINGER DENTS AT LOCATIONS S0,  
S1 AND S2 ..... 119

FIGURE 5.68 RESIDUAL STRINGER DENT LOCATION "S2" ..... 120

FIGURE 5.69 RESIDUAL STRINGER DENT LOCATION "S0" ..... 120

FIGURE 5.70 RESIDUAL DENT RADIAL PROFILE ALONG STRINGER SECTION A-A..... 120

FIGURE 5.71 BUCKLING MODE AT ULTIMATE COMPRESSIVE STRENGTH FOR DENT AT  
LOCATION "S2" ..... 121

FIGURE 5.72 BUCKLING MODE AT ULTIMATE COMPRESSIVE STRENGTH FOR DENT AT  
LOCATION "S0" ..... 121

FIGURE 5.73 COMPRESSIVE LOAD VERSUS END SHORTENING FOR 7MM DENT ON STRINGER MID-WAY BETWEEN FRAMES WITH INDENTOR RADII 15, 30 AND 60MM .....	122
FIGURE 5.74 COMPRESSIVE LOAD VERSUS END SHORTENING FOR 10MM DENT ON STRINGER MID-WAY BETWEEN FRAMES WITH INDENTOR RADII 15, 25, 30 AND 50MM.....	122
FIGURE 5.75 RESIDUAL DENT .....	123
FIGURE 5.76 RADIAL DISPLACEMENT ALONG PATH X-X CASE WITH 25 AND 50MM RADIUS INDENTORS .....	124
FIGURE 5.77 RADIAL DISPLACEMENT ALONG PATH Y-Y CASE FOR 25 AND 50MM RADIUS INDENTORS .....	124
FIGURE 5.78 CYLINDRICAL INDENTOR PERPENDICULAR TO STRINGERS .....	125
FIGURE 5.79 MAX CYLINDRICAL DENT PERPENDICULAR TO STRINGERS .....	126
FIGURE 5.80 RESIDUAL CYLINDRICAL DENT PERPENDICULAR TO STRINGERS .....	126
FIGURE 5.81 FE PREDICTED COMPRESSIVE LOAD VERSUS END SHORTENING FOR A CYLINDRICAL DENT ACROSS TWO STRINGERS .....	126
FIGURE 5.82 RADIAL DISPLACEMENT AT MAX LOAD OF 339KN AT END SHORTENING OF 5.11MM .....	127
FIGURE 5.83 LONGITUDINAL MID-SURFACE STRESS AT MAX LOAD OF 339KN AT END SHORTENING OF 5.11MM.....	127
FIGURE 5.84 LONGITUDINAL MID-SURFACE STRESS ALONG SECTION X-X .....	128
FIGURE 5.85 CYLINDRICAL DENT ALONG A STRINGER.....	129
FIGURE 5.86 MAX CYLINDRICAL DENT ALONG STRINGER .....	130
FIGURE 5.87 RESIDUAL CYLINDRICAL DENT ALONG STRINGER.....	130
FIGURE 5.88 FE PREDICTED COMPRESSIVE LOAD VERSUS END SHORTENING FOR CYLINDRICAL DENT ALONG ONE STRINGER .....	130
FIGURE 5.89 RADIAL DISPLACEMENT AT A MAX LOAD OF 355KN AT END SHORTENING OF 5.65MM .....	131
FIGURE 5.90 LONGITUDINAL MID-SURFACE STRESS AT A MAX LOAD OF 355KN AT END SHORTENING OF 5.65MM.....	131
FIGURE 5.91 LONGITUDINAL MID-SURFACE STRESS ALONG SECTION X-X .....	132
FIGURE 5.92 STRINGER PITCH 150 .....	133
FIGURE 5.93 STRINGER PITCH 145 .....	133
FIGURE 5.94 STRINGER PITCH 140 .....	133
FIGURE 5.95 STRINGER PITCH 130 .....	133
FIGURE 5.96 ULTIMATE STRENGTH REDUCTION AS A FUNCTION OF STRINGER PITCH.....	135
FIGURE 5.97 SCHEMATIC OF MODELLING DIFFICULTIES ENCOUNTERED IN DRESS BACK.....	136

FIGURE 5.98 FE SET UP OF DRESS BACK PROCEDURE ..... 137

FIGURE 5.99 MAX APPLIED DENT DEPTH ..... 137

FIGURE 5.100 RESIDUAL DENT DEPTH..... 137

FIGURE 5.101 TOOL DISPLACING DENT IN RADIAL DIRECTION ..... 138

FIGURE 5.102 DENT RECOVERS TO 6.5MM IN RADIAL DIRECTION ..... 138

FIGURE 5.103 FINAL DRESSED BACK DENT SHOWING OUT-OF-PLANE RADIAL DISPLACEMENT  
..... 139

FIGURE 5.104 COMPRESSIVE LOAD VERSUS END SHORTENING FOR THE PRISTINE, DENTED AND  
DRESSED BACK PANEL ..... 139

FIGURE 5.105 DENT LONGITUDINAL STRESS TOP SURFACE..... 140

FIGURE 5.106 DENT LONGITUDINAL STRESS BOTTOM SURFACE..... 140

FIGURE 5.107 DENT CIRCUMFERENTIAL STRESS TOP SURFACE ..... 140

FIGURE 5.108 DENT CIRCUMFERENTIAL STRESS BOTTOM SURFACE..... 140

FIGURE 5.109 DRESSED BACK DENT LONGITUDINAL STRESS TOP SURFACE ..... 141

FIGURE 5.110 DRESSED BACK DENT LONGITUDINAL STRESS BOTTOM SURFACE ..... 141

FIGURE 5.111 DRESSED BACK DENT CIRCUMFERENTIAL STRESS TOP SURFACE..... 141

FIGURE 5.112 DRESSED BACK DENT CIRCUMFERENTIAL STRESS BOTTOM SURFACE ..... 141

FIGURE 5.113 LONGITUDINAL STRESS AT SECTION X-X ON THE SHELL TOP SURFACE..... 142

FIGURE 5.114 LONGITUDINAL STRESS AT SECTION X-X ON THE SHELL BOTTOM SURFACE . 142

FIGURE 5.115 CIRCUMFERENTIAL STRESS AT SECTION X-X ON THE SHELL TOP SURFACE... 143

FIGURE 5.116 CIRCUMFERENTIAL STRESS AT SECTION X-X ON THE SHELL BOTTOM SURFACE  
..... 143

FIGURE 5.117 COMPRESSION RESPONSES FOR A DENT INCORPORATING RESIDUAL STRESSES  
AND A DENT BASED ON A GEOMETRIC IDEALISATION..... 144

FIGURE 5.118 DENTED PANEL INCORPORATING ACTUAL DENT RADIAL DISPLACEMENT AT AN  
END SHORTENING OF 2.4MM..... 145

FIGURE 5.119 GEOMETRIC IDEALISATION OF DENT RADIAL DISPLACEMENT AT AN END  
SHORTENING OF 2.4MM..... 145

FIGURE 5.120 RADIAL DISPLACEMENT AT AN END SHORTENING OF 3.3MM FOR AN “ACTUAL”  
DENT ..... 145

FIGURE 5.121 RADIAL DISPLACEMENT AT AN END SHORTENING OF 3.3MM FOR A  
“GEOMETRIC” DENT..... 145

FIGURE 5.122 “ACTUAL” DENT LONGITUDINAL MID-SURFACE STRESS AT AN END  
SHORTENING OF 3.3MM..... 146



FIGURE 5.123 "GEOMETRIC" DENT LONGITUDINAL MID-SURFACE STRESS AT AN END  
SHORTENING OF 3.3MM..... 146

FIGURE 5.124 LONGITUDINAL MID-SURFACE STRESS ALONG PATH X-X AT END SHORTENING  
OF 3.3MM..... 147

## NOMENCLATURE

## Symbol

 $\Delta\varepsilon$  $\lambda$  $\Delta\sigma$  $\sigma_1$  $\sigma_2$  $\sigma_3$  $\sigma_c$  $\sigma_e$  $\sigma_y$  $\nu$  $b$  $b_e$  $c$  $E$  $\{F\}$  $F$  $g$  $I$  $k$  $[K]$  $[K^T]$  $L$  $P_c$  $R$  $t$  $u$  $\Delta u$  $x$  $Z$ 

## Definition

Change in strain

Arc length load factor

Change in stress

1<sup>st</sup> principal stress2<sup>nd</sup> principal stress3<sup>rd</sup> principal stress

Critical buckling stress

Von Mises equivalent stress

Yield stress

Poisson's ratio

Plate width

Effective width

Normal contact force

Young's modulus

Nodal force vector

Force

Normal contact gap

Moment of inertia

Stiffness

Stiffness matrix

Tangent stiffness matrix

Length

Critical load

Shell Radius

Shell thickness

Displacement

Change in displacement

Displacement

Batdorf curvature parameter

# PART I

## 1 INTRODUCTION

Recent years have seen progressive growth for European aircraft manufacturers. In fact despite the upset of September 11th, 2001 saw a nominal growth of 11.5% with a total turnover of €80.6 billion [1]. This is largely due to the civil sectors and the achievements of Airbus, which is reaching parity with Boeing in terms of market share.

In order to continue to increase market share European aircraft manufactures are looking to decrease direct operational costs (DOC's) in areas where the US manufacturers still have the edge. One such area is fuselage damage repair. The reason that US manufacturers have an advantage over their European counterparts is due to the fact that there is a much larger US-produced fleet flying today and as a result their experience of allowable damage limits (ADL's) and repair exceeds that of their European counterparts, [2].

“Damage repair” is a broad topic covering such areas as composite patch repairs, friction stir welding, blending, doubler repairs and dent repairs. Damage repair has been identified as a growth area due to current economic trends, which have led to an ageing aircraft fleet well beyond its original design life. An ageing fleet will obviously require greater maintenance and repair therefore adding to the necessity to derive state-of-the-art repair methods.

The area of importance pertaining to this research is impact damage. There are numerous sources of impact damage that an aircraft is exposed to during its lifetime. They can be defined in terms of low velocity impacts, such as collisions between service cars and the structure, see Figure 1.1, and high velocity sources, such as bird strikes.

Dents resulting from low velocity impacts can occur throughout the fuselage with some areas being more prone to impact than others, such as around cargo doors. Of particular interest are the effects of impact damage in the form of dents in areas of the fuselage that experience high compressive loading. While recent years have seen a number of studies into the effects of impact damage on the compressive strength of composite structures due to their susceptibility to delamination [3, 4, 5] a considerable knowledge gap still exists as to the effects of impact damage on metallic structures from a static strength viewpoint.



**Figure 1.1 Dented Fuselage**

Research has shown the susceptibility of thin walled structures, to minor imperfections arising during fabrication, [6, 7]. Although much attention has been focused on the performance of such structures in their “as built” form, little attention has been paid to the methods in which thin-walled structures continue to carry their design loads after experiencing in-service damage [7]. As a result, there is a need for further research into the effects of dents on the structural stability of the aircraft structure, as depending on amplitude and location, these dents could potentially lead to a significant reduction in the ultimate compressive strength of the fuselage structure.

Due to the lack of knowledge regarding the effects of dents on the physical load carrying capability of the structure current repair practices tend to be over conservative. For example, the static compressive strength of a dented stringer is assumed to be negligible regardless of the dent depth, shape or location along the stringer and the entire load is assumed to be carried by adjacent stringers through load by-pass [2]. There are currently no ADL’s for a dent on a stringer and the resulting repair procedure, where the stringer is cut out and replaced, is both complex and costly.

In addition, to the author’s knowledge there is also no published data to show whether the current repair procedure for dents in the panel skin, known as “dent dress back”, have a

positive or negative effect on the ultimate buckling strength of the fuselage. It is apparent that the effects of dents warrant closer investigation in order to improve ADL's, hence reducing DOC's for the airline operators.

The primary contribution of the research presented in this thesis was to investigate the ultimate compressive strength reduction characteristics for aircraft panels due to local denting. The research was carried out in conjunction with a program initiated under the European Fifth Framework, known as "Improve Assess Repair Capability of Aircraft Structures" or IARCAS.

## 1.1 Objectives

The objectives of the research presented in this thesis are as follows:

1. To carry out a detailed literature review of the effects of damage in the form of dents on thin-walled structures.
2. To design and build an experimental rig for denting of coupons to be used as a benchmark for the initial finite element models.
3. To develop a parametric finite element model capable of modelling a generic fuselage structure; The finite element model was to be capable of modelling a quasi-static impact by an indenter, subsequent removal of the indenter and associated elastic recovery of the damaged shell followed by a non-linear compressive buckling analysis.
4. To benchmark the finite element model against full-scale experimental test results of the denting and subsequent compression loading operations.
5. On completion of stages 1-4, to carry out parametric investigations to assess the effects of varying dent damage.
6. To compare the simplified method of modelling the dent as a geometric idealisation and the more accurate representation including residual stresses.
7. To simulate the current repair practice of dent dress-back to assess whether it has any net positive effect from a static strength perspective.

## PART II

### 2 LITERATURE REVIEW

#### 2.1 Introduction

The phenomenon of flight has preoccupied human beings from the earliest of times. It has been the subject of myths and stories as far back as that of Icarus and his father Daedalus and their escape from King Minos' prison on Crete. Interestingly, from the point of view of this research, legend has it that they had difficulty with structural materials rather than aerodynamics.

Materials have remained at the forefront of developing aviation technologies to the present day. Minimum weight has always been a key factor in the design of aircraft for practical flight. For this reason, from 1903 to the 1930's the airframe was a wooden braced structure covered with fabric treated with varnishes. Sitka spruce was the material of choice due to its fine straight grained structure with a minimum of knots.

The first attempts at an all metal aircraft were made in Europe by Anthony Fokker [8], who developed a welded-tube steel fuselage to take the place of wood. Fokker was followed closely by Hugo Junkers. In Junker's early designs he used flat sheet iron but a materials breakthrough in the form of duralumin resulted in the first successful design.

Several of Junker's all metal passenger planes were imported to the United States and as a result the National Advisory Committee for Aeronautics (NACA), investigated its feasibility as an aircraft material and its annual report in 1920 declared that metal was superior to wood because *"metal does not splinter, is more homogeneous, and the properties of the material are much better known and can be relied upon. Metal also can be produced in large quantities, and it is felt that in the future all large airplanes must necessarily be constructed of metal"* [8].

NACA immediately began research into all-metal construction. This research yielded two significant contributions. The first was the development of clad aluminium alloys in conjunction with the Aluminium Company of America (ALCOA) and the second was research into the buckling of thin-walled structural components. The research carried out

by NACA showed that thin-walled cylindrical shells buckled well below the values predicted by classical elastic buckling theory.

Since the early tests at NACA there has been an abundance of research into the buckling behaviour of thin-walled structures, the major findings of which are outlined in section 2.3. However, as mentioned in the introduction, research has tended to focus on the behaviour of the “*as-built*” structure and there is a significant lack of knowledge as to the effects of in-service damage [7], such as dents, on this behaviour. Indeed, to the author’s knowledge, there exists no “official” published work on the effects of dents on the ultimate compressive strength of aircraft structures. The findings of the IARCAS technical report [2], which states “*Today no allowable dent limits on stiffeners exist in the Structural Repair Manual of AIRBUS. There are only allowable dent limits for skin panels, which do not take into account residual stresses introduced by the accident.*”, also indicate the lack of “in-house” knowledge in this area. Correspondence with aircraft structural repair engineers, ex-Boeing employees and Federal Aviation Administration (F.A.A.) employees indicate that this is also the case for Boeing [9].

Although there is a lack of data as regards the effects of in-service damage, such as dents, on aircraft structures, there has been considerable investigation into their effects in other fields, such as marine and off-shore engineering [10,11] . Section 2.6 discusses the major points of interest arising from these studies that are relevant to the present research.

Prior to this a description of the actual structure of the aircraft fuselage and an introduction to the relevant terminology is given in section 2.2. Section 2.3 outlines the development of buckling theory related to thin-walled structures. Section 2.4 details the sources of damage aircraft encounter during their in-service lifetime. Section 2.5 outlines current repair practices for this form of impact damage. Following this section 2.6 examines the findings from other areas of engineering into the effects of in-service damage on the compressive buckling response of thin-walled structures.

Section 2.7 introduces the numerical method employed in this research, the Finite Element Method (FEM) and chronicles the historical development of FEM. This is followed in section 2.8 with a detailed review of the finite element method as applied to the modelling of dents in thin-walled structures.

## 2.2 Fuselage Structure

Prior to discussing the detailed buckling of thin-walled structures it is important to outline the basic functions of conventional fuselage design and the components that make up the structure. The basic functions of an aircraft's structure are to transmit and resist the applied loads, to provide an aerodynamic shape and to protect passengers, payload and systems from the environmental conditions encountered in flight [12]. In order to meet these criteria with minimum weight most modern aircraft utilise the semi-monocoque design, an example of which is shown in Figure 2.1. The semi-monocoque design consists of a cylindrical structure composed of a thin skin covering which is stiffened by longitudinal stringers and circumferential frames to enable it to resist bending, compressive and torsional loads without buckling.



**Figure 2.1** Beluga fuselage, internal view showing semi-monocoque design

In the semi-monocoque design the skin acts to resist the aerodynamic pressure loads and also transfers shear loads by diagonal field tension [12, 13, 14]. The frames maintain the shape of the cross section and also act with the skin in redistributing pressure loads. The stringers act as columns in resisting compressive stresses with an effective length equal to the panel length or frame spacing. Although the thin skin is efficient for resisting shear and tensile loads, it buckles under comparatively low compressive loads. Rather than increase the skin thickness and suffer a consequent weight penalty, the stringers are attached to the



skin and frames, thereby dividing the skin into small panels and increasing the buckling and failing stresses [15].

## 2.3 Buckling of Thin-walled Structures

When a structure subjected to compression or combinations of shear and compression undergoes visibly large displacements transverse to the load then it is said to buckle. For small loads the process is elastic since buckling displacements disappear when the load is removed. Buckling can be stable, where displacements increase in a controlled fashion as the loads are increased and the structures ability to sustain loads is maintained, or unstable, where deformations increase instantaneously, and the load carrying capacity of the structure decreases rapidly [12]. Neutral equilibrium is also a theoretical possibility during buckling; this is characterised by deformation increase without change in load.

The simplest case of buckling is that of a perfectly straight column, Figure 2.2, the behaviour of which is reflected in the shape of its load displacement curve referred to as the equilibrium path. For the case of a perfectly straight centrally compressed column the equilibrium path is characterised by an initial vertical segment with no out-of-plane displacement. This state lasts until the increasing load reaches the critical load,  $P_c$ . When the load reaches the critical load buckling takes place suddenly without any further load increase and lateral deflections grow instantaneously in either equally probable direction. Therefore, the equilibrium path bifurcates into two symmetric secondary paths after buckling as shown in Figure 2.2.

This problem was first solved by Leonard Euler in 1744. Euler found for the case of a perfectly straight, centrally compressed column, built in vertically at the base with the upper end free, that the smallest critical load is

$$P_c = \frac{\pi^2}{L^2} EI \quad (2.1)$$

where  $E$  is the Young's modulus,  $I$  is the moment of inertia and  $L$  is the length of the column. The buckling load for other boundary conditions is easily found by direct solution of the corresponding Eigenvalue problem.

Euler's pioneering work became the basis of what is known as the "classical" theory of elastic buckling of structures, in which the governing equations of the problem are

linearised. The resulting eigenvalue problem yields the bifurcation buckling loads as eigenvalues and the corresponding modes as eigenvectors.

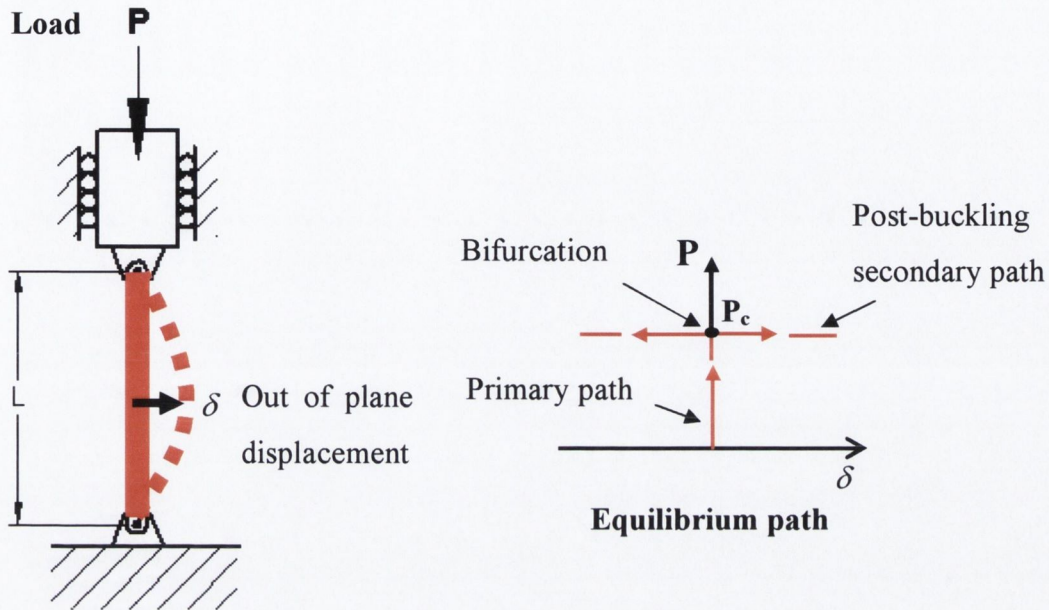


Figure 2.2 Column buckling

By the early 1900's classical elastic buckling theory was thought to be well understood and had been successfully applied in many fields of engineering. The rapid rise in air transportation in the 1930's required lightweight structures that were structurally efficient in supporting high buckling loads. The solution was the stiffened thin shell, or semi-monocoque design as described in Section 2.2. As a consequence, this period saw extensive experimental studies, most notably by Donnell [16] at California Institute of Technology and Lundquist [17] at the National Advisory Committee for Aeronautics, on thin cylindrical shells under compression.

The experimental buckling values arising from these programmes showed values of between 10 and 50% of those predicted by the classical theory which predicts buckling of cylinders under uniform compressive stress  $\sigma_c$ , given by:

$$\sigma_c = \frac{E}{\sqrt{3(1-\nu^2)}} \left( \frac{t}{R} \right) \quad (2.2)$$

where  $E$  is the Young's modulus of the material,  $\nu$  the Poisson's ratio of the isotropic material,  $t$  is the wall thickness and  $R$  is the radius of the shell. Not only were the

experimental results below those predicted by classical theory, but they also showed a wide scatter for specimens that were nominally identical and the buckling failures were often catastrophic. These disturbing results were the impetus for intensified research to explain the physical phenomena and the divergence from the classical theory. An early breakthrough in understanding this buckling behaviour was achieved by Von Karman and Tsien [18]. They argued that the behaviour of a cylindrical shell under axial compression is essentially non-linear and were able to simulate the main features of shell buckling by means of experiments on a simple column that was laterally restrained by a slightly non-linear spring that represented the membrane stretching behaviour of the shell. As a result of intensive research studies over the years [19, 20], the non-linear physical behaviour of thin-walled structures is now well understood and is summarised below.

Figure 2.3 depicts the buckling behaviour of axially compressed columns, flat plates, and cylinders for theoretically perfect elements and those containing imperfections. Referring back to the perfect column, or “Euler Column”, the sudden buckling behaviour which can follow either to the right (0, 1, +A), or to the left (0, 1, -A) is depicted. This horizontal buckling behaviour can be explained by the fact that after buckling no significant transverse tension membrane stresses are developed to restrain the lateral motion and as a result the column is free to deflect laterally under the critical load.

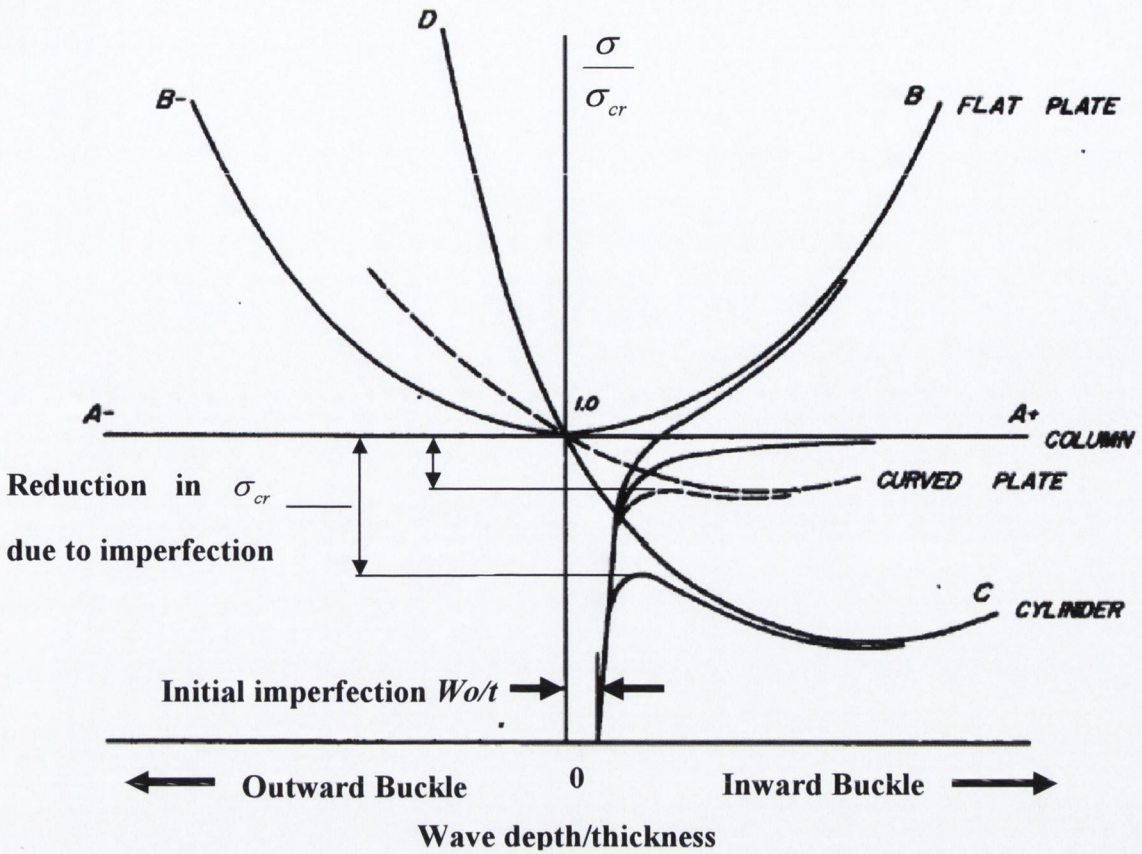


Figure 2.3 Buckling-stress ratio as a function of buckle wave depth for axially compressed columns, plates and cylinders [6]

In contrast to the column, the flat plate does develop significant transverse tension membrane stresses due to the restraint provided by the boundary conditions at the unloaded edges. These membrane stresses act to restrain lateral motion and thus, the flat plate is capable of carrying loads beyond buckling as indicated in Figure 2.3 and Figure 2.4. As was the case for the Euler column the flat plate can also follow either the right (0, 1, B+) or the left (0, 1, B-) path.

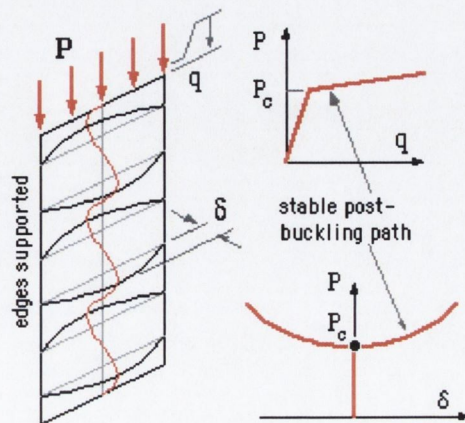


Figure 2.4 plate buckling

For the axially compressed curved plate and cylinder the effect of curvature is to shift the flat-plate postbuckling parabola downward and to the right. By shifting the parabola to the right buckling will only follow the right branch (O,1,C), because of the lower loads involved, with the result that inward buckling is observed in curved plates and cylinders [19].

Unlike the case of the flat plate where transverse tensile membrane stresses are developed, the inward buckling of curved plates and cylinders causes superimposed transverse membrane stresses of a compressive nature, resulting in a buckling form that is unstable. Hence, for curved elements buckling is often coincident with failure, a phenomenon known as “oil-canning” or “snap through”. For structures where tensile transverse membrane stresses are superimposed after buckling classical linear theory has been shown to yield results correlating well with experiments, however for the case where compressive transverse membrane stresses develop, the resulting instability of the buckle form necessitates the use of non-linear theory. This explains the observed sudden failures in the experimental tests performed by NACA in the 1930’s.

Curved plates under axial compression buckle at higher stresses than comparable flat plates due to the increased bending stiffness [19]. This behaviour is described by the curvature parameter  $Z$ , known as the Batdorf parameter, [6]

$$Z = \frac{b^2}{Rt} \sqrt{1-\nu^2} \quad (2.3)$$

where  $b$  is plate width,  $R$  is radius of curvature,  $t$  is plate thickness and  $\nu$  is Poisson’s ratio. For values of  $Z$  below approximately 5 the buckling stress is the same as for a flat plate with comparable boundary conditions. For  $Z$  values greater than 1000 long cylinder behaviour dominates with insignificance of boundary conditions. The intermediate range shows a transition from flat plate to cylinder behaviour.

While the nature of the membrane stresses explained the divergence from classical elastic buckling theory, there was still the large scatter in nominally identical specimens to be accounted for. This has since been attributed to the effects of initial imperfections [20, 21, 22]. Figure 2.3 also plots the curves for the given structural elements with initial imperfections present. Note that for flat plates the effect of the initial imperfection is slight except in the region where the load approaches the buckling load. For the imperfect flat plate the sudden change in stiffness disappears and the onset of buckling is more gradual.

In contrast to flat plates for cylinders and curved plates a substantial decrease in the buckling load may result, as shown in Figure 2.3.

In the case of stiffened curved panels, which are of interest to this research the sensitivity to imperfections is less than for un-stiffened panels, i.e. they exhibit a stable postbuckling behaviour for a larger range of  $Z$  values. There are a number of reasons for this:

1. The stringers carry a large part of the axial compressive load, thus reducing the plate load.
2. They also prevent out-of-plane and in-plane motion and impose a different buckled shape.
3. The built-up nature of the stiffened panel means that the ratio of the depth of the imperfections to the effective plate thickness is smaller than for unstiffened panels.

The stiffened shell optimises the concept of “effective width” first proposed by Von Karman in 1932 [18]. Von Karman's theory was based on observations that up to the point of buckling the stress distribution in flat and curved panels is uniform across the width. After buckling, however, non-uniformities arise in the load and stress distributions. Von Karman noted that this was a non-linear response with the center of the plate incapable of carrying stresses greater than the buckling stress while the edges were stabilised by the boundary conditions and could continue to carry increased loads through an efficient membrane stress system. This response is depicted graphically in Figure 2.5 where (a) shows the stress distribution before buckling, after buckling and far into the postbuckled region and (b) depicts the idealised representation of this response. This concept of effective width is a quick and approximate method for calculating the postbuckled strength of plates and stiffened shells.

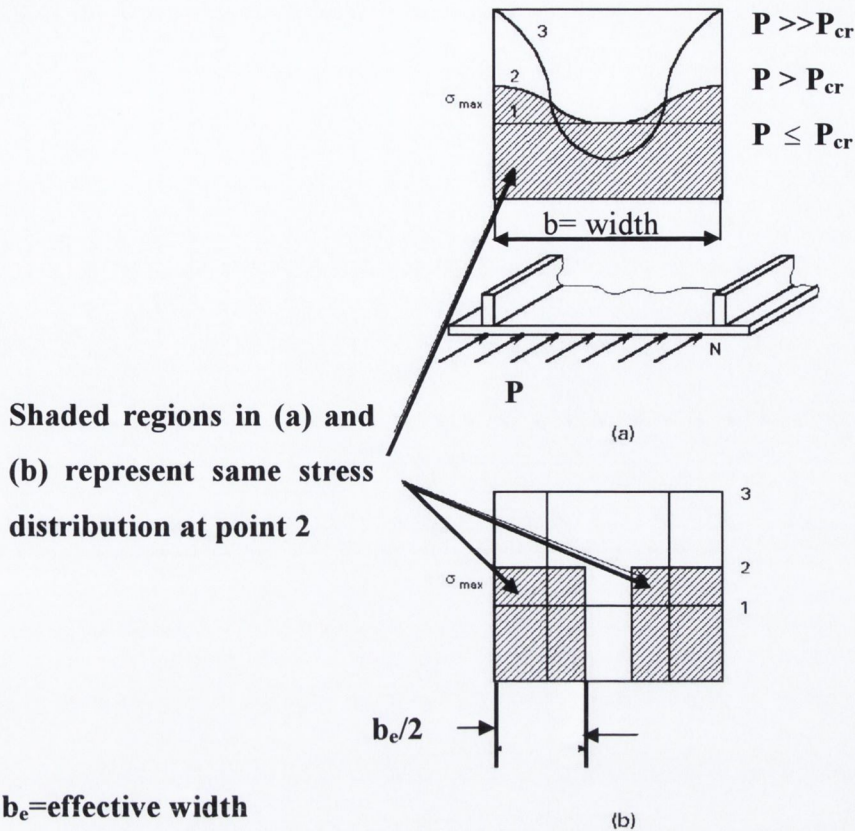


Figure 2.5 Effective widths: (a) true stress distribution, (b) idealised stress distribution

Since the early work of Von Karman a number of important advances have been made in explaining the postbuckled behaviour of thin-walled structures. The most notable advances were made by Cox [23], whose approach considered averaged membrane strains and neglected some in-plane effects, resulting in an underestimation of postbuckling strength and stiffness. This approach came to be known as the “lower bound approach”, due to the inherent conservatism of the method. Marguerre [24] developed a more rigorous approach determining the in-plane stresses and strains from exact satisfaction of compatibility conditions with the out-of-plane deflections and the principle of Minimum Potential Energy to calculate the final relationships between loading and displacements.

While great strides have been made, from both a theoretical and an experimental viewpoint, in explaining the divergence from classical buckling observed in the NACA experimental studies in the 1930’s the focus has been on structures in their as built form [25]. As a result, there still remains a considerable lack of knowledge on the response of thin-walled structures with in-service damage, such as dents, to compressive loading. Such damage, while not unlike the case of initial imperfections of large amplitude, has the associated complication of residual stresses. The coupling of the effects of change in shape

and elastic stress redistributions cause the thin-walled structure to develop high bending stresses to compensate for the loss in membrane resistance to the applied loads.

## 2.4 Impact Damage

Having outlined the complexity of the factors affecting the buckling response of thin-walled structures, this section outlines the sources of impact damage on aircraft structures. Aircraft impact damage can be caused by a number of sources, such as low velocity collisions between service cars, boarding bridges or cargo and the structure. In addition to baggage handling mishaps and dropped tools during maintenance.

Figure 2.6 shows a cargo loading system and although preventative measures are taken to safeguard against impact, such as rubber guards to dampen impact energies and prevent dents with sharp notches, as shown in Figure 2.7, impact damage is still a major problem.



**Figure 2.6 Cargo loading system**

Despite all preventative measures and training in-service impacts are unavoidable occurrences. Figure 2.8 shows a repair to the skin around the front entry door of an Airbus; the damage was caused by impact with the boarding bridge.





**Figure 2.7 Rubber pads to safeguard against impact**



**Figure 2.8 Repair of impact damage to front entry door of Airbus A320 at Dublin Airport**

In addition to low velocity impacts, aircraft can experience dents due to a number of high velocity sources such as runway debris, hail, bird strikes, ice from propellers striking the fuselage, engine debris and tyre shrapnel from thread separation and tyre rupture.

Figure 2.8 shows a dent on the upper surface of the rear fuselage of an Easyjet Airbus aircraft. The aircraft was caught in an electrical hail-storm outside of Zurich and suffered substantial impact damage. The photo was taken by the author at FLS Aerospace facilities at Dublin airport. The damage, which was mainly in the form of dents, resulted in large sections of the skin being cut out and replaced while smaller dents without cracks were reworked. In total, the cost of the repairs was almost 1 million euro. But more importantly, it took six months to repair resulting in the loss of revenue.

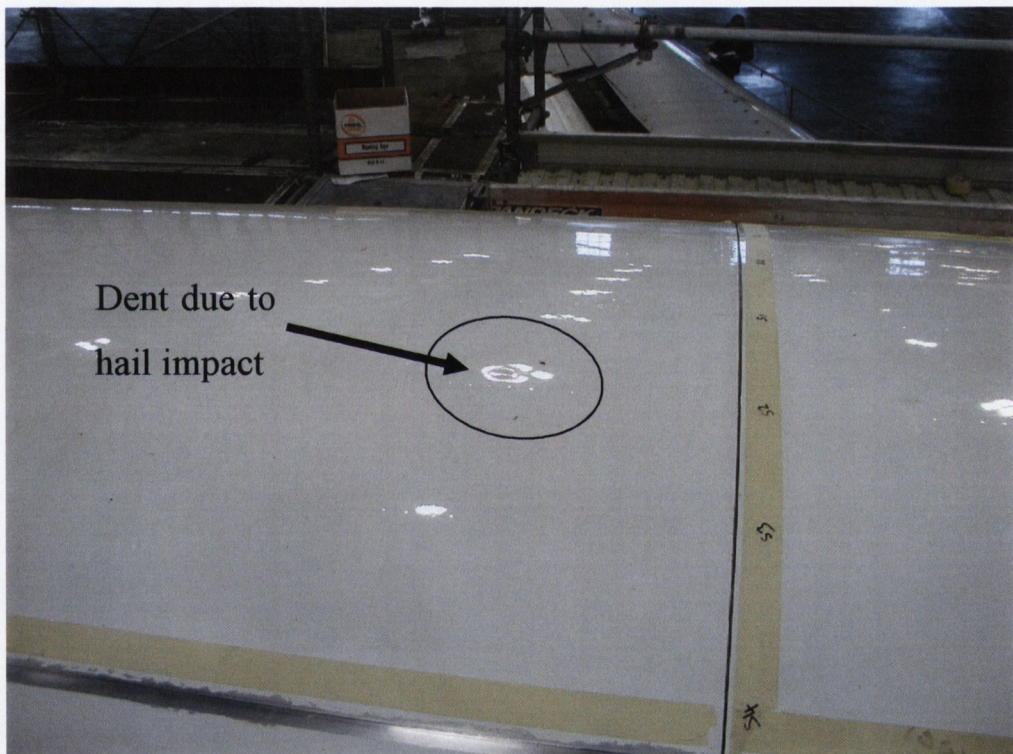


**Figure 2.9 Dent to hail on upper fuselage of Easyjet Airbus**

Figure 2.10 illustrates dents on the leading edge of the right wing of a McDonnell Douglas MD-81. A hail storm was also the cause of damage in this case [26].

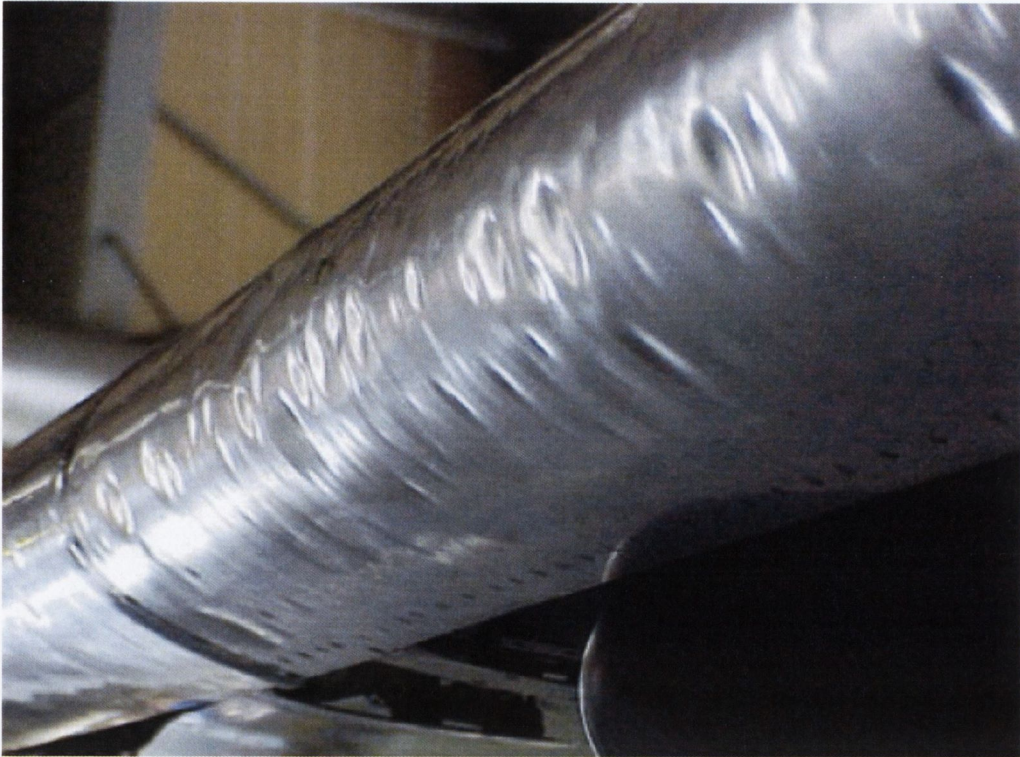


Figure 2.10 Dents on right wing leading edge of Finnair McDonnell Douglas DC-9-81 [26]

## 2.5 Aircraft Repair

### 2.5.1 Introduction

Aircraft repair and maintenance is both a costly and safety critical process where damage-tolerance is the key factor. Damage-tolerance is a structural design and inspection methodology used to maintain safety by considering the possibility of metal fatigue or other structural damage. The underlying principle for damage-tolerance is that the initiation and growth of structural fatigue damage can be anticipated with sufficient precision to allow inspection programs to detect damage before it reaches a critical size. A damage-tolerance evaluation predicts where fatigue cracks are most likely to start in the airplane structure, their trajectories and rates of growth under repeated structural loading [27]. The evaluation also predicts the size of the damage at which strength limits are exceeded and performs an analysis of the potential inspection opportunities for detecting the damage. This information is used to establish an inspection program for the structure which, if rigorously followed, will enable crack detection before it causes major structural failure.

A repair that satisfies the static strength and durability of the original structure is damage-tolerant if the existing inspections are adequate. The "as-built" aircraft structure must be capable of carrying all stresses caused by ground and flight loads without undergoing any plastic deformation. The repair must also be capable of carrying these stresses across the repair and transferring them back into the original structure. This must be achieved without introducing any stress concentrations, due to abrupt changes in cross-section or material stiffness.

Aircraft repairs represent a challenging problem in that they are unique, occurring in varied locations and across all aircraft models. In addition, the behaviour of a repair and its effect on the characteristics of the original structure are generally not known to the same extent as the behaviour of the basic unrepaired structure. Although service histories indicate that repairs have performed well, as economic constraints result in aircraft being operated beyond their original intended service life the necessity for a greater understanding of the effects of damage and damage repairs increases because:

1. As aircraft age, both the number and age of existing repairs increase thus increasing the possibility of unforeseen repair interaction, failure or damage in the repaired area.
2. The practice of damage-tolerance has evolved gradually over the last 25 years and therefore, some or all repairs described in the airplane manufacturers' Structural Repair Manuals (SRM) are not designed to current standards.

The continued airworthiness of these airplanes depends primarily on an adequate maintenance and inspection program that ensures inspections are conducted at the right time, in the right place, and using the most appropriate procedures and techniques.

## 2.5.2 Inspection

A key component of a successful repair programme is inspection. Every repair requires some level of inspection to maintain airworthiness. That level of inspection is dependent upon the original design of the structure, the design of the repair, and the maintenance schedule of the operator. Efficient repair inspection takes advantage of the operator's maintenance or inspection program to satisfy a repair's inspection requirements. These inspections must meet certain standards in order to satisfy the inspection requirements of a repair [27]. The requirements are as follows:

- External Inspection:
  - The repair and/or base structure must be inspected within arm's length.
  - The lighting must be sufficient to find distress in the repair and in the base structure
  - Fairings must be displaced or removed.
- Internal Inspection
  - The repair and/or base structure must be inspected within arm's length.
  - The lighting must be sufficient to find distress in the repair and in the base structure.
  - Interior furnishings must be displaced or removed (interior panels, insulation, liners, etc.).

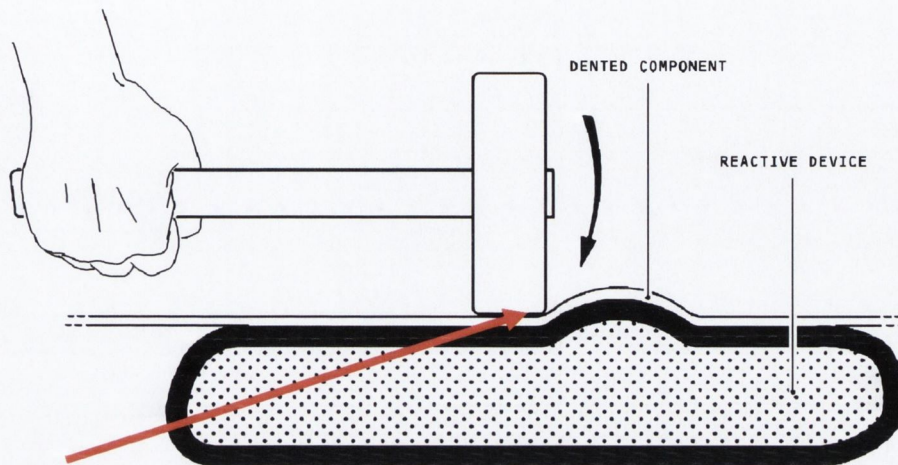
### 2.5.3 Current Repair Procedures for Dents

Having looked at the factors common to all repairs such as inspection intervals, static strength requirements and damage tolerance, the specific repair of interest to this research repair is described in detail in this section. The repair procedure for dents is broken down into two areas; one for dents on skin which can be dressed out and the other for dents on structural members which currently are not allowed and must be replaced.

#### 2.5.3.4 Dents on Skin Material

The Airbus Structural Manual allows “dress out” or “dress back” of dents provided certain criteria are met. The dress out operation is similar to “panel beating” for automotive mechanics. The added complications for the aircraft mechanic are that in order to carry out the dress out, the dent must be accessible from both sides. This often requires time consuming removal of internal furnishings in the fuselage structure. In addition, it requires two experienced personnel, one on each side, with adequate communication between them.

The dent must first be inspected using Non-Destructive Testing (NDT). This is to ensure that there are no cracks present in the dent before dress out, as the dress out could close a crack thereby preventing discovery during the NDT subsequent to dress out. The dented area is then cleaned using a specified cleaning agent as stated in the SRM. The dent is then reworked using a lead filled plastic hammer with a smooth surface, Figure 2.11; the lead filled hammer helps avoid kickback and the plastic covering helps to avoid causing damage to the skin.



**Start at edge with lowest deformation.**

**Figure 2.11 Dress out procedure [28]**

In addition it is necessary for the mechanic on the concave side of the dent to hold a reactive device. Such as a bag filled with sand to dissipate the force and prevent a “snap through” of the dented area during repair. The dress back should be started at the corner of the dent with the lowest deformation and continued in around the circumference of the damage spiralling inwards, until the centre of the dent is reached.

Depending on the deformation ratio, or dent depth to dent length, a complete dress out is not always successful. In such cases it may be possible to bring the dent to within acceptable limits. Care should be taken to ensure that no “Oil can effect”, where the skin simply pops back and fourth, is set up in the repaired area. The repaired dent must then be cleaned and NDT performed from inside and outside to inspect for cracks.

Strict criteria are applied to assess whether a dent can be dressed out or whether the skin must be replaced. This is due to a lack of knowledge as to the effects of dent dress back on the characteristic properties of the sheet material from both a static and a fatigue viewpoint. Currently no consideration is made of the effects of the induced residual stresses due to dress back. The criteria are also based on the limitations of the technician’s

ability to successfully dress back dents. While it is possible for highly skilled technicians to dress back deeper dents in thicker skins, the allowables are based on the results of a small experimental test involving technicians from the Hamburg test facility [29]. The current limits are based on the ability of the average technician in that experimental test as an indication of what a typical aircraft mechanic can successfully dress out to within acceptable dimensions. These tests combined with heuristic data resulted in the following criteria being set:

- The dent must be in skin made from an aluminium alloy material
- The skin thickness must not be greater than 1.6mm.
- The dent must be free of sharp edges or severe local distortion
- The internal structure and adjacent fasteners must not be affected.
- The dent must be dressed out to within specified dimensions; otherwise the skin panel must be replaced.

Furthermore, the dent must meet certain criteria related to depth and location, which are aircraft and panel specific. Figure 2.12, plots the diagram used in assessing allowable dents for dress back, where T is the skin thickness in the dented area, D is the maximum depth of the dent, A is the distance from the maximum depth of the dent to the edge of the adjacent stiffening member and B is the distance between the outer contour of the dent to any cut-out in the skin or any fastener row.

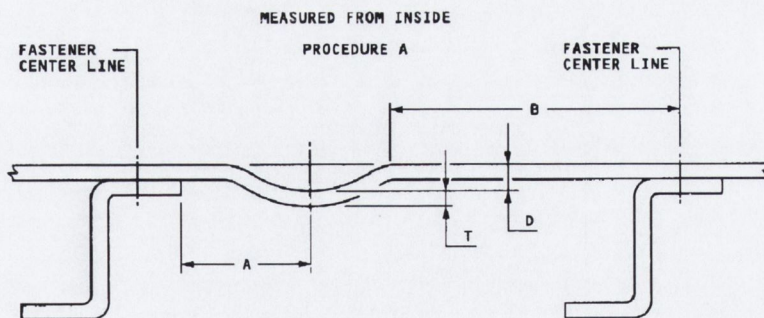


Figure 2.12 Measurement of allowable dent in skin [28]

Figure 2.13 plots the corresponding allowable damage limit diagram from the Airbus Structural Repair Manual for the A300-600 aircraft. This graph relates dent depth to skin thickness for cases where  $D \leq 0.1A$  and  $B \geq 15\text{mm}$ .

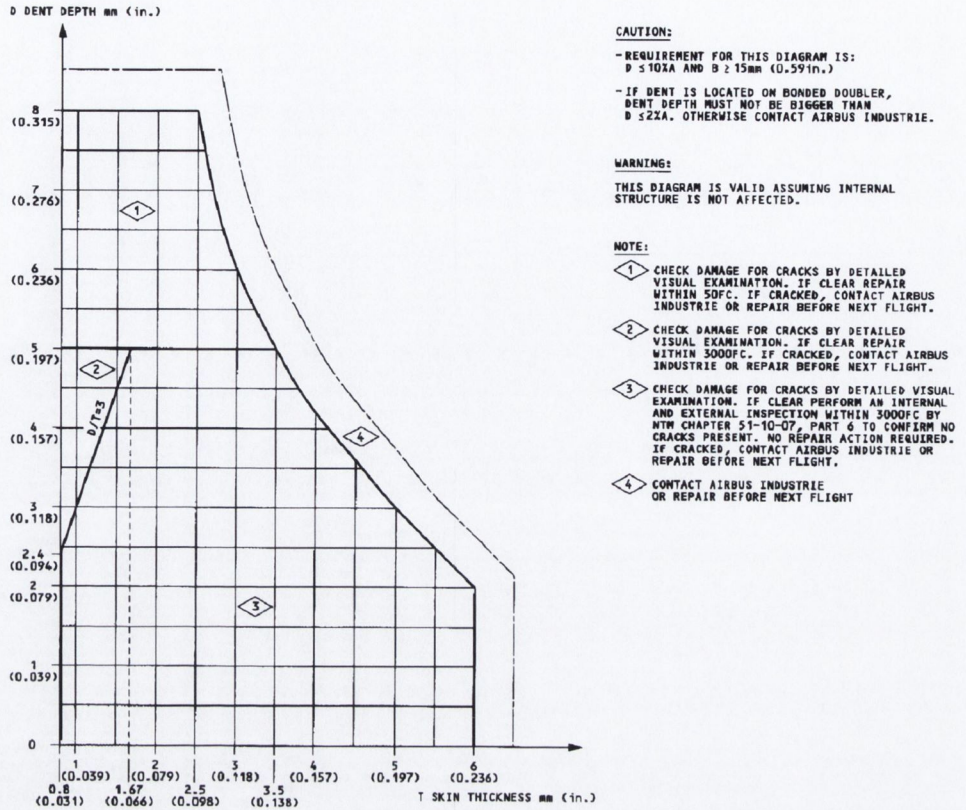


Figure 2.13 Allowable dent limits in skin sheet for given flight cycles (FC) [28]

As can be seen from the graph there are four corrective actions that must be undertaken depending on the location on the ADL diagram. A number of separate ADL charts exist for each aircraft based on D and B values.

As mentioned previously in section 2.1 and documented in the IARCAS technical report [2], the dent dress-back procedure does not account for residual stresses in the skin. This is an area of interest not only from the static viewpoint as to whether the residual stresses due to a dent or reworked dent cause instability, but also from a fatigue viewpoint. This is because cold working the aluminium sheet to dress back the dent can increase the temper and reduce the toughness. A recent study by Simmons et al [30] of Gulfstream Aerospace Corporation, on the effects of dent removal found a reduction in fatigue life of between 5% and 20% for the reworked specimens. This raises the question as to whether the repair could potentially cause more problems than the original dent.



### 2.5.3.5 Dents on Stiffeners

Stiffener members are broken down into the frames and stringers. In the case of the frames, they are not in contact with the skin. They are attached by clips and, as a result it is the clip that experiences deformation if a dent occurs on the external skin where the clip meets the skin. Usually this can be repaired by replacement of the clip. Since it is a small component this is not costly and is a relatively straightforward operation. Figure 2.14 shows an example of a failed clip rivet due to a dent on the outer skin surface. The major precaution that must be taken is that no force is used to “encourage” existing parts to line up with the clip. For example, if the skin also contains some degree of plastic deformation and the clip must be forced to meet it and the frame, this can result in very high residual elastic stresses in the clip which, under cyclic loading, could result in crack growth and fatigue failure.

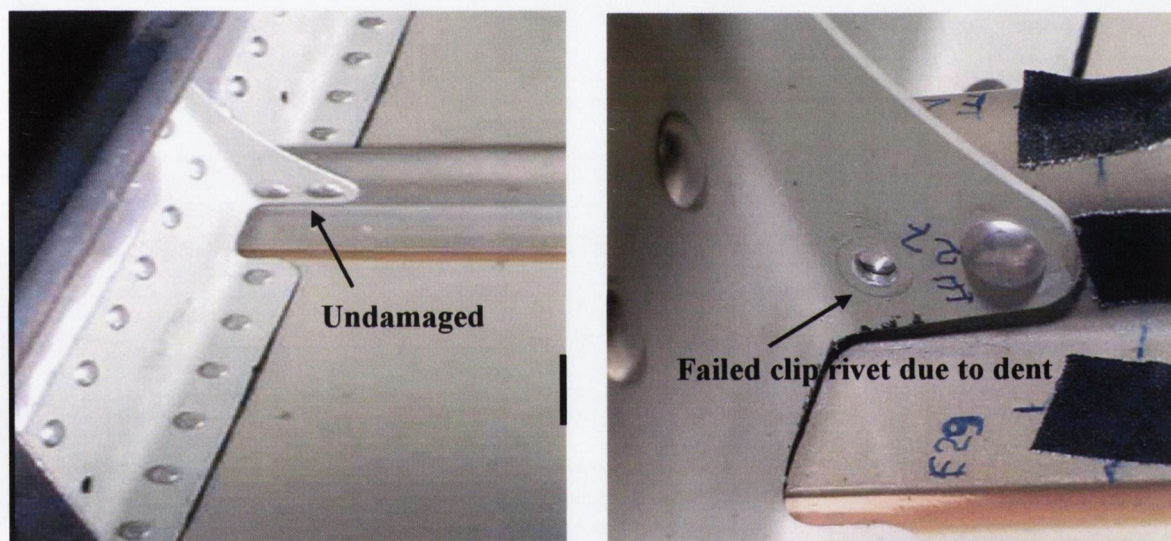


**Figure 2.14 Undamaged and damaged clip due to dent on external skin**

In the case of a dent on a stringer there are currently no allowable damage limits in the SRM and the current practice is to cut out the affected area, replace it and apply a coupling or splice, bridging the original structure and the replaced section. This is a complex and time intensive process.

Initially, the rivets in the damaged area must be drilled out. The damaged section of the stringer is then cut out and eased away from the skin using a plastic wedge. In certain cases there may be complications in separating the stringer from the skin and heat application is permitted up to a maximum temperature of 130°C. Next the edges of the damaged area are deburred and the repair parts are prepared to fit the damaged area.

Figure 2.15 shows the details from the Airbus A320 Structural Repair Manual for this repair. Number 1 and 2 refer to the stringer and the replacement stringer coupling respectively. The stringer coupling is formed from the same material as the stringer, is of the same profile and is one gauge thicker.

The parts are then placed in position to a tolerance of  $\pm 1\text{mm}$ , a filler piece being added beneath the coupling to ensure the repair is flush with the skin. The existing rivet holes are then transfer drilled to line up with the repair section and additional holes are drilled, specific details of which are contained in the SRM. Hi-Lok<sup>R</sup> fasteners are then used to install the repair. Subsequently, the parts are degreased, pre-treated for painting with chromic acid anodizing or chemical conversion coating and a primer coat applied. Finally, the parts are painted and a sealant applied.

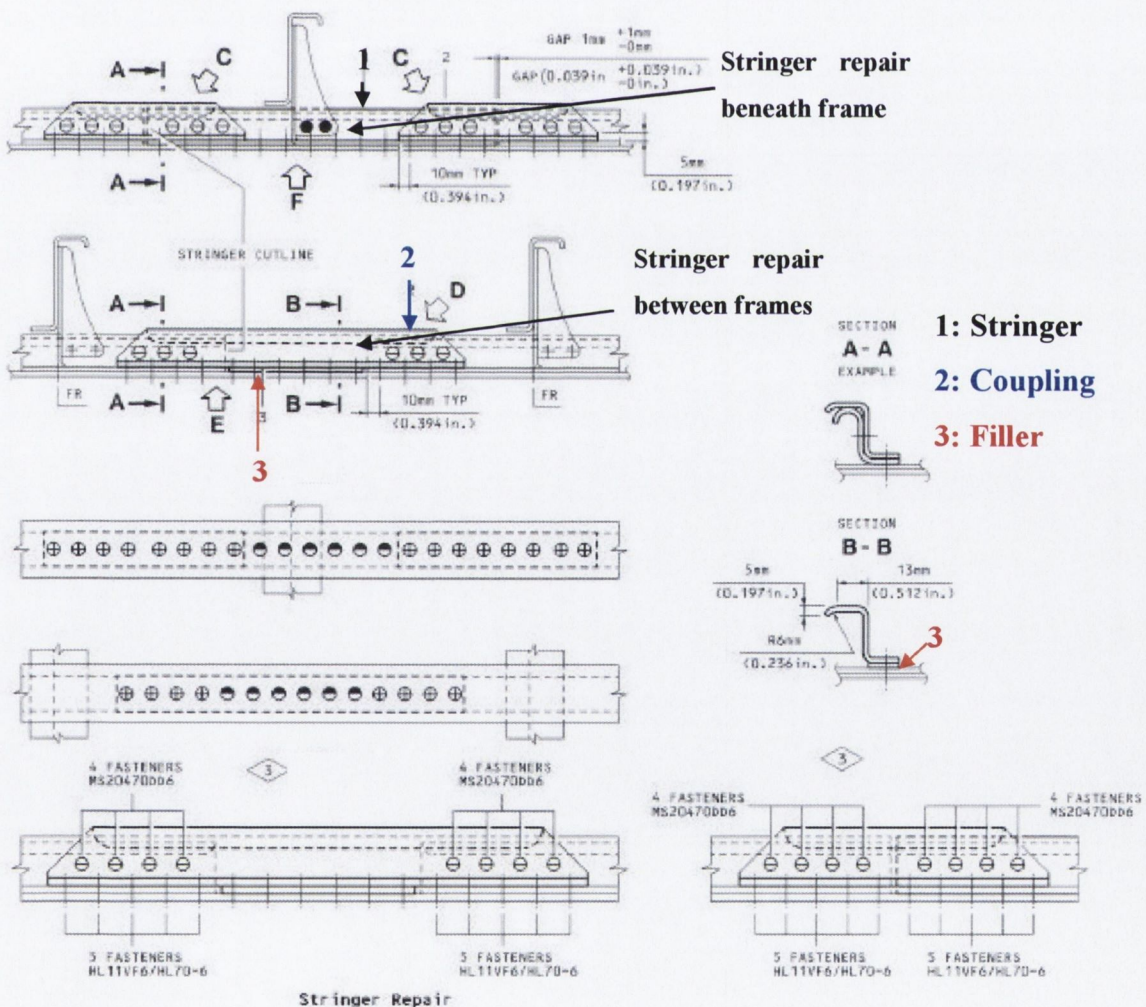


Figure 2.15 Complete Stringer Repair [28]

## 2.6 Buckling of Damaged Thin-walled Structures

In order to assess the load carrying capacity of a damaged structure, it is necessary to understand the new stress distributions due to the presence of the damage. Thin-walled structures carry loads by a very efficient membrane action, only a marginal part of the load being carried by bending stresses [31]. In the damaged form the structure still has to carry the design loads without collapsing. However, the presence of the dent introduces a change in geometric curvature which introduces large local bending and membrane stresses. This induces a local out of balance moment equal to the membrane forces multiplied by the eccentricity due to the damage which must be balanced by the structure. This is balanced by two mechanisms; bands of membrane stresses which have a moment resultant and by bending across the thickness [32]. It is important to evaluate these stress redistributions. Godoy [25] notes, *“For linear elastic structures under increasing load, the stress redistributions are uniquely defined, but for non-linear systems, there may be several redistributions. Thus, the state of stresses of a structure with damage and the way it provides equilibrium may be quite different from what was considered in the design”*.

As outlined in section 2.1 there is a lack of data regarding the effects of dents on structural stability in the field of aircraft engineering. A number of studies, however, have been conducted into the effects of damage in the form of dents of thin-walled structures in other fields of engineering, most notably in the fields of off-shore and marine engineering. The relevant findings of this research are summarised below.

In 1982 a report commissioned by the U.K. Department of Energy on stiffened shell structures for offshore platforms concluded that *“many platforms were in close proximity to major shipping lanes and that the risk of collision was very high in terms of normal design code requirements.”* [33]. The 1982 report noted the high sensitivity of shell members, particularly those in the intermediate slenderness range as are found on tension leg platforms (TLP), to damage due to the unstable nature of the elastic post-critical response of a curved plate or cylindrical system. A study of damage due to accidents on off-shore platforms in 1985 found that 17% were produced by impact with a marine vessel, while 12% were due to dropped objects and 14% of these accidents led to major structural problems [34].

Due to the economic importance of oil and as a result of the 1982 report a comprehensive investigation on the effects of dents on thin shell structures was carried out at Imperial College London [10, 35, 36], and the University of Surrey [11, 33, 37, 38]. The tests involved measurement of initial imperfections, introduction of a controlled dent and loading until failure. Axial compression loading was carried out at Imperial College London while external pressure loading and combined external pressure and axial compression loading were carried out at the University of Surrey.

In the Imperial College experimental program, a total of eighteen damaged stiffened shells were tested, nine of which were stiffened by circumferential rings only. The remaining nine being stiffened by stringers in the longitudinal direction in addition to the circumferential rings [35]. The specimens tested were all representative of the thin-walled components of semi-submersed and TLP structures of off-shore platforms. The diameter for all specimens was 320mm, they were between one and five bays in length, their radius to skin thickness ratio, ( $R/t$ ), was between 133 and 267 and their length to radius ( $L/R$ ) was between 0.15 and 1.08. They were dented using a knife-edge wedge across the longitudinal stringers to residual dent depths of between 3.36mm and 17.12mm [36].

The University of Surrey experimental test programme consisted of six tests, two plain ring-stiffened shells, two T-ring stiffened shells and two orthogonally stiffened shells with forty and twenty stringers respectively. All specimens had at least three inter-ring bays. The T-ring and plain ring stiffeners were dimensioned to have the same second moment of area. This allowed the effect of torsional rigidity to be investigated. It was of interest to see whether the greater torsional rigidity of the T-ring stiffeners would have an effect on arresting the development of the damage zone when compared against the plain ring stiffener with the same flexural rigidity. As mentioned, the stringer stiffened specimens had significantly different geometries, one with forty and one with twenty stringers. These were chosen because previous tests on undamaged cylinders had shown that with forty stiffeners the shell behaves in a quasi-orthotropic manner, with the buckles which formed during the collapse encompassing several stringers. On the other hand in tests on shells with twenty stringers or fewer the buckling deformations were confined to the longitudinal panels between the stringers. Hence, the tests were designed to determine whether the presence of significant damage in the form of a dent would significantly alter this pattern.

The major lessons learned from the tests [10, 11, 35-38] are that, although the dent deformation was very local, the resulting damage spread over several bays under loading. The effect of differing geometries in resisting the spread of damage was highlighted in that the plain ring stiffened shells collapsed under very low external pressure, the plasticity developed under denting having so undermined the radial load bearing capacity of the rings that considerable load was placed on adjacent rings. When those rings in turn collapsed, due to local tripping, a cascade effect was set off. These geometries were designed to fail through local inter-ring buckling but the presence of the dent completely undermines the strength of the damaged stiffener, resulting in a different failure mode. In contrast, the greater torsional rigidity of the T-ring stiffeners arrested the spread of damage and the cylinders failed by local inter-ring buckling, as per their design.

For the orthogonally stiffened tests carried out at Imperial College London and University of Surrey, both general and local buckling modes were observed. However, the presence of the dent often promoted the initiation of a general buckling mode where a local buckling mode was expected. Although the strength loss for the axially compressed cylinders was less than expected, under external pressure and axial compression the presence of the dent overloaded the rings locally, causing the rings to collapse. The authors' note [38], "*this potentially would give rise to the cascading effect*".

Although based on a small number of tests the results from the study indicate the detrimental effect that even small amounts of damage can have on the load carrying capability of the stiffened structure. Of particular significance to the research presented in this thesis are the results from the orthogonally stiffened panels, particularly the possibility of a "cascading effect", causing multiple stiffeners to trip. This is of concern in aircraft panels due to the proximity of stiffeners.

Studies into the effects of dents on plated steel structures such as those found in the hull structures of marine ships have been carried out [39-41]. Such structures commonly suffer in-service damage such as berthing collision and cargo impact during loading or unloading. Paik and Thayamballi [39] carried out a finite element investigation into the effects of dents on the ultimate compressive strength of a simply supported rectangular plate. The complex nature of dent formation is idealised as an in-built geometric deformation and studies are carried out varying dent location, size and depth. While the finite modelling as used by Paik and Thayamballi is detailed further in section 2.8, the major findings of the

research were that dent diameter was of greater influence than dent depth, and proximity to the unloaded simply-supported edges resulted in a 20% reduction in ultimate strength. Hu et al [40, 41], report the findings of an experimental and finite element investigation into the ultimate collapse strength of stiffened plate shell structures. The primary goal of the programme involved developing a compressive test rig for intact steel plates with one central longitudinal stiffener for the Canadian Forces and United States Interagency Ship Structure Committee. Two experimental tests were carried out on dented specimens, one with a dent of 19.97mm and one with a deeper dent of 35.51mm. The ultimate compressive loads, when compared with identical intact specimens, were reduced by 23 and 36% respectively. Finite element models of the test procedure predicted reductions of 23 and 32%. Both dented panels failed due to a combination of plate buckling and overall flexural buckling. An interesting result observed in both the experimental and finite element tests as reported by Hu et al [40, 41] is that, after the limit load is reached, the dented panels show a more controlled and gradual loss in stiffness than the undamaged panels.

This was a point also noted by Hambly and Calladine [42]. They carried out a number of experiments on the compressive strength of dented aluminium drink cans, these specimens being chosen for their ready availability, low cost and strict manufacturing tolerances. The authors reported on the possible benefits of introducing controlled damage to act as an early sign of impending failure as *“the undamaged cans failed abruptly and without warning, whereas the damaged cans had a phase of stable growth of the dent before failure”* [42].

## 2.7 Finite Element Method

### 2.7.1 Historical Background

The Finite Element Method (FEM) is a numerical procedure that can be applied to solve a wide range of problems in engineering. The method is based on the discretisation of a real world continuous system into a finite number of well defined components, or elements [43]. This discretisation is necessary since continuous systems can only be defined using the mathematical fiction of an infinitesimal, and mathematical solutions using differential equations exist only for oversimplified situations. While discretisation as a method of solving larger problems has been used for centuries, Courant has been credited with being the first person to develop the finite element method for his investigation in 1943 of torsional problems using piecewise polynomial interpolation over triangular sub-regions

[44]. The first significant step in the utilisation of the finite element method was taken at Boeing during the 1950's where Turner formulated the direct stiffness method and the first continuum based finite elements [44]. It was a subsequent paper by Turner, Clough, Martin and Topp, that is recognised as the start of modern FEM as used in the majority of present day commercial codes.

It is no coincidence that the roots of the FEM can be traced to the aeronautics industry, as at that time large aircraft companies were among the few who could afford the mainframe computers necessary to run finite element simulations. However, with the phenomenal increase in computing power since the late 1970's the application of the finite element method has grown rapidly. This development coupled with the simultaneous increase in complexity of engineering problems, for which analytical solutions are not applicable, has been the primary driver in the development of finite element technology. This growth in the application and use of the FEM is set to continue as computer processing power increases and finite element commercial packages become more user-friendly and intuitive.

## 2.7.2 Finite Element Analysis Theory

Finite element analysis (FEA) is the application of the finite element method. As described in section 2.7.1, the basic concept is that a continuous problem can be subdivided into discrete components or elements of finite dimensions known as "Finite Elements". The original body or structure is then considered as an assembly or "mesh" of these elements connected at a finite number of joints known as "Nodes" or "Nodal Points". Numerically, an FE mesh is represented by a system of algebraic equations, describing the geometry, material properties and loading conditions of the structure. These equations are then solved for unknowns at the nodes. After obtaining a solution for one element, the solution procedure is applied to all of the remaining elements in turn. An assembly of all the partial element solutions leads to an overall solution.

Since the finite element model has only a finite number of unknowns, it can yield only an approximate solution, the answer converging to the true solution as the number of elements tends to infinity. To achieve the actual solution, the element size would have to tend toward the mathematical fiction of the infinitesimal. Obviously, since computational power

is finite, this is not possible and there is therefore a trade off between accuracy and run times. The key is to balance this trade off for each model. Bakker [45] states,

*"The objective of the FE method is not to describe reality as accurately as possible, but to find the simplest model resulting in a sufficiently accurate description of reality."*

To achieve this, the analyst must be very clear on what it is they wish to learn from the mechanical model. This will often require a lot of insight into the behaviour of the structure. Good practice is therefore to start with a simple model, increasing the complexity step-by-step as necessary. Caution must be applied not to over complicate the model. Without sufficient knowledge this idealisation of reality into a simpler mechanical model can result in serious errors. During this initial phase, known as pre-processing, the following decisions must be made:

1. The choice of mechanical approach describing the behaviour, e.g. beam theory, shell theory or 3D stress theory. This choice determines how the geometry of the structure will be described, namely as a line, a plane or a solid and what the corresponding choice of element will be.
2. Assumptions regarding the magnitude of deflections, strains and rotations. This determines the type of geometrical non-linear analysis that should be run.
3. How the material behaviour will be modelled.
4. How accurately the geometry of the structure must be modelled in order to get accurate results.
5. How loads and supports should be modelled.

These steps must be carried out for every model and they account for the majority of the analyst's time in performing an FE analysis. Following this, the solution is run before post-processing of the results. It is in the post-processing of the result that the analyst must have a fundamental grasp of the real mechanical behaviour of the structure. This is because while the finite element model may yield results, they are merely representative of the numerical approximation of the real life problem set up in the pre-processing phase and an inaccurate model of reality will yield misleading results.



## 2.8 Finite Element Modelling of Dented Structures

The literature relating to FEM contains a number of papers on the finite element modelling of damaged thin-walled structures. This section summarises the methods used and conclusions drawn in the papers of most relevance to the current research.

An early attempt at finite element modelling of damaged thin-walled structures was made in conjunction with the experimental programme carried out at the University of Surrey and the Imperial College London, as described in section 2.6. The finite element models were developed using an in-house finite element program developed by Trued and Bates, [46, 47] to perform non-linear studies on plates and shells. The program was used to perform correlation studies with the experimental tests and to carry out an investigation into varying the dent parameters [33]. In the finite element model the material was modelled as elastic-perfectly plastic and the dent was modelled by its geometrical characteristics only. What this means is that the shape of the dent was built into the structure during modelling. This simplification neglects the associated residual stresses caused as a result of indentation and also assumes that the dent deformation is restricted to the locality of the dent thereby neglecting any global deformation removed from the dent, such as residual deformations that may occur near supports due to plasticity. Despite these simplifying assumptions the finite element models showed acceptable correlation with the experimental results, concluding that while damage in the form of dents due to operational impact is significant, the effect on load carrying capacity can range from only slight reductions up to about 30% for slender geometries. The author notes

*“While the results are complex there is a general indication that the major reductions in strength are due mainly to stress concentrations occurring in the region adjacent to the dent...These stress concentrations cause early yielding and trigger collapse”, [33].*

Further finite element investigations into the effects of varying dent depth concluded that predicted strengths showed a gradual decrease with increasing dent depth, but no dramatic changes. The information gained from both the finite element and experimental program has since been used in the construction of TLP's. A double skin is now incorporated into the splash zone so that damage to the outer skin by ship impact can be catered for by load transfer through the inner skin, [33].

Paik and Thayamballi, in a 2003 paper on the ultimate strength of simply supported dented steel plates, also modelled the dent as an assumed hemi-spherical geometric idealisation [39], again neglecting the residual stresses as was done by Harding and Onoufriou some eight years earlier [33]. Paik and Thayamballi indicate that these residual stresses are of secondary importance to the change in shape, but no evidence to quantify this is given. The simplification taken in the research also highlights the numerical difficulty involved in accounting for geometric, material and contact non-linearities. Paik and Thayamballi also simplified the material modelling, assuming an elastic-perfectly plastic model. Paik and Thayamballi carried out a number of investigations into the effect of varying the dent depth, diameter and location. He concluded that the depth had little effect on compressive strength as long as the diameter was small, that increasing diameter had a significant effect on compressive strength and that locating the dent near the unloaded edges resulted in a reduction of compressive strength of 20% compared to a dent located at the centre of the plate.

The literature reveals a number of cases of finite element modelling of dented structures for a different load case; of sub-sea or onshore pipelines, where cylindrical shells are continuously supported along their base. These pipelines can experience in-service damage from a number of sources such as dragging anchors in the offshore case [48], and earth moving equipment in the onshore case [49], [50]. Brooker [48-50] cites the lack of published research on the effects of denting, noting that the available Norske Veritas risk assessment guidelines for assessing the effects of dents are based on an inherently conservative rigid-plastic model. Brooker's finite element model was developed in the commercial general purpose FE package, ABAQUS. Brooker's models were based on 1/4 symmetry using shell elements with the end restrained from translation and cross-sectional distortion. The indenter was modelled as a knife-edged rigid object with a horizontal radius of 10mm to improve convergence properties. This was a significant improvement on the modelling of the dent from the geometric dent modelled in [33] and [39]. The material model, however, was assumed perfectly plastic and as a result the effects of strain hardening of the material were not accounted for after the denting operation. The significant improvement in Brooker's modelling technique relates to the incorporation of the residual stresses by modelling the indentation phase. An interesting result, from the point of view of the present research, was that although radial deflection was localised to within a few diameters of the dent, the plastic yield zone could extend well beyond this. Obviously this is of importance in the present study to ascertain whether the effects of the

dent cause local plasticity at stringer-frame supports due to the greater rigidity of the frame cross-section.

The paper on dent removal by Simmons et al [30] cited in section 2.5.3.4 reported a finite element model where the dent was created by incrementally applying forces to nodes in order to create a residual dent comparable to the experimentally measured geometry. This method has also been used in recent investigations by Airbus [51] into the residual stresses after dent dress-back. This technical report [51] details how the dent is created and dressed back incrementally using nodal forces.

It is clear from the available literature on the finite element modelling of the effects of dents, that there is considerable scope and need for the research carried out in this thesis. The research presented in this thesis aims to improve on the above studies, accounting for residual stresses and contact non-linearities by modelling a rigid object impacting on the structure. The present research will also establish the importance of these residual stresses by modelling the geometric damage without the stresses and investigating the compressive response of such a model. This will establish whether the modelling assumption of a geometric dent is a valid one from an ultimate strength perspective.

## PART III

### 3 EXPERIMENTAL METHODS

#### 3.1 Introduction

This chapter describes the experimental testing programme carried out at Trinity College Dublin and at the Airbus structural testing facilities in Hamburg, Germany. The loading and boundary conditions are outlined in detail as it was the objective of the finite element model to replicate these conditions as accurately as possible.

#### 3.2 Coupon Denting Test Rig

Prior to the full scale panel testing, an initial testing programme was carried out in Trinity College Dublin on rectangular coupons of aluminium 2024T3. This testing was carried out to establish a baseline against which the FE methodology being employed could be benchmarked before full scale results were available, thus giving confidence in the choice of element, contact criteria, boundary conditions and material models used in the finite element model.

Having verified the finite element modelling techniques using the coupon sized model, a model of the full panel geometry was then developed and the predicted denting loads were used in designing the full-scale denting rig. In addition, the coupon sized test rig provided a tangible “*feel*” for the process, the scale of loads and deformations involved. The basic requirements of the rig were to:

1. consist of a simple cost effective design
2. simulate a simple denting process
3. allow measurement of force vs. deflection during the process
4. allow measurement of the residual dent depth
5. be easily simulated in the finite element environment

These objectives were achieved in the original design shown in Figure 3.1. The rig consists of two frames of extruded aluminium profiles, which acted as clamps to hold the flat sheet test piece. The test piece was aerospace grade aluminium alloy 2024T3, and the coupon size for the tests was 220mm x 340mm. The indenter had a radius of 50mm and was

attached to an Instron 1196 250KN Universal Testing Machine. The displacement of the indenter was controlled using the Instron Merlin software, allowing measurements of load versus applied displacement to be obtained.

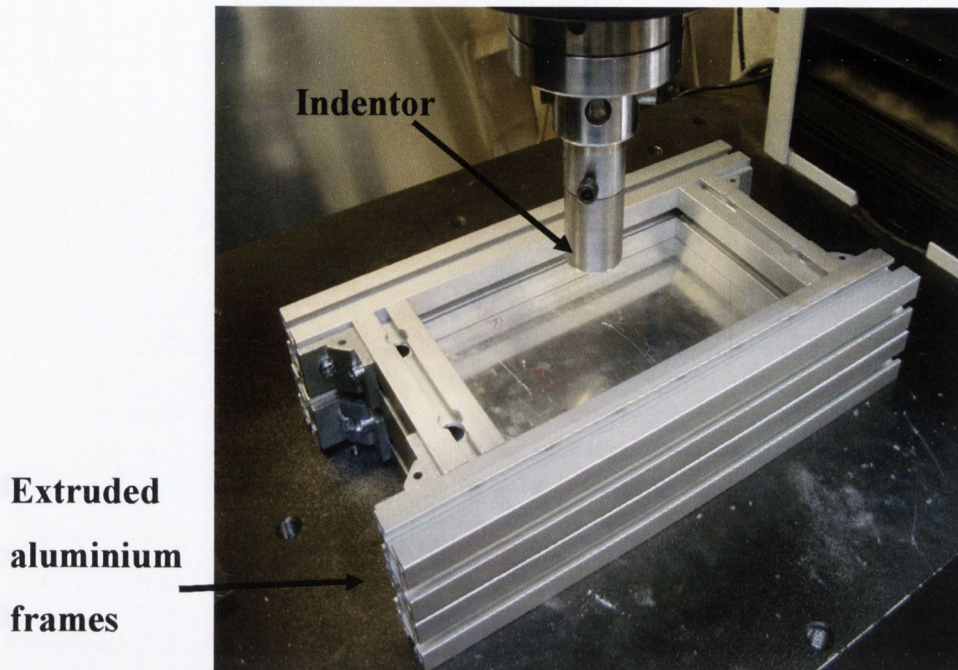


**Figure 3.1 Original coupon denting test rig**

The original design shown in Figure 3.1 met most of the aforementioned design requirements. The design was cost effective as it was constructed from off the shelf parts. The Instron, indenter and associated software allowed for the application of a realistic dent and also for the capture of accurate data for analysis. A fully clamped flat plate was selected as the coupon because it was far easier to build a test rig for this geometry than for a curved shell. In addition, fully clamped boundary conditions were easier to set up both experimentally and in the finite element model.

Initial experimental tests did, however, reveal the inherent difficulties in establishing fully clamped experimental boundary conditions between the aluminium frames and the aluminium coupon. Due to the loads involved and the low friction between the test specimen and the aluminium frames there was an inevitable amount of slippage, Figure 3.2.

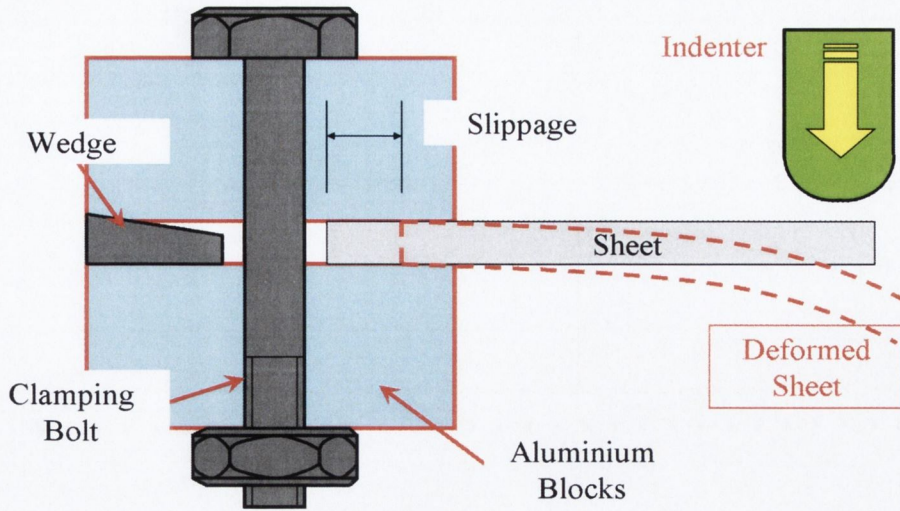


Figure 3.2 Slippage of aluminium

A number of methods were investigated to increase the friction between the aluminium frames and the coupon; the surface roughness of the frames was increased and emery paper was used to increase the friction. Eventually the top aluminium frame was removed and replaced with a steel frame with ten M12 clamping bolts. This set-up solved the slippage problem and the results presented in section 5.1 are from this final set-up.

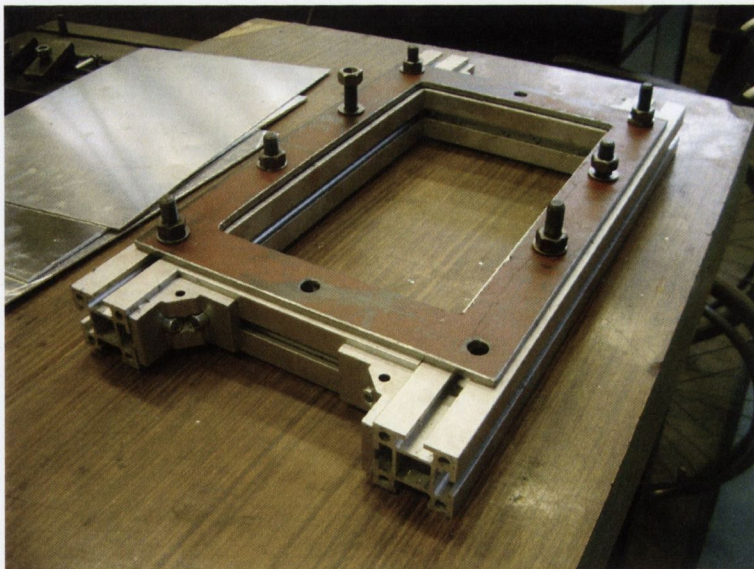


Figure 3.3 Modified coupon denting test rig

### 3.3 Full Scale Denting Rig

As outlined in Chapter 1, one of the primary objectives of the research was to develop an experimentally validated finite element model capable of simulating denting and subsequent compression of an aircraft panel. This section details the full scale denting test rig designed as part of the IARCAS programme, against which the finite element model was benchmarked.

As outlined in the objectives, the developed finite element model was to be parametric in nature to allow easy generation of various fuselage panel geometries. Full scale experimental testing was to be carried out on six panels as detailed in Table 3.1. The finite element model was to be benchmarked against the first two panels Table 3.1 Both panels are from the larger A380 aircraft geometry and have welded stringers.

Panel #	Type	Hull radius (mm)	Fame pitch (mm)	Stringer pitch (mm)	Skin thickness (mm)
1	Riveted	2828	3X530	145	2.4
2	Riveted	2828	3X530	145	3.2/2.0
3	Bonded	2820	3x530	185	1.6
4	Riveted	2828	3X530	145	1.6
5	Welded	3390	571.5,635,571.5	154	1.8
6	Welded	3390	571.5,635,571.5	154	1.8

**Table 3.1 Test panel details**

While the design of the full scale denting rig was necessarily more complex than for the coupon denting rig described above, the basic aim was the same; to realistically replicate the denting process as experienced by the panel. As a result, the basic requirements of the rig were to:

1. be capable of testing different geometries
2. be sufficiently stiff so as to experience almost zero deflection during loading
3. be instrumented to measure force vs. deflection and strains during the denting process
4. realistically simulate actual boundary conditions

In order to meet the first requirement at a low cost, a design was decided on where the test rig would consist of a rigid frame with interchangeable wooden panel support fixtures.

This was necessary due to the different hull radii as listed in Table 3.1, panels 1 through 4 being of an A340-500/600 geometry and panels 5 and 6 being from the larger A380 geometry. Figure 3.4 shows the denting test rig with a test panel in place. The wooden interchangeable panel fixtures support the panel on the inner frame flange and on the outer panel skin directly above the frame; see Figure 3.4, Figure 3.5 and Figure 3.6.

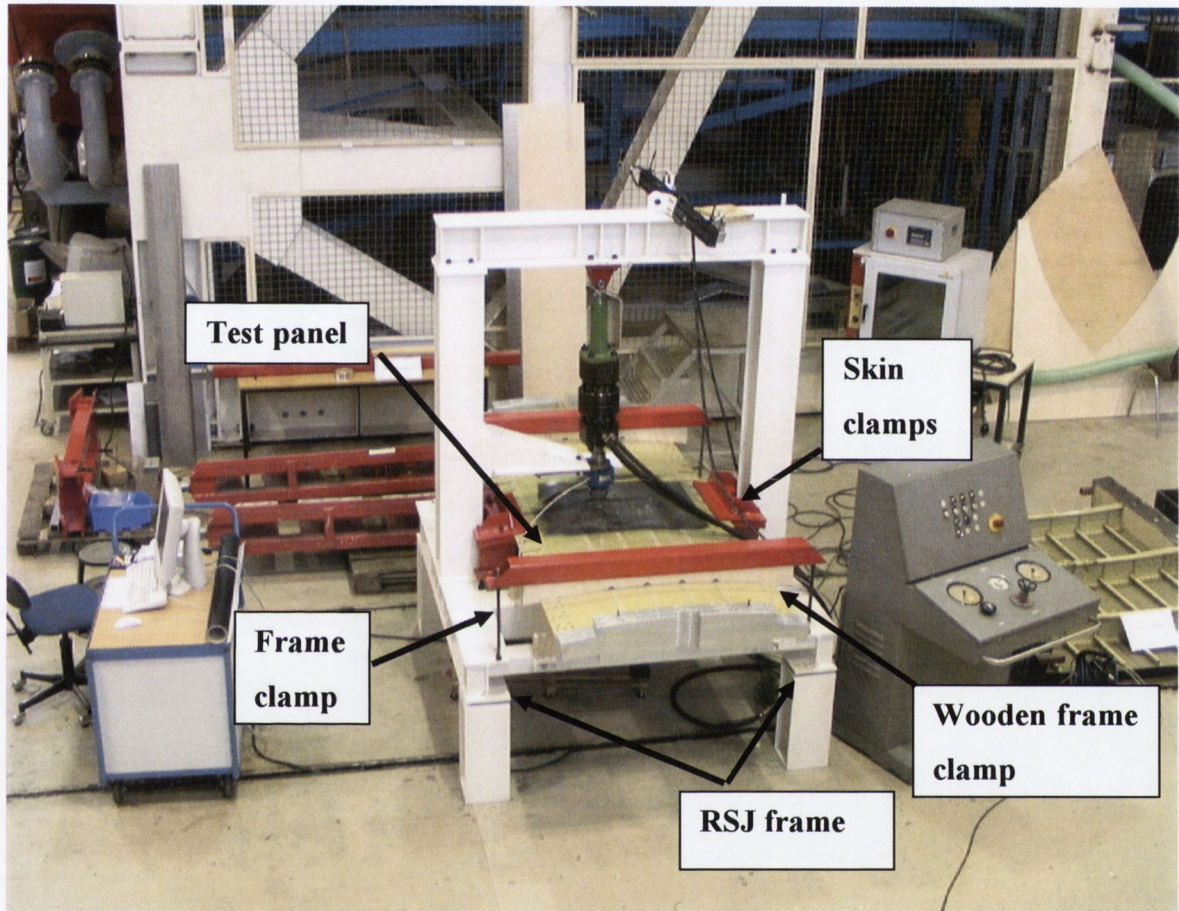


**Figure 3.4 Full scale denting test rig**

While the interchangeable wooden supports facilitated a cost effective method of accommodating alternative panel geometries, they also acted as boundary conditions for the panel. The actual boundary conditions for the panel are dependent on the assembly of neighbouring panels and stiffening members as these provide a finite torsional restraint at the edges of the panel. In reality, the true support condition along the panel edges is somewhere between the idealised simply supported case, where rotation about the plate edge is possible, and the fully clamped condition, where the restraints are prohibited. A number of researchers have investigated the effects of varying the boundary conditions between simply supported and fully clamped on the ultimate compressive strength, [52-56].



For the denting rig these boundary conditions were simplified to the set-up shown in Figure 3.4 and Figure 3.5. The test section skin was clamped, providing restraint against rotation and displacement at the panel skin edges. It was decided that it was unnecessary to fabricate clamping mechanisms for the entire longitudinal edge as finite element analysis had predicted that almost all the material deformation was confined to the test section. The wooden supports, described above to accommodate different panel geometries, also simply support the panel in the radial direction on all four frame inner flanges, Figure 3.6. This boundary condition simulates the rigid support of the internal circumferential stiffening frames. In addition to the wooden supports provided for all four frames on the inner flange, frames 1 and 4 have an additional restraint provided directly above the frames on the outer skin, Figure 3.5. This was added to prevent the panel skin from deflecting upwards, in a manner similar to a simply supported beam subjected to a point load at its centre, see Figure 3.7. Adjacent panels would provide this restraint to bending and rotation on the fuselage structure.

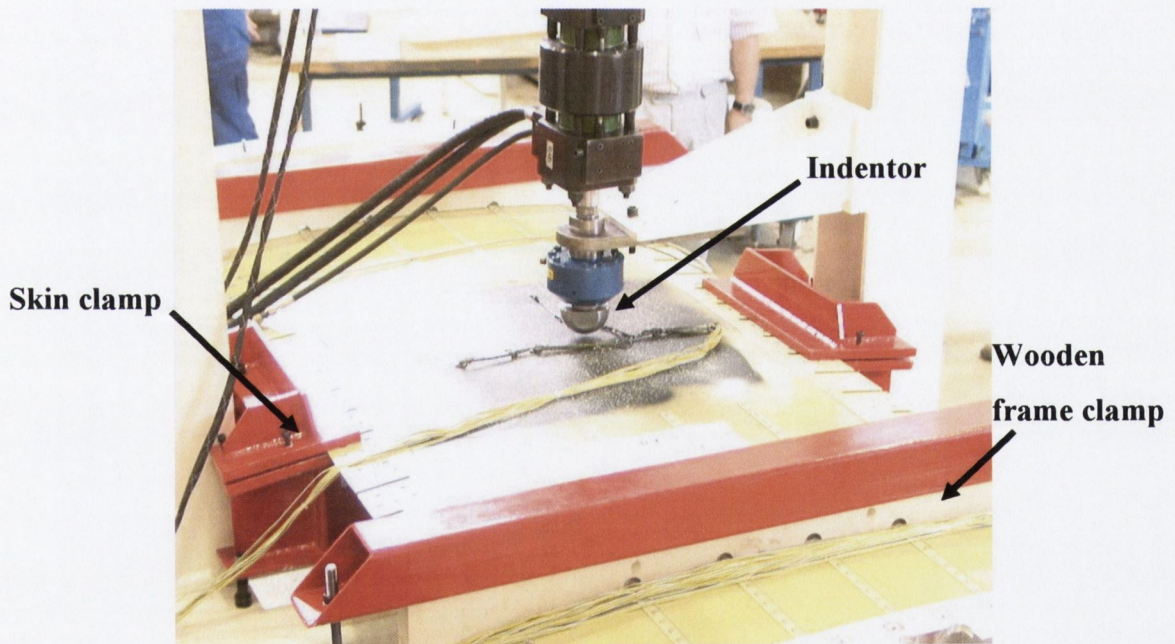


Figure 3.5 Denting rig test section close up



Figure 3.6 Frame inner flange wooden support

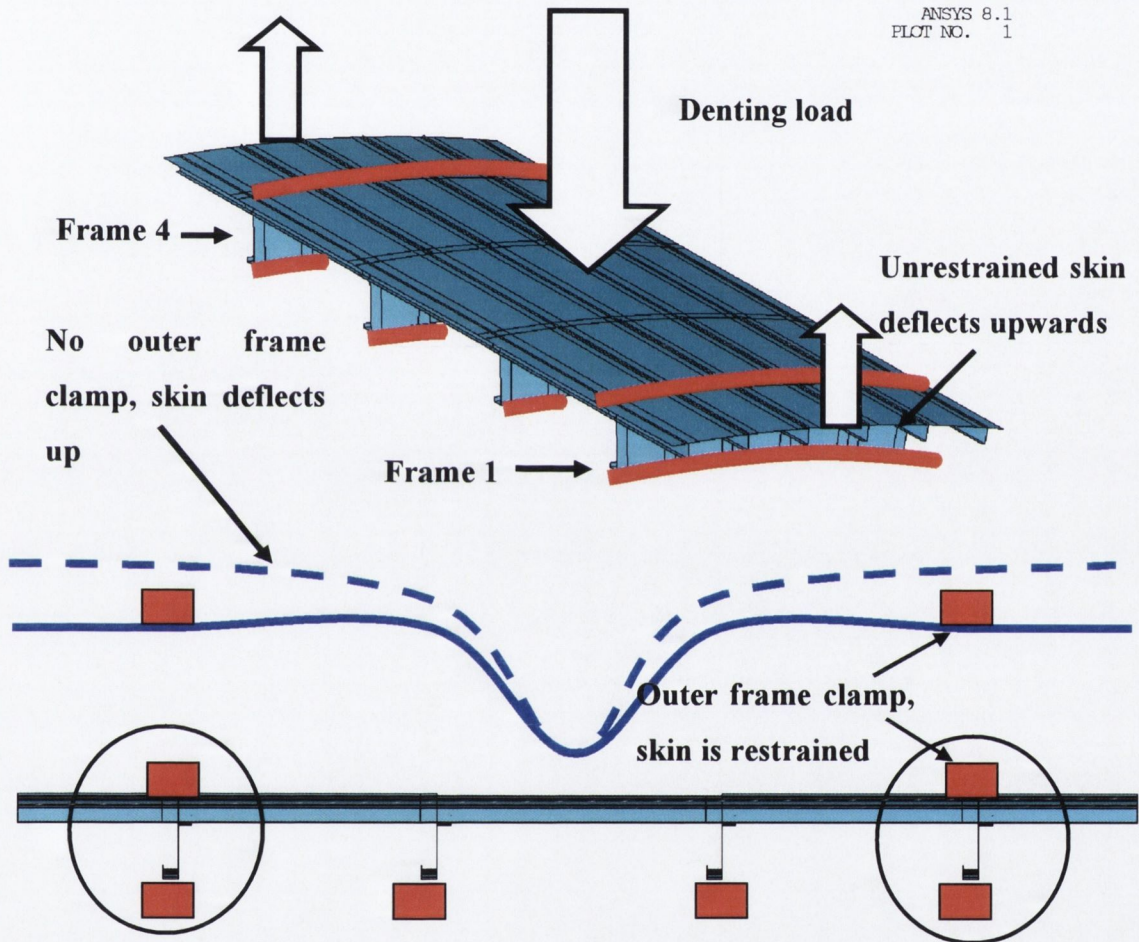
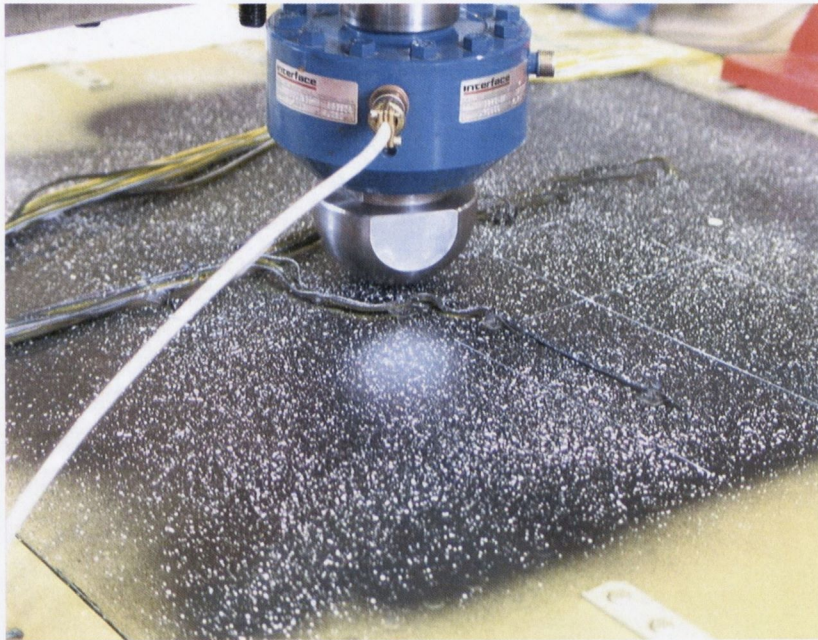


Figure 3.7 External frame clamp reasoning

Once confidence had been established in the finite element methodology employed by comparing the experimental coupon tests with the predicted finite element results, finite element models of the full panel were developed and used to predict the denting loads that would be experienced during the full scale tests. These results were used to ensure the test rig would be sufficiently stiff not to undergo deformation during loading. The loads predicted were higher than initially presumed, and as a result, a very stiff test rig was

designed. The frames were designed from I-beam sections, Figure 3.4, thus the stiffness criterion was met at an acceptable cost.

Indentation was performed using a spherical indenter of radius 50mm, Figure 3.8. The indenter was supported on a hinged arm, Figure 3.5, which allowed application of the dent normal to the skin for the different panel geometries. The quasi-static denting loads were monitored using a load cell while the strains were measured quantitatively using a series of strain gauges, Figure 3.9.



**Figure 3.8 Indenter**

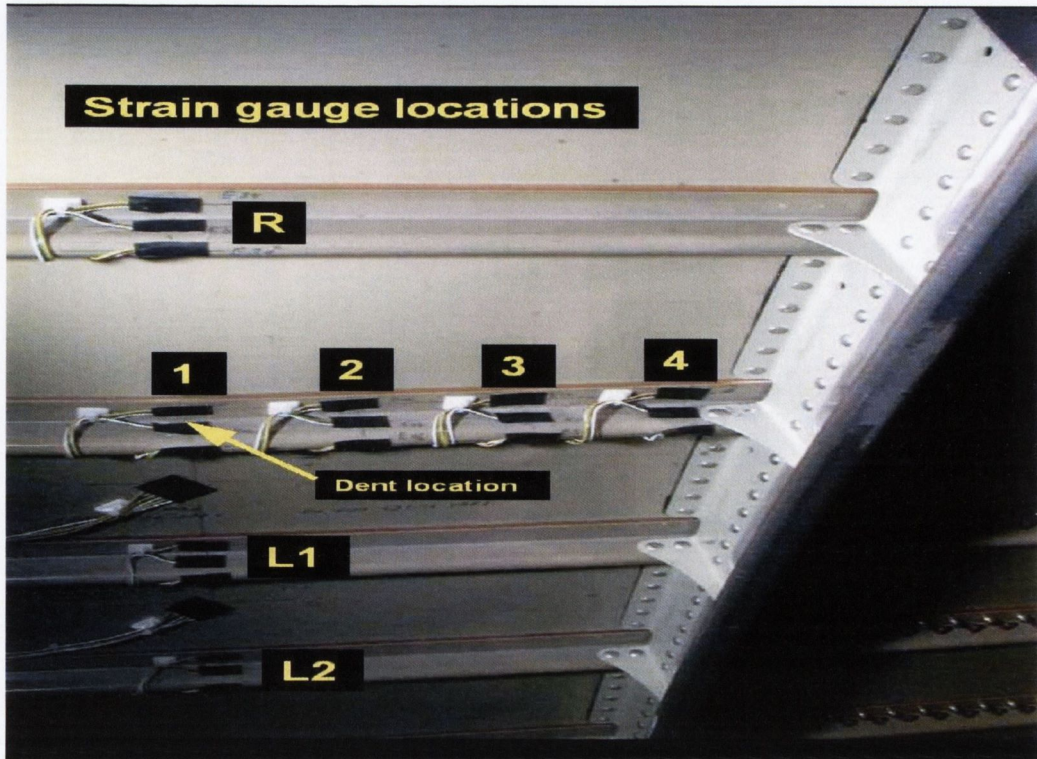


Figure 3.9 Internal strain gauge locations

### 3.4 Full Scale Compression Rig

The full scale compression testing was carried out at the Airbus test facilities in Hamburg. Two test rigs had already been developed for the testing of curved stiffened panels, the first for certification tests of the Airbus A330/340 aircraft [57], and the second for testing the larger A380 geometries. Both test rigs can be seen in Figure 3.10 and Table 3.2 details their testing capabilities.

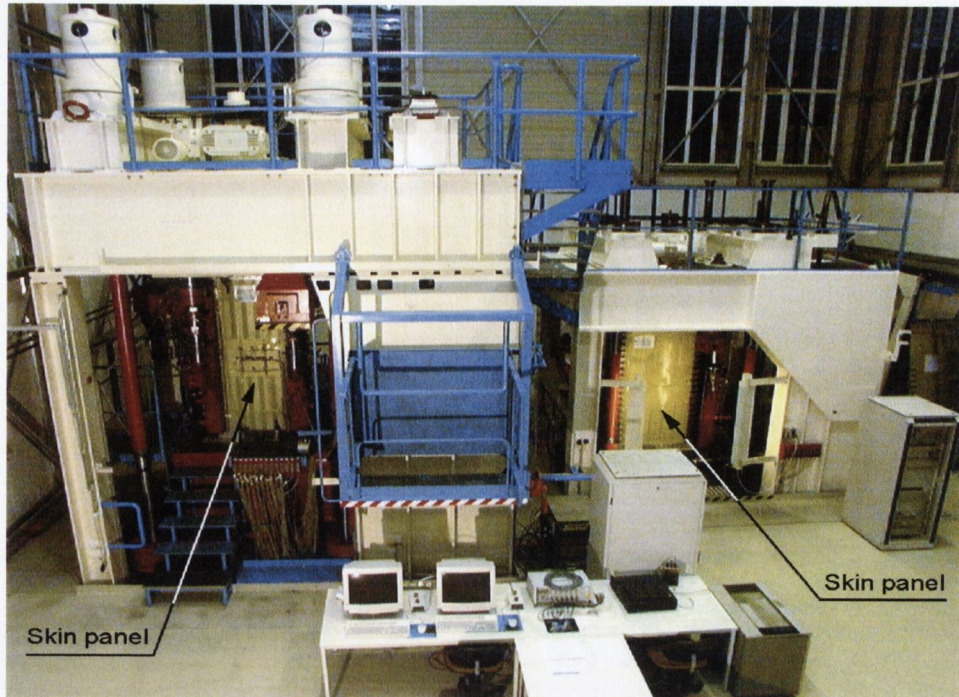


Figure 3.10 Test rig I and II [58]

	Test rig I	Test rig II
Size of specimen		
Length	2,208 mm	2,708 mm
Width	600-1,200 mm	600-1,200 mm
Thickness	2.8 mm	2.0 mm
Radius	1,500-3,000 mm	1,900-4,000 mm
Maximum mechanical loads		
$F_{CO}$ (compression)	2,000 KN	3,500 KN
$F_{shv}$ (Shear force vertical)	1,200 KN	4,250 KN
$F_{shh}$ (Shear force horizontal)	400 KN	200 KN

Table 3.2 Test rigs I and II specifications [58]

Figure 3.11 shows an isometric view of the test rig I. Both test rigs use the same boundary conditions as explained here for test rig I. The test rig holds the curved panel in position by hinged supports, which support the frame, restricting radial translation. These supports are equal in length to the panel radius and rotate about the axis of the panel Figure 3.12.

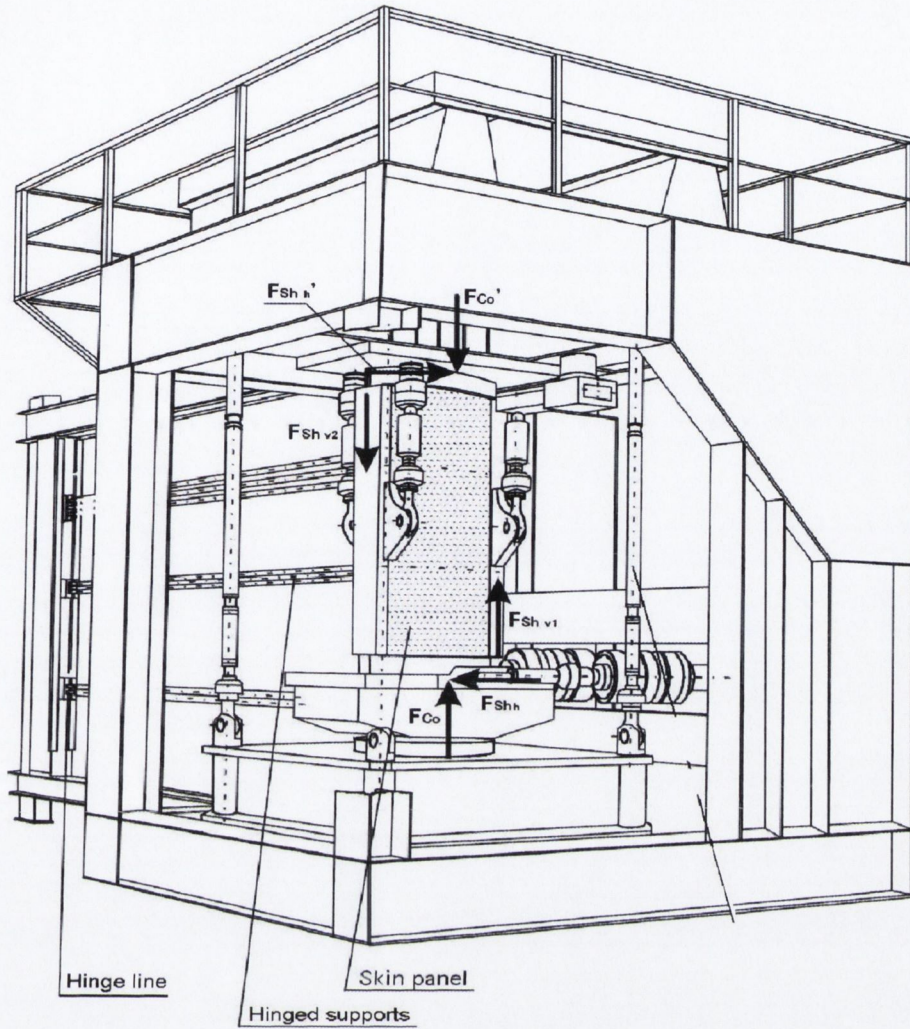


Figure 3.11 Full scale test rig, isometric view [58]

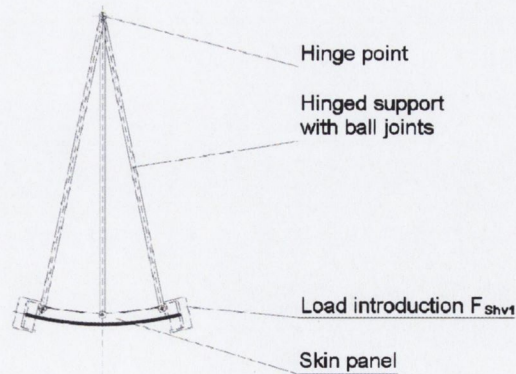


Figure 3.12 Plan view of curved panel and hinged supports [58]

The circumferential ends of the panel are securely clamped; see section B-B Figure 3.14 and Figure 3.15, and compression loading is applied from below via a hydraulic jack and load introduction plate, Figure 3.13. The loading is applied with the aid of a computer

which is integrated into the test system. The computer monitors the deformations of the panel and controls the hydraulic jacks.

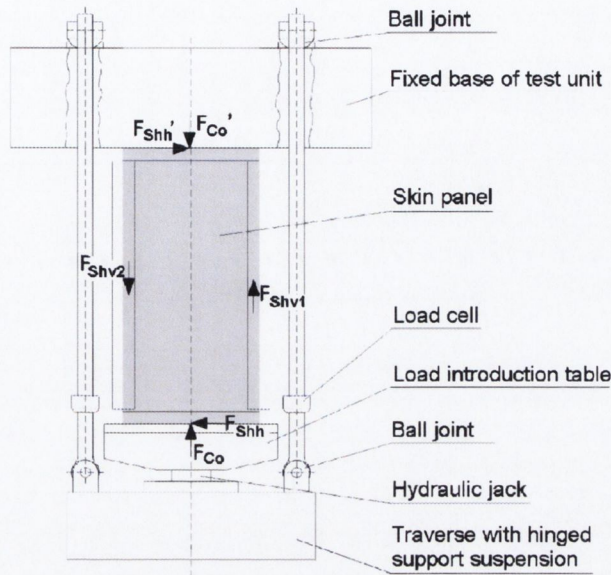


Figure 3.13 Elevation view curved panel load introduction [58]

As noted in section 3.3, the actual boundary conditions for a fuselage panel are between the extremes of simply supported and fully clamped, the torsional rigidity being equal to zero for simply supported and equal to infinity for fully clamped [55]. For the experimental set-up a complex series of cut-outs were machined into the test section panel edges, Figure 3.14. The skin between the cut-outs was restrained with clamps from translating in the radial and circumferential directions. These cut-outs were based on heuristic knowledge and have been shown to aid the panels to buckle in a manner similar to full scale barrel experiments. The same boundary support was applied along the rest of the longitudinal edge outside the test section.

In addition to the described boundary conditions, the panel was also stiffened outside the test section. This was achieved using extra skin doublers on the outer and inner skin surface and extra stiffeners. Figure 3.16 shows the detailed cross section A-A from Figure 3.14. The external reinforcements are clearly shown as are the extra stiffeners added to the stringer web and the skin doublers. This allowed for load introduction to the test section from the compressed end and ensured failure occurred in the test section first.

Since buckling was expected to occur in the test section, this is also the section that was instrumented with strain gauges. In addition to strain, panel shortening was measured by

inductive displacement transducers, the forces were measured by load cells and deformation patterns were recorded by photography. All the measured data was recorded and reduced by data loggers, coupled with the computer.

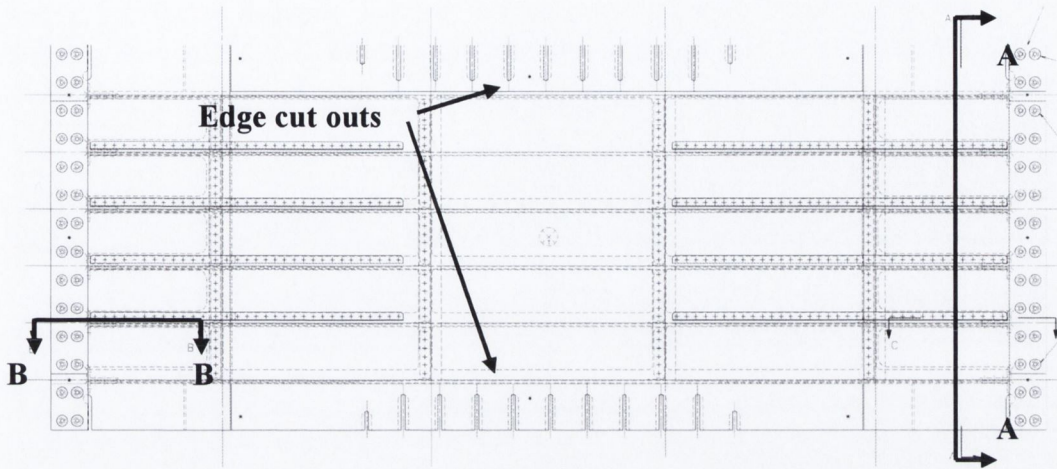


Figure 3.14 Test panel detailing longitudinal cut-out and end clamps

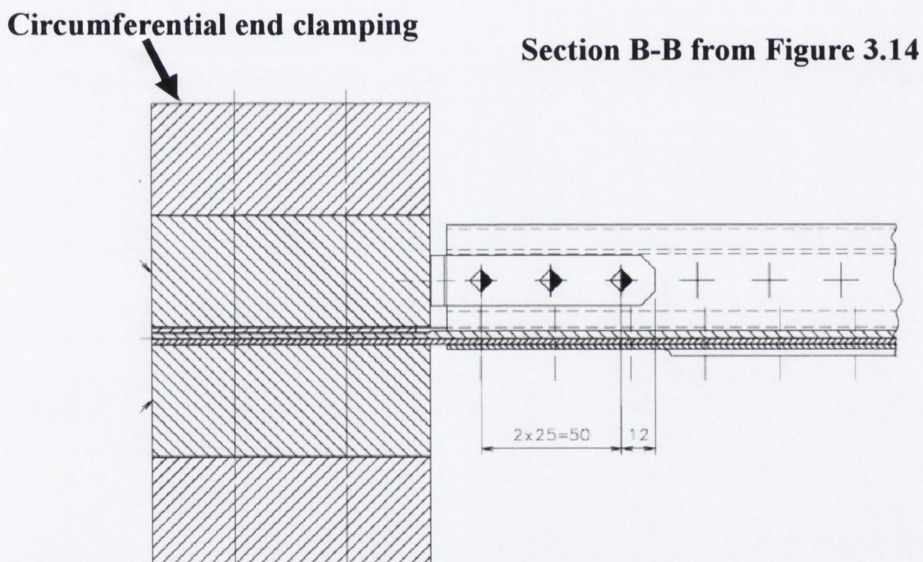
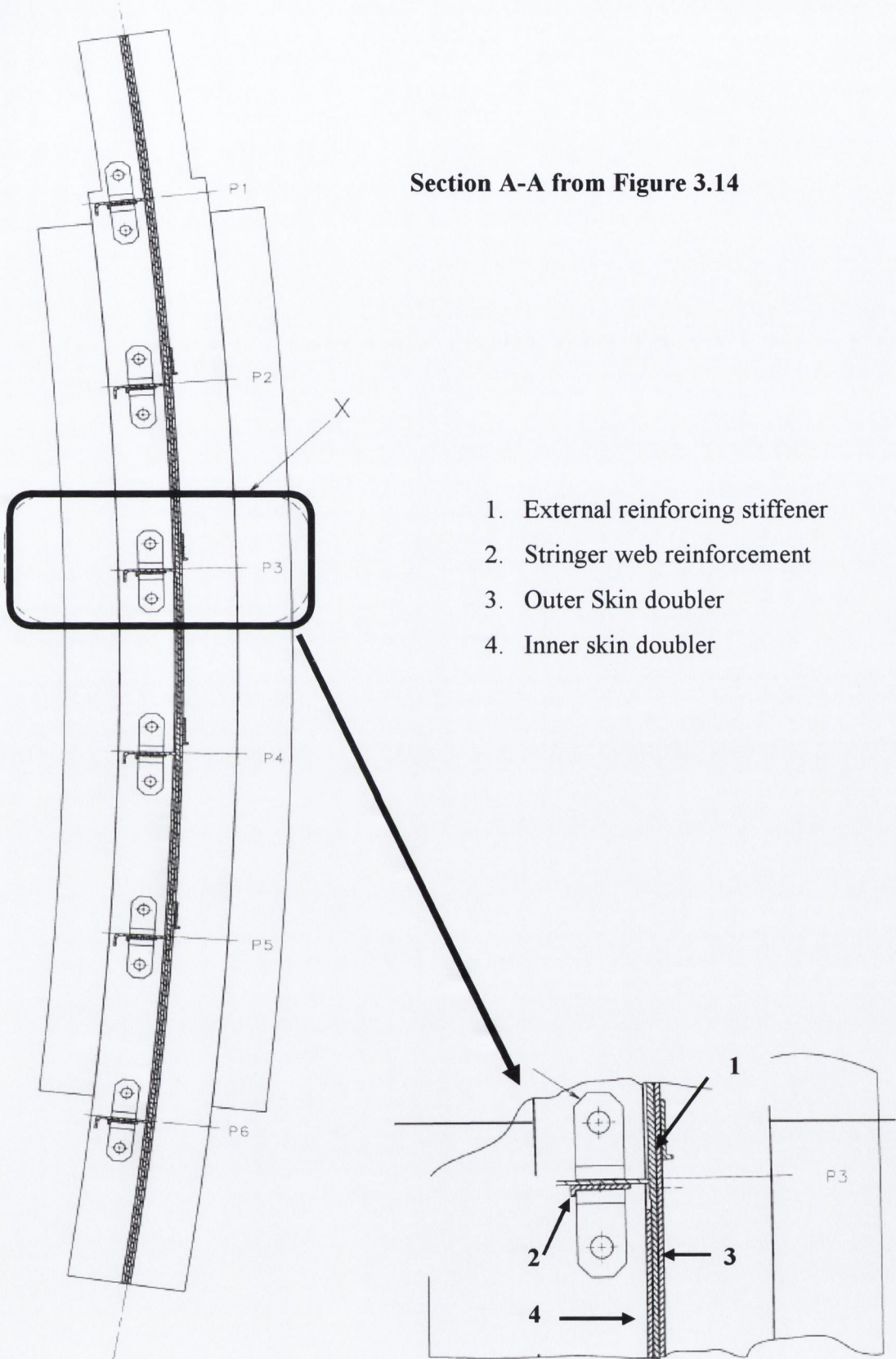


Figure 3.15 Section B-B Circumferential end clamping





**Figure 3.16 Panel reinforcements**

## PART IV

# 4 NUMERICAL METHODS

## 4.1 Introduction

The finite element models presented in this thesis have been modelled in the commercial FE package ANSYS. Initially another FE package, MSC Patran/Nastran, was used. The Nastran solver, however, was limited in its contact modelling capabilities and, as a result, ANSYS was selected. The finite element model described in this chapter is representative of a generic fuselage panel. The entire panel geometry is modelled using shell elements and considerable detail is included to represent the geometric non-linear response of the buckled skin, cross section deformation of the stiffening components, and details of the skin-stiffener attachment clips, Figure 4.1. In addition, a spherical rigid body indenter is modelled to impart damage to the structure through an indenting operation and a master-slave arrangement of multi-point constraints is modelled for controlled compressive end-shortening. This chapter details the methodology behind the finite element model used in this research, and justifications are provided for specific modelling choices.

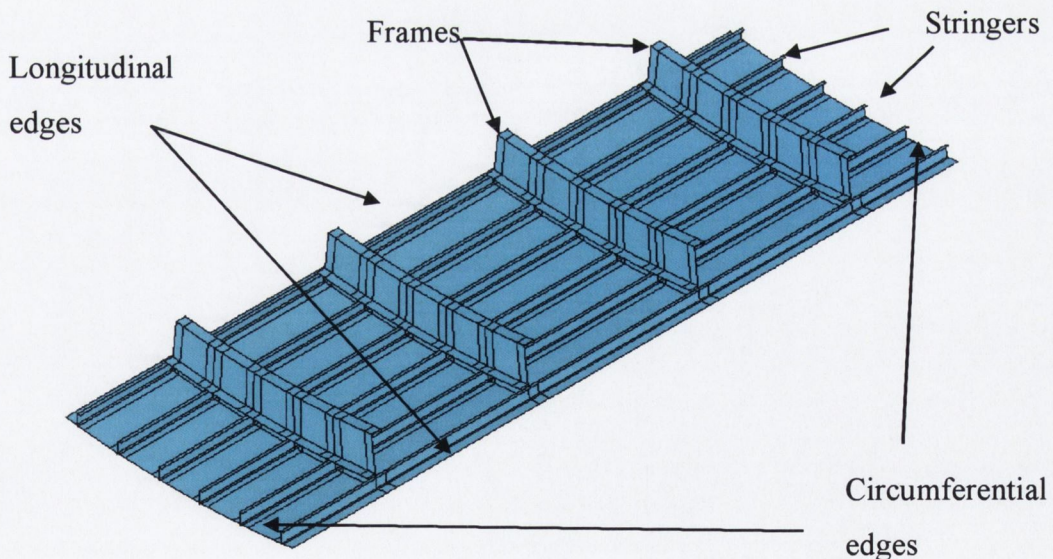


Figure 4.1 Finite element representation of generic aircraft panel

## 4.2 Finite Element Analysis Type

The initial step in any finite element analysis is to decide on the analysis type, linear or non-linear, based on the structural mechanics of the problem. Non-linear structural behaviour arises for a number of reasons, which can be broken down into three main categories:

1. Geometric non-linearities e.g. large strains, large deflections or stress stiffening
2. Changing status non-linearities e.g. contact behaviour
3. Material non-linearities e.g. plasticity

Geometric non-linearities arise in the present analysis due to changes in the structural stiffness of the panel as it undergoes buckling deformations which must be accounted for in the stiffness matrix of the model. An additional non-linearity is present during the indentation phase of the loading due to the changing status of the contact elements as they come into contact with each other and on removal of the indenter when they break contact. In order to account for the residual stresses due to the denting process as accurately as possible it was necessary to model the material as elastic-plastic. This material model is also necessary for an accurate post-buckled analysis, as it is likely that the plastic limit is reached at points of maximum deflection in the post-buckled region.

Therefore, to capture the mechanics of the problem as laid out in the objectives in section 1.1, the three non-linearities had to be considered. As a result it was necessary to run a full non-linear analysis, with the associated difficulties, such as high run times and convergence issues. These non-linearities also affect the choice of element, section 4.3.

## 4.3 Element Choice

The choice of element is largely dependent on two factors, the structural mechanics of the problem, which dictated the analysis type in section 4.2, and the information the analyst wishes to gain from the model. A full three dimensional model using solid elements might be considered the best solution for all analyses. For the case of thin-walled structures, however, there would have to be several solid elements through the thickness to capture local bending effects and avoid shear locking [59]. Shear locking is depicted graphically in Figure 4.2; the graphics represent an infinitesimal particle under bending, with the top in tension and the bottom in compression. The figure on the left represents the actual

deformation of the beam, while the figure on the right depicts the deformation as modelled by a linear element. The linear element is unable to accurately model the displacements caused by curvature and, as a result, a shear stress which does not exist in the infinitesimal particle is introduced into the element by this deformation state. This causes the element to reach equilibrium with smaller displacements as the strain energy is absorbed by the shear, with the result that the element does not predict the bending displacements accurately and is “numerically stiffened”.

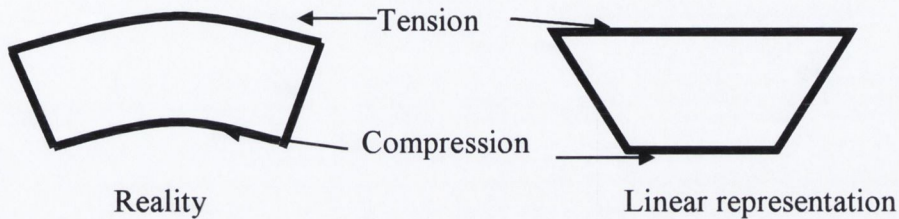


**Figure 4.2 Problem of shear locking for beam under bending**

By meshing the model with several elements through the thickness, the bending response in each element becomes more linear and therefore will model the reality more accurately. This would, however, lead to very high numbers of elements in thin-walled structures and as a result shell elements have been developed for modelling thin-walled structures.

Shell elements take advantage of the fact that the only shear on the free surfaces is in-plane. Shell elements include out-of-plane bending effects in their fundamental formulation, as well as transferring shear, tension and compression in the plane. ANSYS has a number of different shell elements to choose from. The element formulation bending theory for ANSYS shells is based on Mindlin kinematics [60]. Mindlin kinematics or discrete Kirchhoff conditions as they are also known, are similar to standard Kirchhoff conditions in that the normals to the shell mid-surface called a shell “*director*”, remain straight, perpendicular to the mid-surface and unchanged in length during deformation, with the addition that Mindlin kinematics allow for a rotation of the director independent of the deformation of the shell’s mid surface [61].

Of the shell elements available within ANSYS it was necessary to select an element that was capable of accurately modelling all the active non-linearities. For these reasons, the Shell 181 element was chosen to model the panel skin. This is a four node element with six degrees of freedom (d.o.f) at each node, translations in the x, y, and z directions, and rotations about the x, y, and z-axes. This element is capable of accounting for large strain,

large rotation and stress stiffening. The Shell 181 formulation is based on the Bathe-Dvorkin assumed transverse shear treatment, which alleviates the aforementioned problem of shear locking. Shell 181 combines uniform reduced integration, or full integration with enhancement of membrane behaviour using incompatible modes [60, 62]. This alleviates the necessity of a very fine mesh when in-plane bending of the element dominates, such as in the stringer cross section. The element also supports inclusion of element thickness during contact, which means contact is detected at the shell surface and not the at shell mid-plane.

The necessary inputs for the element definition are four nodes, as defined by the discretisation of the geometry in the meshing stage, section 4.7. Element attributes are defined using the ANSYS environment variables known as “*Real Constants*” or “*Section Controls*”. These environment variables allow the user to associate values for thickness, material property definitions, direction of shell offset and number of integration points through the element. Five integration points through the thickness were used in the models presented in this thesis.

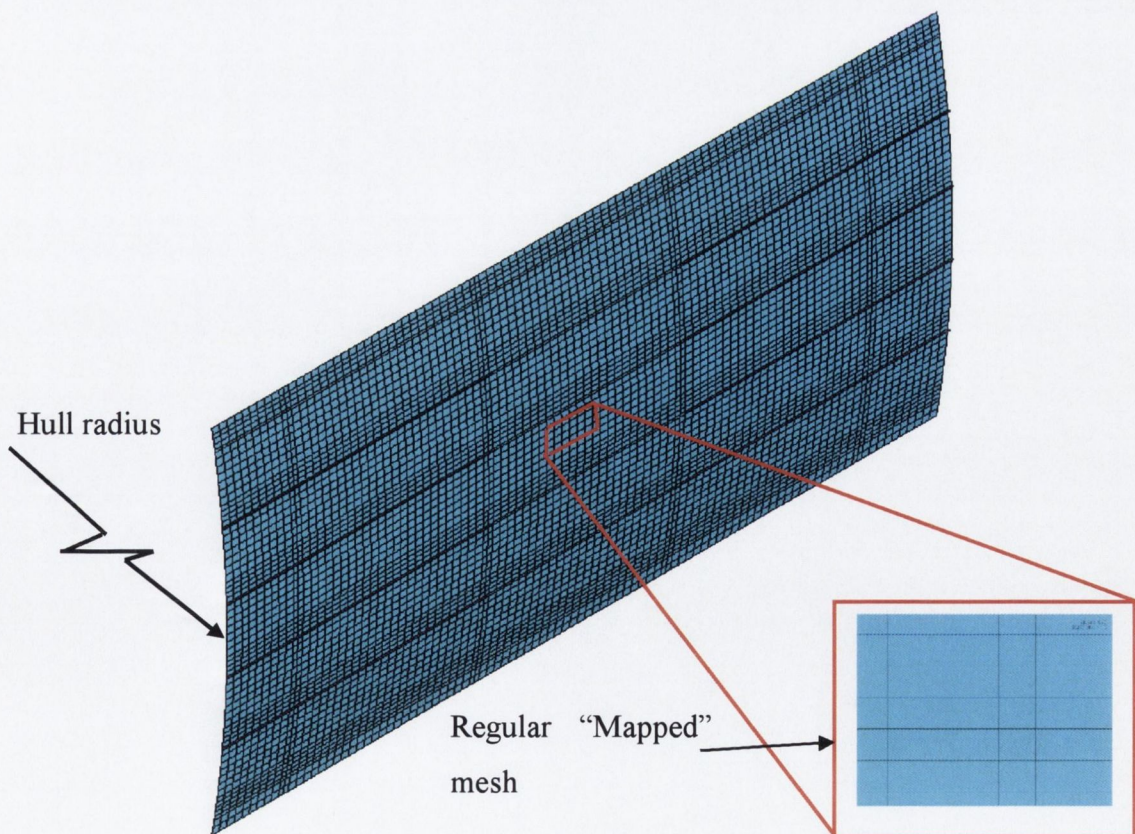


Figure 4.3 Panel skin showing mapped shell 181 element mesh

After establishing the model for the panel skin, two models for the stiffeners were evaluated. The simplest method is to model the stiffeners with discrete beam elements. These one dimensional elements are assigned user defined values for the cross-section properties of the stiffeners, thereby accounting for the inertias and torsional constants of the stiffener, and offsets from the skin mid-plane to the stringer neutral axis are also pre-defined, Figure 4.4.

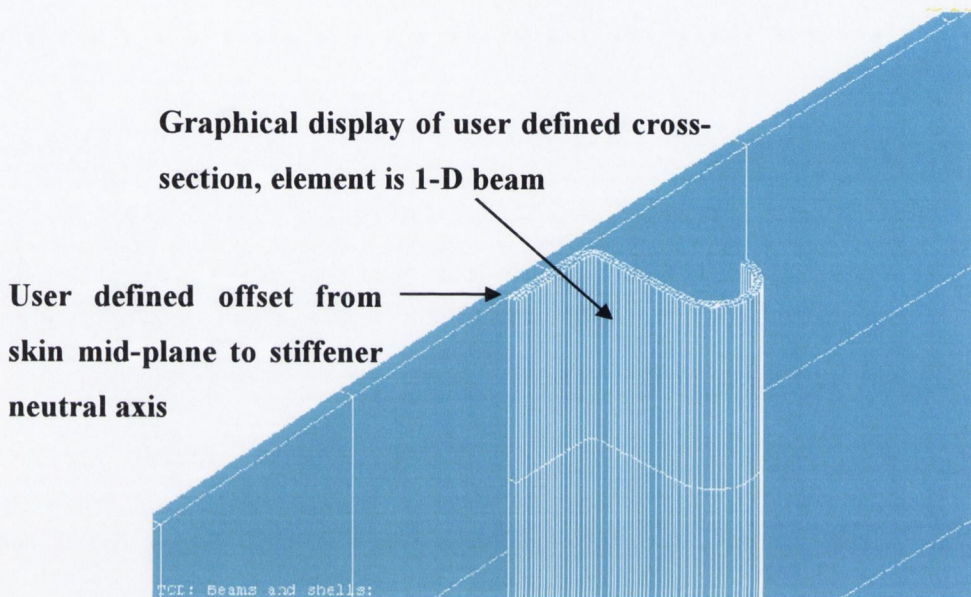


Figure 4.4 Early stiffener model using beam elements

These attributes, coupled with the computational efficiency of beam elements are the major advantages of the beam elements. However, a major drawback of the beam elements is that it is not possible to model the stringer-frame cut-outs. This is an area that undergoes complex load redistribution, as the clip support between the frame and stringer acts in establishing an effective length for the stringer. Indeed in a recent paper [63], Buehrle et al report on the results of an FE modal investigation of an aircraft fuselage. The paper reports on two FE models and in both models the skin was modelled using shell elements. In the first model the stiffeners were modelled using beam elements and in the second model shell elements were used. Differences of 30% were observed between predicted FE and measured experimental values for the beam model, versus 7% for the shell model.

For these reasons, and to account for cross section deformation the stringer and frame cross sections were modelled using the same shell element as the skin, Shell 181. Direction of shell offset, as mentioned above, is a recent development in shell element formulation and is accounted for in the Shell 181 formulation. This is particularly useful when modelling built-up stiffened structures. Figure 4.5 shows a plot of a standard shell element thickness

representation where the thickness is distributed either side of the mid-plane. This simplification in representing the true geometry results in a consequential reduction in flexural stiffness compared to the actual structure. Figure 4.6 shows the shell element thickness offset above the nodal line. This is an accurate representation of the actual structure and shows the applicability of Shell 181 in modelling built up stiffened structures.

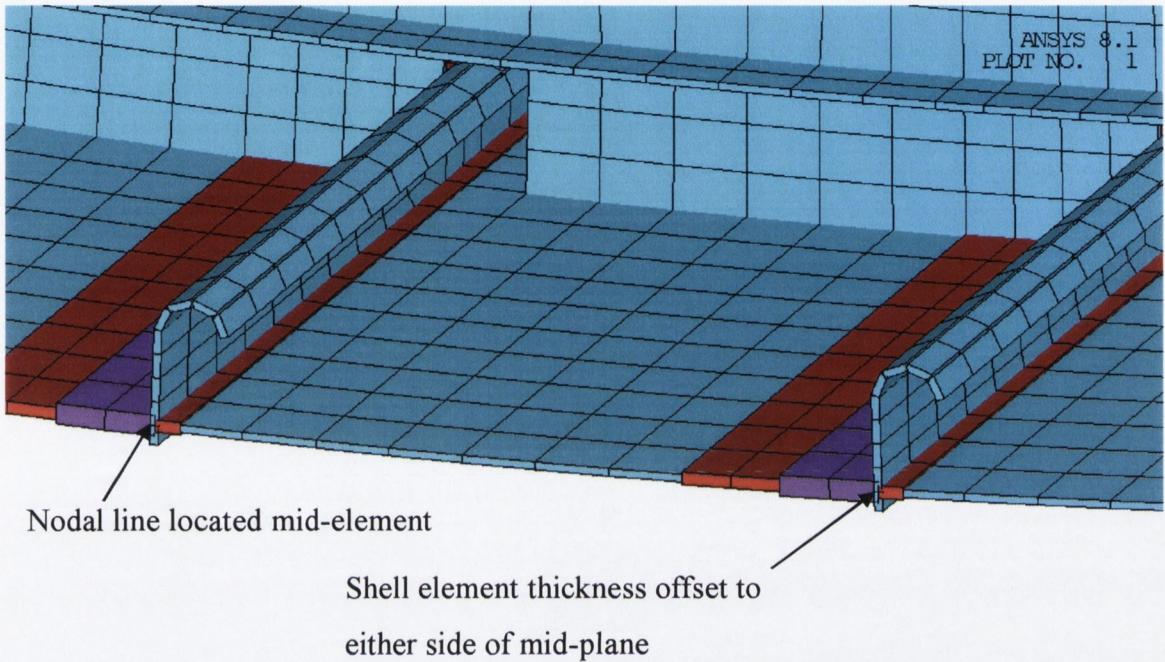


Figure 4.5 Traditional shell element with thickness offset about the mid-plane

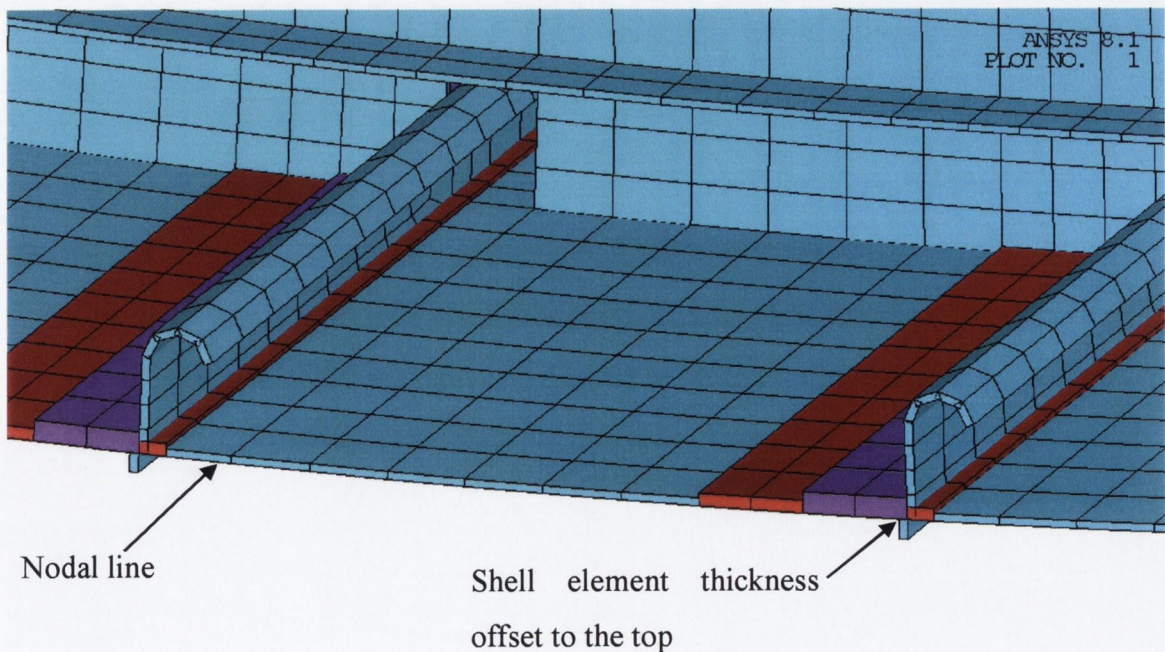


Figure 4.6 Element plot showing the element thickness offset to the top

## 4.4 Material Modelling

In order to model the non-linear behaviour of the aerospace aluminium alloys, it was necessary to select an appropriate numerical model of the material. For the most accurate results the model had to incorporate the post yield strain hardening behaviour of the material. This was achieved through the use of incremental plasticity theory, which provides a mathematical relationship that characterizes the increments of stress and strain,  $\Delta\sigma$  and  $\Delta\varepsilon$ , to represent the material behaviour in the plastic range [64]. The incremental plasticity theory is modelled in ANSYS using three basic components:

1. Yield criterion
2. Flow rule
3. Hardening rule

The material models used in this thesis, known as multi-linear isotropic hardening, are based on the von-Mises yield criterion, which states that yielding begins when the equivalent stress exceeds a certain value. The von Mises equivalent stress  $\sigma_e$  being defined as:

$$\sigma_e = \sqrt{(\sigma_1 - \sigma_2)^2 + (\sigma_2 - \sigma_3)^2 + (\sigma_3 - \sigma_1)^2} \quad (4.1)$$

where  $\sigma_1$ ,  $\sigma_2$  and  $\sigma_3$  are the principal stresses. Yielding occurs for the von Mises criterion when the equivalent stress  $\sigma_e$ , exceeds the yield stress of the material  $\sigma_y$ . The flow rule then describes the direction of plastic straining once yielding has occurred. The isotropic hardening rule used in these analyses assumes that the yield surface expands uniformly in all directions with plastic flow.

Figure 4.7 plots the stress-strain curves for the aluminium alloys modelled in the analyses, as input into the ANSYS finite element models. The true stress-strain curves for AL2024T3 are based on values from tensile testing conducted in Trinity College Dublin, while the values for AL6110, AL6013 and AL7349 were supplied by Airbus. The frame material was AL2024T3, the skin was AL6013 and the stringers were AL6110.



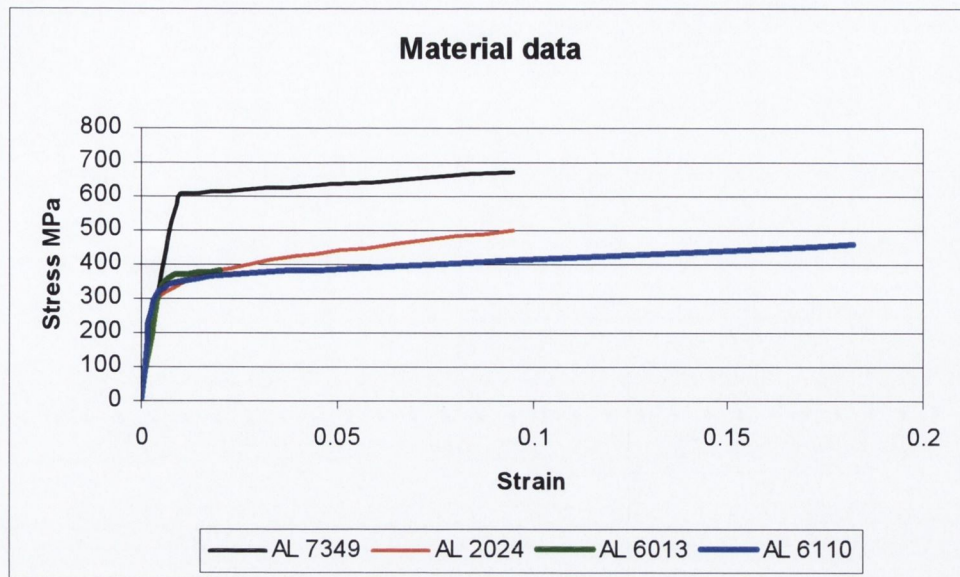


Figure 4.7 Material data plots

## 4.5 Parametric Modelling

As outlined in the objectives it was a prerequisite of the numerical tool developed in the course of this research that it be based on parametric user input. There were a number of advantages to such a design. Parametric input allows users to investigate the effects of varying parameters, such as dent depth, location, radius or shape across a range of geometries. Such numerical parametric studies have a distinct advantage over the more traditional method of extensive experimental testing in terms of lower costs. In addition, the automation of the finite element model generation based on these user input parameters increases the versatility of the numerical tool, in that users without specialist finite element expertise can utilise the programme.

The initial step in developing the parametric model was to establish the essential parameters. Table 4.1 lists the minimum geometric parameters that an analyst must specify in order to build the geometric model of the fuselage panel. As can be seen from the table the parameters have physical design significance and, as a result, the user of the modelling programme developed in this research need not necessarily be a finite element specialist. It is sufficient that the user has an understanding of the input parameters and the structural mechanics of the fuselage, allowing them to assess the effects of the dents on the structural integrity of the fuselage from the finite element results.

Panel data	Stringer data	Frame data
Skin thickness	Number	Number
Hull radius	Profile	Pitch
Overhang of first stringer	Pitch	Height
Overhang of first frame	Height	Thickness
	Thickness	

Table 4.1

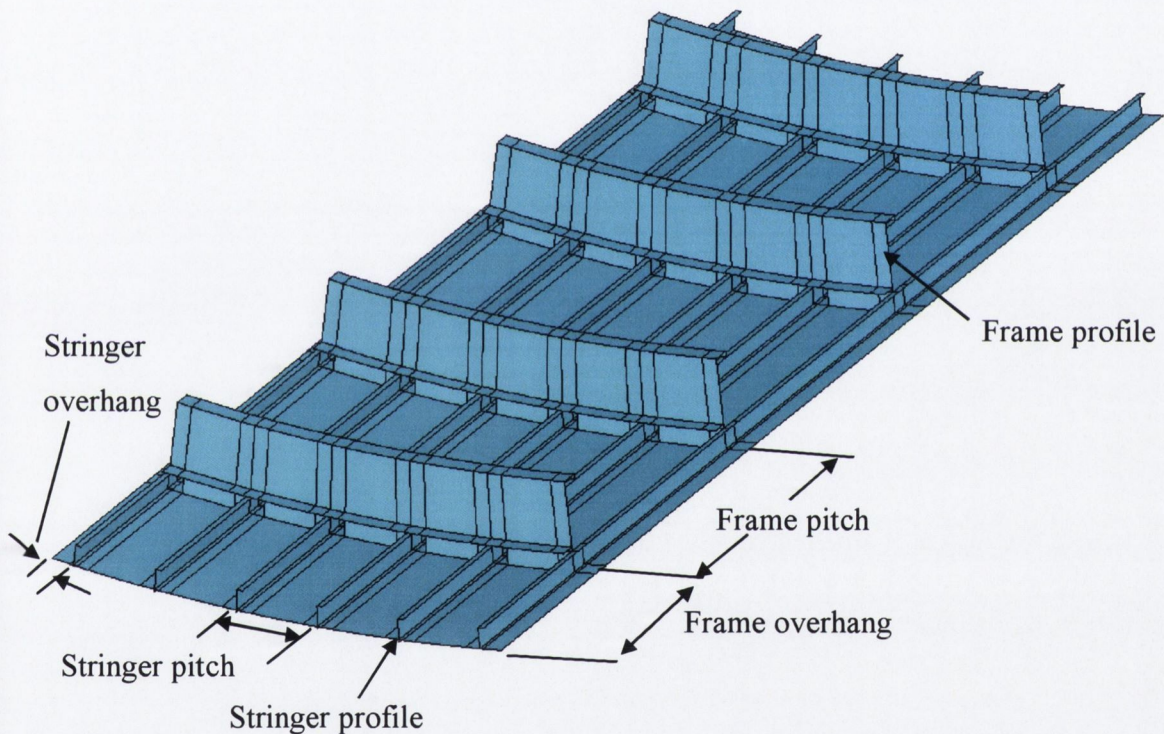
ANSYS 8.1  
PLOT NO. 1

Figure 4.8 User defined parameters

The stringer profiles programmed into the model and the terminology used in describing them are shown in Figure 4.9. Having defined the parameters, it is necessary to establish the geometrical relationships between them and to automate the process of developing the model. This is achieved by programming the geometrical relationships, in mathematical terms, into the finite element model.

For example, when defining the cross section of the curved skin, the formula for the length of an arc is used,  $S = R\theta$  where  $R$  is the arc radius and  $\theta$  is the angle of the arc. By

substituting for panel radius and the panel length, which is a function of both the number of stringers and the stringer pitch, the angle  $\theta$  can be found. This allows for plotting of cross section key points or nodes in the cylindrical co-ordinate system,  $(R, \theta, Z)$ , based on the radius and angle  $\theta$ .

Due to the complexity of the fuselage structure, it is necessary to break it down into more manageable units, such as stringer cross-section, frame cross-section, and stringer-frame bays. Once these base models have been developed, the entire panel can be constructed by performing iterative loops based on the number of frames, stringers etc. that the user specifies. This high level of programming capability is developed in the programming code known as APDL or ANSYS Program Design Language, which contains all the features found in a traditional programming language with the addition of all ANSYS commands as conventionally accessed from the ANSYS graphical user interface (GUI) [62].

The steps taken in the geometric build are as follows:

1. Read in user defined parameters.
2. Calculate necessary variables.
3. Plot circumferential panel and stringer cross-sections.
4. Extrude circumferential cross-sections to create longitudinal panel and stringer surfaces.
5. Plot the frame cross-section
6. Extrude the frame cross-section to create frames.

For ease of use, step one has been automated via a graphical user interface developed during the course of this research. This is described in detail in section 4.6. Once the necessary variables have been generated based on the user defined parameters from the GUI, step two is performed within the ANSYS environment via the pre-programmed APDL code.

Steps one and two are performed automatically on execution of the tool and the initial output of step three is shown in Figure 4.10, the circumferential panel cross-section. This cross section generation is programmed in an iterative loop controlled by the user input, "*stringer number*". Figure 4.10 shows a cross section with six stringers.

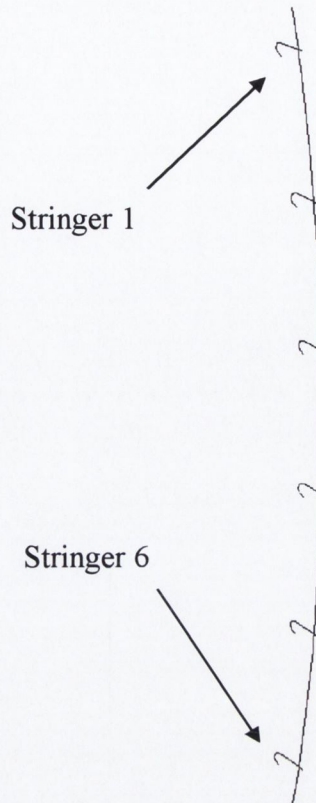
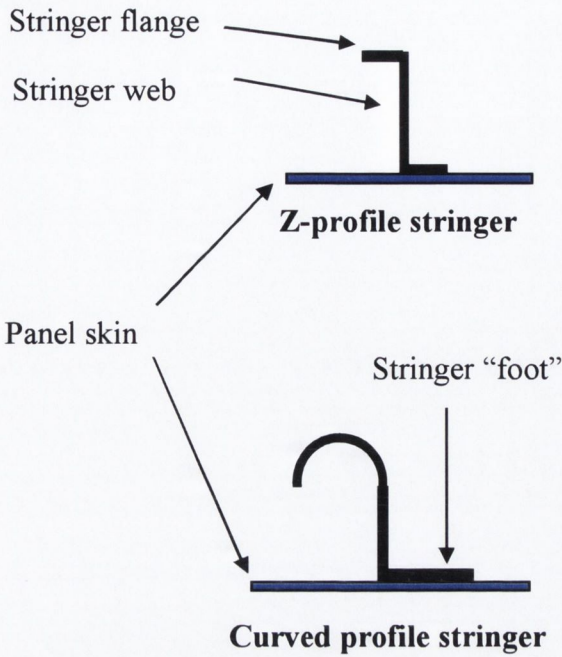


Figure 4.9 Possible stringer cross sections

Figure 4.10 Circumferential panel cross section

With the panel cross section defined, the panel surfaces are generated using the ANSYS extrude function, the inputs for this are the line to be extruded and an axis and distance along which to extrude. Again this operation was programmed in “do” and “for” loops based on the number of stringers. The actual surface generation was broken down into areas that had similar attributes. This allowed for the grouping of these areas into components, which were stored as variables to which these attributes could be assigned. Figure 4.11 shows an example of differing attributes, in this case skin thickness, for the panel skin. The pocketed area has been chemically milled to a thickness of 2mm while the virgin panel skin thickness is 3.2mm for this panel.

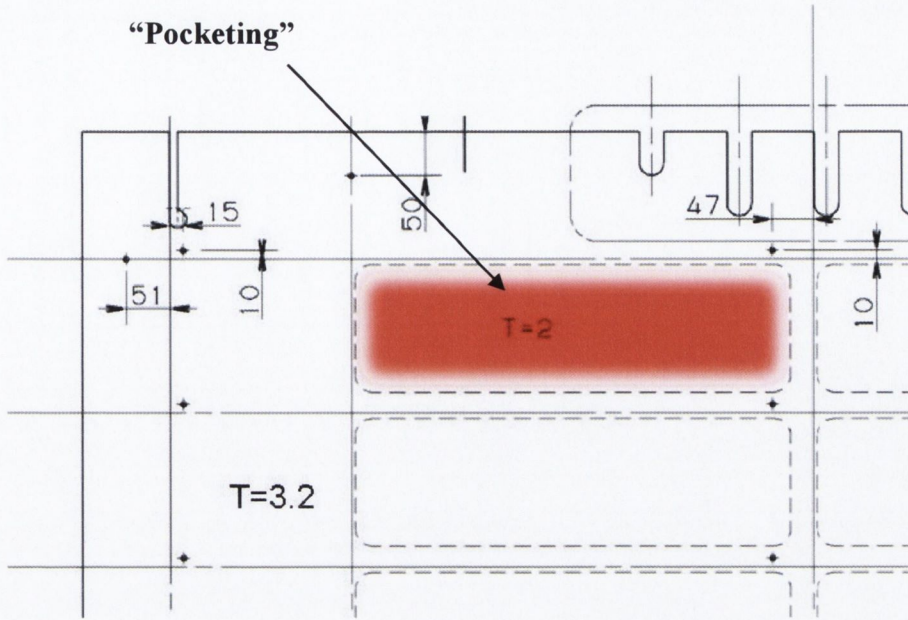


Figure 4.11 Example of change in skin thickness or "pocketing" due to chemical milling

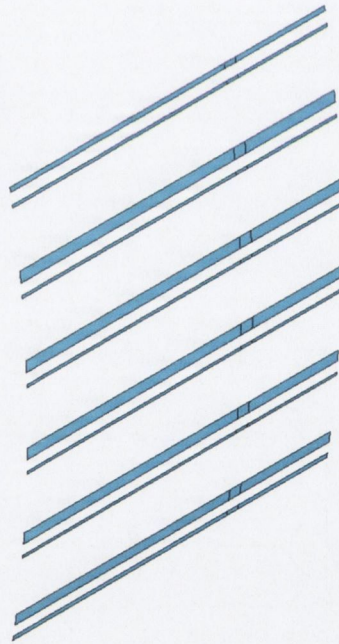
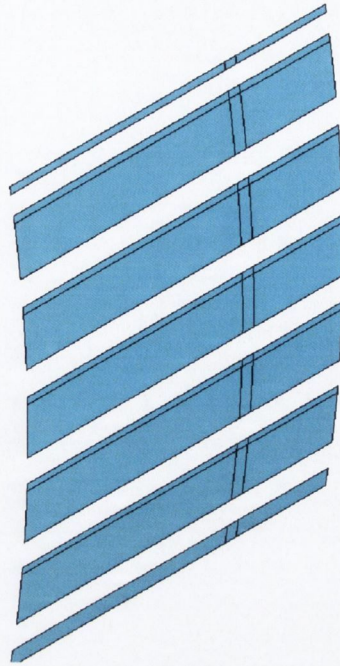


Figure 4.12 As manufactured skin thickness areas



**Figure 4.13 Chemically milled skin thickness areas**

The extrusion of the skin and stringer areas were also divided into sections comprising of the outer frame bays and the test section, so that the extra stiffening applied outside the test section could be assigned to the components in question. Figure 4.14 plots the stringer surfaces in the test section.

The created components are then assigned the relevant material properties, thickness and offsets. For the case of the extra stiffener added to the web of the stringer outside the test section, an equivalent increase in the cross-sectional area was smeared into the main stringer to account for the added area. During the meshing operation, when the geometrical model is discretised into a finite element model these components are retrieved and meshed with their attributes being assigned to the given elements.

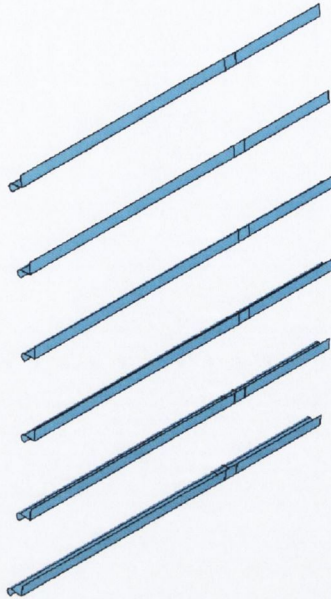


**Figure 4.14** Stringer surfaces

The generation of the panel skin was divided into sections to ensure connectivity between key-points on the panel skin, the frame clips and the frame. This process essentially ensures that areas meeting at a line share key-points that can then be “merged”, effectively deleting one key-point and joining the areas. To guarantee that the frame, clip, stringer and skin all share key-points that can be merged, necessitates careful planning and coding of the geometry generation from the very beginning. As the different components are generated their key-points, lines and areas that are of use at a later stage, such as is the case for the clip generation, Figure 4.15, are stored as variables for retrieval. This ensures that the geometries can be merged, thereby ensuring a connected panel geometry. For the frame generation, the cross section is generated and extruded in the circumferential direction to create the surface. This process is repeated within a loop accounting for the stringer pitch and stringer cut-outs. The extruding of the frame cross section is also staggered to ensure that the frame areas line up with the clip areas and that their key-points are coincident, Figure 4.16

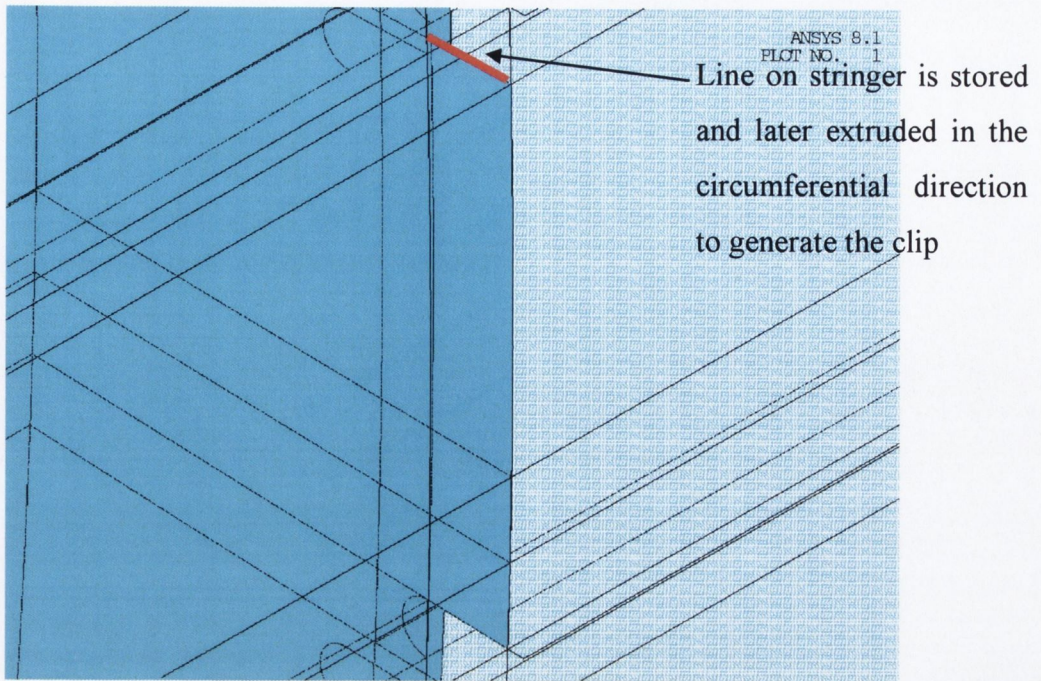


Figure 4.15 Clip surface generation

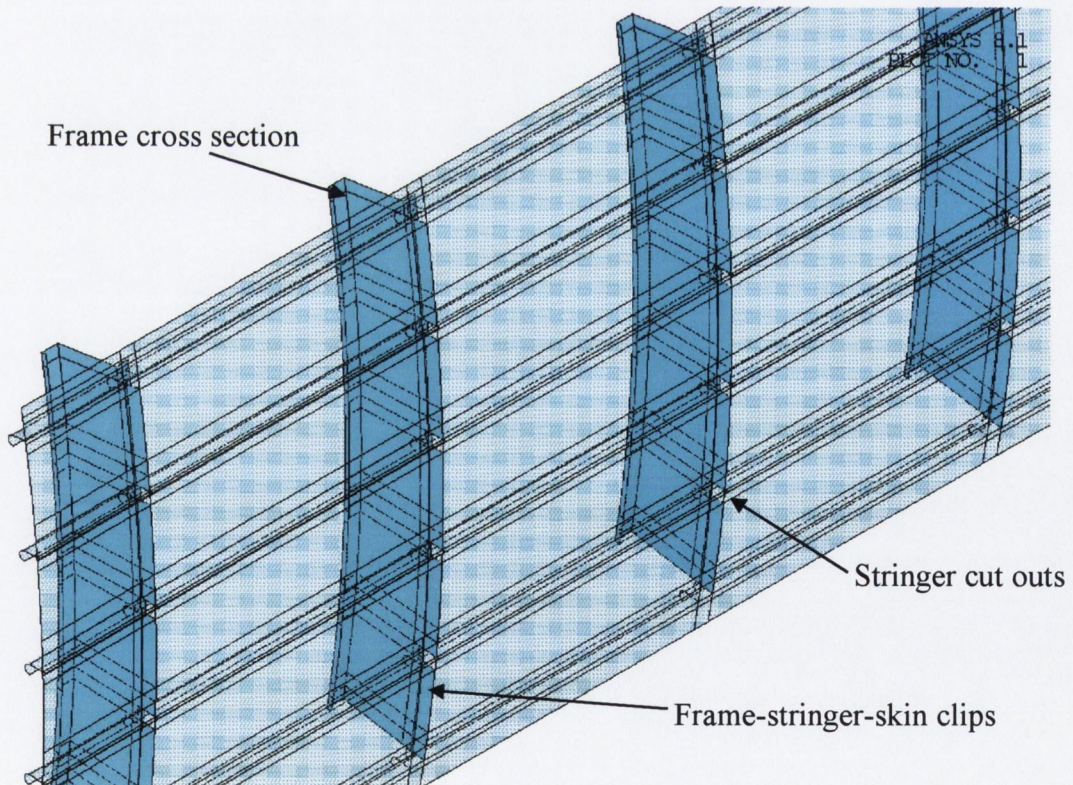
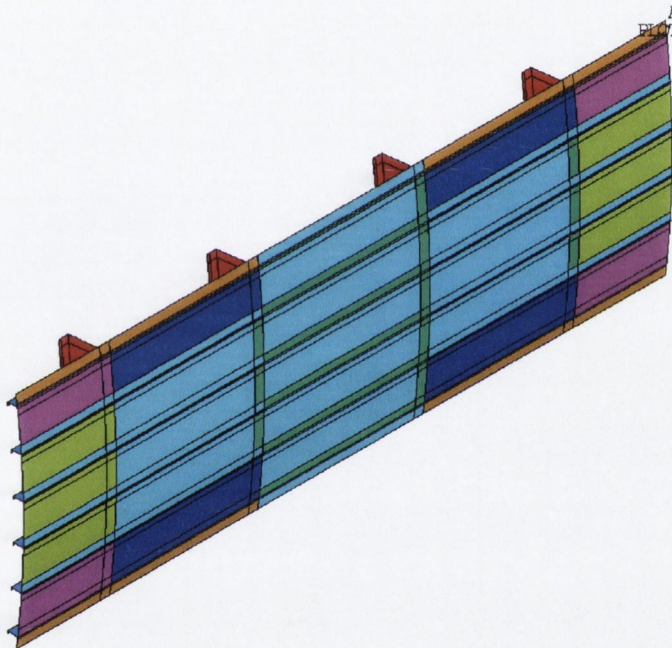


Figure 4.16 Frame cross section showing cut outs and translucent skin and stringer surfaces

From Figure 4.17 we can see the efficiency that the parametric build imparts to a standard FE analysis. The figure clearly shows the differing skin thicknesses assigned to the areas



outside the inner frame bay or “test section” to model the doublers which were added to ensure maximum load transfer to the test section, as well as the chemically milled areas. It can easily be appreciated that to manually assign the differing real constants depicted graphically in Figure 4.17 requires a large amount of time and is an inefficient use of the FE analyst’s time. An additional advantage of these variables is that they can be retrieved after the analysis during post-processing. For this reason, they have been grouped in terms of their design parameters, for example “*Unmilled skin*” contains the elements corresponding to the areas of the panel that have not been chemically milled. This allows the user to quickly select an area of interest without having to be an expert user of the finite element software.



**Figure 4.17 Panel surfaces with assigned thicknesses corresponding to colours**

## 4.6 Graphical User Interface

As outlined in section 4.5, before the model could be generated, the necessary parameters had to be input by the user. This was done by means of a graphical user interface developed using Microsoft Visual Basic 6.0. While it is possible to input the parameters directly into the ANSYS environment, it was a request from Airbus that a GUI be developed so that structural engineers unfamiliar with the ANSYS finite element software could set up and run models quickly.

Figure 4.18 through to Figure 4.20 show the data entry forms for the panel geometry. Two stringer cross sections are accounted for, Z- profiles and curved profiles. The data entry form for the curved profile is shown, Figure 4.19.

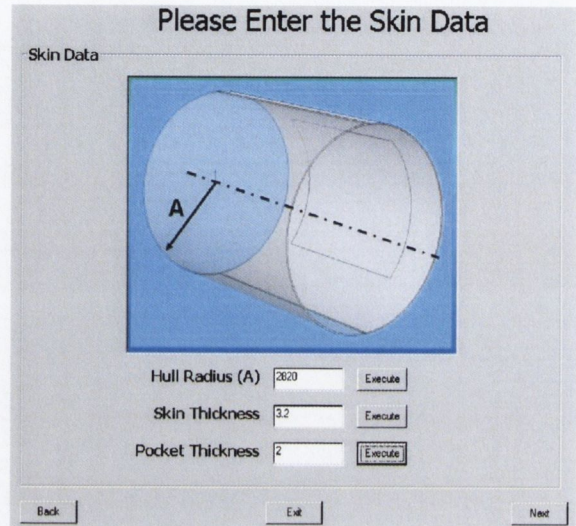
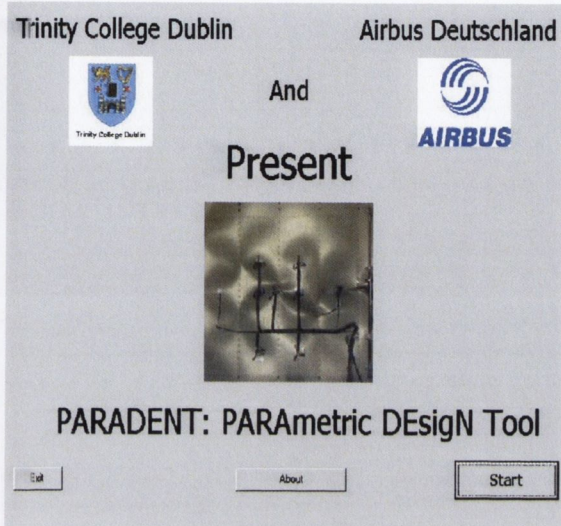


Figure 4.18 GUI entry and skin data entry form

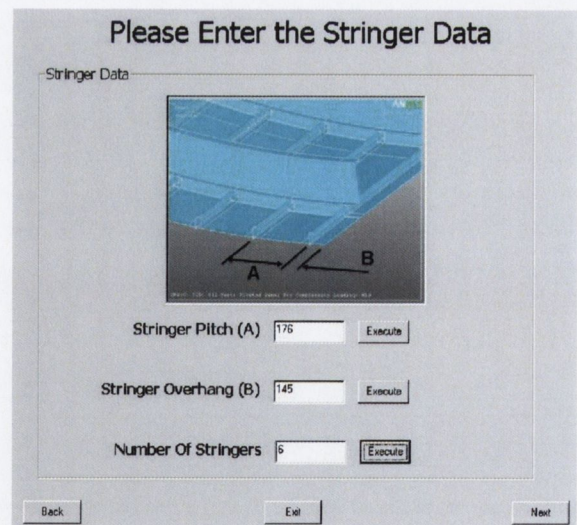
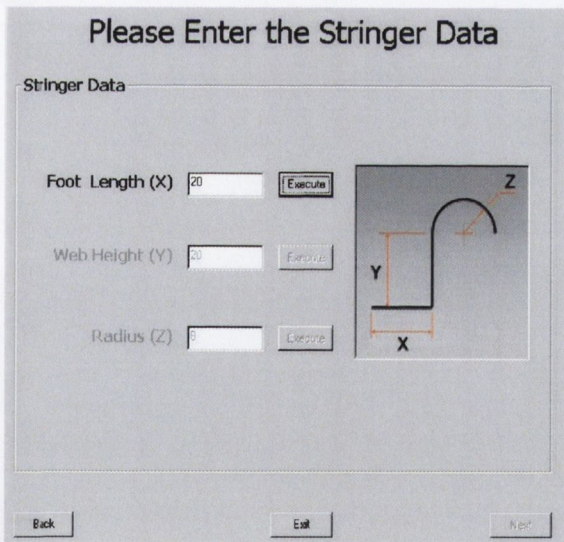


Figure 4.19 Stringer data entry form

In addition to the geometric variables shown, the user is prompted in additional data forms for a mesh density, dent depth, dent location, and indenter radius. Once the data has been entered, the visual basic executable generates an input file of the user-defined parameters which can then be read directly into ANSYS. When the user becomes familiar with the

process they can by-pass using the GUI and manually alter the input file directly if they so wish.

The figure consists of two side-by-side screenshots of a software interface titled "Please Enter the Frame Data".

The left screenshot shows a 2D diagram of a frame with dimensions A, B, C, and D. Below the diagram are four input fields, each with an "Execute" button:

- Dimension A: 22
- Dimension B: 110
- Dimension C: 30
- Dimension D: 9

The right screenshot shows a 3D perspective view of the frame. Below the view are three input fields, each with an "Execute" button:

- Frame Pitch (A): 530
- Frame Overhang (B): 309
- Frame Thickness: 2

Both screenshots have "Back", "Exit", and "Next" buttons at the bottom.

Figure 4.20 Frame data entry form

## 4.7 Finite Element Mesh

On completion of the geometric build, the geometry is discretised in a process known as meshing. As outlined in section 2.7, the accuracy of a solution converges to the true solution as the mesh density increases. While mesh density is very important, the "quality" of the mesh is equally important. The quality of the mesh refers to the shape and aspect ratio of the individual elements in the mesh. A balance between mesh density and run times is necessary and a mesh sensitivity analysis was therefore carried out from the point of view of the ultimate buckling load to establish an appropriate density for the models. It is at this stage that the element attributes assigned to the individual components, as described in section 4.5, are accessed and assigned to the elements. Figure 4.21 shows the panel meshed using a mesh density for which the element edge length was set to 21mm. The model contains 672 areas, 11182 elements and 16544 nodes. The mesh shown in Figure 4.21 was generated using quadrilateral shell elements. This form of a mesh, known in ANSYS as a "mapped" mesh, gives more accurate results than the other form of mesh available, a "free" mesh. While a free mesh can be applied to any geometry, there are strict rules regarding the application of a mapped mesh. These rules govern the shape of the geometry that a mapped mesh can be applied to. Hence, the parametric geometry build was programmed to create areas that followed these rules as the benefits in terms of accuracy outweighed the extra coding development required.

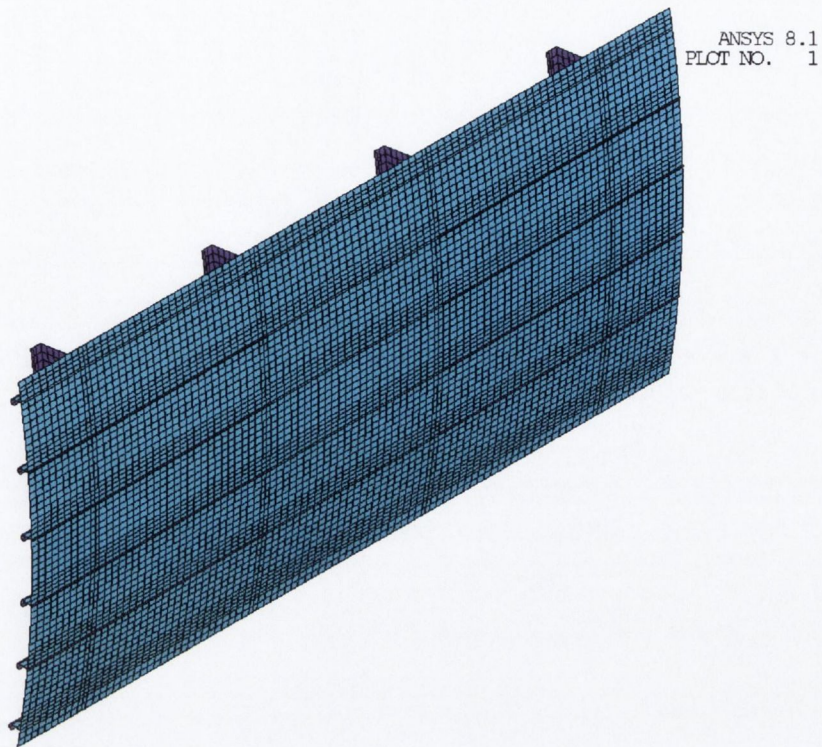


**Figure 4.21 Finite element meshed panel**

The edge length of 21mm was selected based on the mesh sensitivity analysis and is applied across the panel with the exception of the stringers. The mesh density on the stringer cross section is set using a parametric input, for the curved stringers four elements are used to describe the curvature of the stringer flange, while for both curved and Z-stringers four elements are used in the web to account for in-plane bending as described in section 4.3, see Figure 4.22. The panel, stringer and web and stringer flange mesh density can all be easily changed by user-defined parameters; thereby facilitating more approximate models with faster run times should the user so wish.

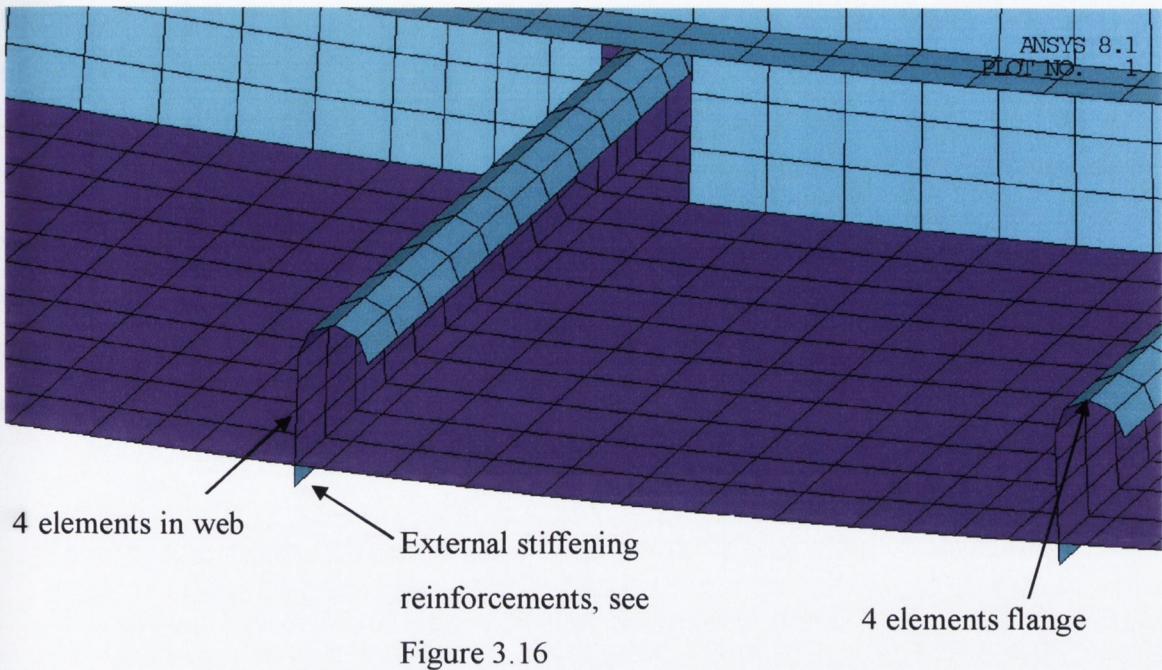


Figure 4.22 Stringer mesh

## 4.8 Contact Analysis

Contact analysis is based on the fact that in a continuum model it is not allowed that two points occupy the same space. This essentially means that for multiple bodies no penetration can occur, mathematically this is described by the governing conditions for normal contact, known as the Karush-Kuhn-Tucker equations, [65, 66]. These can be summarised as:

$$g \geq 0 \quad (4.2)$$

$$c \leq 0 \quad (4.3)$$

$$g \cdot c = 0 \quad (4.4)$$

here  $g$  indicates the normal gap measured from the target end and  $c$  is the normal force acting upon the target at the point of contact. The first condition (4.2) states that no penetration can occur, the second (4.3) that the contact normal force should be compressive for contact to occur and the third (4.4), states a complimentary condition that if there is no contact, no compressive forces can occur, or alternatively, if there are no compressive forces then the distance must be positive. These are the simplest form of the contact conditions but serve to illustrate the concept. Additional equations are derived for

sliding contact and to account for plasticity. A detailed derivation of these equations based on continuum mechanics can be found in Bathe [67].

From a numerical viewpoint contact is considered as a boundary non-linearity [68], and in order to implement the Karush-Kuhn-Tucker equations finite element solvers must allow some degree of initial penetration, which is then minimised using Lagrangian multipliers, the penalty method or a combination of both. ANSYS supports all three types of contact algorithms, namely:

1. The pure penalty method
2. The pure Lagrange method
3. The augmented Lagrange method

All three contact algorithms aim to establish a mathematical relationship based on the physical reality that two bodies in contact cannot interpenetrate. When the finite element program seeks to prevent interpenetration of two surfaces, defined as a “*target surface*” or master surface, and a “*contact surface*” or slave surface, it is said to “*enforce contact compatibility*” [69]. The penalty method achieves contact compatibility through the use of a contact parameter, which can be thought of as a “*spring*”, establishing a relationship between the two contacting surfaces, see Figure 4.23. The spring will deflect an amount  $\Delta$ , such that equilibrium is satisfied for, where  $F$  is the contact force and  $k$ , the spring stiffness, is called the penalty parameter, or more commonly the contact stiffness

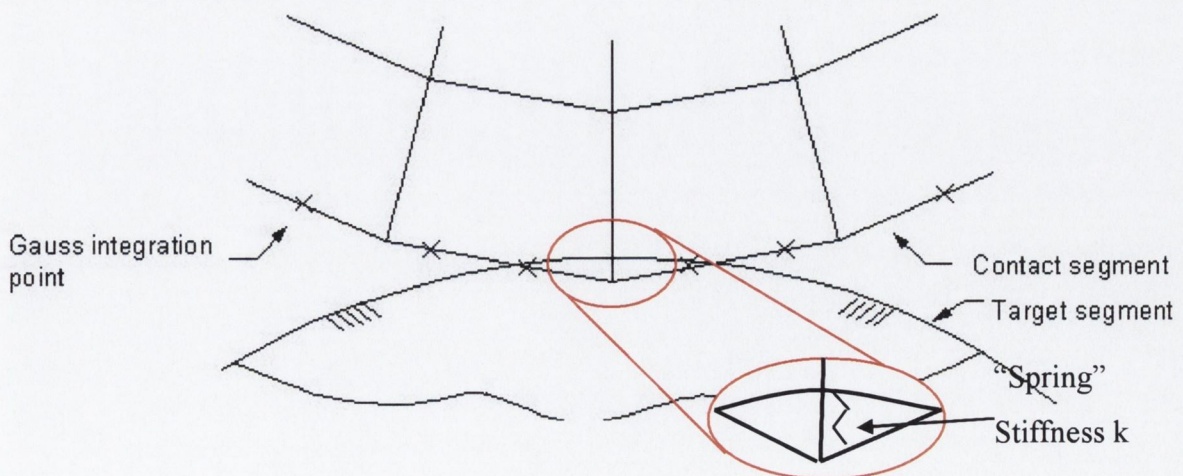


Figure 4.23 Schematic representation of penalty stiffness [62]

In ANSYS contact is monitored at the Gauss integration points, not at the nodes as is the case in many FE solvers. This is -advantageous in that the gauss points can only belong to one element and, in addition, there are more of them resulting in a smoother distribution of contact forces. Penetration is monitored and returned to the surface if the penetration exceeds a certain tolerance by means of a pushback force, which is a function of the penetration. In order to minimise the amount of penetration  $\Delta$ , a very high value of contact stiffness must be used, but this can lead to convergence difficulties by throwing the contact pair apart between successive iterations due to the high contact force. An alternative method the Lagrange method adds additional d.o.f to the model, namely contact tractions. This method is less sensitive to the magnitude of the contact stiffness but usually requires additional iterations.

A hybrid combination of these two contact algorithms is used in the analyses presented in this thesis, known as the augmented Lagrange method. Its advantage is that it controls penetration through additional iterations with the Lagrange-Parameter and improves the functionality of the penalty method.

Broadly speaking, contact problems can be broken down, in order of increasing complexity into three categories,

1. Node-to-node contact.
2. Node-to-surface contact.
3. Surface-to-surface contact.

Node-to-node contact, “*gap*” elements were the first to be developed for simple cases with little or no sliding. Their implementation is relatively straightforward, although the mesh on opposing faces should be controlled to ensure node to-node definition. Node-to-surface elements can handle sliding behaviour and dissimilar meshes, while the most recent surface-to-surface contact elements are based on contact checking at Gaussian integration points as mentioned above. These elements overcome most of the limitations of the earlier methods, supporting lower and higher order elements and therefore have no restrictions on the shape of the target or contact surface.

The models presented in this thesis were based on surface-to-surface contact. This was necessary to model a three dimensional object, the spherical indenter, impacting on a

curved surface. Contact 173 elements were used on the contact surface. These are 4 noded surface-to-surface contact elements. The Target 170 was used to represent the indenter.

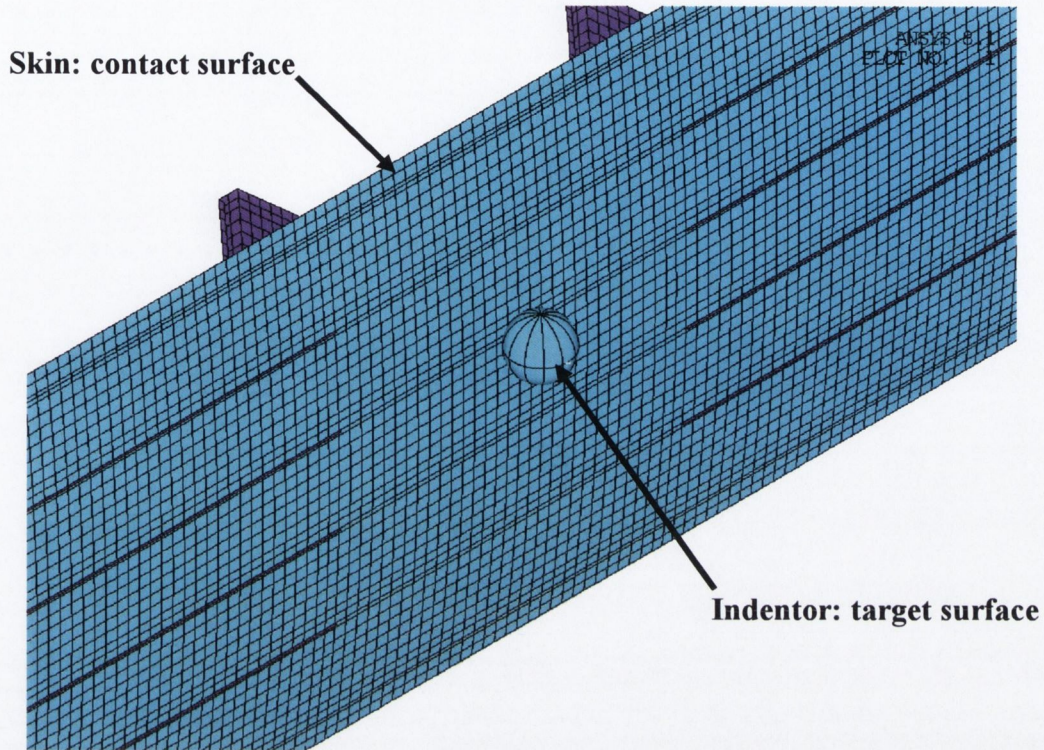


**Figure 4.24 Target and contact surfaces**

In order to decrease the numerical complexity of the problem, and thereby decrease convergence issues, a decision was taken to model the target surface, or indenter, as a rigid object. The resulting rigid-flexible contact analysis differs from a flexible-flexible analysis in that there are no deformations calculated for the rigid object, hence decreasing run times. This is an acceptable assumption since the steel hemispherical indenter has a far higher stiffness than the thin-shell aluminium skin, due to its geometric shape and the material properties.

The basic steps performed in generating the surface-to-surface contact analysis are listed and explained below.

1. Create the model geometry and mesh.
2. Identify the contact pairs.
3. Designate contact and target surfaces.
4. Set the element options and attributes.
5. Define/control the motion of the target surface (rigid-to-flexible only).
6. Apply necessary boundary conditions.



7. Define solution options and load steps.
8. Solve the contact problem.
9. Review the results.

The initial and final steps are common to all finite element analysis, while steps 2 to 5 are specific to a contact analysis. Step 2 involves identifying where contact will occur. This is often the most difficult task, but in the present model it is known that contact will always occur in the test section, or middle frame bay, on the external surface. The definition of the contact surfaces is controlled using parametric definitions as defined in section 4.5. Having identified potential contact surfaces, they must be defined via target and contact elements, steps 3, 4 and 5, which will then track the mechanics of the deformation process.

The indenter or target surface was modelled using a pilot node and associated primitive element to represent a rigid sphere. This had the advantage that the pilot node controlled the motion of the element. As a result, the loading conditions for the indentation and subsequent indenter removal only had to be applied to this node. Since the loads were applied at a single load all the reaction forces were transferred to this node, allowing for direct comparison with the loads read from the load cell in the experimental set-up. Both the indenter radius and location were parameterised for user-input as described in section 4.5.

The contact surface was defined by overlaying a surface of Contact 173 elements on the existing finite element mesh. When carrying out this step, it is necessary to ensure that the outward normals of the contact elements are facing towards the target surface. If they are not ANSYS incorporates a command to flip the normals in the correct direction. This has also been accounted for in the parametric model. As mentioned in section 4.3, ANSYS has the capability of accounting for shell element thickness in surface-to-surface contact. Traditionally, shells are discretised at their mid-surface and the penetration distance is calculated from the nodal points on this surface. The analyses presented in this thesis use a new feature of ANSYS which automatically shifts the contact surface to the bottom or top of the shell surface, hence calculating penetration distance from the correct location.

## 4.9 Boundary and Loading Conditions

Following the generation of the finite element model, the boundary and loading conditions were applied. As the model geometry was parametric, the boundary conditions also had to be developed in a parametric manner since the elements to which they were applied were dependent on the given panel configuration specified. Two sets of boundary conditions were developed; one for the indenting phase and one for the compression phase, these conditions were a finite element representation of the actual experimental test conditions described in sections 3.3 and 3.4.

### 4.9.1 Denting Boundary Conditions

The experimental denting boundary conditions are described in detail in section 3.3. The inner flanges of the finite element frames were constrained in the radial direction. This boundary condition represented the wooden supports applied beneath the inner frame flanges in the experimental test. In addition to this constraint which was applied to all frames, the flanges of frames 1 and 4, Figure 4.25, are constrained in all d.o.f., effectively clamping them to account for the extra restraint provided by the wooden support clamped on the external skin in the test set up, Figure 3.5.

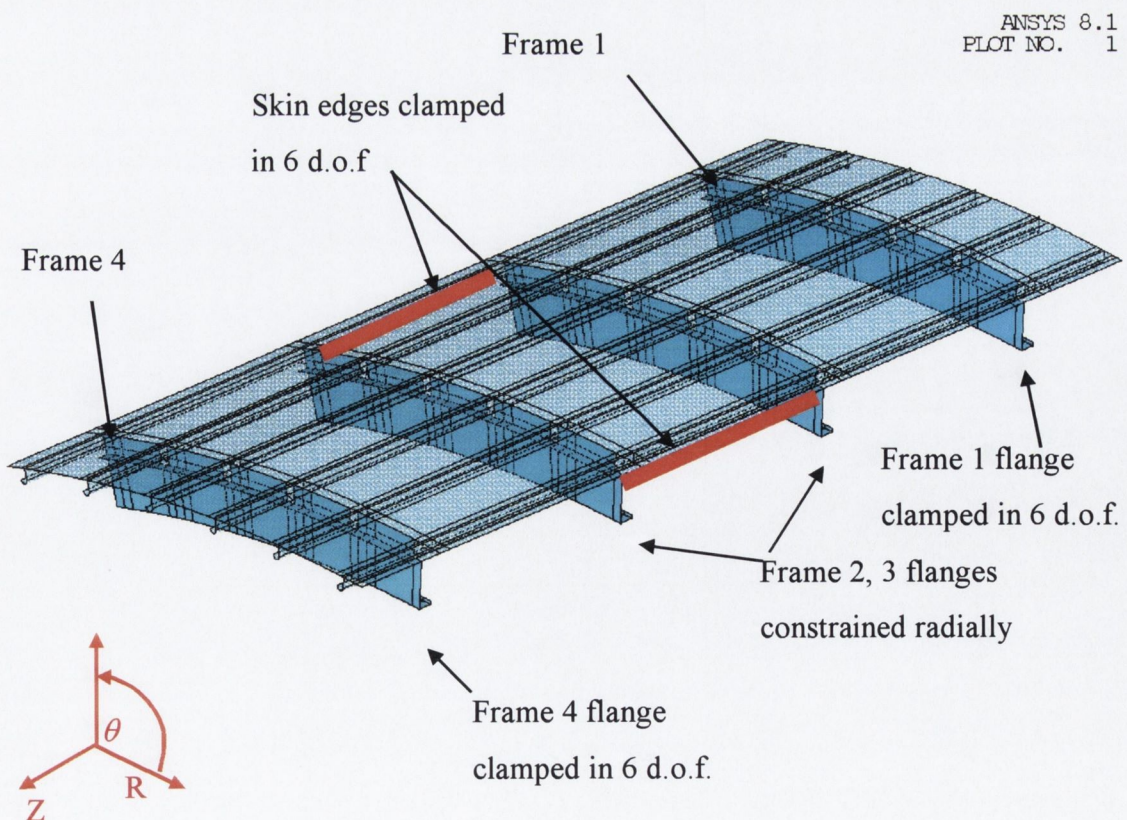


Figure 4.25 Denting boundary conditions

The application of the indentation was carried out via displacement control. Force control was initially evaluated but it can lead to solver difficulties as singular matrices are set up. This is because, as described in section 2.7, the finite element method is a displacement based problem, where the relationship between bodies is described in terms of the stiffness matrix. However, for the two bodies shown in Figure 4.26, the resulting stiffness matrix has no coupling terms between the two bodies 1 and 2,

$$\begin{Bmatrix} F_1 \\ F_2 \end{Bmatrix} = \begin{pmatrix} K_1 & 0 \\ 0 & K_2 \end{pmatrix} \begin{Bmatrix} x_1 \\ x_2 \end{Bmatrix} \quad (4.5)$$

where  $F$  is force,  $K$  is stiffness,  $x$  is displacement and subscripts 1 and 2 denote bodies 1 and 2 respectively.

Since there is no stiffness relationship between the two bodies until it is provided by the contact stiffness parameter when the bodies come into contact this set up can result in a singular  $K_1$  matrix, which is unsolvable because its inverse does not exist. There are a number of methods to overcome this difficulty such as adding weak springs to the indenter, careful control of offset and displacement control.

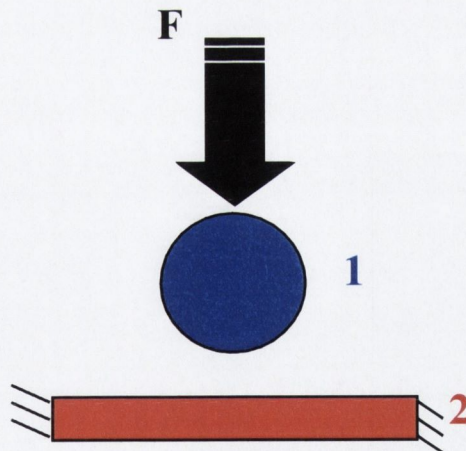


**Figure 4.26 Force controlled contact, constraints on sphere established when in contact**

Displacement control was the method selected for a number of reasons. Not only does displacement control overcome the problem of singular matrices, it also allows the user to define the maximum indentation of the dent. The displacement was applied to the pilot node which governs the motion of the entire target surface. The use of the pilot node allowed the forces over the entire target surface to be summed from the pilot node. This

was an important modelling technique as it was necessary to compare the force-displacement readings from the experimental set-up against the finite element model. ANSYS supplies a number of so called “*primitives*” or basic shapes which can be associated with the pilot node. This modelling technique ideally suited the definition of the spherical indenter, Figure 4.27.

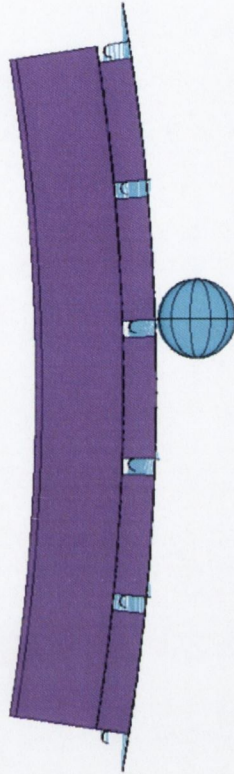


**Figure 4.27 Indentor loading**

Using displacement control also aided in easily changing the denting parameter, via the “*dent depth*”, a user defined parameter which controlled the maximum dent depth. Since it was the objective to investigate the effects of dents of a given residual dent depth, a macro was written to create a dent with a specified “*residual dent depth*”. The control flow of the macro is shown in Figure 4.28. It should be noted that implementing the residual dent depth required a little fore knowledge to ensure a value of max dent depth was not chosen that resulted in a deeper than desired residual dent depth. The incremental nature of applying an indenter, removing it, and reapplying it would obviously result in a certain amount of strain hardening. To avoid this when applying incrementally deeper dents, the previous load steps were cleared and the incremented dent depth applied to an “*as new*”, or undented pristine panel.

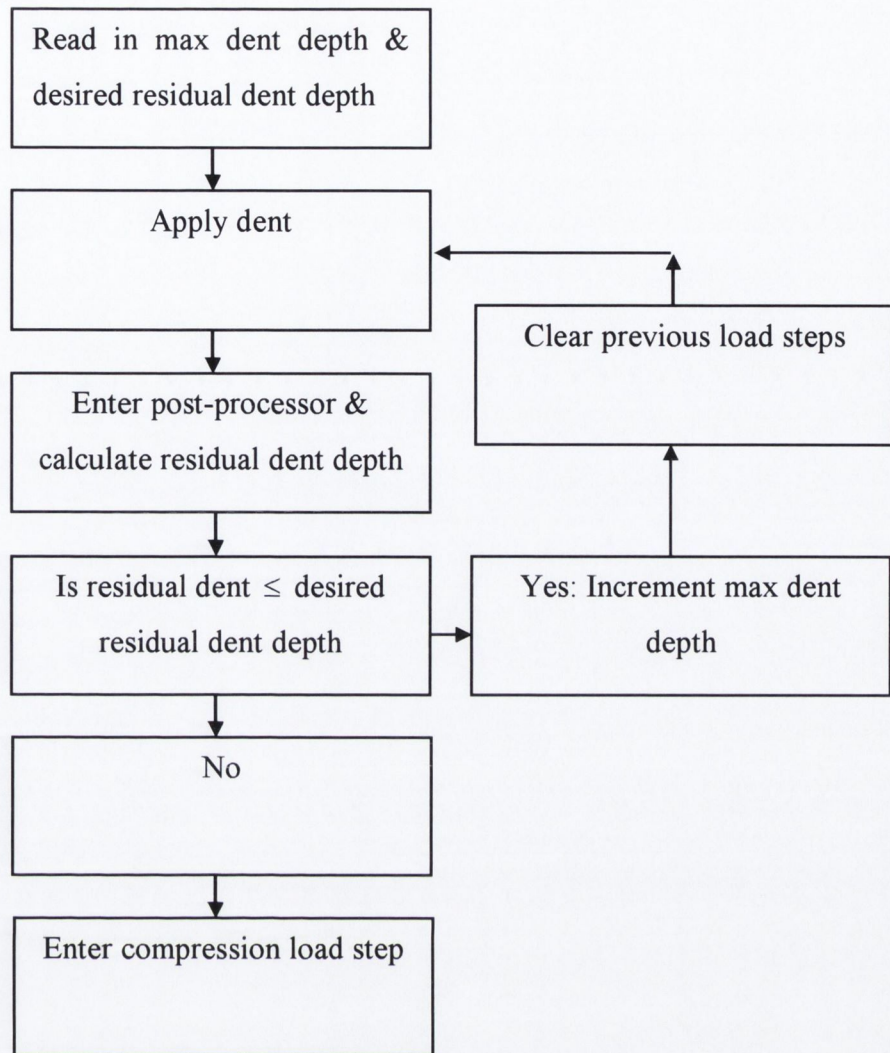


Figure 4.28 Control flow residual dent depth macro

## 4.9.2 Compression Loading

The experimental set-up, as described in section 3.4, uses a system of hydraulic jacks to apply a uniform axial compressive force to the end of the panel, and inductive displacement transducers to measure the resultant panel shortening. Since it is the aim of the finite element simulation to model this as accurately as possible, the first attempt at modelling the end compression was by applying a uniform force to all the nodes on the end of the panel.

In order to account for follower forces due to the deforming structure, the force was applied as a pressure load. There were, however, a number of convergence issues with this form of loading which can be explained by the nature of the ANSYS non-linear convergence algorithm, namely the “*Newton-Raphson*” method. These are explained as follows; the Newton-Raphson method works by iterating the equation

$$[K_{n,i}^T] \{\Delta u_i\} = \{F_n^a\} - \{F_{n,i}^{nr}\} \quad (4.6)$$

where  $[K_{n,i}^T]$  is the tangent matrix at time step  $n$  iteration  $i$ ,  $\{F_n^a\}$  is the total applied force vector at time step  $n$  and  $\{F_{n,i}^{nr}\}$  is the restoring force vector for time step  $n$  iteration  $i$ ; until the residual  $\{F_n^a\} - \{F_{n,i}^{nr}\}$  falls within a certain convergence criteria [67, 70]. The Newton-Raphson method increments the load by a finite amount at each sub-step of the analysis, and keeps that load fixed throughout the equilibrium iterations, Figure 4.29.

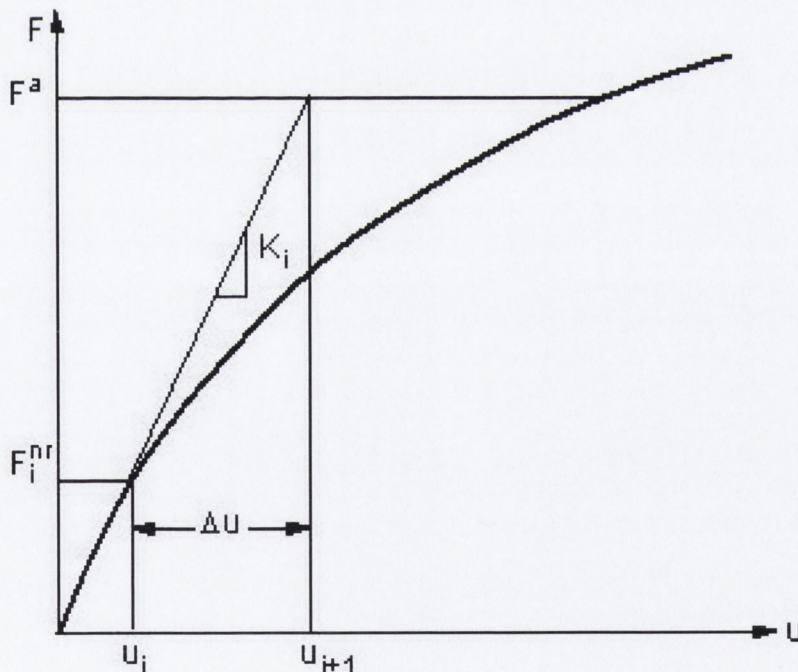


Figure 4.29 Newton-Raphson solution- one iteration [62]

When the Newton-Raphson method is employed in structural non-linear analysis where the slope of the force-deflection curve at any point is zero or negative, see Figure 4.30, as is often the case in buckling analyses due to snap-through and post-buckling behaviour, the

tangent stiffness matrix becomes singular. As described above this leads to convergence difficulties.

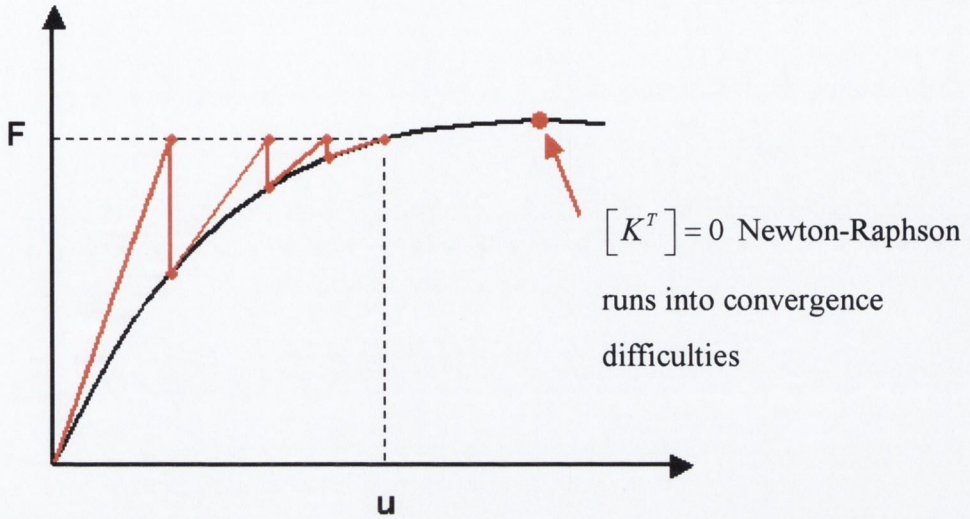


Figure 4.30 Newton-Raphson develops singularity [71]

To deal with the zero and negative tangent stiffnesses ANSYS employs the arc-length algorithm in combination with the Newton-Raphson method [62, 64]. The arc-length multiplies the incremental load by a load factor  $\lambda$ , where  $\lambda$  is between -1 and 1 [71]. This addition introduces an extra unknown, altering the equilibrium equation slightly to

$$[K_{n,i}^T] \{\Delta u_i\} = \lambda \{F_n^a\} - \{F_{n,i}^{nr}\} \quad (4.7)$$

The arc length method imposes another constraint, through the stipulation that:

$$\sqrt{\Delta u_n^2 + \lambda^2} = l \quad (4.8)$$

throughout a given time step, where  $l$  is the arc-length radius, Figure 4.31

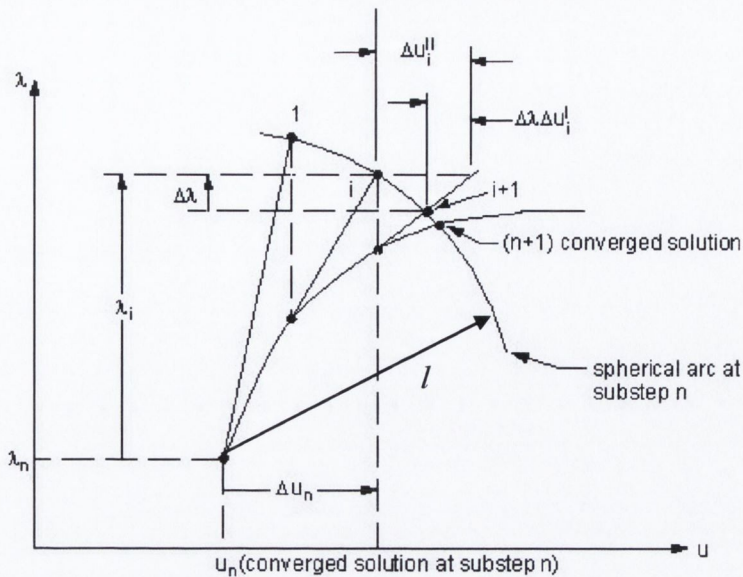


Figure 4.31 Arc-length methodology [62]

Evaluation of this solution control proved it to be very sensitive to user input values “maxarc” and “minarc”, where maxarc is the maximum allowable multiplier of the reference arc-length radius and minarc is the minimum allowable multiplier. In addition, this method did not always guarantee convergence due to the number of active nonlinearities in the problem, material, structural and contact. Since the objective of the research was to develop a parametric model whose users might not necessarily be experienced with the finite element, it was decided to use the more robust method of uniform end displacement control.

Displacement controlled loading allows for the both global and local collapse to be modelled, and for the load to decrease after failure. While it is a straightforward procedure to create a component comprising of the nodes on the circumferential end of the panel to apply this displacement to, a method using multi-point constraints was used. Multi-point constraints (MPC) employ the concept of a “*master node*”, whose motion controls a set of “*slave nodes*”. The MPC used was a new addition to the ANSYS finite element environment, the MPC 184 element. MPC 184 comprises of a general class of multi-point constraint elements that implement kinematic constraints using Lagrange multipliers [62]. The MPC 184 element works like constraint equations, in that certain nodes are constrained to follow other nodes. Constraint equations, however, cannot be used in large deflection problems such as non-linear buckling, because they use the nodal coordinate systems to define their direction, and nodal coordinate systems do not get updated for large



rotation effects. To account for cases where the user changed the mesh density or the panel geometry, the generation of the MPC constraint was automated. A macro was written to select all the nodes on the circumferential end of the panel where the displacement was to be applied. A master node was then created at their average coordinate and beam elements were generated between the master node and each node on the panel end, Figure 4.32. The uniform end displacement and boundary conditions were then applied to the master node and all the slave nodes were constrained to behave as it did. The boundary conditions were as described in section 3.4 where the circumferential end is restrained from displacement in the radial and circumferential directions.

The MPC method was compared against directly applying the displacement to all the end nodes and results were identical as expected, the reason for using the MPC method was that it eased post-processing for users unfamiliar with ANSYS in that only one node needed to be selected to access the displacement and force on the panel when generating force vs. displacement plots. This allowed for direct comparison with experimental results thus, adding to the usability of the parametric model.

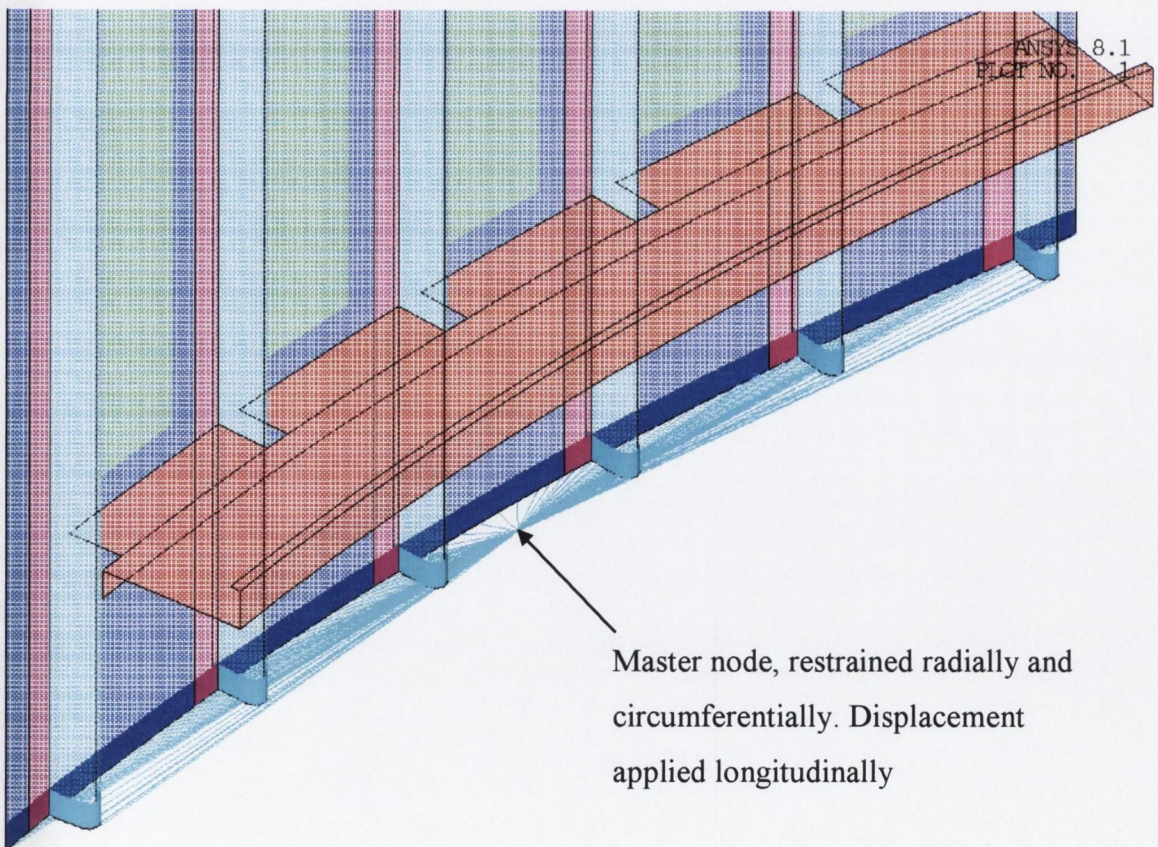


Figure 4.32 Multi-point Constraint set-up, showing elements on circumferential end of panel only

## PART V

# 5 FINITE ELEMENT AND EXPERIMENTAL RESULTS

In this chapter, results are presented from the coupon denting test rig. Experimental and FE results are then presented for the indentation of a full scale aircraft panel, corresponding to the geometry listed for panel number one in Table 3.1. Following this, FE results are presented for the case of a pristine panel under axial compression loading with no damage in order to demonstrate the effect of local skin buckling on the stress distribution in the panel. These FE results are compared against experimental results available from full scale panel certification tests in order to bench-mark the accuracy of the developed numerical model. Results are then presented for the FE compression loading of the dented panels and compared with experimental results to demonstrate the effect of dents on both the local skin buckling, and the global collapse of the panel. Results are then presented from a series of parametric studies. Following this, results from a numerical model of the dent dress back procedure are presented. Finally, the results of an investigation into the effects of including or omitting the residual stresses in the FE modelling of the dent are presented. In all cases, results are presented in the cylindrical co-ordinate system,  $(R, \phi, Z)$ , where  $R$  corresponds to the panel radius,  $\phi$  is the radial angle and  $Z$  is the longitudinal distance from the global origin, see Figure 5.4.

### 5.1 Denting Results: Coupon Test Rig

As described in section 3.2, a coupon sized test rig was designed and built in Trinity College Dublin. This test rig was designed in order to verify the FE methodology employed prior to the availability of full scale experimental test results. The finite element model of the coupon denting test rig is shown in Figure 5.1. The model is meshed with Shell 181 elements which are clamped in all 6 d.o.f along all four edges. The indenter is modelled using as a rigid spherical element which is controlled by a pilot node as described in section 4.8.

Figure 5.2 graphs the experimental and finite element load curves. Denting load in KN is graphed on the y-axis versus dent depth in mm on the x-axis. Both the experimental and finite element indentation depths were set at 10mm. From the results it is clear that the

predicted FE results and the measured experimental results show good correlation. The experimental tests recorded a maximum force of 10.4KN at a depth of 10mm. This compared well with the finite element predicted result of 10.18KN, an error of 2.1%. Figure 5.3 plots the FE predicted residual dent deformation. The FE predicted value of 2.6mm shows an error of 7.14% when compared with the experimental value of 2.8mm.

As can be seen from the presented results, the modifications made to the coupon denting test rig solved the problem of aluminium slippage in the clamping frames. The close correlation between the modified coupon test rig denting results, shown in Figure 5.2, gave confidence in the FE modelling methodology being employed. This methodology was then applied to the full scale panel model, the results of which are presented in section 5.2 and 5.3.

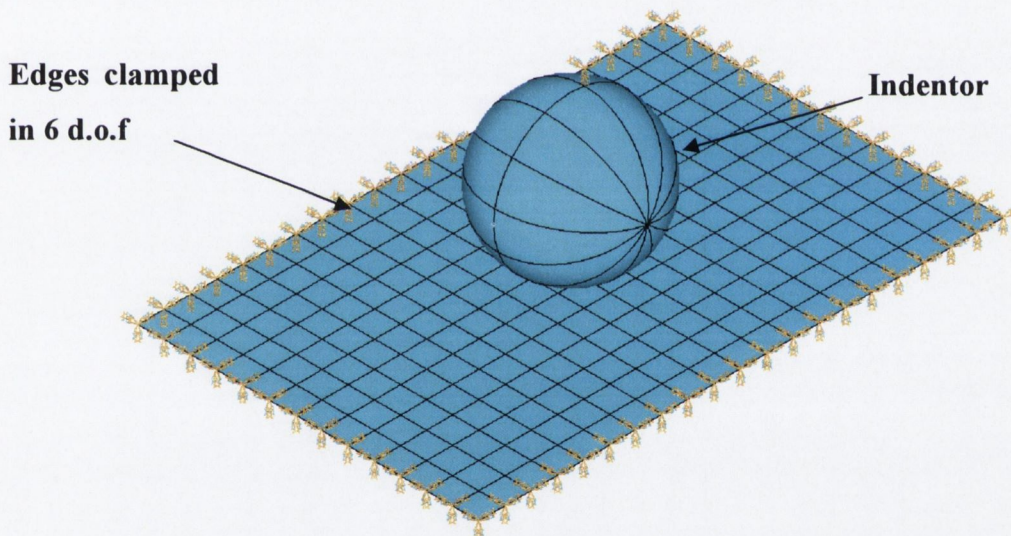


**Figure 5.1** Finite element of coupon denting test rig

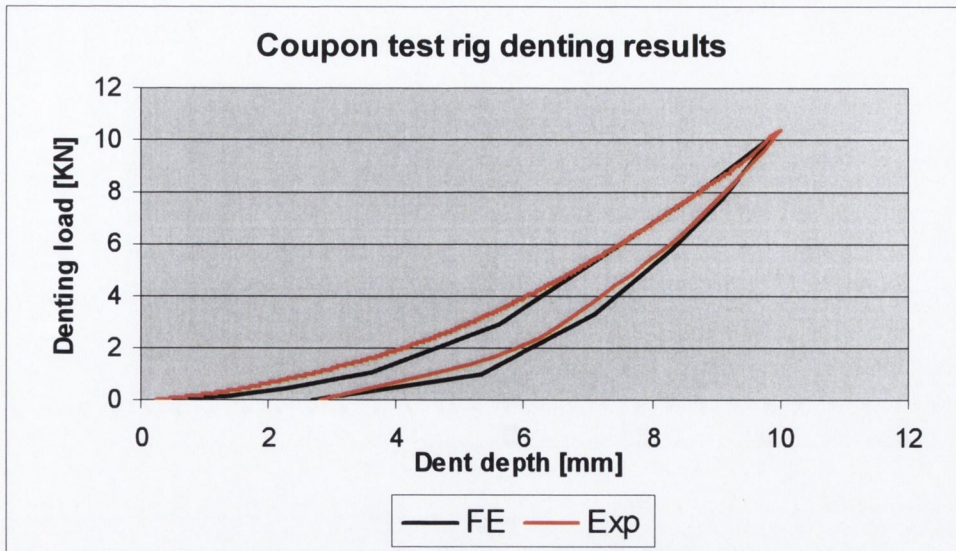


Figure 5.2 Experimental vs. FE indentation load curves

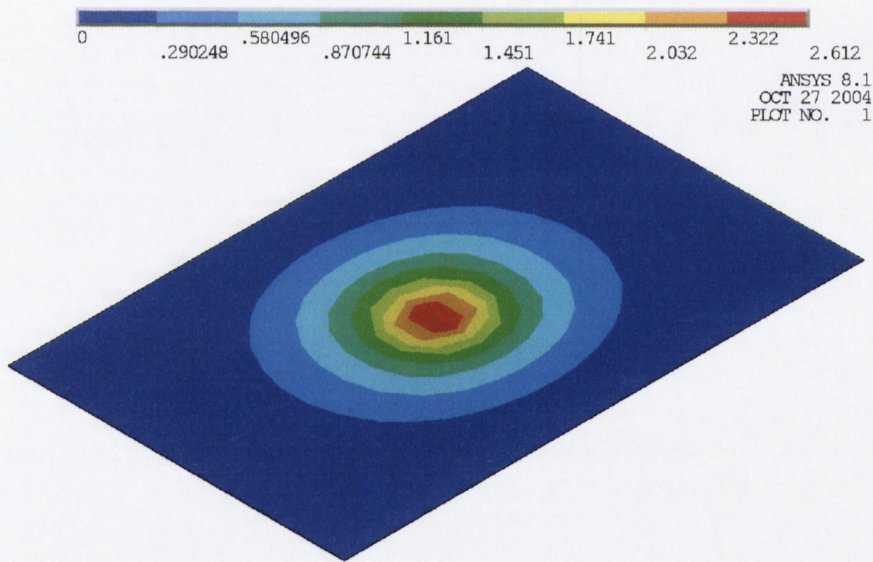


Figure 5.3 FE predicted residual dent due to 10mm indentation

## 5.2 Denting Results: A380 Welded Panel

Due to the capital cost of each full scale panel, only one experimental test was carried out on each panel geometry at the Airbus Germany test facilities in Hamburg. It was therefore decided to select the worst case scenario location for the dent. The dent was applied using a 50mm radius spherical indenter on a stringer, located mid-way between two frames, Figure 5.4. Initial investigations were carried out to establish the maximum residual dent depth achievable on a stringer under static loading conditions. It was established that a residual dent depth of 10mm was achievable as an upper limit, as attempting to reach a deeper dent of 12mm on panel number one from Table 3.1 resulted in fracture of the stringer flange. This compares well with the experience of the Airbus structural repair engineers dealing with daily dent repair requests from the airlines where the majority of dents reported are less than 10mm [72].

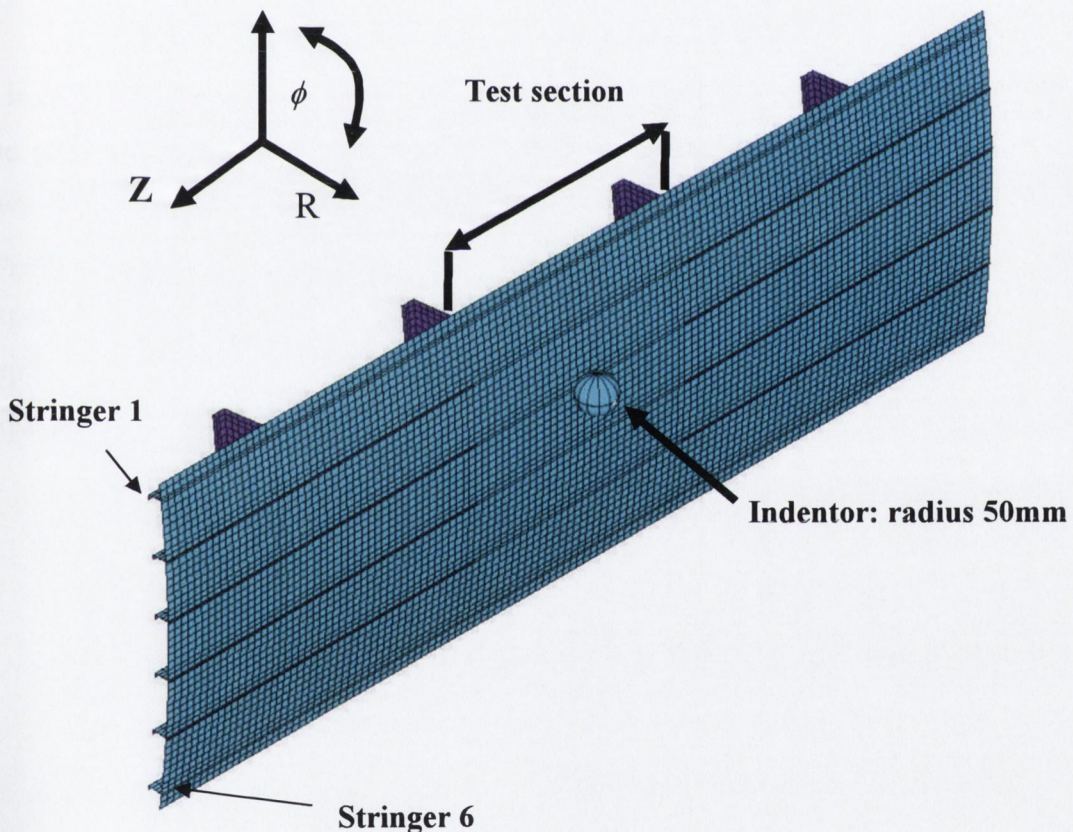


Figure 5.4 Dent location

### 5.2.1 Experimental vs. FE Load-Displacement Results

Figure 5.5 graphs the denting load versus dent depth for both the experimental and finite element results. Load in KN is plotted on the y-axis versus dent depth in mm on the x-axis. From the graph, it is clear that the finite element predicted results show close agreement with the measured experimental values. The experimental results record a maximum load of 18.27KN at a dent depth of 20mm which creates a residual dent depth of 10.49mm. The finite element results predict a maximum load of 19.1KN at a dent depth of 19.5mm resulting in a residual dent depth of 11.14mm. Figure 5.6 shows a plot of the radial displacement at maximum indentation. The results show a maximum radial displacement of 21.994mm and not 19.5mm as graphed in Figure 5.5. This is because the results graphed in Figure 5.5 are taken from a node 20mm away from the point directly beneath the indenter, coinciding with the position of the inductive displacement transducer in the experimental set-up as shown in Figure 5.7.

It is clear that a close correlation is shown between the predicted finite element results and the measured experimental results. The accuracy of the predicted results varies slightly over the load curve due to changes in stiffness. From a minimum error at an indentation depth of 10mm, where the finite element model predicts a load of 9.3KN versus an experimental load of 9.16KN, an error of 1.5%. To a maximum error at an indentation depth of 19mm, where the finite element model predicts a load of 18.42KN versus the experimental load of 16.79KN, an error of 9.7%.

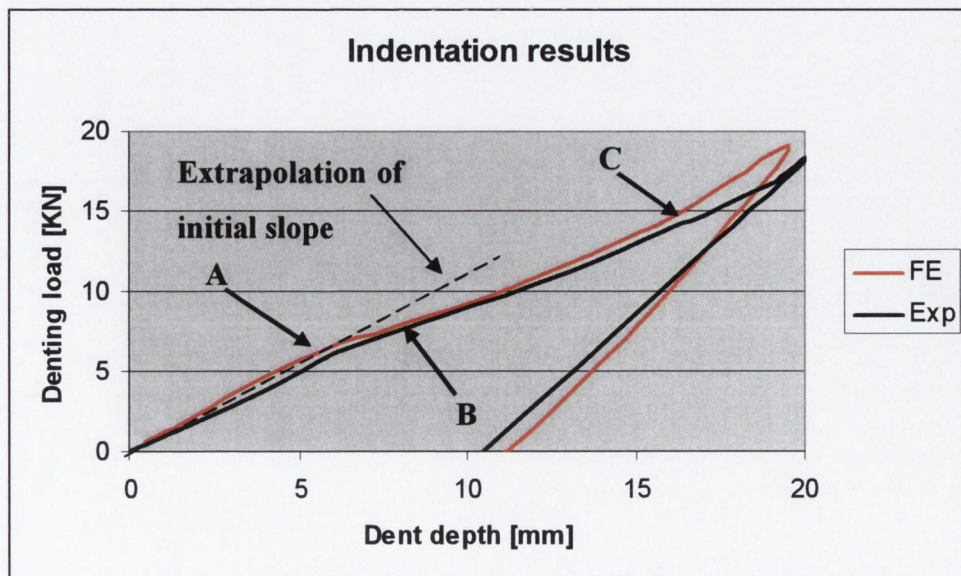


Figure 5.5 Denting load vs. dent depth

Figure 5.5 shows a distinct change in stiffness marked point A, which is evident in both the experimental and finite element results. Up to this point the load has been carried primarily through bending of the dented stringer with the frames acting as supports and deformation being restrained to the test section, as illustrated in Figure 5.6. By point A, however, the material in the stringer flange is under very high strains and the stresses have exceeded the stringer material AL6110 yield stress of 320MPa, see Figure 5.8. This results in local material yielding in the stringer flange and a drop in stiffness as evidenced at point A in Figure 5.5.

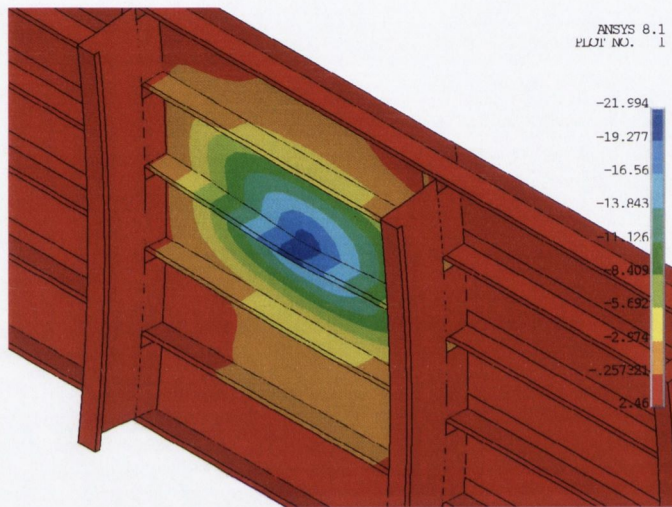


Figure 5.6 Radial displacement at maximum indentation

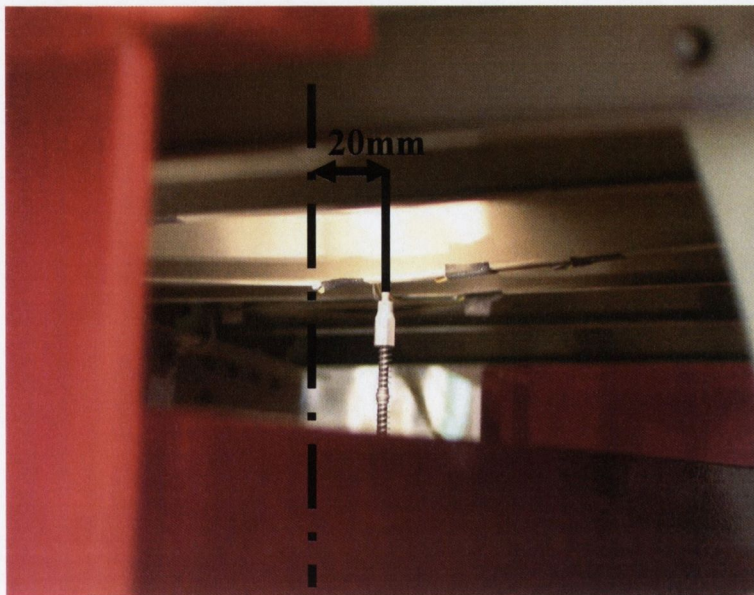


Figure 5.7 Inductive displacement transducer position on stringer flange

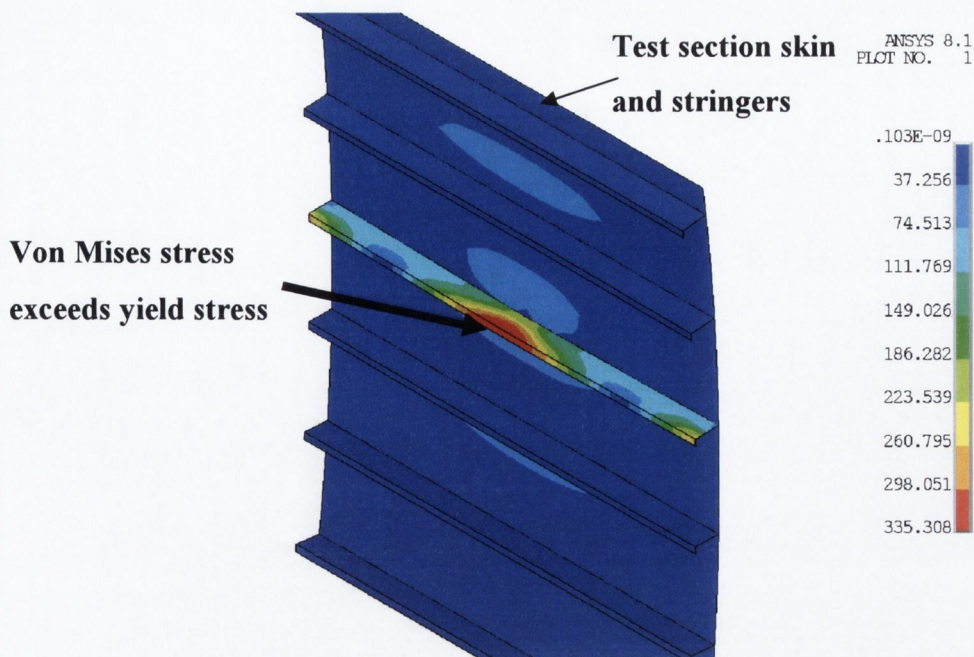


Figure 5.8 Von Mises Stress at Point A

After the local yielding of the dented stringer and the consequential drop in stiffness, the panel sustains the increasing load of the indenter through load redistribution via membrane stresses in the skin into neighbouring stringers. Figure 5.9 shows a plot of the von Mises stress distribution in the test section skin and stringers corresponding to the point marked B on Figure 5.5. Comparing the stress distribution at point B with that at point A as shown in Figure 5.8, the change in load carrying mechanism is evident through the increased stress levels in the stringer-frame bay skin. Figure 5.9 also shows the low levels of stress in the adjacent stringers as the panel begins to transfer load via the skin into these stringers.

By point C on Figure 5.5 the stringers adjacent to the dented stringer are under increased load, this is shown by the increased stress levels in the stringers in Figure 5.10. The rise in stiffness as evidenced at point C in Figure 5.5 is due to the resistance to radial deformation contributed by these stringers. This change in load carrying mechanism as predicted by the finite element results correlates well with the experimental strain results. The strain readings in the adjacent stringers showed an increase between point B and C as the stringers are placed under increased load due to load redistribution from the dented stringer. Experimental and finite element strain results are presented and compared below in the section 5.2.2.



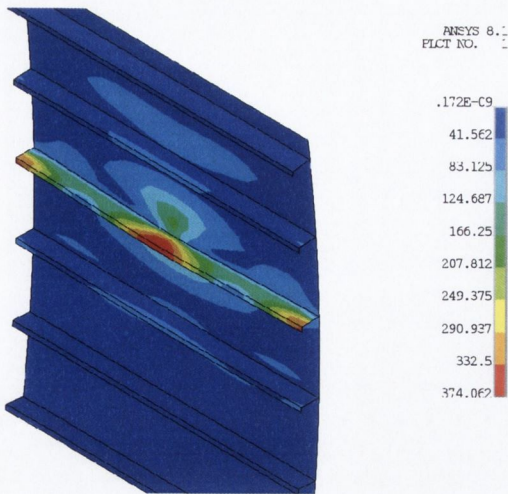


Figure 5.9 Von Mises Stress at Point B

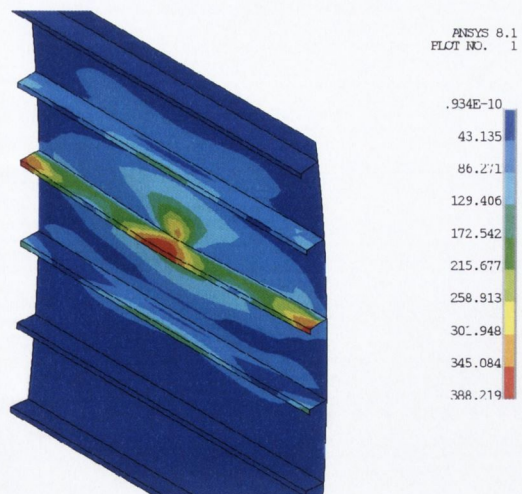


Figure 5.10 Von Mises Stress at Point C

### 5.2.2 Experimental Strains vs. FE Predicted Strains

In addition, to the recorded force and displacement readings the test panel was also instrumented with a number of strain gauges. For the indentation phase, longitudinal strains were recorded at positions on the external skin as depicted in Figure 5.11.

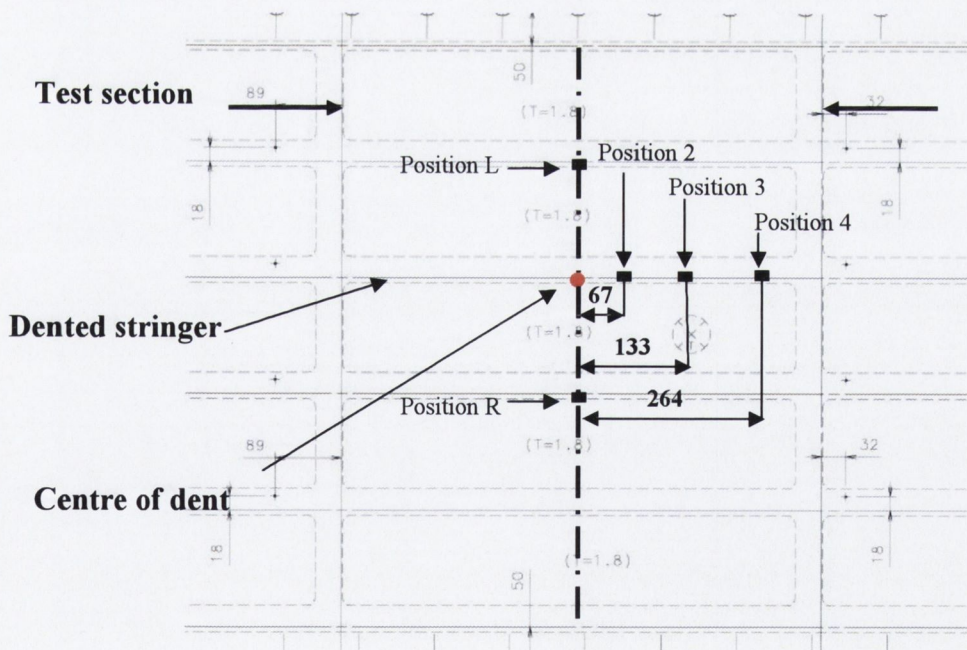


Figure 5.11 External skin stain gauge locations

The experimental longitudinal strains for indenting up to the maximum dent depth are graphed and compared against the finite element predicted strains from the corresponding locations on the model in Figure 5.12 and Figure 5.13. It can be seen that the predicted

finite element and measured experimental readings at positions 2, 3, and 4 on the dented stringer and positions L and R on adjacent stringers show excellent agreement over the indenting phase.

The strain histories for position 2 and 3 have been graphed on separate plots for clarity. The strain on the outer skin surface at positions 2 and 3, see Figure 5.12 and Figure 5.13, show an initial period of increasing compressive strain until a dent depth of approximately 6mm. At this point, the magnitude of the strain slope changes and the compressive strains decrease. Tensile strains are established at position 3 when a dent depth of 9mm is reached and subsequently at position 2 when a dent depth of 11mm is reached. These changes in strain at positions 2 and 3 coincide with the change in load carrying mechanism described in section 5.2.1. Before the stringer flange yields locally, the outer skin surface of the panel at positions 2 and 3 experiences compressive strains as the stringer behaves like a centrally point loaded simply supported beam, where the outer surface experiences compression and the inner surface experiences tension. At this point the only region under tensile strain is at location 4 since it is fixed by the frame clip, see Figure 5.14. However, when the stringer flange yields and the load is redistributed the deformation of the outer surface changes and the tensile region of strain gradually extends from position 4 to position 3 and then position 2. Only the area under the indenter remains in compression as evidenced in Figure 5.15.

From Figure 5.12 and Figure 5.13 it can be seen that when the compressive strains at positions 2 and 3 decrease and change to tensile strains the compressive strain at positions R and L show a corresponding increase in strain as they come under increased loading. This is in excellent agreement with the finite element results presented in section 5.2.1 indicating the change from an initial bending dominated deformation of the dented stringer to a redistribution of load into the adjacent stringers after local yielding of the stringer flange.

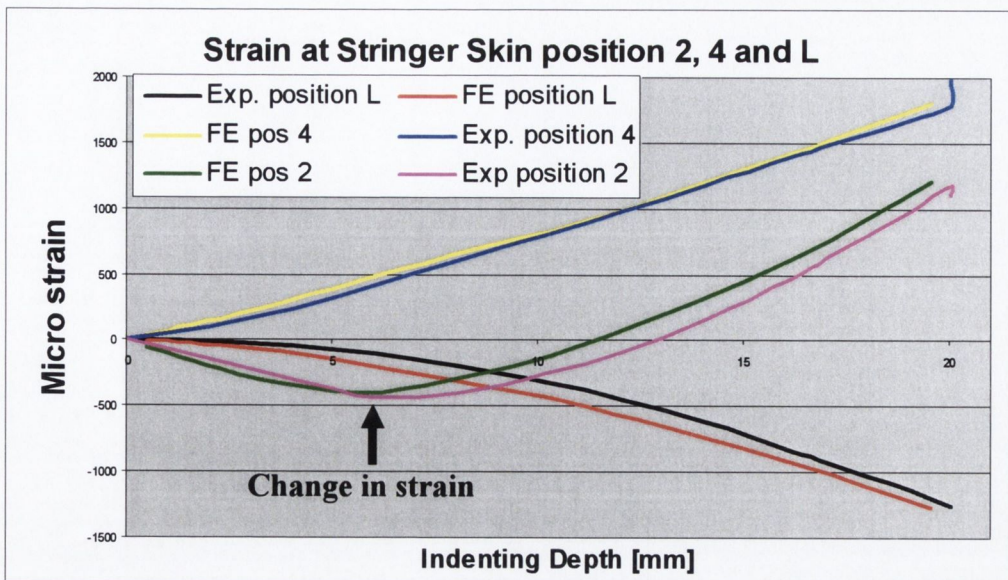


Figure 5.12 Experimental versus finite element strain at positions 2, 4 and L

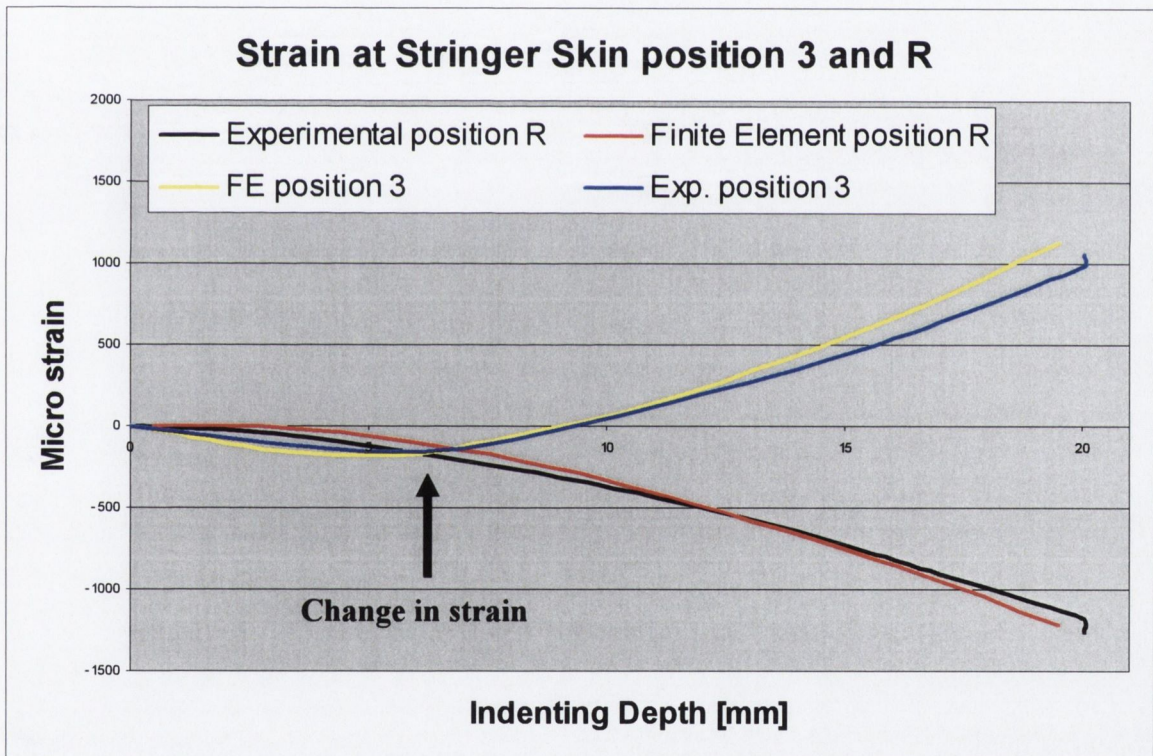


Figure 5.13 Experimental versus finite element strains at positions 3 and R

This change in state of the longitudinal strain is of particular interest due to the importance of fatigue as a failure criterion in aircraft design. While Figure 5.14 and Figure 5.15 plot the strain when the skin is still restrained by the indenter, it is the residual strain distribution that is of importance. Figure 5.16 and Figure 5.17 plot the residual longitudinal strain in the test section skin on the outer and inner skin respectively, the stringer elements

have been omitted for clarity. It is clear that on removal of the indenter the external skin along the stringer-skin connection remains in a state of tension, with only the area in the centre of the dent experiencing compressive strains. The corresponding strains on the internal surface of the skin show the expected tensile stresses along the stringer-skin connection line, Figure 5.17.

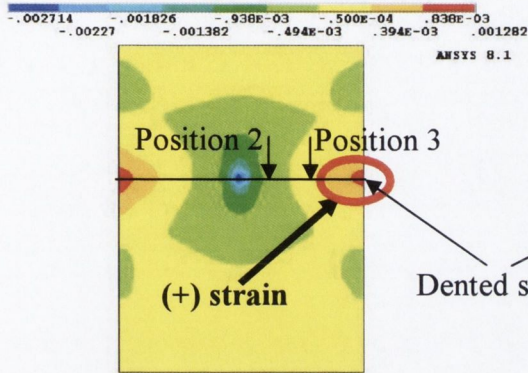


Figure 5.14 Longitudinal strain on outer skin surface at 8mm indentation

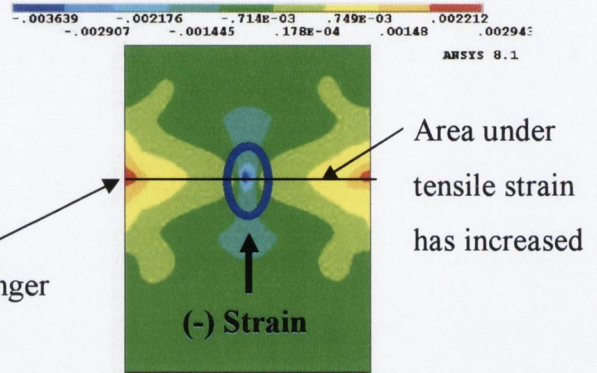


Figure 5.15 Longitudinal strain on outer skin surface at 16mm indentation

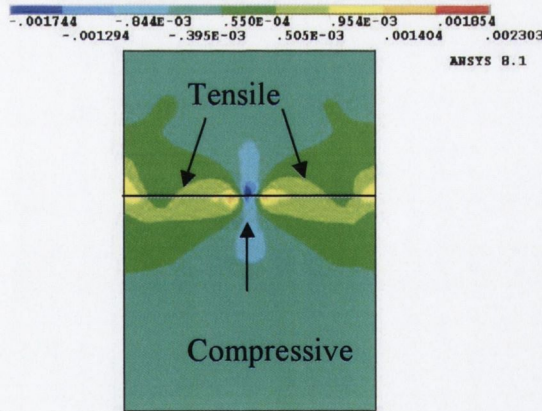


Figure 5.16 Residual longitudinal strain outer skin

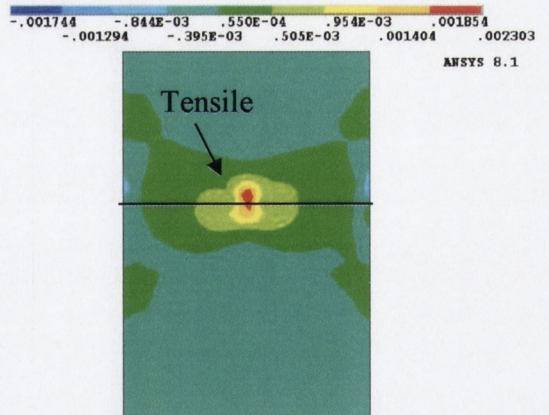


Figure 5.17 Residual longitudinal strain inner skin

In addition to measuring the surface skin strains during indentation, the longitudinal strain was recorded on the stringer flange at positions corresponding to positions 2, 3, 4, L1 and R, as shown in Figure 5.18. Both the experimental and finite element strains are plotted in Figure 5.19 and Figure 5.20.

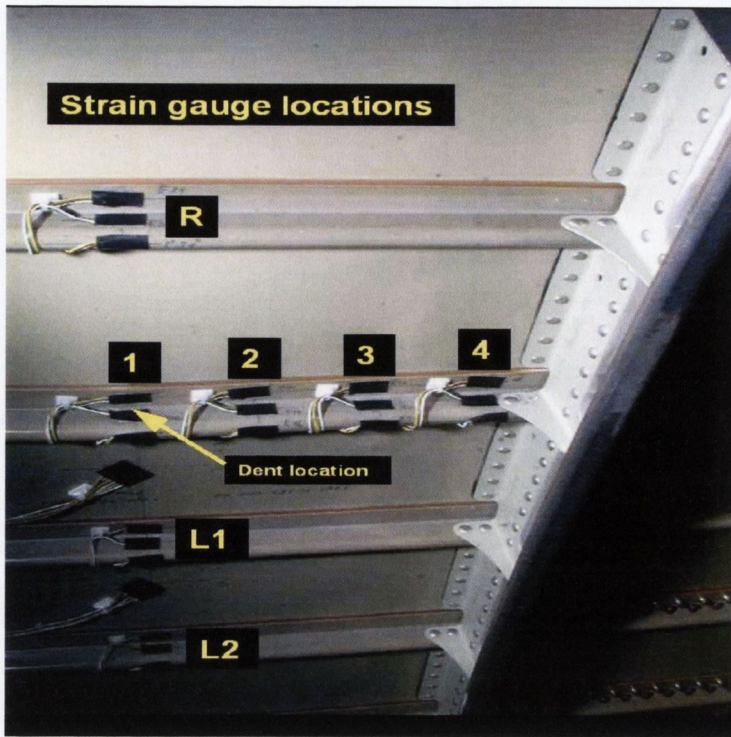


Figure 5.18 Strain gauge locations on inner panel surface

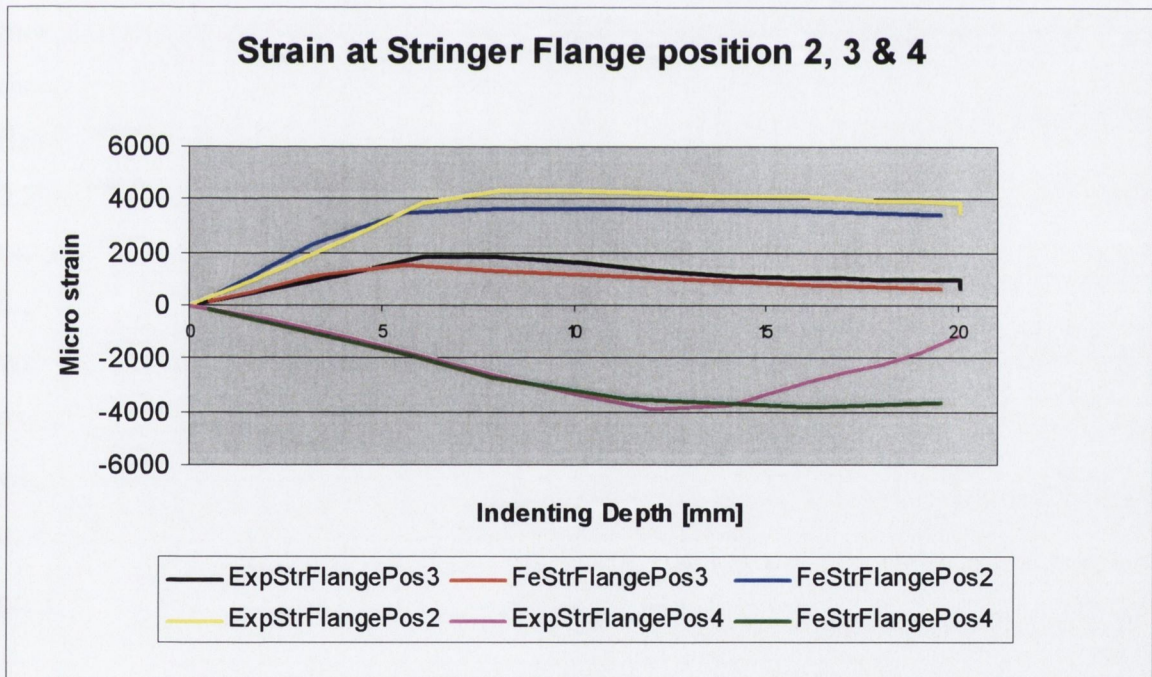


Figure 5.19 FE versus experimental Strain in stringer flange

As was the case for the external skin strains the finite element predicted strains show a close correlation with the measured experimental strains. On the dented stringer there is, however, an obvious divergence for position 4, see Figure 5.19. The experimental strain, see “ExpStrFlangePos4” Figure 5.19, records a decrease in compressive strain from -3879

$\mu$ -strain at an indentation of 12mm to -1102  $\mu$ -strain at the maximum indentation of 20mm. The FE predicted strain in the flange at position 4 shows very close correlation with the experimental strain up to an indentation of 11.5mm. At this point, however, the FE predicted strain shows a divergence from the experimental result recording only a slight decrease in compressive strain from a maximum of -3796  $\mu$ -strain at 16mm to -3659  $\mu$ -strain at 20mm. Although the FE predicted strain did not show the large decrease in compressive strain observed in experimental test the FE model did predict a change in strain at this point as evidenced by the change in slope at 11.5mm. In order to rule out the possibility that this was a discretisation error, a model with a finer mesh in the stringer flange and web was run. This model yielded results in line with those graphed in Figure 5.19. Due to the close correlation between the FE predicted strains and the experimental strains at the other locations on the stringer flange, it is reasonable to assume that there was a failure of this gauge, possibly due to debonding, and that the large decrease in compressive strain is an experimental error.

In contrast to the external skin where initially large regions of compressive strains were measured before changing to tensile strains, the stringer flange experiences tensile strains throughout the indentation. However, on removal of the indenter the strains in the stringer flange at positions 2 and 3 changes from tensile to compressive. This can be seen in Figure 5.21 and Figure 5.22 where the strain in the stringers has been plotted with the skin removed for clarity. This was also observed in the experimental tests where, unlike the loading phase where the strain was sampled at increments in dent depth of 2mm, the strain was only recorded for the final residual dent depth. After complete unloading the residual experimental strain measured at position 3 was a compressive strain of -2924  $\mu$ -strain, which showed close agreement with the finite element result of -2785  $\mu$ -strain, an error of 4.7%, while for position 2 the experimental result was -3124  $\mu$ -strain and the FE model predicted residual strains of -3296  $\mu$ -strain, an error of 5.5%.

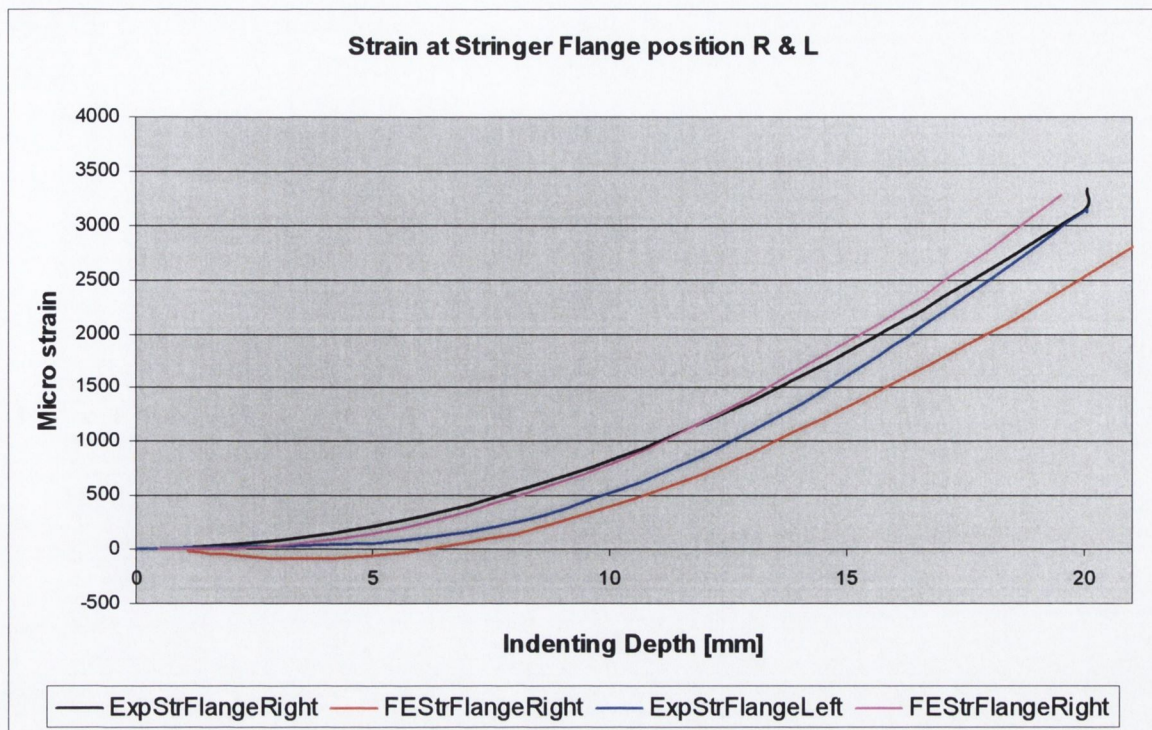


Figure 5.20 FE versus experimental strain in stringer flange

A detailed analysis of both the finite element and experimental results can explain this reversal in strains. As the stringer attempts to recover elastically on removal of the indenter it is restrained at the stringer-frame connection and, as a result, compressive strains develop along the stringer from the stringer-frame connection towards the dent. This can be seen in Figure 5.21 and Figure 5.22 by the extent of the compressive and tensile strain zones in the dented stringer flange at maximum indentation and on removal of the indenter.

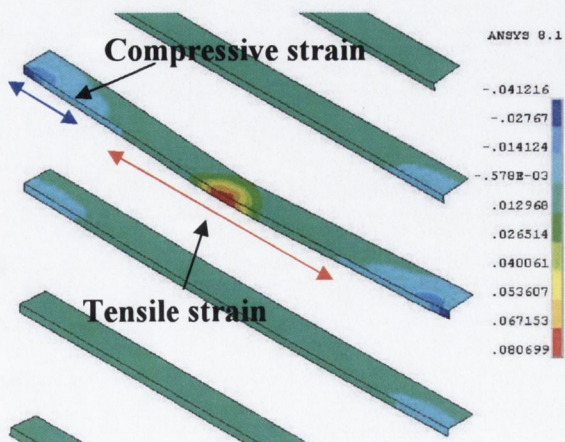


Figure 5.21 Maximum longitudinal strain

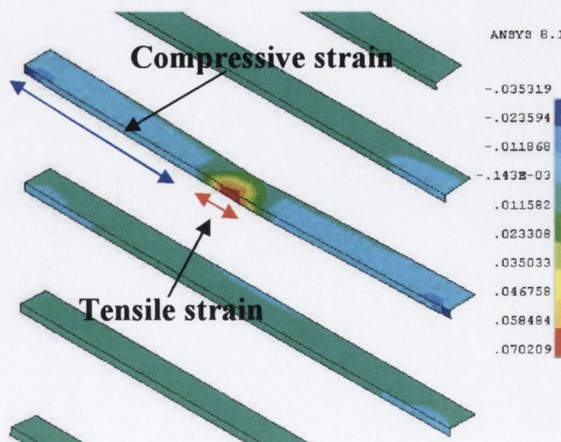


Figure 5.22 Residual longitudinal strain

Overall the finite element results show a close correlation with the experimental results for the denting process. While Figure 5.5 shows close agreement with the predicted results, the greater residual dent depth predicted for the finite element for a slightly shallower maximum indentation is partly explained by the idealisation in boundary conditions. Particular mention must be made of the frame flange supports. In the finite element model these were modelled as simply-supported in the radial direction preventing any displacement in this plane. However, during the experimental test the author noted an initial period of “settling”, where the panel was compressed into the wooden supports. Obviously this could not be accounted for in the finite element model. The corresponding finite element constraints which prevented radial deformation of the frame flanges resulted in a numerically stiffer model. This extra rigidity would result in slightly greater regions of plasticity which would consequently result in a slightly deeper residual dent as was predicted in the finite element model.

### 5.3 Compression Response: A380 Welded Panel

Subsequent to the indentation loading the test panel was placed in the compression test rig as outlined in section 3.4 and loaded until ultimate compressive failure. In this section experimental and finite element results are presented for the case of the dented panel, and for the case of a pristine undamaged panel. Unfortunately for the case of the experimental results a failure in instrumentation occurred for both panels before the ultimate compressive strength of the panel was reached and as a result displacement readings are only available for a portion of the load curve. However, the load values continued to be recorded and the ultimate compressive load is available for comparison with that predicted from the finite element models.

#### 5.3.1 Pristine Panel

Figure 5.23 plots the finite element and experimental results for the compression loading versus end-shortening of the pristine panel. The experimental and finite element results show close correlation, the predicted load of 341KN at 4.16mm comparing well with the measured load of 337KN, an error of 1.2%. Although the displacement instrumentation failed at this point, load readings were still available up to the ultimate compressive strength, again the finite element and experimental results show close agreement, with the



finite element predicting a maximum load of 423KN versus the experimental reading of 429KN, an error of 1.4%.

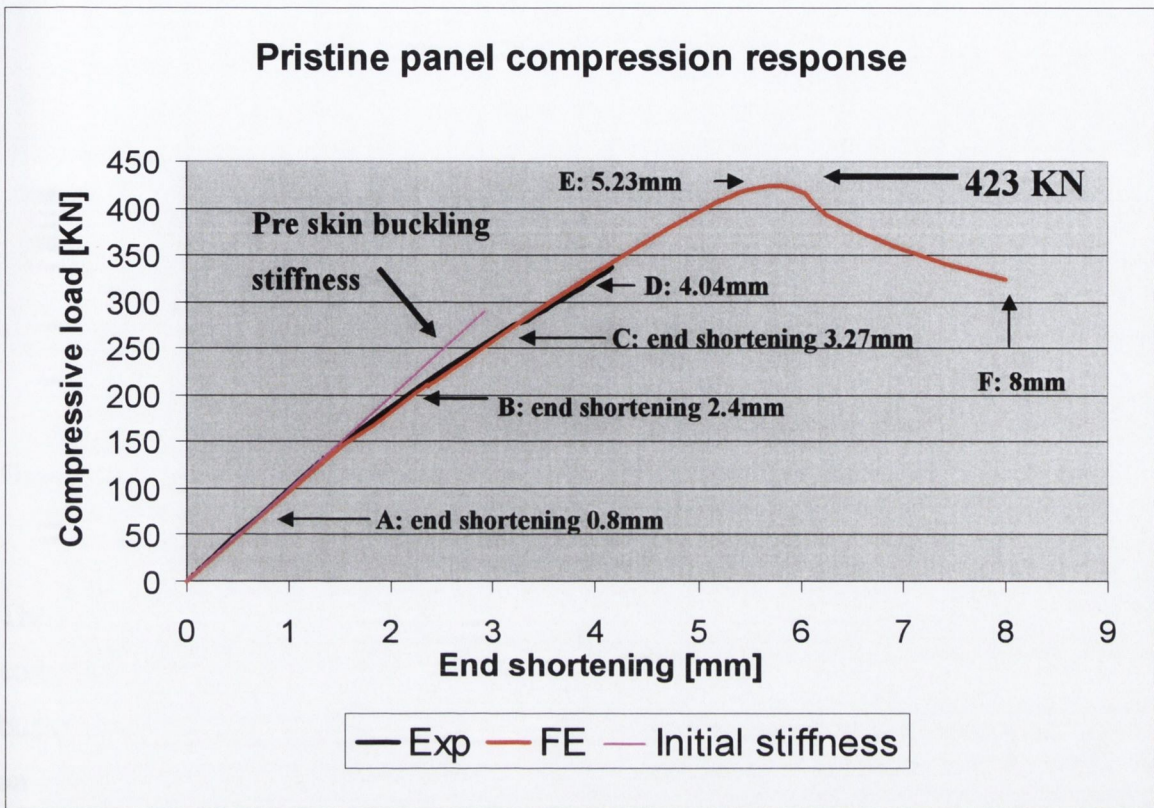


Figure 5.23 Experimental & Finite element compressive load versus end shortening curves

From Figure 5.23 it can be seen that both the experimental and finite element results track the drop in stiffness due to local skin buckling in the stringer-frame bays. A trendline has been added to Figure 5.23, extrapolating the slope of the initial pre-skin buckling results to highlight this drop in stiffness. Figure 5.24 and Figure 5.25 plot the radial displacement in the panel for an end displacement of 0.8mm and 2.4mm respectively. These plots correspond to the points marked A and B in Figure 5.23.

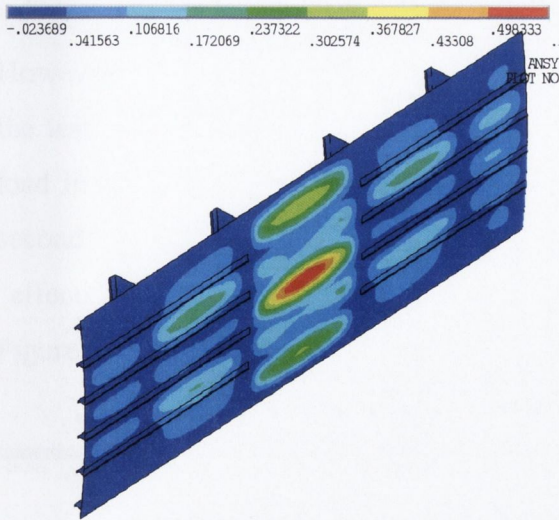


Figure 5.24 Radial displacement at point A

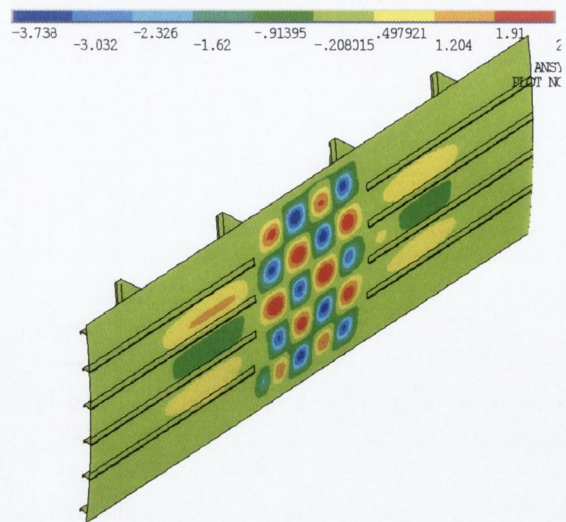


Figure 5.25 Radial displacement at Point B

The radial displacement plots shown in Figure 5.24 and Figure 5.25 indicate that axial compression increases the deformation of the unsupported skin and, consequently, a buckling pattern with multiple axial half-waves between the frames starts to develop. For an end-shortening of 0.8mm, and corresponding compressive load of 78.75KN, a single half-wave was developed in the longitudinal direction. The magnitude of this initial mode ranges from -0.02mm to +0.49mm, the (-) and (+) indicating displacement into and out of the plane respectively. The panel stiffness at this point is indicated by the “initial stiffness” trendline in Figure 5.23.

When the axial compression is increased to an end shortening of 2.4mm at a load of 212.2KN, Figure 5.25, the skin deforms into a fully developed buckling pattern, which is symmetric with respect to each stringer in the test section, with four half-waves between the frames and one circumferential half-wave between the stringers. The magnitude of the deformations has increased at this point to between -3.7mm and +2mm. This increase in local buckling of the skin causes large gradients in longitudinal stress. This is evidenced by the mid-surface longitudinal stress plots for an end shortening of 0.8mm and 2.4mm as illustrated in Figure 5.26 and Figure 5.27 respectively. From the longitudinal stress plots and the corresponding tabulation of these stresses against their circumferential coordinate at section X-X in Figure 5.28, it can be seen that at an end shortening of 0.8mm the entire skin is effective under axial load. The variation in longitudinal stress between the skin in the bay centre and the skin adjacent to the stringers ranging from  $-32\text{N/mm}^2$  and  $-38\text{N/mm}^2$ .

However, for an end-shortening of 2.4mm a greater variation in stress distribution across the test section skin was evident as shown in Figure 5.28. From a minimum compressive load in the second bay, "B2" of  $-43\text{N/mm}^2$  to a maximum at the skin connection to the second stringer "S2" of  $-127\text{N/mm}^2$ . This phenomenon commonly referred to as the "effective width" results in a consequential drop in overall panel stiffness as evidenced in Figure 5.23

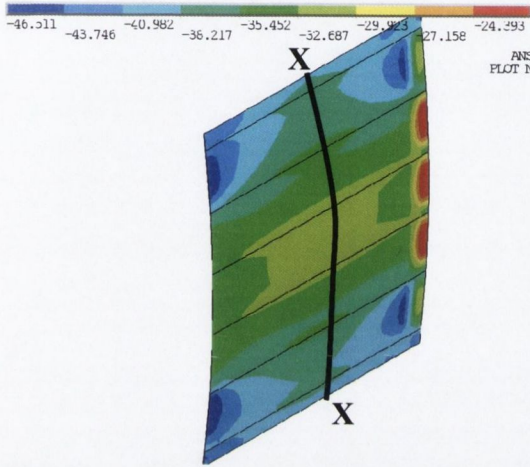


Figure 5.26 Longitudinal mid-surface stress in test section skin at end shortening of 0.8mm

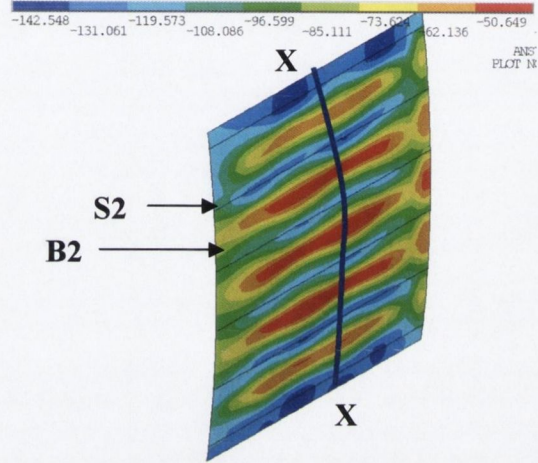


Figure 5.27 Longitudinal mid-surface stress in test section skin at end shortening of 2.4mm

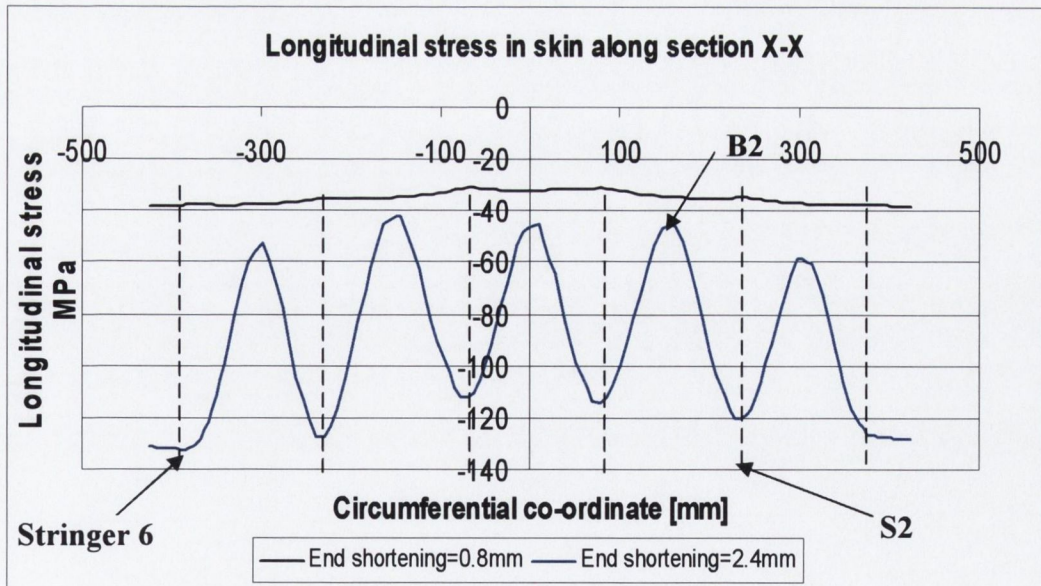


Figure 5.28 Longitudinal mid-surface stress along path X-X

Figure 5.29 and Figure 5.30 plot the radial displacement in the panel corresponding to point C and D on Figure 5.23 respectively. Comparing these plots with Figure 5.25, it is

clear that the same buckling mode exists and, under the increasing axial load, the radial deformations have increased to between -5.9mm and +2.365mm. In addition, it can be seen that a number of buckles have developed outside the test section in the stiffened regions.

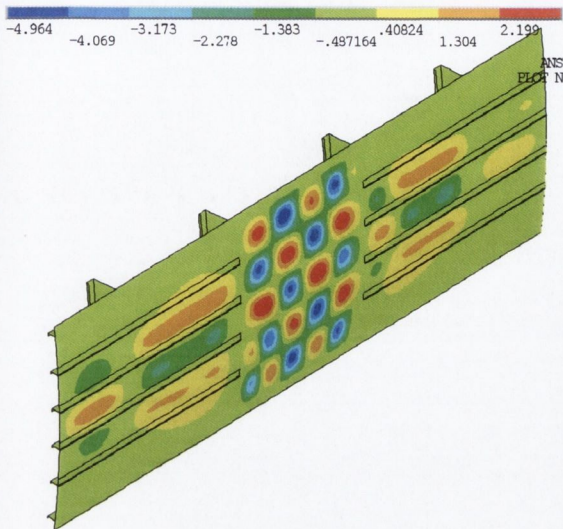


Figure 5.29 Radial displacement at point C

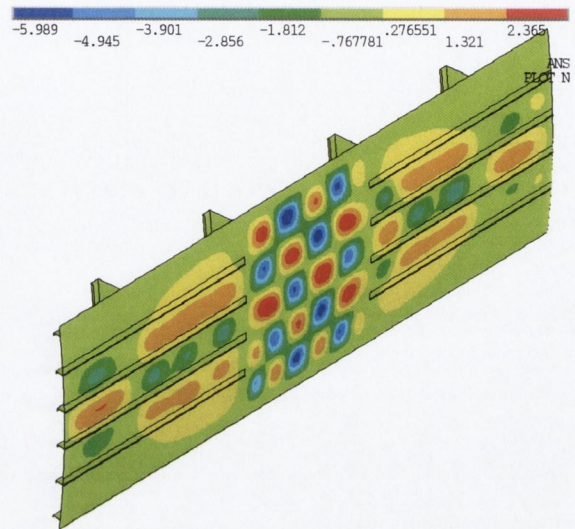


Figure 5.30 Radial displacement at Point D

The skin continues to undergo local buckling, redistributing the in-plane compressive stress through circumferential membrane stresses up to the ultimate compressive strength of 423KN. The radial displacement at ultimate load, corresponding to point E on Figure 5.23, is shown in Figure 5.31. At this stage, the panel has yet to undergo global collapse and the fully developing local skin buckling mode is still evident. However, by point F on Figure 5.23 the local buckling has been replaced by global buckling of the panel as the entire test section deforms radially inwards, Figure 5.32.

From Figure 5.23 it is clear that this collapse in local skin buckling results in a reduction in load carrying capability from a maximum of 423KN to 324KN at point F. The corresponding mid-surface longitudinal stress plots for the test section skin are shown in Figure 5.35 and Figure 5.36. By point F, due to the out-of-plane bending deformation of the stringer, there are large longitudinal stresses present along the stringer-skin connection that are due to both axial compression and the bending deformation of the stringer. The radial deformations for a path along the stringer-skin connection, see Y-Y Figure 5.31, are plotted in Figure 5.33, where the X-axis corresponds to the test section frame pitch of 635mm.

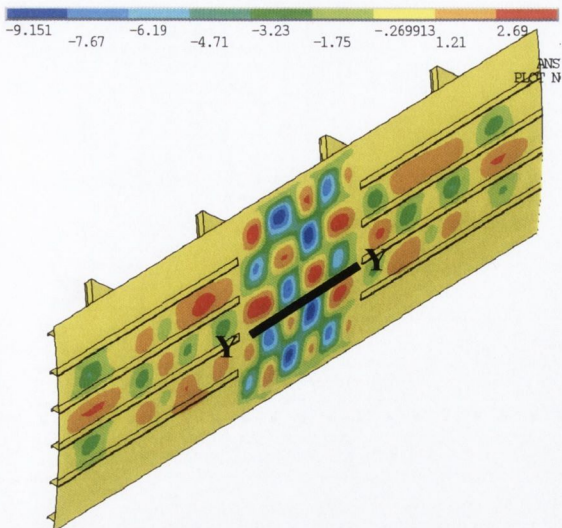


Figure 5.31 Radial displacement at point E

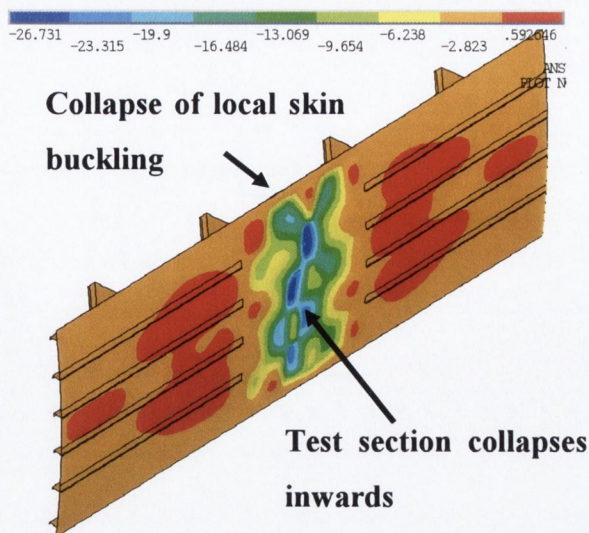


Figure 5.32 Radial displacement at point F

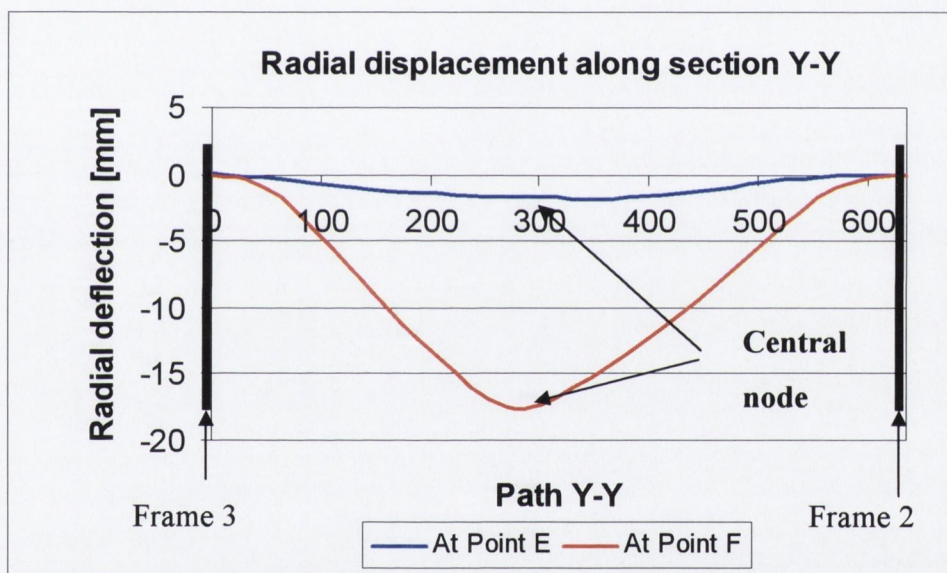


Figure 5.33 Radial displacement at stringer-skin connection along path Y-Y

Figure 5.33 clearly shows that, at an end-shortening of 5.53mm, which corresponds to the ultimate load of 423KN at point E in Figure 5.23, the radial deformation at the stringer-skin connection is minimal with a maximum of -1.78mm occurring in the centre. However, subsequent global buckling of the panel results in a dramatic increase in radial deformation, the central node reaching a maximum of -17.625mm by point F. In order to highlight this sudden increase in radial displacement, Figure 5.34 plots the displacement of a node located mid-way between the frames on the stringer-skin connection. It is clear that, up to the ultimate compressive load at an end-shortening of 5.53mm, there has been relatively minor out-of-plane radial deformation due to the rigidity of the stringer. This is

followed by an increase in out-of-plane deformation, indicating buckling of the stringer and collapse of the test section.

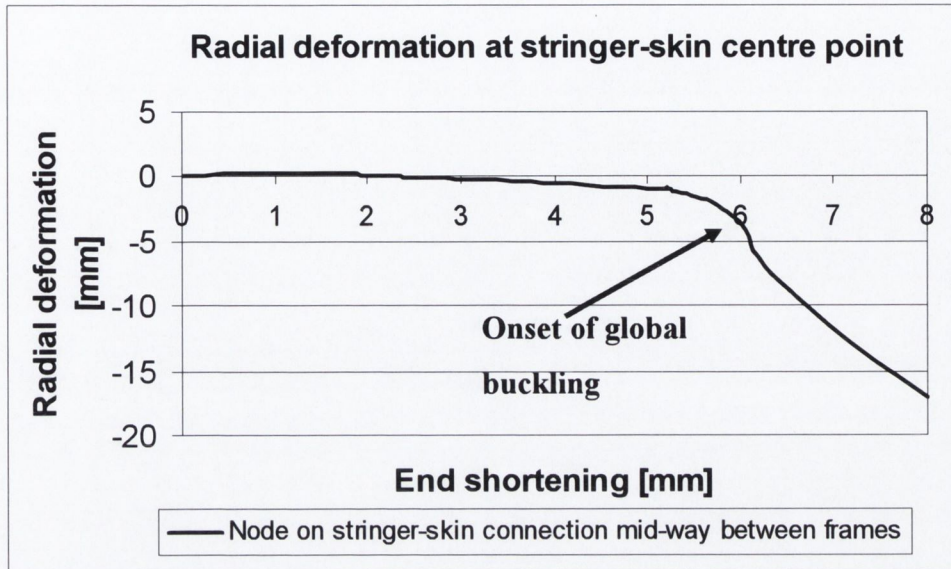


Figure 5.34 Radial displacement for central node on stringer-skin connection

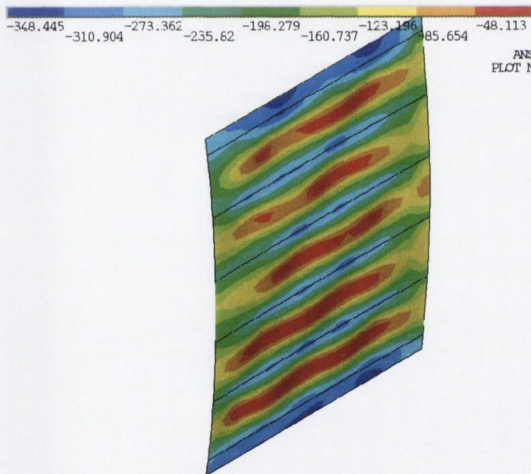


Figure 5.35 Longitudinal mid-surface Stress in test section skin at end shortening 5.53mm

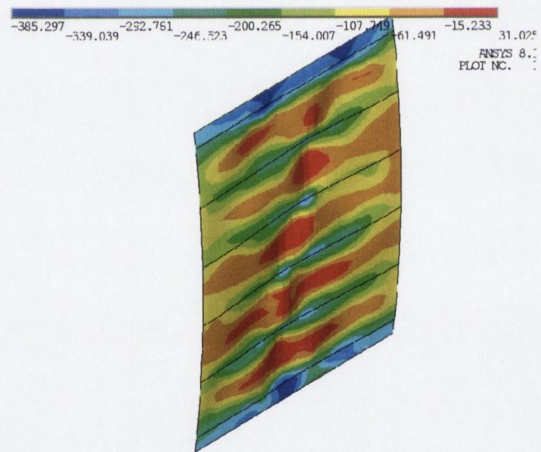


Figure 5.36 Longitudinal mid-surface Stress in test section skin at end shortening 8.0mm

### 5.3.2 Dented Panel

Subsequent to the denting operation described in section 5.2, the dented panel was placed in the compression test ring and loaded until failure. Unfortunately, as was the case for the pristine panel, experimental results were only available for a portion of the loading curve due to a failure with the experimental instrumentation. The finite element predicted results do, however, include loading up to the ultimate strength and into the postbuckled region.

The available experimental results are plotted in Figure 5.37 against the predicted finite element results, while Figure 5.38 graphs the predicted response for both the pristine and dented panels up to the ultimate compression strength and into the postbuckled region.

From Figure 5.37, it is clear that, as in the case of the pristine undamaged panel, the numerical model accurately predicts the load-displacement response for the dented panel, showing a close correlation with the experimental results. The maximum error over the available results occurs at an end shortening of 2.21mm. The finite element predicted load at this point was 197KN, an error of 5.2% versus the experimentally measured load of 208KN. Although experimental displacement readings were only available up to 3.96mm the ultimate load was recorded at 398KN, showing close agreement with the finite element predicted ultimate load of 383KN, an error of 3.76%.

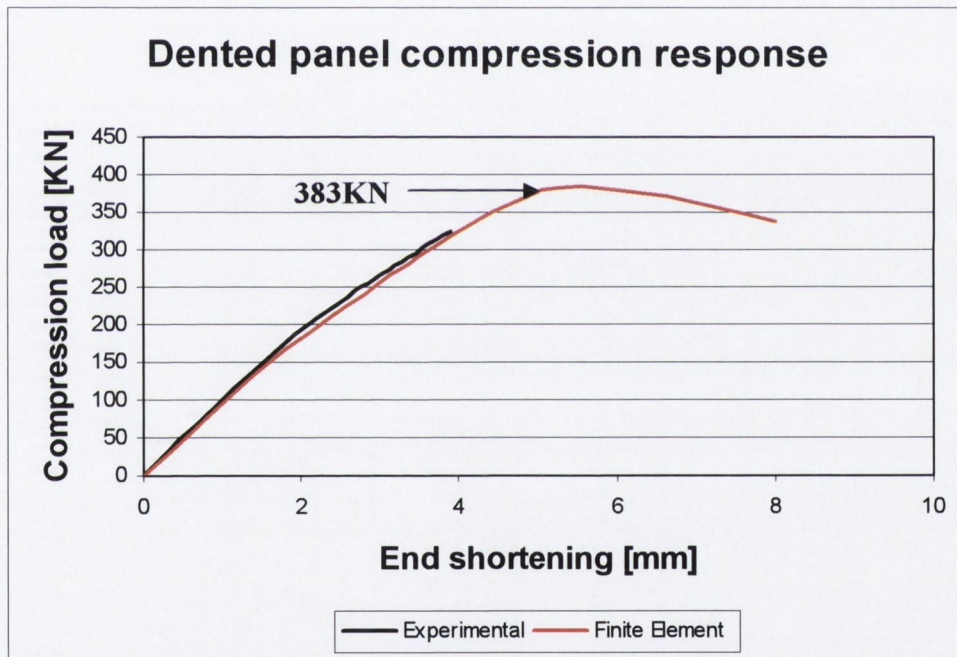


Figure 5.37 Experimental & finite element compressive load versus end shortening curves

Comparing the two response curves shown in Figure 5.38 allows investigation into the effects of the dent on the load carrying mechanism of the damaged structure in contrast to the pristine structure. It can be seen that the dent causes a reduction in the predicted ultimate compressive strength from 423KN to 383KN, a drop of 9.5%. It is of interest, however, to note that the effect of the dent is not evident until a load of 265KN is reached at an end-shortening of 3.13mm. At this point, the stiffness of the dented panel diverges from that of the pristine panel.

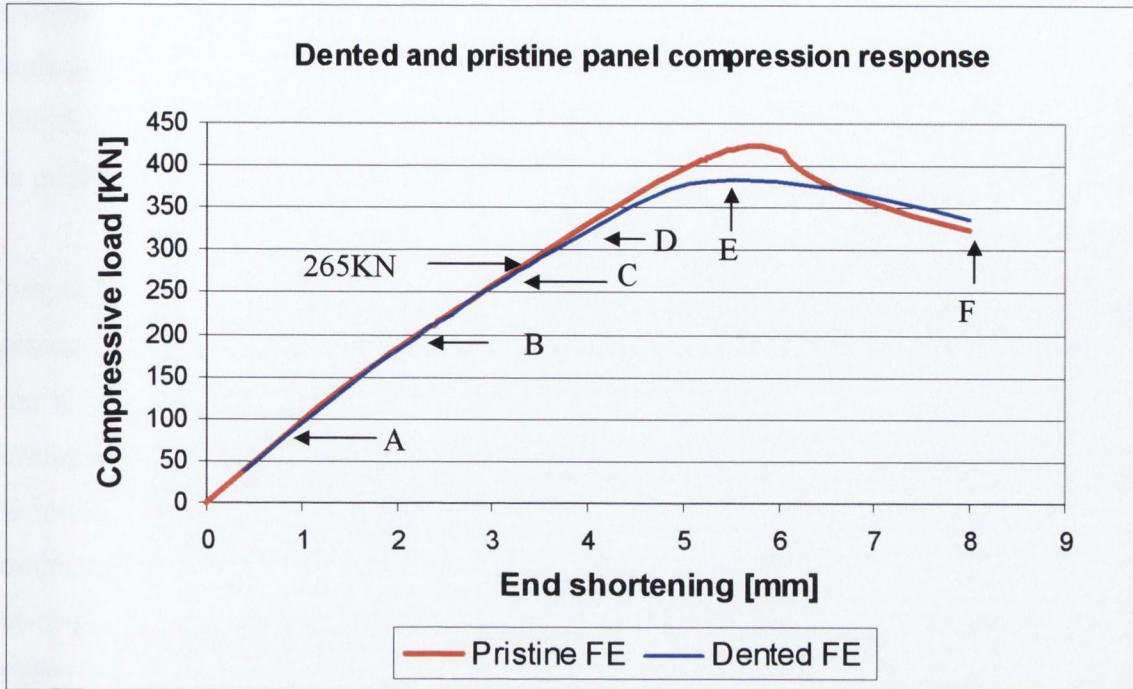


Figure 5.38 Finite element predicted compression response for pristine and dented panels

While it is clear from Figure 5.38 that the effect of the dent on the global response of the panel is not significant in the initial stages of compression, analyses of the numerical and experimental strain results show that, locally, the dent does have a significant effect on the load carrying mechanism of the panel. From the commencement of compression loading, the out-of-plane deformation of the dented stringer results in a bending dominated response in this stringer to the applied compression load. This is shown in Figure 5.39 and Figure 5.40. As a result, the dented stringer “sheds” load which is redistributed into the other stringers.

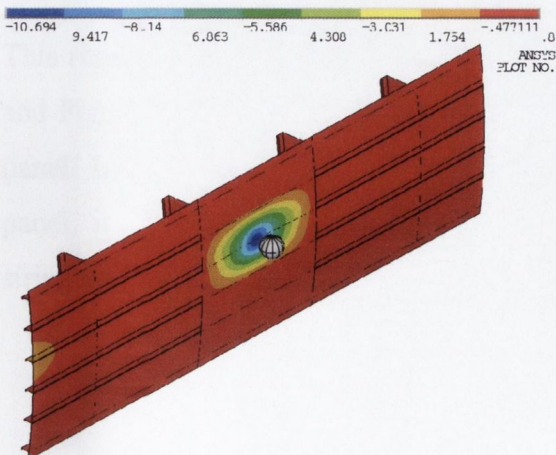


Figure 5.39 Residual dent full panel view

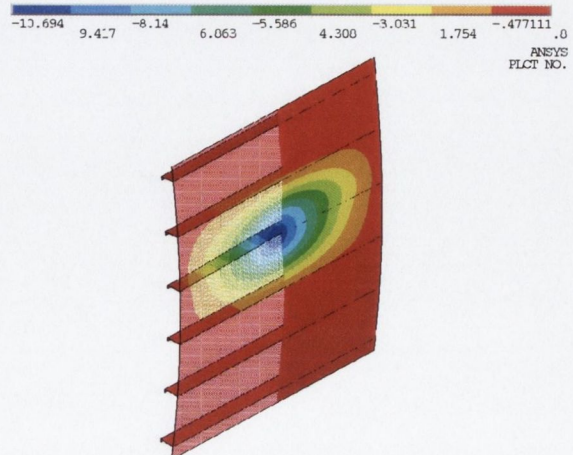


Figure 5.40 Residual dent stringer view



In order to compare the response of the dented panel with the pristine panel, the radial displacements of the dented panel are plotted for an end-compression of 0.8, 2.4, 3.27, 4.04, 5.23 and 8mm, corresponding to point A through F on Figure 5.23, as was done for the pristine panel. These points are also plotted on Figure 5.38 for clarity.

Comparing Figure 5.41 with Figure 5.24 it is evident that for the same end shortening the presence of the dent results in a very different response. By an end displacement of 2.4 mm, it is clear that the effect of the dent is to undermine the establishment of the fully developed buckling mode in the stringer bays adjacent to the dented stringer. This is due to the initial out-of-plane radial deformation in the skin caused by the dent and the bending dominated response of the dented stringer. The result is that, as the dented stringer bends out-of-plane, the dent depth increases and the skin in the bays is displaced radially inwards.

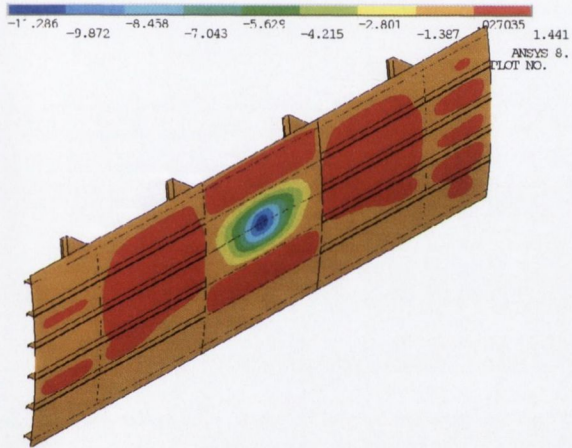


Figure 5.41 Dented panel radial displacement at point A

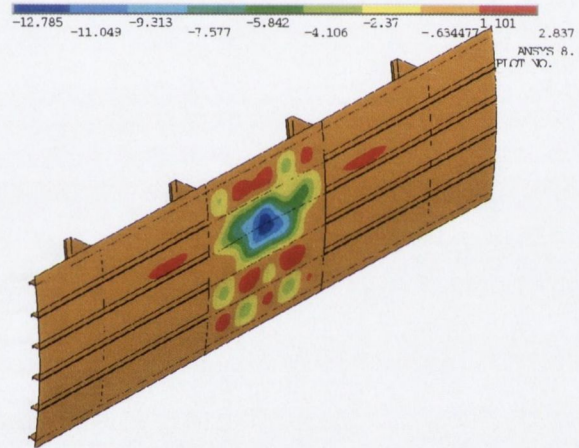


Figure 5.42 Dented panel radial displacement at Point B

This results in an internal redistribution of load away from the dented region. Figure 5.43 and Figure 5.44 plot the mid-surface longitudinal stress in the test section for the dented panel. In contrast to the equivalent plots in Figure 5.26 and Figure 5.27 for the pristine panel, it is clear that there is a very definite drop in compressive stress in the dented stringer and the skin in the adjacent bays, as shown in Figure 5.44 and Figure 5.45.

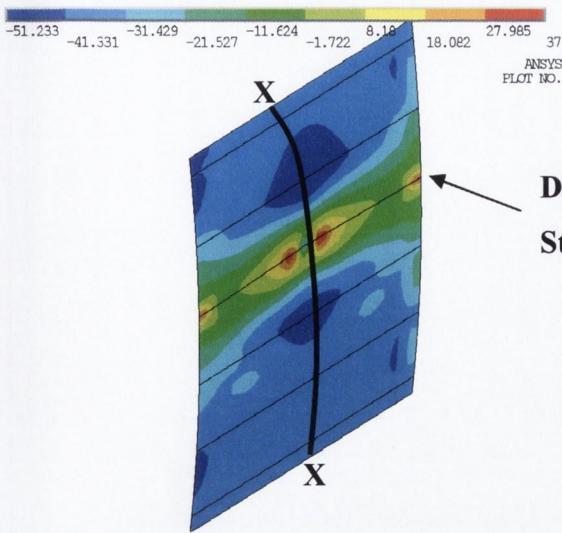


Figure 5.43 Dented panel longitudinal mid-surface Stress in test section skin at an end shortening 0.8mm

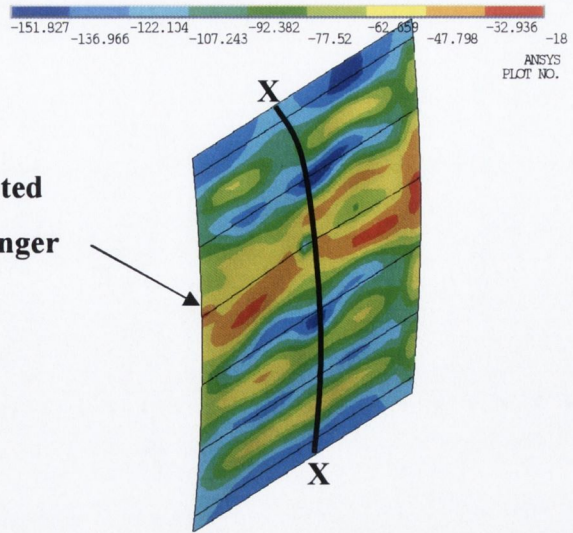


Figure 5.44 Dented panel longitudinal mid-surface Stress in test section skin at an end shortening 2.4mm

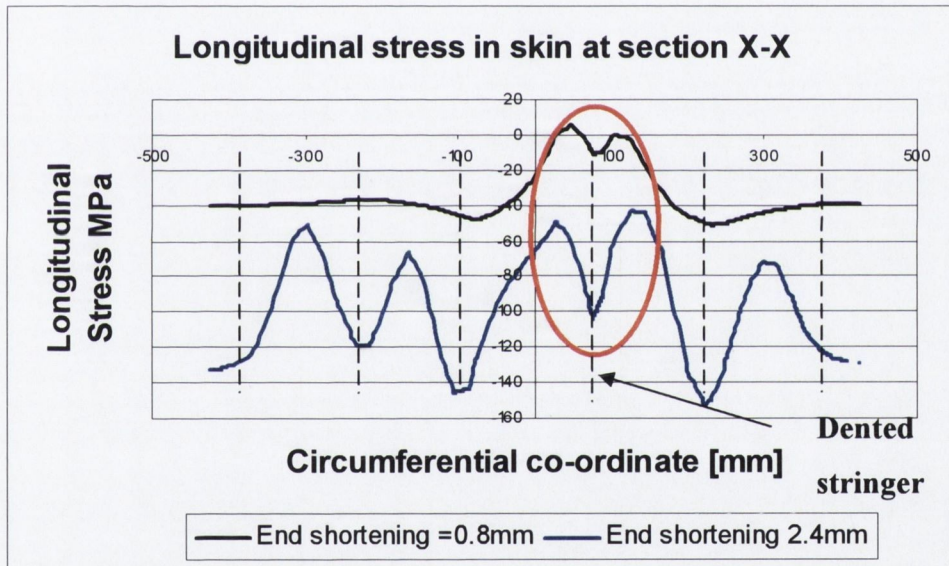


Figure 5.45 Longitudinal mid-surface stress along path X-X

The reduction in the longitudinal compressive stress in the region of the dent necessitates a redistribution of the load since, as evidenced in Figure 5.38, the stiffness of the dented panel at this point is comparable to that of the pristine panel. This redistribution of load can be seen in Figure 5.46. In comparison to the pristine panel, there is a reduction in the longitudinal compressive stress in the dented stringer and the adjacent bays at an end shortening of 2.4mm. This results in a corresponding increase in the longitudinal stress in the adjacent stringers, stringer 2 showing an increase of 20%, as load is redistributed.

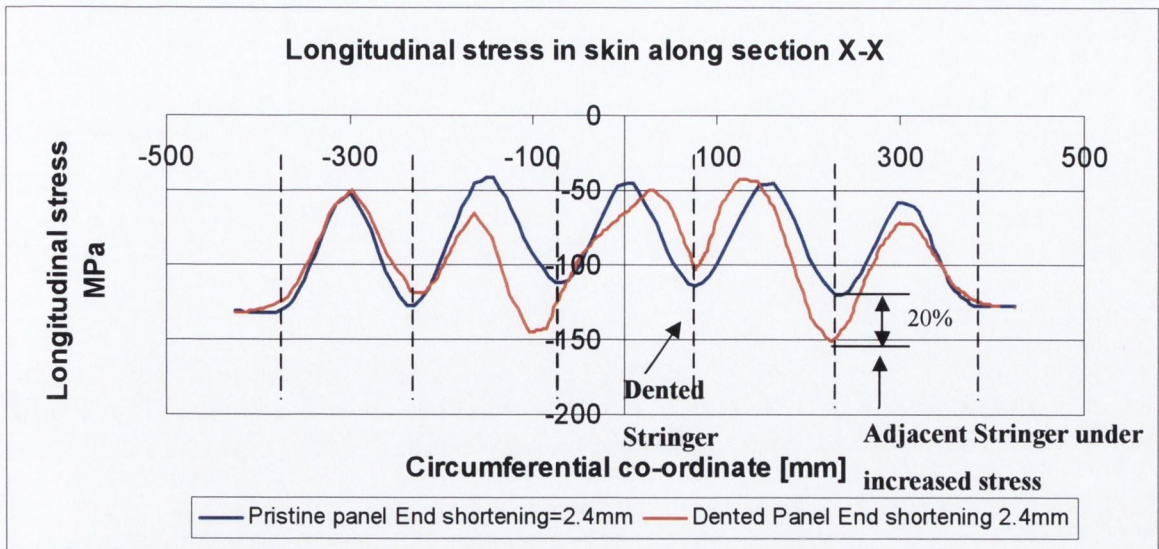


Figure 5.46 Longitudinal mid-surface stress in section X-X at end shortening 2.4mm

From Figure 5.38, it can be seen that this redistribution of load continues under increasing axial compressive load without significantly altering the panel stiffness until a load of 265KN is reached. Figure 5.47 and Figure 5.48 plot the radial displacement at point C and D, corresponding to compressive loads of 274 and 323KN respectively. Comparing the radial displacement at point C and D with that at point B before the panel stiffness has diverged, it can be seen that the dent has increased in depth to 14.6mm and, with this continued deformation the influence of the dent has also increased. In fact, by point D, Figure 5.48, the out of plane deformation of the dented stringer has caused the two stringers to the left and right of the dented stringer to buckle radially inwards, resulting in a consequential loss in geometric stiffness as evidenced by the divergence from the pristine panel results in Figure 5.38.

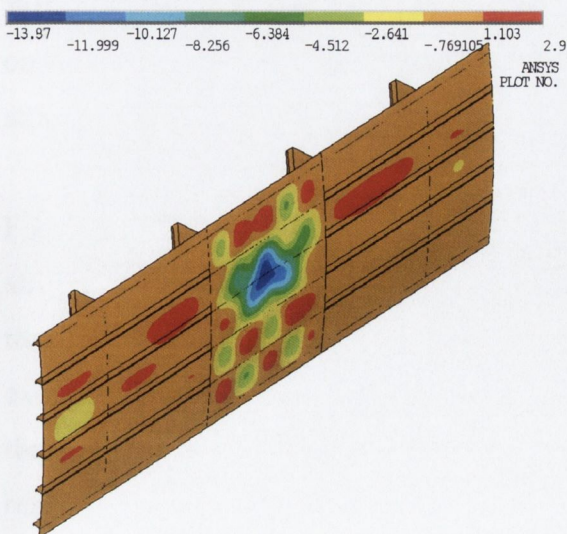


Figure 5.47 Dented panel radial displacement at point C

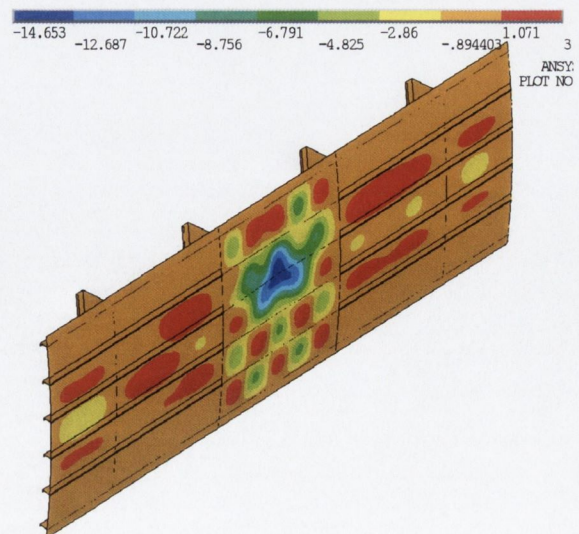


Figure 5.48 Dented panel radial displacement at point D

The dented panel, however, continues to support increases in load up to a maximum load of 383KN at an end shortening of 5.53mm. Figure 5.49 plots the radial displacement at point E; this corresponds with the ultimate compressive strength of the dented panel of 383KN and shows a reduction of 9.45% when compared with the pristine panel ultimate compressive strength of 423KN. Figure 5.50 plots the radial displacement after global collapse of the panel, corresponding to point F on Figure 5.38.

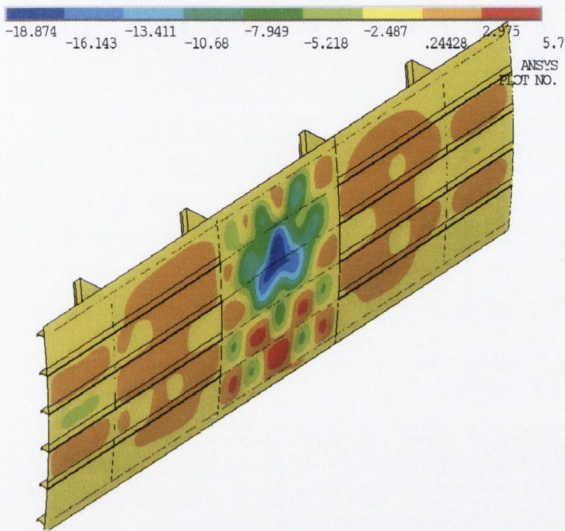


Figure 5.49 Dented panel radial displacement at point E

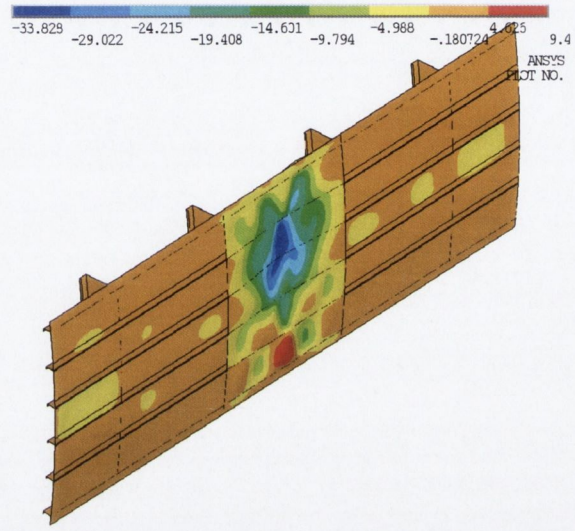


Figure 5.50 Dented panel radial displacement at point F

As mentioned previously, current structural repair codes assume 100% load by-pass in the dented stringer and a key objective of this research was to establish the extent to which the load carrying capabilities of the stringer were undermined by the presence of the dent. While the radial deformation plots exhibit the change in local skin buckling and ultimate collapse mode, it is also necessary to analyse and compare the change in load history in the stringers between the pristine and dented panels.

Figure 5.51 and Figure 5.52 plot the load history at the stringer-skin connection of each stringer, for the pristine and dented panels respectively. From Figure 5.51, it can be seen that all six stringers experience a general rise in load against end-shortening. The only exception being a sudden, but slight, drop in stiffness at 2.47mm as the buckling mode in the skin changes from three to four half-waves in the longitudinal direction. An interesting result is that “stringer 1” carries less load than the other stringers throughout the entire load history. This is due to the orientation of the stringer foot, which is between stringer 1 and the supported edge. As a result of the extra stiffening in this stringer overhang, the load is

distributed more uniformly, resulting in a smaller proportion of the load being carried at the stringer-skin connection.

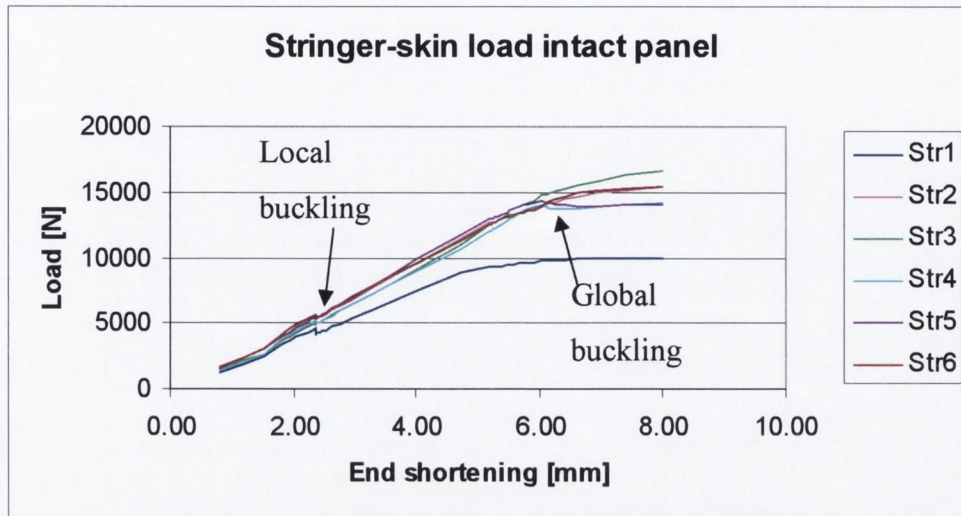


Figure 5.51 Load at stringer-skin connection in pristine panel

In contrast to Figure 5.51, Figure 5.52 shows all stringers displaying a rise in load against end-shortening with the exception of the dented stringer. The dented stringer shows an initial load due to the residual stress from the denting operation. On commencement of compression, this load drops off as the stringer deforms out-of-plane. At this point, all the compressive load is being carried by the other stringers. Effectively by-passing the dented stringer as assumed in current repair practices. However, at an end compression of 1.8mm stringer 2, experiences a sharp rise in stiffness as the skin in the bay adjacent to it changes mode from an initial single half-wave in the longitudinal direction to five half-waves. At this point, the dented stringer comes under load and is once again effective in compression.

This pattern is maintained up until global buckling of the panel, at which point the dented stringer is carrying 6826 N, approximately 50% of 13698 N, the load it supports at collapse in the pristine panel. Figure 5.52 also shows that the stringers adjacent to the dented stringer, stringer 2 and 4, are under the greatest load up to the point of global collapse due to the redistribution of load from the dented stringer. After collapse the load at the stringer-skin connection for the dented stringer continues to rise, reaching a peak in the post-buckled region of 13597N.

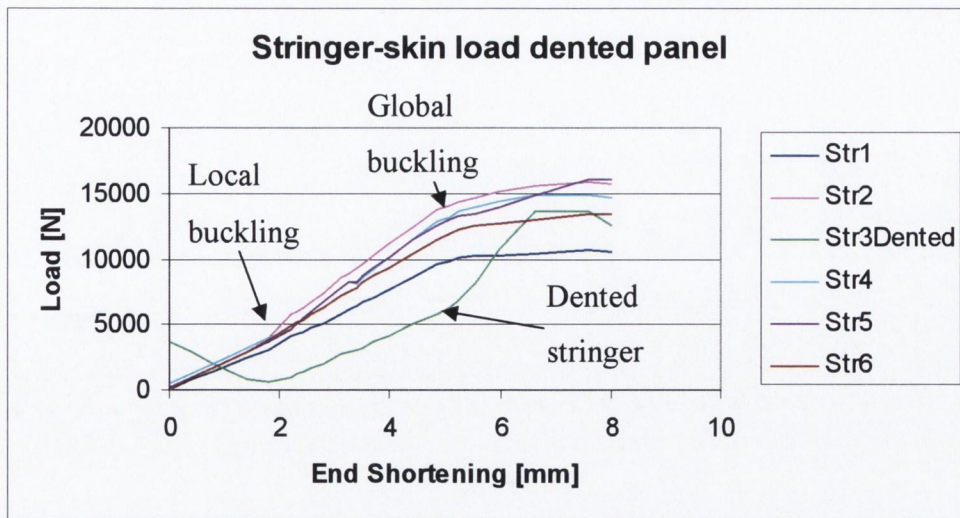


Figure 5.52 Load at stringer-skin connection in dented panel

In summary, it has been shown that while the overall panel stiffness does not experience any significant reduction up to a load of 265KN, the effect of the dent is to cause a complex redistribution of load on a local level. This, combined with the bending dominated deformation of the dented stringer and the consequential undermining of local skin buckling in adjacent bays, results in a reduction in ultimate compressive strength of 9.5%. In addition, the presented results have shown that current repair methods underestimate the effectiveness of a dented stringer in compression. The finite element method has proved effective in capturing the complex non-linearities active in both the denting and compression phase, showing close correlation with the experimental results. The use of experimental testing to benchmark complex finite element models is a necessary measure and gives confidence in applying the finite element model in parametric studies. A number of parametric studies into the effects of dents were carried out using the model presented in this section and the results are presented in the following sections.

## 5.4 Dent Depth Investigation

In order to assess the effects of dent depth for the case of a dent on a stringer, as a limiting criterion on the ultimate compressive strength, a parametric study was carried out varying the dent depth between 1mm and 10mm. This range of dent depths were selected as they account for the vast majority of dents experienced in everyday repair submissions to the structural engineers at Airbus Germany, from aircraft operators worldwide. It was also of interest to assess whether there was a dent depth below which the effects of a dent on a

stringer were negligible from the point of view of ultimate strength. In total eleven models were run, eight of which converged without any problems and three of which failed to reach the ultimate compressive strength.

Figure 5.53 plots the compressive load versus end shortening for the eight converged analyses, detailing their respective dent depths in the legend. The load displacement response, shown in Figure 5.53, is divided into two areas, A and B. Initially all the dented panels responded in a similar manner as seen in section A. This corresponds to the initial end-shortening before the panel skin buckles locally. As can be seen there is no appreciable reduction in overall panel stiffness for the deeper dents before the local skin buckling.

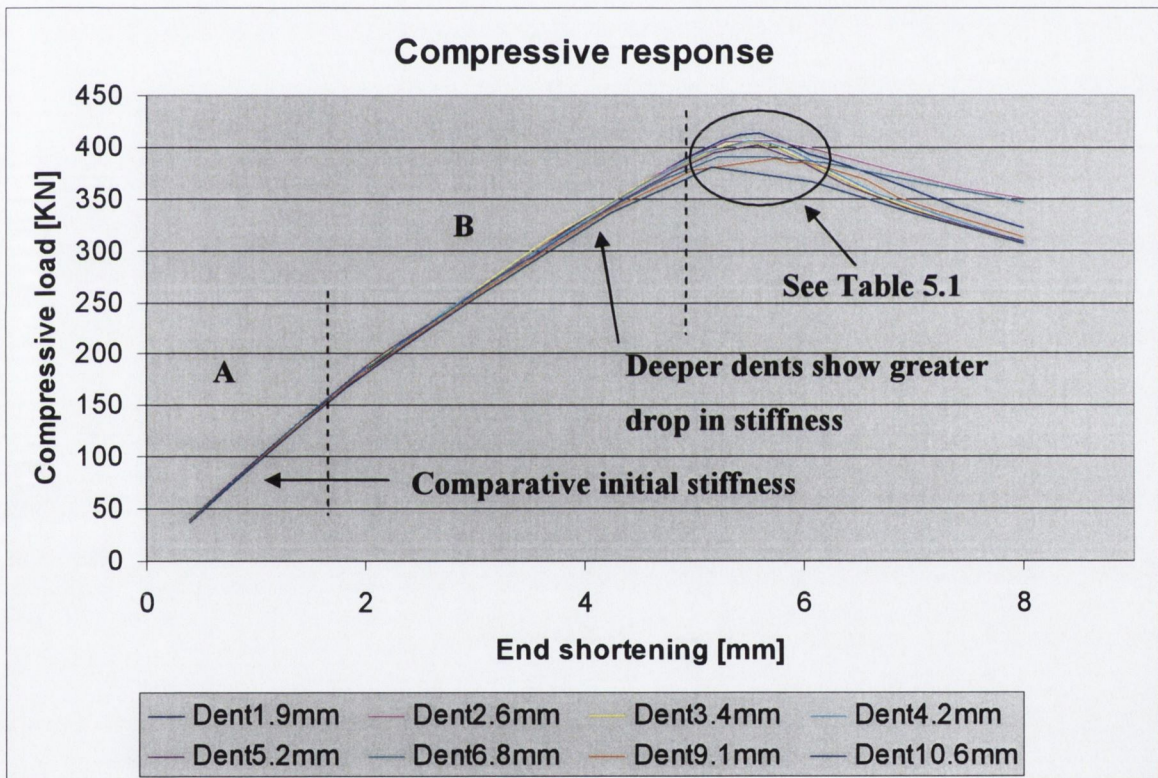


Figure 5.53 Compressive load versus end shortening for increasing dent depths

After local skin buckling, see section B Figure 5.53, the effects of the deeper dents are more significant. The analysis for the deepest dent, see “Dent10.6mm” Figure 5.53, shows the greatest reduction in overall panel stiffness before ultimate strength is reached. The values of ultimate compressive load, as plotted in the circled area in Figure 5.53, are tabulated for clarity in Table 5.1. In addition Table 5.1 also tabulates the ultimate

compressive load as a factor of the pristine panel ultimate compressive load for each analysis.

Analyses	Residual dent Depth	Converged	Ultimate Strength	Factor of pristine ultimate load
Pristine panel	_____	Yes	423KN	1
Dent1.9mm	1.9mm	Yes	413.6KN	0.977
Dent2.6mm	2.6mm	Yes	406.7KN	0.96146
Dent3.4mm	3.4mm	Yes	405.8KN	0.959
Dent4.2mm	4.2mm	Yes	404.1KN	0.955
Dent5.2mm	5.2mm	Yes	403KN	0.9527
Dent5.9mm	5.9mm	No	_____	_____
Dent6.8mm	6.8mm	Yes	391.7KN	0.926
Dent8.4mm	8.4mm	No	_____	_____
Dent9.1mm	9.1mm	Yes	389KN	0.919
Dent9.9mm	9.9mm	No	_____	_____
Dent10.6mm	10.6mm	Yes	381KN	0.9

**Table 5.1 Increasing dent depth analyses**

The factors of pristine ultimate load and dent depth, taken from Table 5.1, have been plotted in Figure 5.54. The graph shows an overall reduction in ultimate compressive strength as dent depth increases. While there is a general decrease in the ultimate compressive strength of the panel as the dent depths increase, the relationship shows a number of changes in slope as evidenced in Figure 5.54 by the regions marked A, B and C. For instance, while a dent depth of 10.6mm results in an ultimate compressive strength reduction of 9%, almost 4% of this load reduction is evidenced from a shallow dent of 2.6mm. This is shown in section A in Figure 5.54. So, it can be concluded that the presence of a shallow dent results in a marked decrease in ultimate strength. However, once a dent is present the panel responds in a less sensitive manner to increases in dent depth. Section B depicts an insensitivity to the increasing dent depth, where increases in depth from 2.6mm to 5.2mm resulted in an increased reduction in ultimate compressive strength from 3.8% to 4.73%. The slope changes again in section C Figure 5.54 where the next dent depth of 6.8mm results in a reduction of 7.4%, illustrating an increased sensitivity of the panel to increases in dent depth.



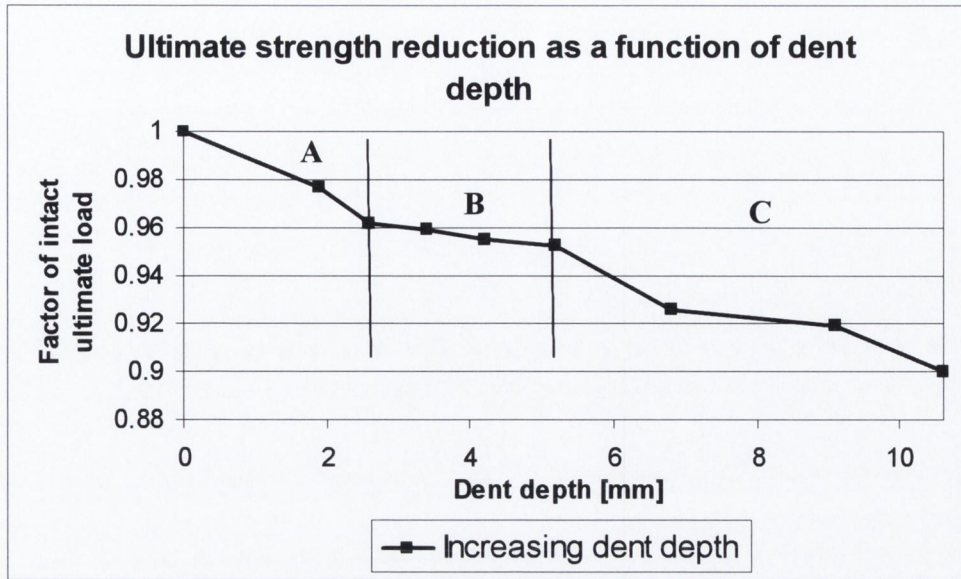


Figure 5.54 Ultimate strength reductions as a function of dent depth for stringer dents

Figure 5.55 plots a similar load reduction versus dent depth for the case of a dent located in the stringer bay mid-way between the frames. Six cases of increasing dent depth up to 11mm are plotted. The load curve for the dented stringer from Figure 5.54 has been plotted alongside it to highlight the greater sensitivity to dents on the stiffener versus those on the skin for shallow dents. Indeed the graph shows that dents in the bay up to 6.7mm have had little effect on the ultimate load, causing a reduction of only 3% versus 7.4% for an equivalent dent on a stringer. It can also be seen, however, that this is not a consistent relationship. At a dent depth of 11mm the gap has narrowed to 3%. This is an important result as it indicates that for certain depths a dent on a stringer does not perform substantially worse, than an equivalent dent in the bay, under compressive loading. Currently dents on stringers are not allowed in the Airbus SRM as it is assumed they carry zero load and all the load is carried through load by-pass in the adjacent stringers. The results of the research presented in this thesis indicate that this is not the case. A dented stringer can in fact support a substantial percentage of its undented load, 50% in the case presented in section 5.3., for a dent mid-way between the frames on a stringer. These results indicate that the current ADL's are over conservative and the model developed in the course of this research could be of direct use in the ongoing task of updating the SRM.

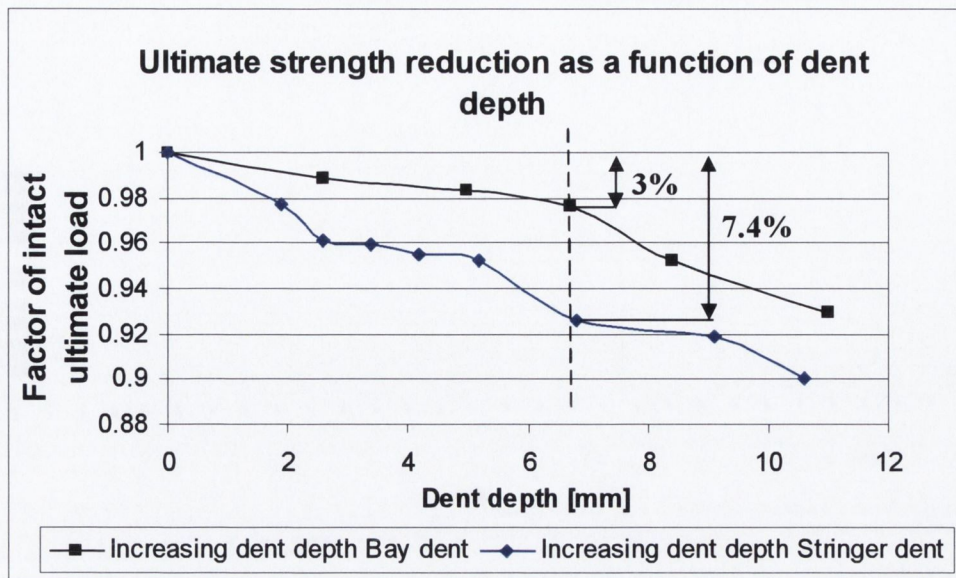


Figure 5.55 Ultimate strength reductions as a function of dent depth for stringer and bay dents

In conclusion, it appears that the presence of a dent on a stringer results in an initial reduction in ultimate compressive strength. However, due to the complex load redistribution in the panel increasing dent depth does not necessarily result in a linear decrease in panel strength. For the dent depths analysed, it was clear that there were three distinct phases of strength reduction; an initial drop where the panel was sensitive to even very shallow dents, followed by a period of relative insensitivity to increasing depth, followed by a third period where the panel once again showed sensitivity to increasing depth.

## 5.5 Effect of Dent Location

The dent analysed in the experimental test and initial finite element model was located on a stringer mid-way between two frames. In order to investigate the effects of location, a parametric investigation was carried out on dents both in the bay and on the stringer.

Figure 5.56 shows the location of the stringer and bay where the dents were applied on the panel. Figure 5.57 shows a close up of the dent locations. The lettering scheme is “B” for “bay” and “S” for “stringer”, and the numbering scheme “0”, “1” and “2” represents the distance from the exact centre of the frame bay in a longitudinal direction. Where “0” is in the centre, “1” is 100mm from the centre and “2” is 200mm from the centre.

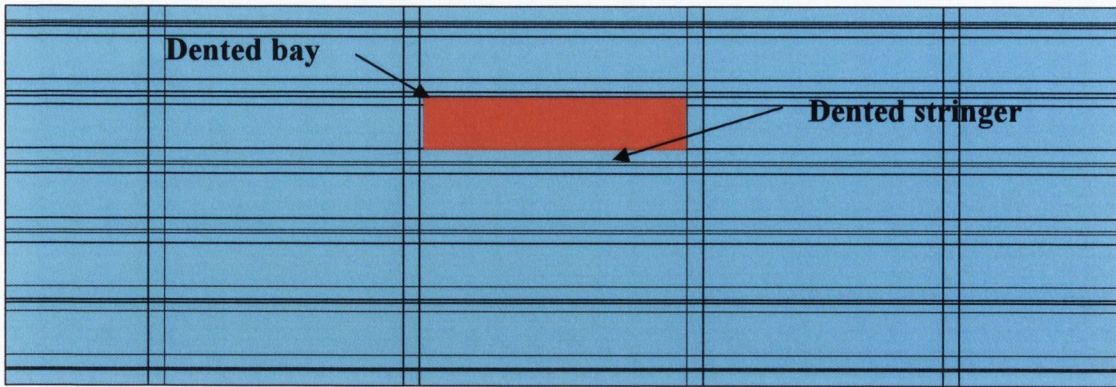


Figure 5.56 Dented bay and stringer on panel

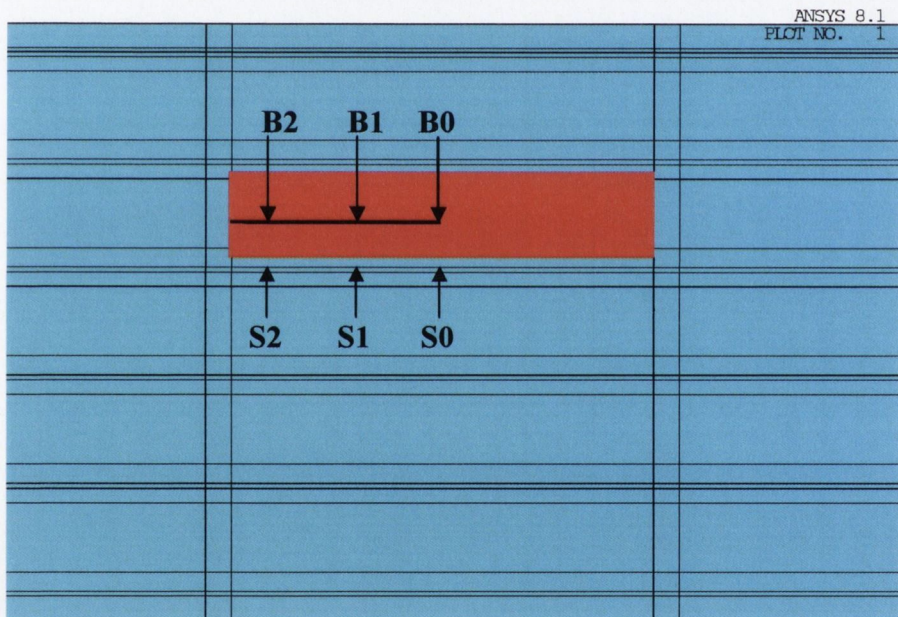


Figure 5.57 Locations of dents on stringer and in bay

### 5.5.1 Effects of Location on Bay Dents

Figure 5.58, Figure 5.59 and Figure 5.60 plot compressive load versus end-shortening for bay dents of 4mm, 8mm and 10mm respectively. Results are graphed for location "B0", "B1" and "B2".

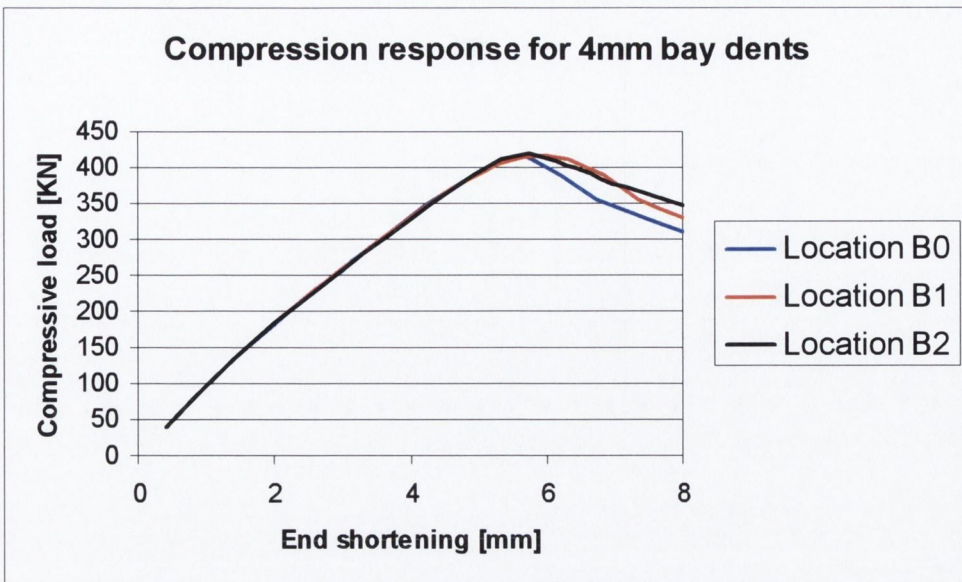


Figure 5.58 Compression response for 4mm depth bay dents at locations B0, B1 and B2

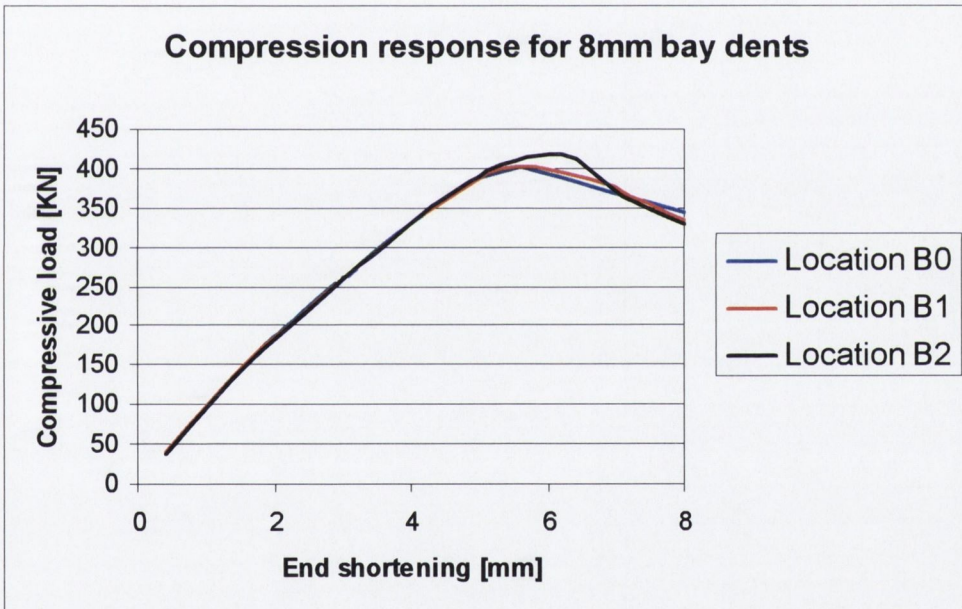


Figure 5.59 Compression response for 8mm depth bay dents at locations B0, B1 and B2

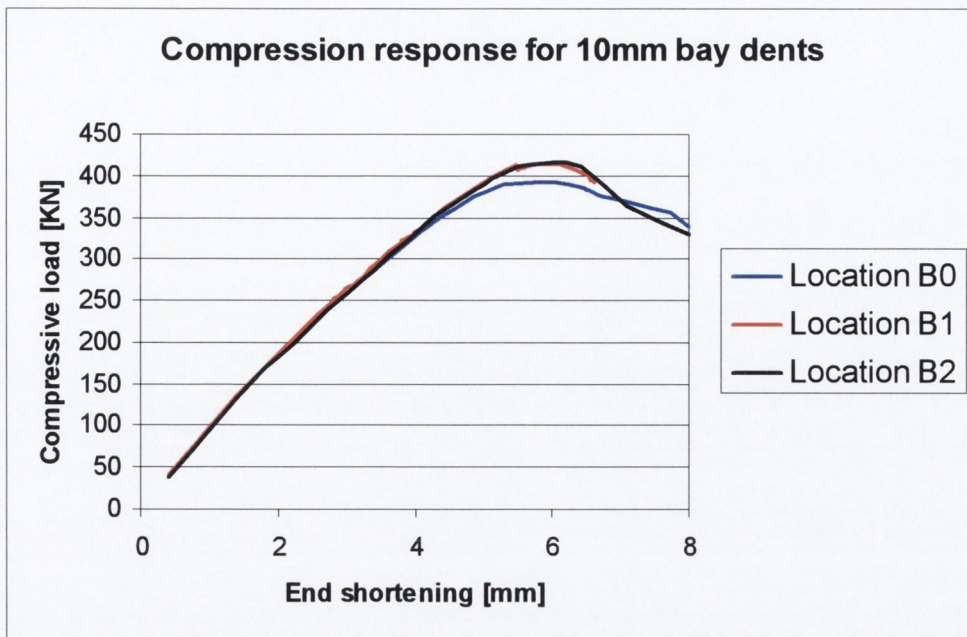


Figure 5.60 Compression response for 10mm depth bay dents at locations B0, B1 and B2

Table 5.2 tabulates the ultimate strength for every dent depth at each dent location and Table 5.3 tabulates these ultimate strengths as a factor of the pristine ultimate strength of 423KN. Two conclusions can be drawn from the results presented here. The first relates to an increased reduction in ultimate load with increased dent depth. The second is that the effect on ultimate load is diminished as the dents move from the centre “B0” towards the frame support “B2”. In addition, the sensitivity to increasing dent depth is also reduced. At “B2” a dent depth of 4mm and 10mm cause reductions in ultimate strength of 1% and 1.7% respectively. While at “B0” for the same dent depths the ultimate strength reduction increases from 1.665% to 7%.

Dent location	Dent depth 4mm	Dent depth 8mm	Dent depth 10mm
B0	416KN	403KN	393.4KN
B1	416.5KN	410KN	414KN
B2	419KN	417KN	416KN

Table 5.2 Ultimate compressive strength for bay dents at 4mm, 8mm and 10mm

Dent location	Dent depth 4mm	Dent depth 8mm	Dent depth 10mm
B0	0.984	0.953	0.930
B1	0.985	0.969	0.978
B2	0.990	0.986	0.983

**Table 5.3 Ultimate strength of bay dents as a factor of pristine ultimate strength**

Examination of the finite element model reveals the reason for these trends. Figure 5.61 and Figure 5.62 plot the deformation due to two dents with the same residual dent depth at locations "B2" and "B0" respectively. Comparing Figure 5.61 and Figure 5.62, it is clear that the dents have a very different field of influence. For the dent at location "B2", Figure 5.61, the increased rigidity of the frames restricts the residual deformation of the dent to the immediate stringer-frame bay. While for the dent at location "B0" Figure 5.62, the residual deformation of the dent extends into the two adjacent stringer-frame bays.

This extra support afforded by the frame results in less deformation growth of the dent as the panel buckles locally under end shortening. Figure 5.63 and Figure 5.64 plot the buckling mode at ultimate load in the test section skin for both dent locations. Comparing Figure 5.63 with Figure 5.61 it can be seen that the dent at location "B2" has grown in depth to approximately 12mm. This contrasts with the increase in depth shown at location "B0" where Figure 5.64 shows a dent depth of 16mm.

Figure 5.63 also shows that the local skin buckling in the bays adjacent to the dent in location "B2" depicts a fully developed mode. However, Figure 5.64 shows that the dent located at "B0" has undermined the local skin buckling in adjacent bays. This is as a result of both its initial field of influence, which extended into these bays, and also the fact that the stringers are less stiff in the radial direction at the centre of the bay than near the frames, which allows the influence of the dent to increase under compressive loading.

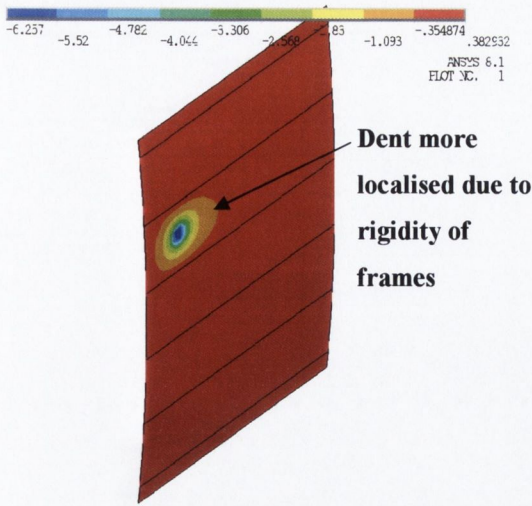


Figure 5.61 Bay dent location "B2"

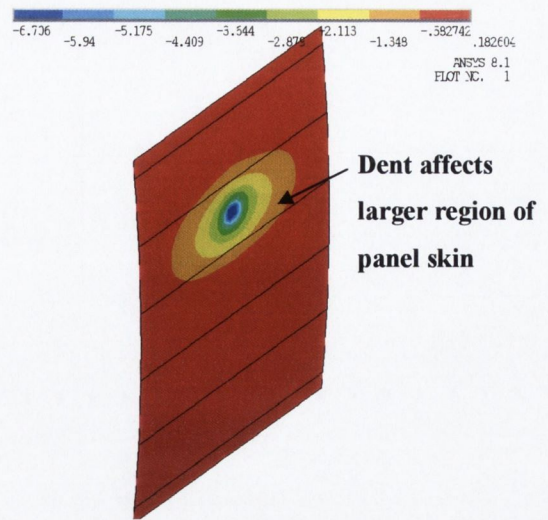


Figure 5.62 Bay dent location "B0"

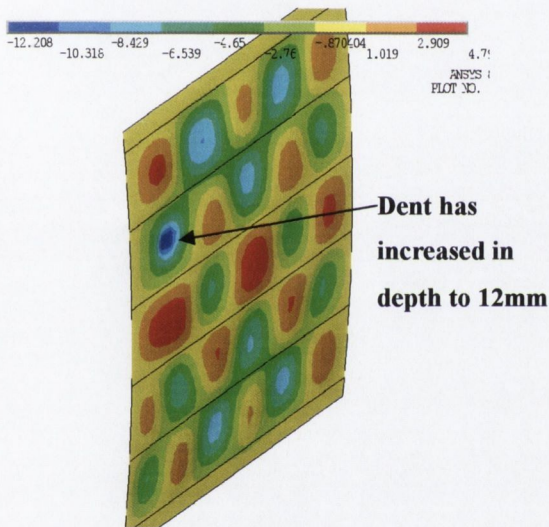


Figure 5.63 Buckling mode at ultimate compressive strength for dent at location "B2"

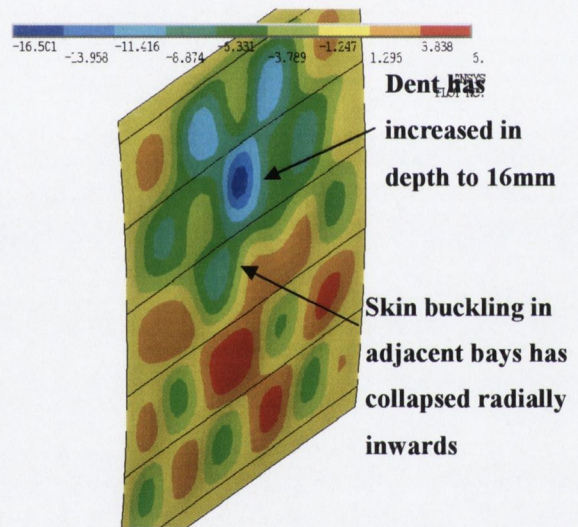


Figure 5.64 Buckling mode at ultimate compressive strength for dent at location "B0"

In summary, the finite element results have shown that a stiffened aircraft panel is more sensitive from an ultimate compressive strength perspective to bay dents located mid-way between the frames than to dents located nearer the frames. It should, however, be noted that dents closer to the frames are more likely to cause failure of a clip or rivets.

### 5.5.2 Effects of Location on Stringer Dents

Analyses varying the dent location from the centre of the frame bay along the stringer at 100mm intervals were also carried out; see Figure 5.57. Dent depths of 4, 8 and 10mm were investigated. The compressive load versus end-shortening curves are shown in Figure

5.65, Figure 5.66 and Figure 5.67 for dent depths of 4, 8 and 10mm respectively. The results show a decrease in the influence of the dent as it nears the frame. The exception to this is for location “S1” for dents of 4 and 8mm. In these two cases, the actual residual dent was deeper than aimed for 4 and 8mm, at 5.5mm and 8.9mm respectively. Therefore, the discussion focuses on the dent depths for locations “S0” and “S2” and the dent depth of 10mm for location “S1”.

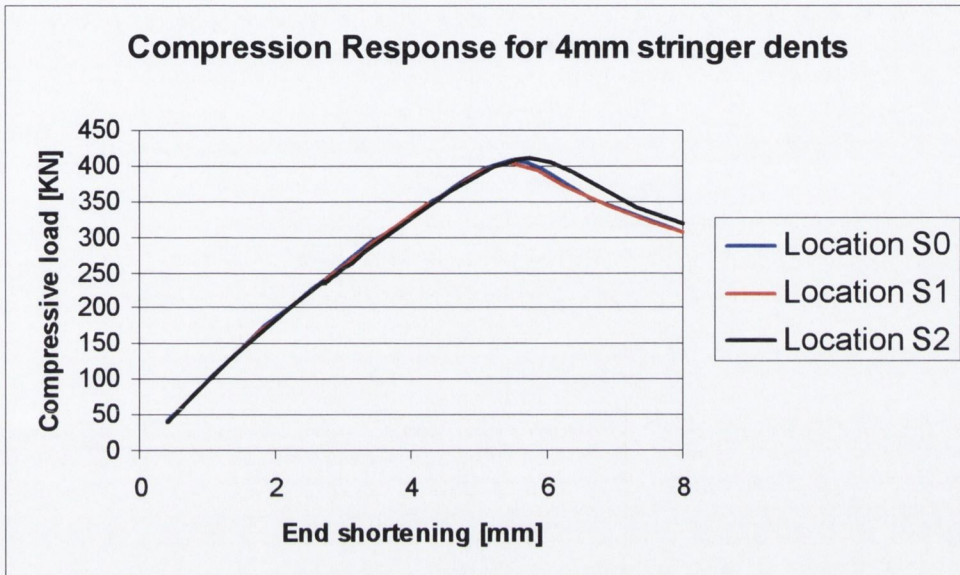


Figure 5.65 Compression response for 4mm depth stringer dents at locations S0, S1 and S2

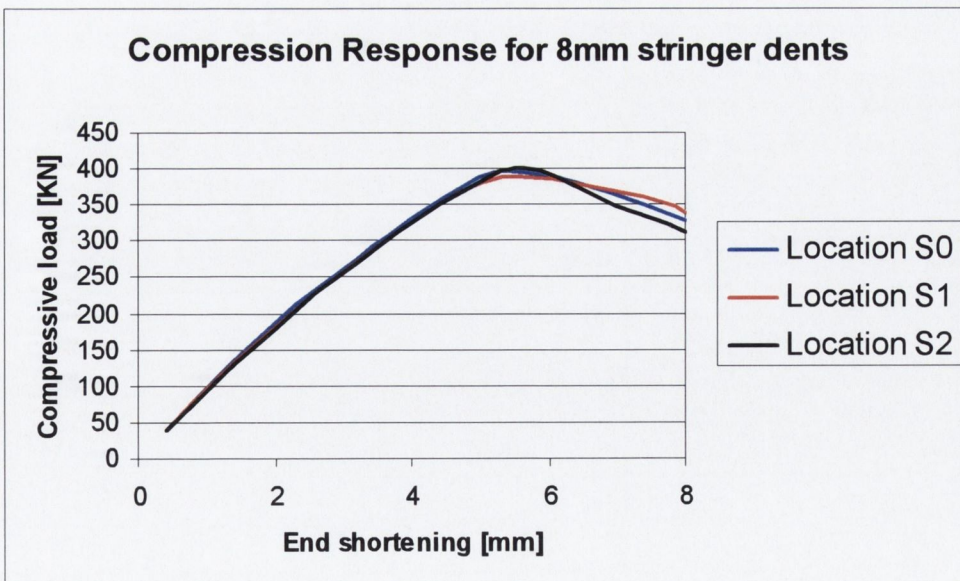


Figure 5.66 Compression response for 8mm depth stringer dents at locations S0, S1 and S2



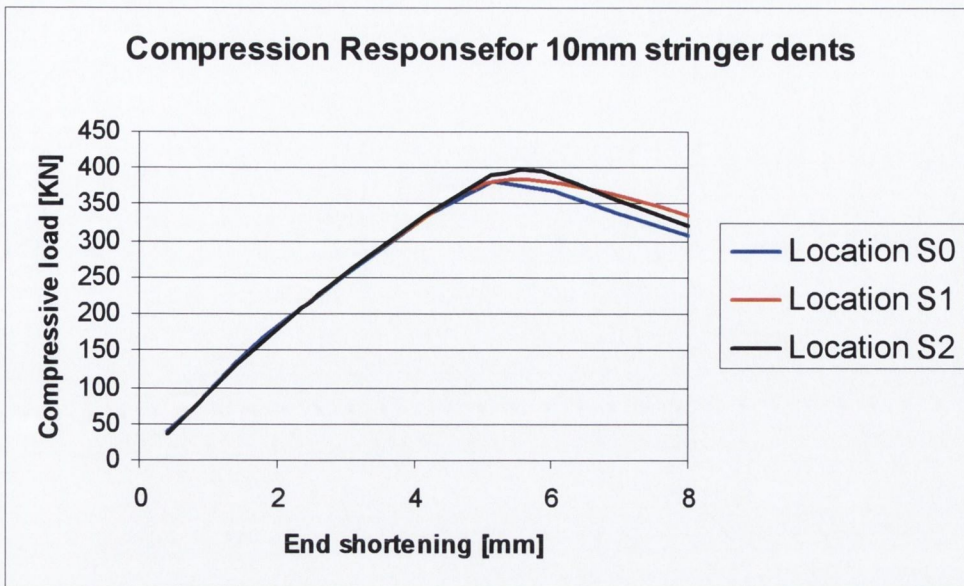


Figure 5.67 Compression response for 10mm depth stringer dents at locations S0, S1 and S2

Table 5.4 plots the ultimate compressive strength for each dent depth at the given locations. Table 5.5 plots these values as a factor of the pristine ultimate compressive strength of 423KN.

Dent location	Dent depth 4mm	Dent depth 8mm	Dent depth 10mm
S0	407KN	396KN	382KN
S1	404KN	390KN	385KN
S2	410KN	399KN	397KN

Table 5.4 Ultimate compressive strength for stringer dents at 4mm, 8mm and 10mm

Dent location	Dent depth 4mm	Dent depth 8mm	Dent depth 10mm
S0	0.962	0.936	0.90
S1	0.955	0.922	0.91
S2	0.969	0.943	0.938

Table 5.5 Ultimate strength of stringer dents as a factor of pristine ultimate strength

While the overall reduction in load for a dent on a stringer is greater than for a dent in the bay, the relative reductions due to varying the location of a dent along a stringer are not as significant as varying the location in the bay. Varying the location along the stringer towards the frame does, however, result in a slight decrease in the reduction of ultimate compressive strength. Again, this is attributed to the greater boundary support provided by

the frames. Figure 5.68 and Figure 5.69 plot the residual stringer dents at location “S2” and “S0” respectively. As can be seen, both dents affect the bays adjacent to the dented stringer; the dent at “S2” affects a more localised area from the point of view of dent depth because of the proximity of the frame. This is shown clearly in Figure 5.70, where the radial displacement of both residual dents along section A-A has been plotted.

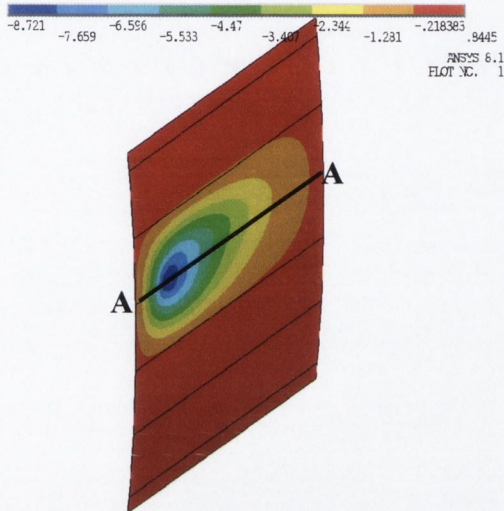


Figure 5.68 Residual stringer dent location “S2”

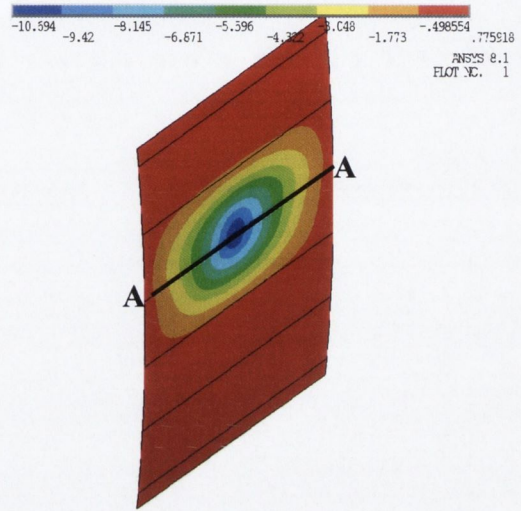


Figure 5.69 Residual stringer dent location “S0”

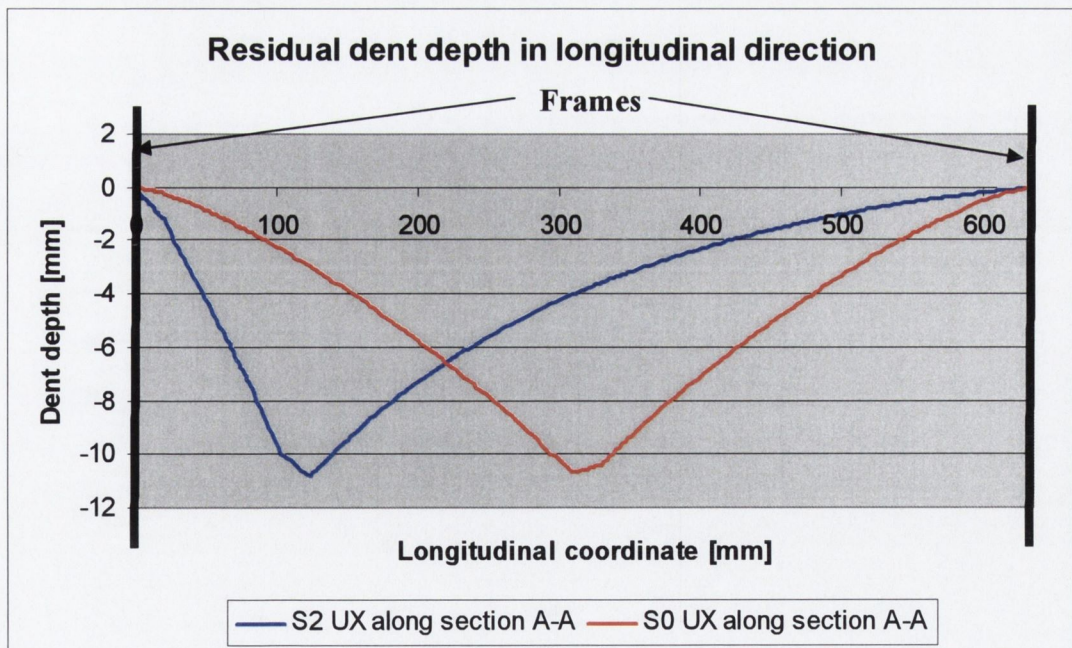


Figure 5.70 Residual dent radial profile along stringer section A-A

This difference in dent shape, coupled with the rigidity of the frame, results in a different buckling response under loading. Figure 5.71 plots the local skin buckling for dent “S2” at

ultimate compressive load and Figure 5.72 shows the corresponding plot for location “S0”. It is clear that the field of influence of the dent in the centre of the stringer is greater than that of the dent near the frame. As was the case with the bay dents, the effect of location is most severe in the stringer centre and decreases as the dent nears the frame supports. Since, the Airbus structural engineers report almost all daily dent repair requests to be for dents below 10mm; this would indicate the results from the experimental and FE tests for a 10mm dent on a stringer mid-way between frames, as presented in section 5.3.2, are an upper bound for compressive strength reduction of 9% for this panel geometry for typical dents.

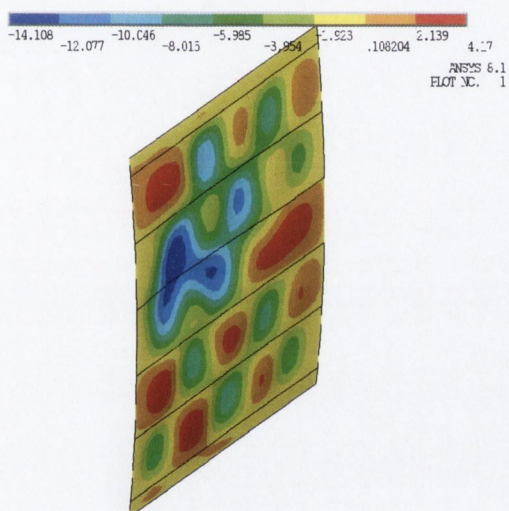


Figure 5.71 Buckling mode at ultimate compressive strength for dent at location “S2”

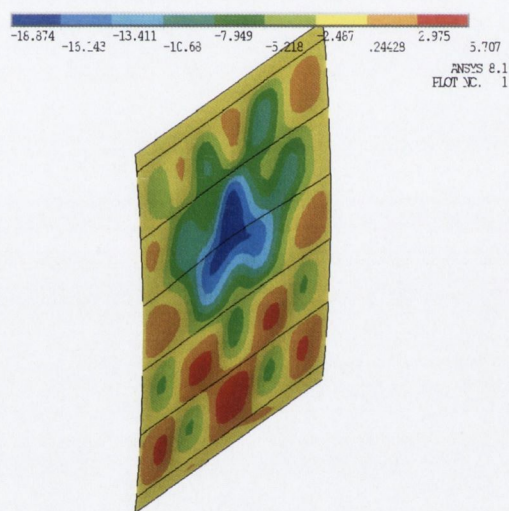


Figure 5.72 Buckling mode at ultimate compressive strength for dent at location “S0”

## 5.6 Effect of Dent Size

Investigations into the effects of size of the dent were carried out using indentors of different diameters. Figure 5.73 and Figure 5.74 plot the compressive load versus end shortening curves for indentors of different radii for dents of 7 and 10mm respectively.

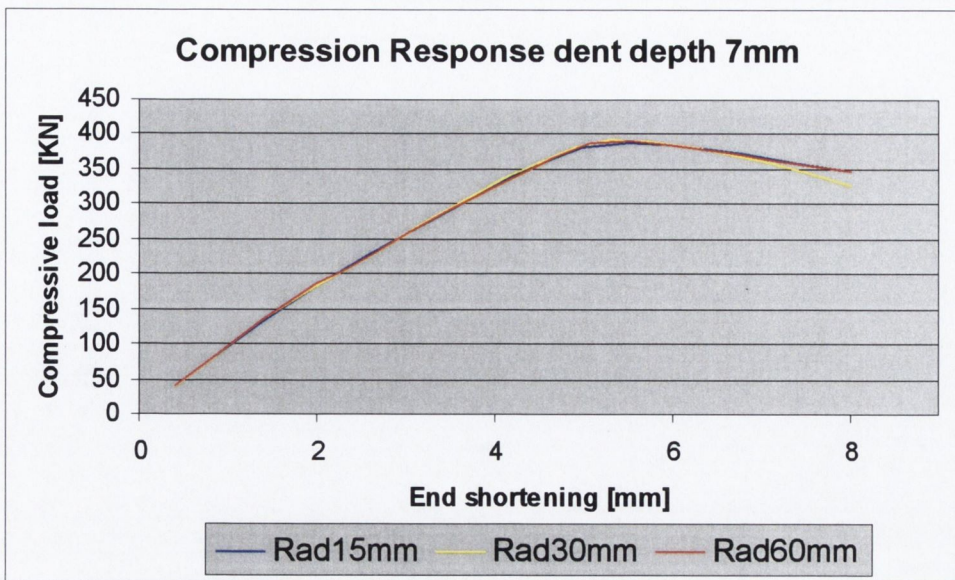


Figure 5.73 Compressive load versus end shortening for 7mm dent on stringer mid-way between frames with indenter radii 15, 30 and 60mm

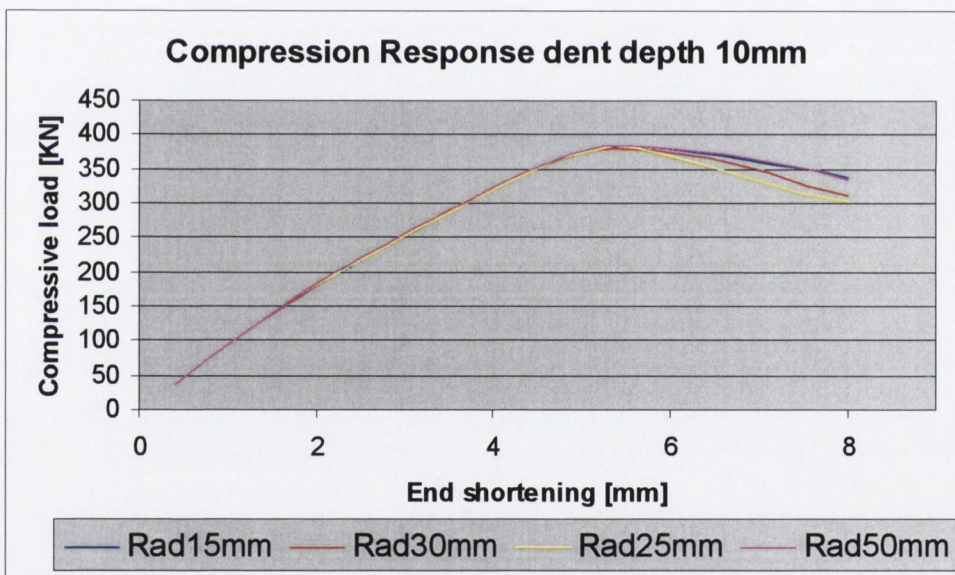


Figure 5.74 Compressive load versus end shortening for 10mm dent on stringer mid-way between frames with indenter radii 15, 25, 30 and 50mm

It is clear from Figure 5.73 and Figure 5.74 that the change in radius had little effect on the ultimate compressive load. In fact, for all the 7mm dents, the ultimate compressive strength values showed differences of only 0.9% between the maximum and minimum values tested. The 10mm dent depths showed similar results with a range of only 1.2%.

This result contradicted that of Paik and Thayamballi [39], who noted that changing the dent radius, resulted in large reductions in ultimate compressive strength. In order to explain this apparent contradiction, the actual residual dent, and not the indenter, was examined. Figure 5.75 shows the test section skin for the case of a residual dent from a 50mm radius indenter. Two paths are superimposed on the skin; X-X in the circumferential direction and Y-Y in the longitudinal direction.

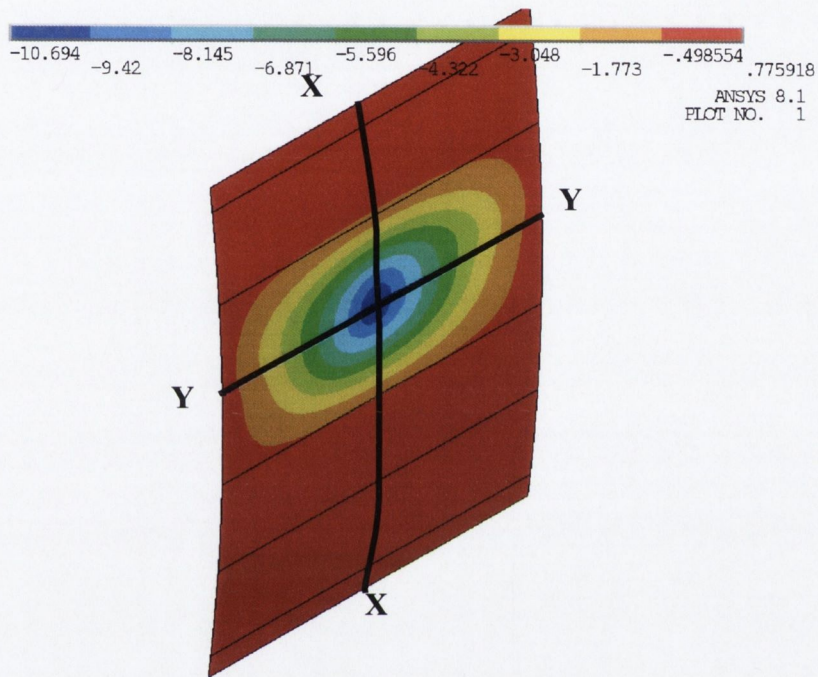


Figure 5.75 Residual dent

The radial displacements along these paths for residual dents caused by a 25 and 50mm radius indenter are plotted in Figure 5.76 and Figure 5.77. These plots explain the discrepancy between the results presented in Figure 5.73 and Figure 5.74, and those of Paik and Thayamballi [39]. In the model presented by Paik and Thayamballi, the dent was a geometric idealisation where the dent diameter was the diameter of the geometric damage modelled into the surface. For the models presented here, it is clear that large increases in indenter diameter do not necessarily result in large increases in the deformed geometry of the residual dent. From Figure 5.76 and Figure 5.77, it can be seen that multiplying the indenter radius by a factor of two, in this case from 25mm to 50mm, results in almost an identical residual dent. This is due to the nature of the non-linear surface-to-surface contact between the indenter and the panel skin. As a result, an increase in radius does not necessarily result in an increase in the region of contact between the skin and indenter.

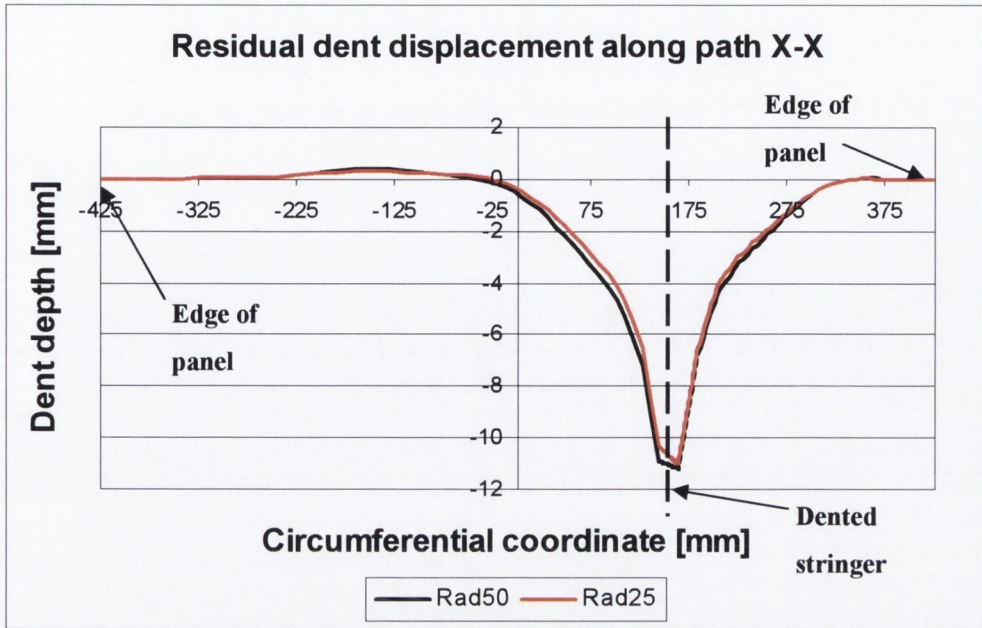


Figure 5.76 Radial displacement along path X-X case with 25 and 50mm radius indentors

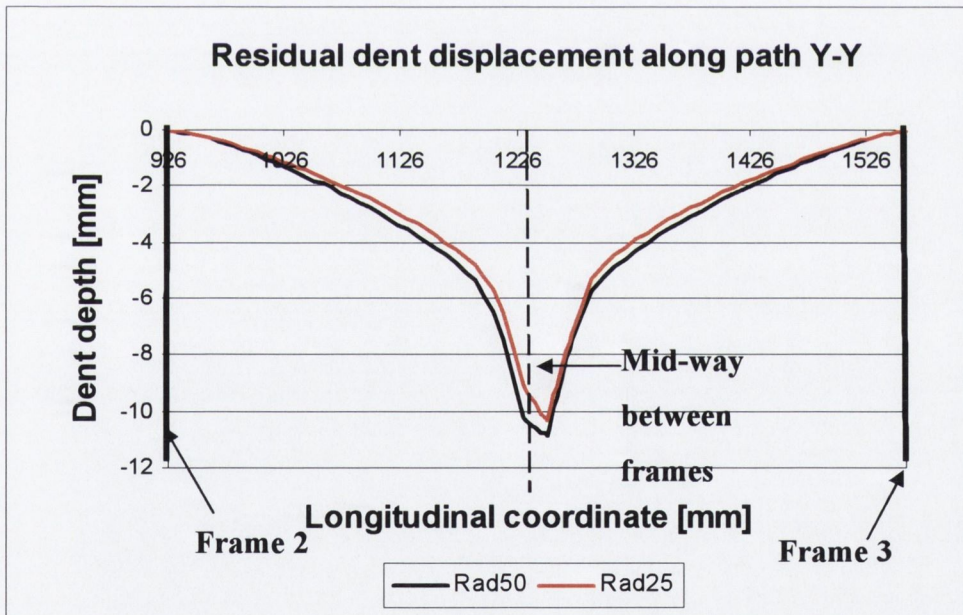
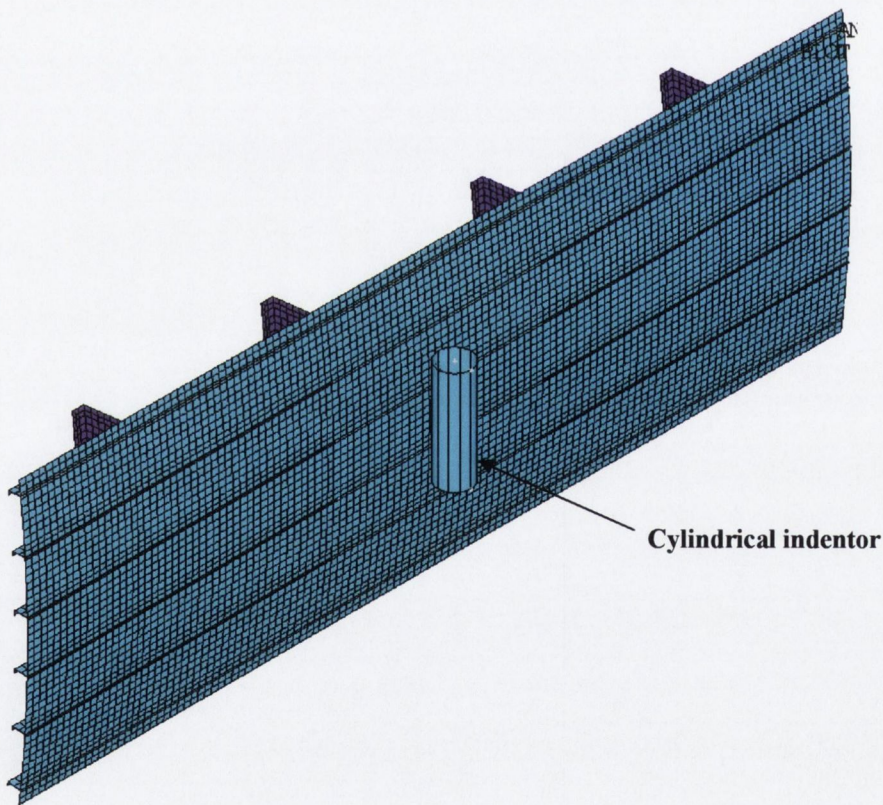


Figure 5.77 Radial displacement along path Y-Y case for 25 and 50mm radius indentors

## 5.7 Cylindrical Dents

### 5.7.1 Cylindrical Dent across Stringers

Subsequent to an on-site visit to the FLS Aerospace facilities in Dublin Airport and inspection of the likely sources of dents on aircraft, it was decided to model a cylindrical dent impacting on the panel. This was because the dents seen in practice were generally as a result of contact with the edges of loading trolleys and boarding stairs and were often of a cylindrical nature. In practice, due to the depth of dent selected, the dents modelled in this section would normally require immediate replacement of the affected stiffeners and skin. However, it was of interest to model these “deeper dents” to establish if there is a dramatic drop in ultimate compressive strength for large deep dents. Particularly since the investigation into varying the dent diameter had yielded nominally identical residual dents.



**Figure 5.78 Cylindrical indenter perpendicular to stringers**

Figure 5.78 shows the set-up for the first model in which the cylinder was modelled perpendicular to the longitudinal stringers, with radius 50mm and length 308mm. The dent was applied to create a residual dent of 15mm. Due to the length of the indenter, two stringers, their stringer-frame bay and half of the next bays were affected. Figure 5.79 and

Figure 5.80 plot the radial displacement at maximum indentation and the residual dent respectively. It is clear that the cylindrical dent affects a far greater region of the skin surface than the spherical dent. The result is that the ultimate compressive strength of the panel is reduced to 339KN, a reduction of 19.8% in comparison to the pristine panel ultimate strength of 423KN, as shown in Figure 5.81. From Figure 5.81, it is clear that, unlike the case of the spherical dents, the cylindrical dent across two stringers results in a drop in panel stiffness from the commencement of end-shortening.

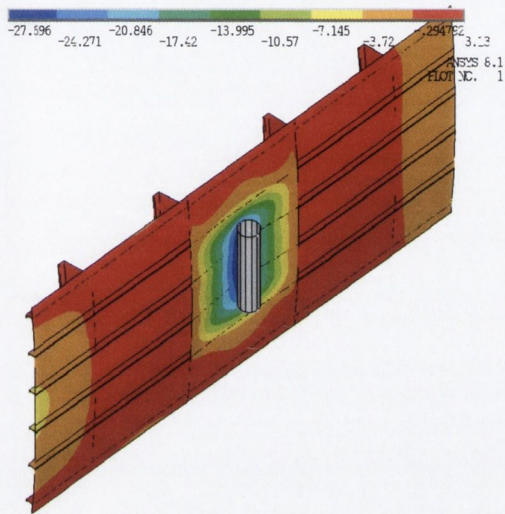


Figure 5.79 Max cylindrical dent perpendicular to stringers

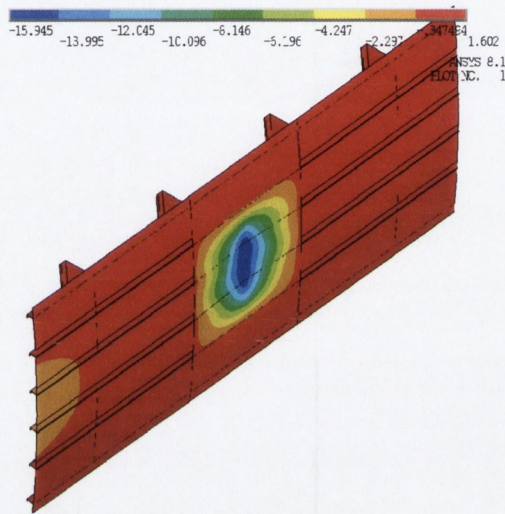


Figure 5.80 Residual cylindrical dent perpendicular to stringers

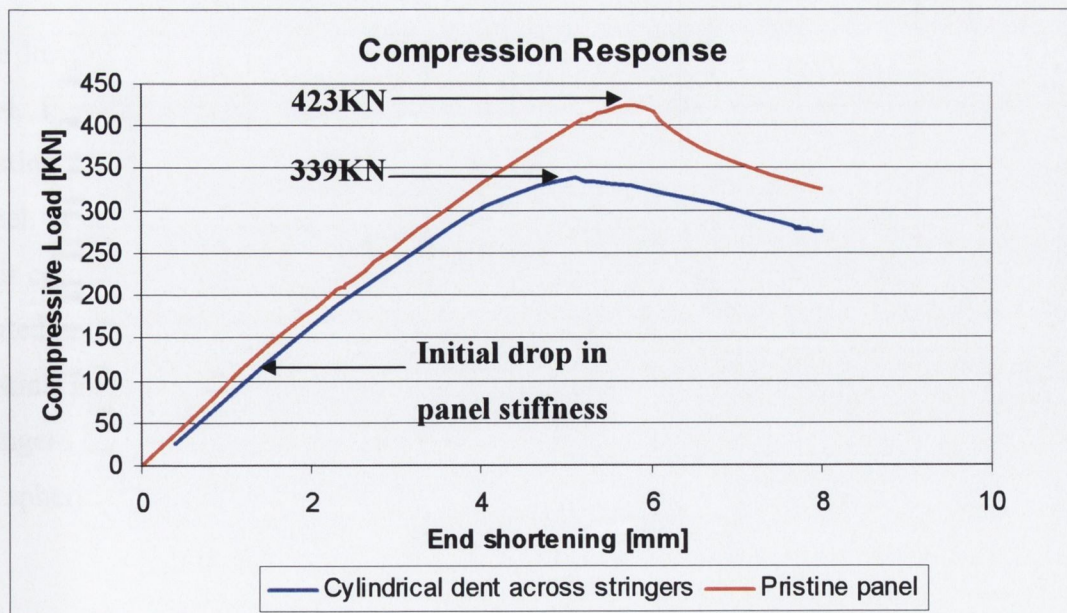


Figure 5.81 FE predicted compressive load versus end shortening for a cylindrical dent across two stringers



Figure 5.82 plots the radial displacement at ultimate load and, compared with Figure 5.79 it can be seen that the dented area has been prevented from setting up a local skin buckling response and has deformed in a bending dominated mechanism radially into the panel. The maximum deformation increased from a residual dent of 15mm to almost 27mm at ultimate load. In order to assess the load distribution across the panel, the mid-surface longitudinal stress in the test section has been plotted in Figure 5.83.

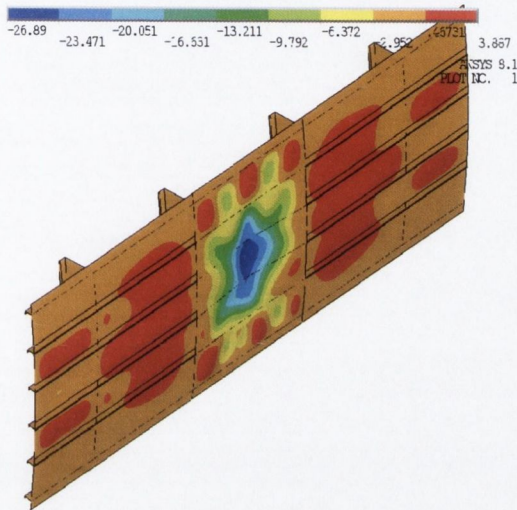


Figure 5.82 Radial displacement at max load of 339KN at end shortening of 5.11mm

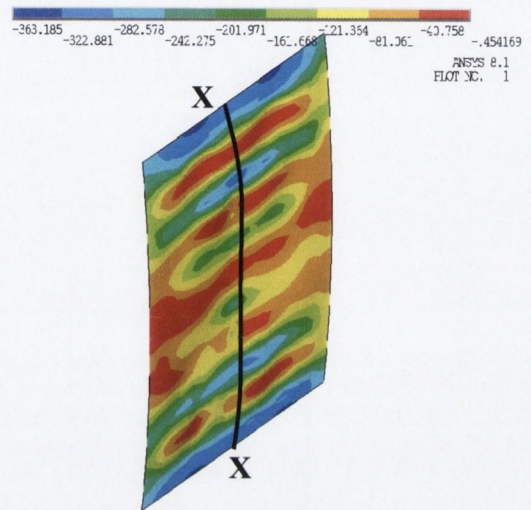


Figure 5.83 Longitudinal mid-surface stress at max load of 339KN at end shortening of 5.11mm

The longitudinal mid-surface stress at section X-X in Figure 5.83 is graphed in Figure 5.84. Figure 5.84 also plots the longitudinal stress in section X-X for the case of the pristine panel. Comparing both plots it is possible to assess the effects of this dent on the panel. It is apparent that the two dented stringers are under less longitudinal stress than their counterparts in the pristine panel. It can also be seen that the stringers adjacent to the dented stringers are under increased longitudinal compressive stress in comparison to the pristine panel. This indicates that the reduction in load carrying capacity of the dented stringers is overcome through load by-pass into the adjacent stringers, as was also the case for spherical dents.

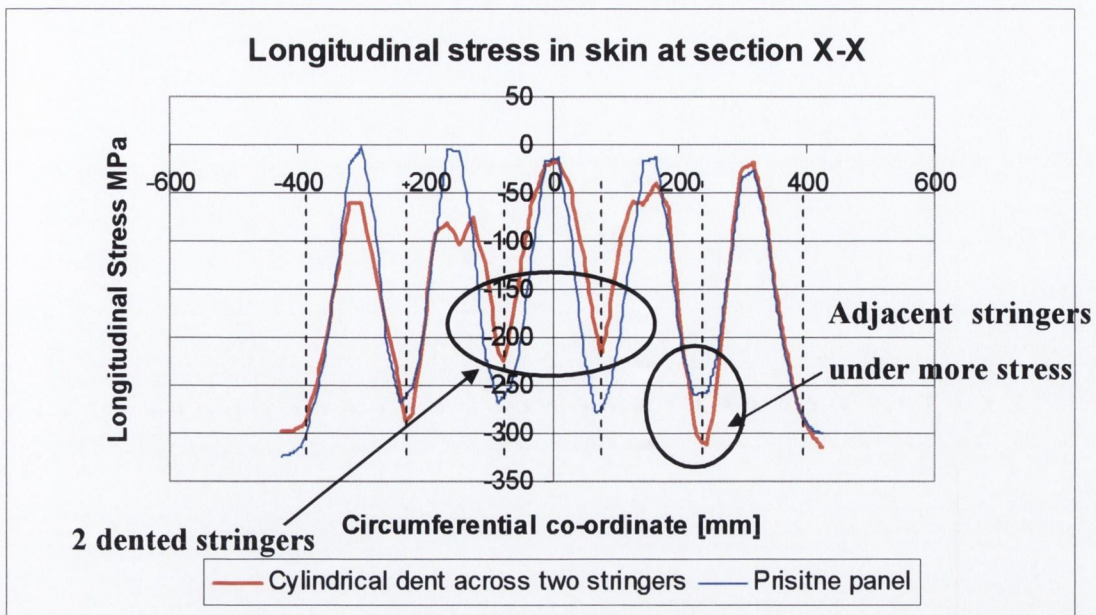


Figure 5.84 Longitudinal mid-surface stress along section X-X

### 5.7.2 Cylindrical Dent along a Stringer

In addition to a cylindrical dent across two stringers, the case of a dent along a stringer was also investigated. Figure 5.85 shows the finite element set up for this model. The cylinder is modelled along stringer 3, has a radius of 50mm and is three quarters of the length of the frame pitch.

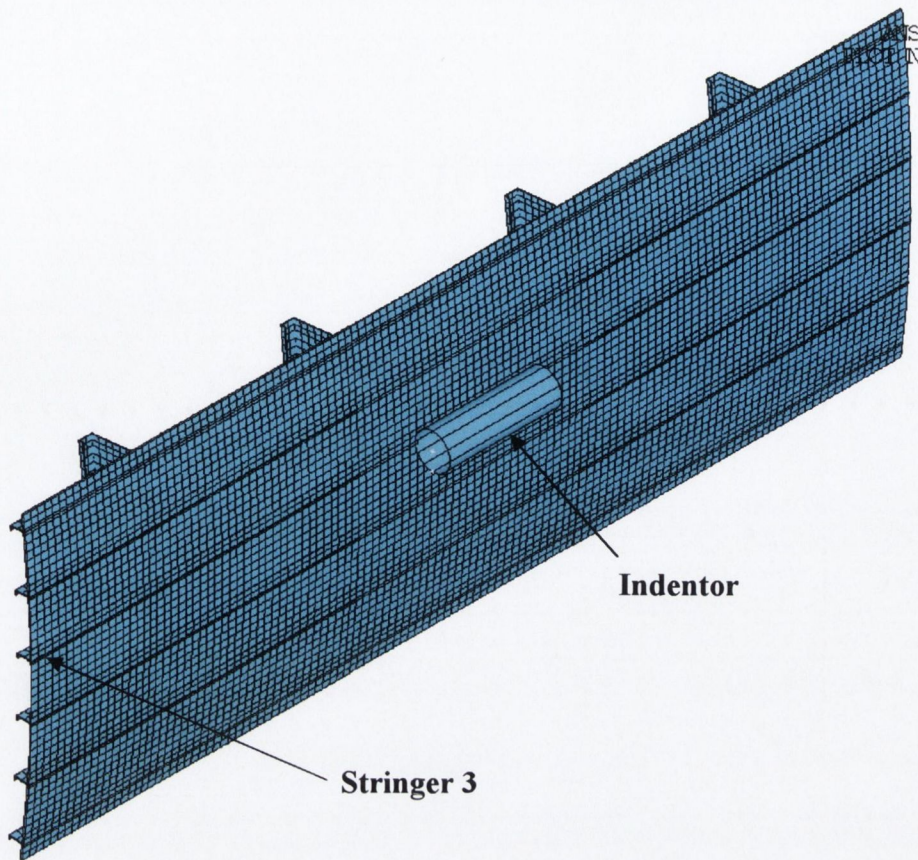


Figure 5.85 Cylindrical dent along a stringer

As was the case with the cylindrical dent across two stringers, the dent was applied to leave a residual dent of 15mm. Figure 5.86 and Figure 5.87 plot the radial displacement at maximum indentation and the residual dent respectively. From Figure 5.87 it can be seen that while the dent was applied to stringer number three, the effects of the dent encompass both of the adjacent stringer bays and are only arrested by the radial stiffness of the adjacent stringers. Figure 5.88 plots the compressive load versus end shortening for this model and the pristine panel for comparison. As was the case with the cylindrical dent across two stringers, there is a drop in overall panel stiffness from the commencement of loading, although in this case, the ultimate load is reduced from 423KN to 355KN, a drop of 16%.

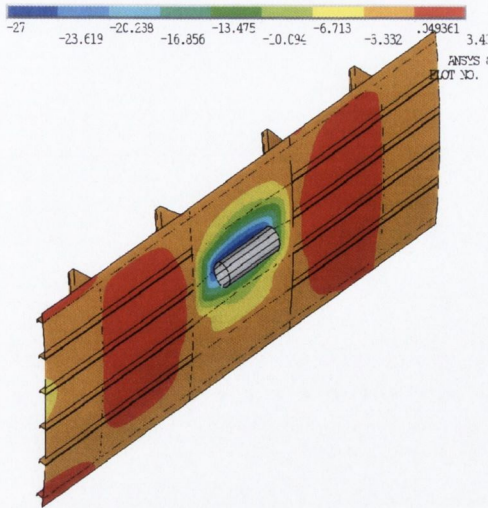


Figure 5.86 Max cylindrical dent along stringer

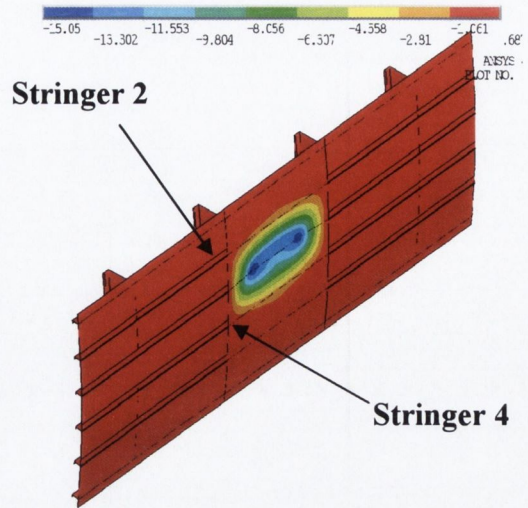


Figure 5.87 Residual cylindrical dent along stringer

This load reduction is not as severe as in the case of the dent across two stringers. Figure 5.89 plots the radial deformation at the ultimate compressive strength. From this graph it can be seen that the dent does not undermine the establishment of local skin buckling as great a region as was the case for a dent across two stringers, as shown in Figure 5.82. The result is that, although the response of the dented stringer is to deform out of plane from the commencement of loading, much of the panel is still effective in supporting compressive load and the characteristic local skin buckling is established in all but two bays.

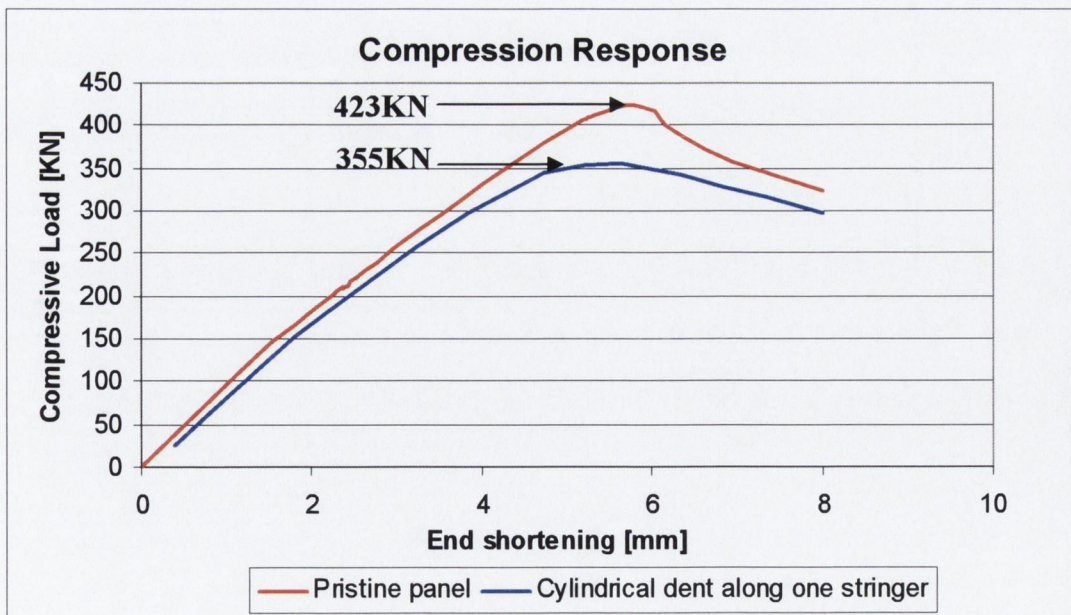


Figure 5.88 FE predicted compressive load versus end shortening for cylindrical dent along one stringer

Figure 5.90 plots the longitudinal mid-surface stress at the ultimate compressive load. From the graphical plot in Figure 5.90, it can be seen that the skin at the dented stringer skin attachment is under less compressive longitudinal stress than all the other stringers. The longitudinal stress along cross section X-X at ultimate load is graphed in Figure 5.91 and the corresponding pristine panel stress is also plotted for comparison purposes.

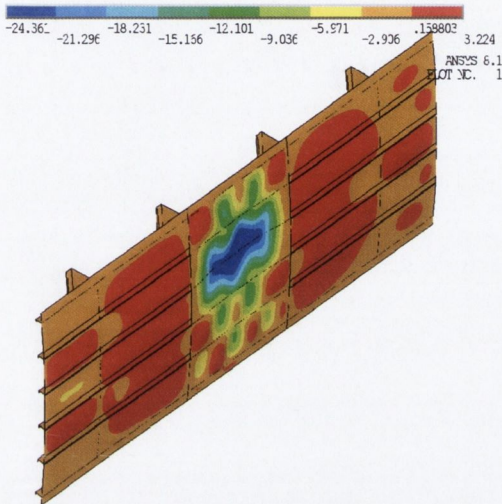


Figure 5.89 Radial displacement at a max load of 355KN at end shortening of 5.65mm

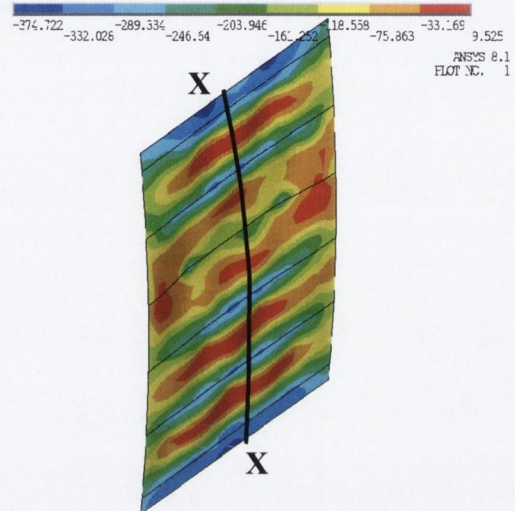


Figure 5.90 Longitudinal mid-surface stress at a max load of 355KN at end shortening of 5.65mm

The longitudinal stress in section X-X for this dent on one stringer closely follows the pristine case, displaying a sine-wave type response with increases in compressive stress in the areas close to the stringers and decreases in the centre of the bays, corresponding well with the “Effective Width” theory. The major divergence from this response relates to stringer number three, the dented stringer. Here, a reduction in compressive stress is shown and, as a result, the load is redistributed into the adjacent stringers, as shown in the black circles in Figure 5.91.

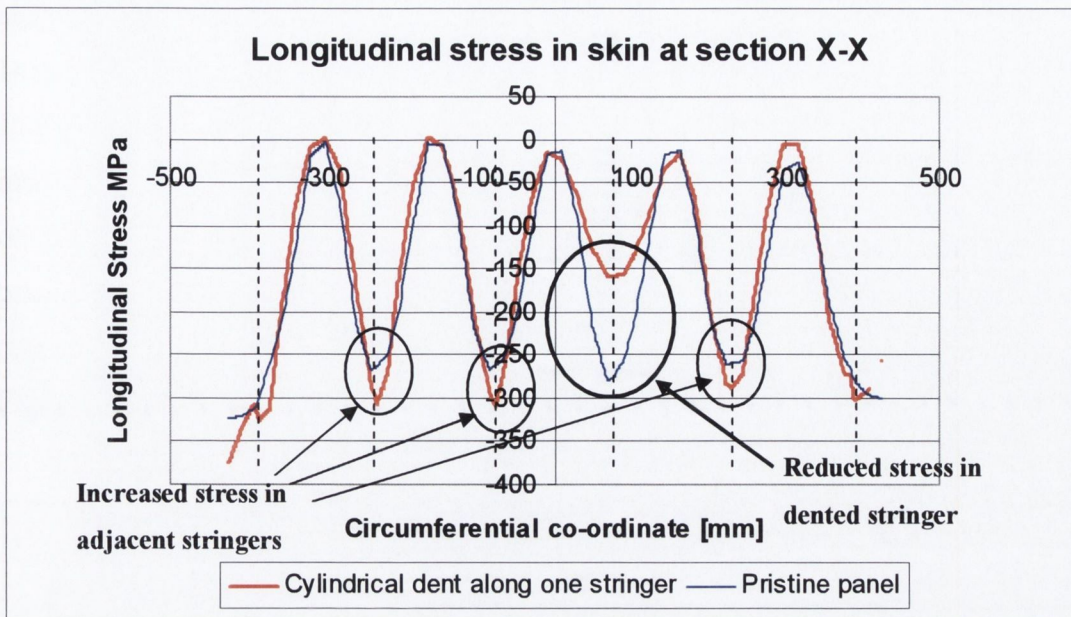


Figure 5.91 Longitudinal mid-surface stress along section X-X

The finite element models of the two cylindrical dents presented in this section represent rather extreme cases. Due to their length, large regions of the panel surface were affected and, at a depth of 15mm were beyond what the stiffeners are likely to experience without failing through fracture of the stiffener or rivet failure. However, they were modelled to assess whether the panel would be able to sustain any significant compressive loading with dents of this magnitude. The results presented show the excellent capability of the panel to redistribute the load away from the damaged area and thereby continue to support increases in compressive load.

## 5.8 Effect of Stringer Pitch

As mentioned in the literature review, Walker et al [37] raised the possibility that narrow stringer pitches could result in a “*cascading effect*” where a dented stringer could “*trip*” neighbouring stringers into a buckling well below their design load. Obviously, due to the built up nature of aircraft panels, this could potentially be of concern. For this reason a parametric study was carried out into the effects of stringer pitch on the reduction in ultimate compressive strength of a panel with a dented stringer. The stringer pitch values selected were based on discussions with structural engineers in Airbus Germany and were representative of the stringer pitch values across Airbus aircraft. While stringer pitch may vary up to 180mm, the tests modelled stringer pitch values less than that of the experimental test panel of 154mm in order to see if narrowing the pitch resulted in a

cascading effect and hence, greater ultimate strength reductions. Stringer pitches of 150, 145, 140, 135 and 130mm were selected for the investigation. All models, except the 135mm stringer pitch, converged. As in the case for the experimental test panel, all the FE modelled panels were dented to a residual dent depth of 10mm. These dents were located on a stringer mid-way between the two inner frames. For all analyses, a model of the pristine panel with the given stringer pitch was also simulated in order to calculate a relative load reduction for each panel. The results are presented in Figure 5.92 through to Figure 5.95.

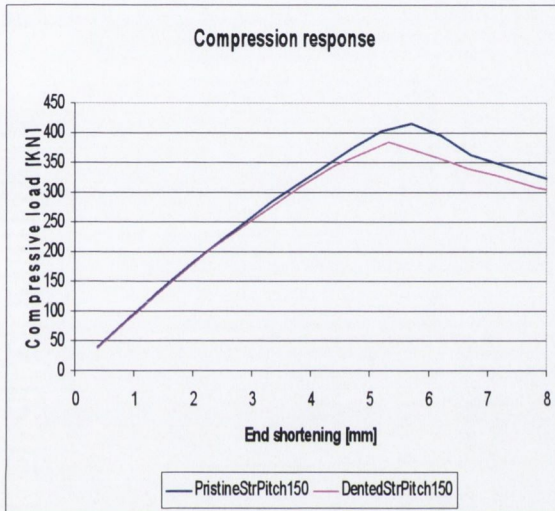


Figure 5.92 Stringer pitch 150

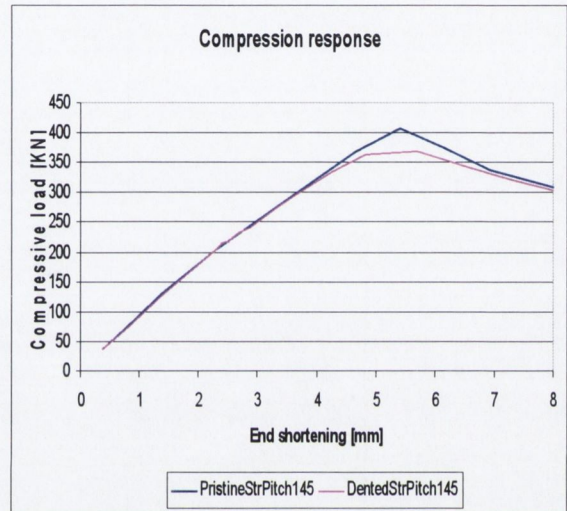


Figure 5.93 Stringer pitch 145

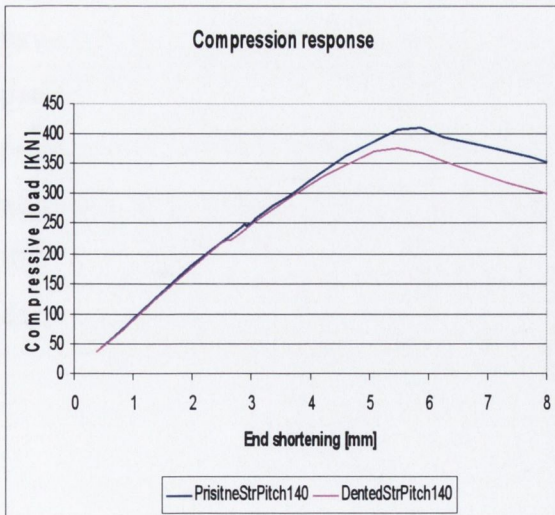


Figure 5.94 Stringer pitch 140

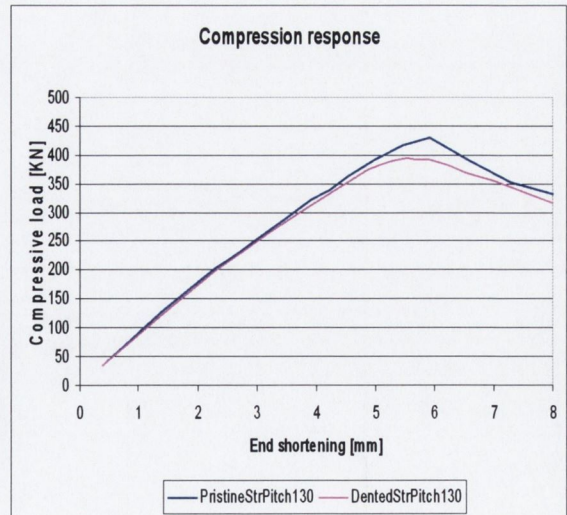


Figure 5.95 Stringer pitch 130

A similar compressive load versus end-shortening response is depicted in all cases. Initially the effect of the dent on overall panel stiffness is not significant until a point is reached where the load path of the dented panel diverges from that of the pristine panel. The load path for the dented panels then rises to an ultimate compressive strength which, in all cases shows a reduction from the pristine case.

In order to assess the effect of stringer pitch on relative reductions in ultimate compressive strength. These have been tabulated in Table 5.6, showing stringer pitch, dent depth, the pristine ultimate compressive load for each panel, the dented ultimate compressive load and the dented ultimate compressive load as a factor of the pristine load.

Stringer pitch	Dent depth	Pristine ultimate compressive strength	Dented ultimate compressive strength	Factor of pristine ultimate load
150mm	10mm	417KN	383KN	0.918
145mm	10mm	408KN	369KN	0.904
140mm	10mm	410KN	375KN	0.91
135mm	10mm	Unconverged	_____	_____
130mm	10mm	430KN	394KN	0.916

**Table 5.6 Ultimate compressive strength varying stringer pitch**

From the results tabulated in Table 5.6, it can be seen that varying the stringer pitch did not have a marked effect on the reduction in ultimate compressive strength for the tested panels. The strength reductions varied between 8.2 and 9.6%, and the decreasing stringer pitches did not necessarily yield increases in % reduction as shown in Figure 5.96. In fact although the first change in stringer pitch from 154mm to 145mm resulted in an increase in the % reduction in ultimate strength from 8.2 to 9.6%, further reductions actually decreased the percentage reduction.



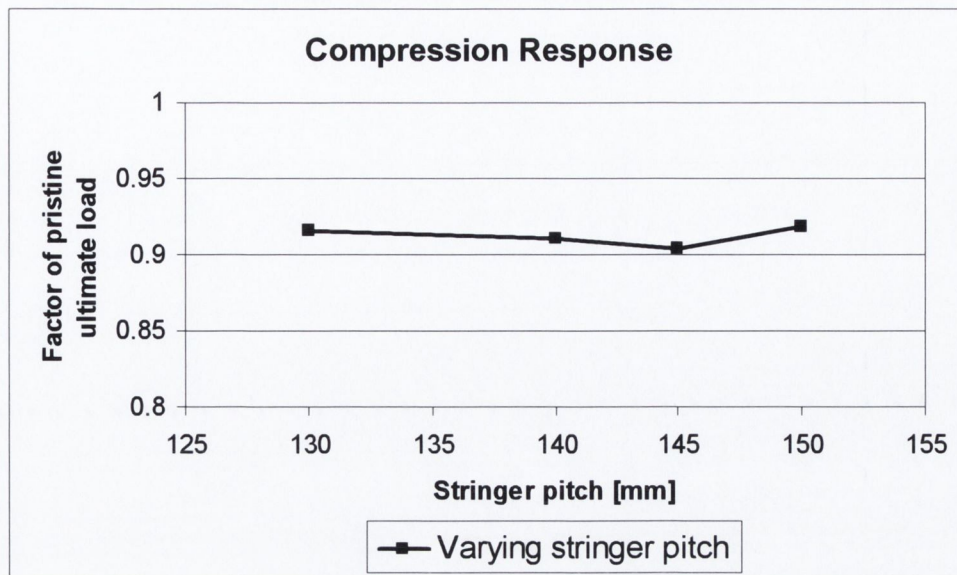


Figure 5.96 Ultimate strength reduction as a function of stringer pitch

These results indicate that the given aircraft geometry is not sensitive to changes in stringer pitch from an ultimate strength reduction perspective, and the effect of stringer “tripping” as raised by Walker et al [37] in their work on offshore structures, is not evident. It is clear that the built up nature of the aircraft panels provides an excellent inherent ability to redistribute load away from the damaged area and therefore maintain stability.

## 5.9 Efficacy of Dent Dress Back from a Static Strength Perspective

Due to the fact that there was no experimental evidence relating to the effects of dent dress back on the static strength of aircraft panels, an investigation was carried out into the feasibility of modelling this process using the developed model.

The dent dress back procedure, as described in the literature review, is essentially a panel beating style process and therefore dynamic in nature. This aspect of the process was not accounted for in the FE modelling of dress back presented here. As a result, the stress fields in the FE model would be different to an actual repair. The aim, however, was to establish what percentage of the static strength of the panel could be recovered due to a reduction in the size of the damaged dent. For such an investigation, the simplifying assumptions in modelling the dress back were acceptable.

The finite element model was set up in the same way as the previous models, with the addition of a second contact pair between the inner skin surface and a dress back “tool”. Initial attempts at modelling the dent dress back “tool” used spherical rigid objects of varying diameters, to represent a hammer head. The main difficulty with this method was that when “dressing back” one region, a previously dressed back region would simply pop back out due to the high elastic stresses, this was a manifestation of the so called “oil can effect”. Figure 5.97 depicts this graphically.

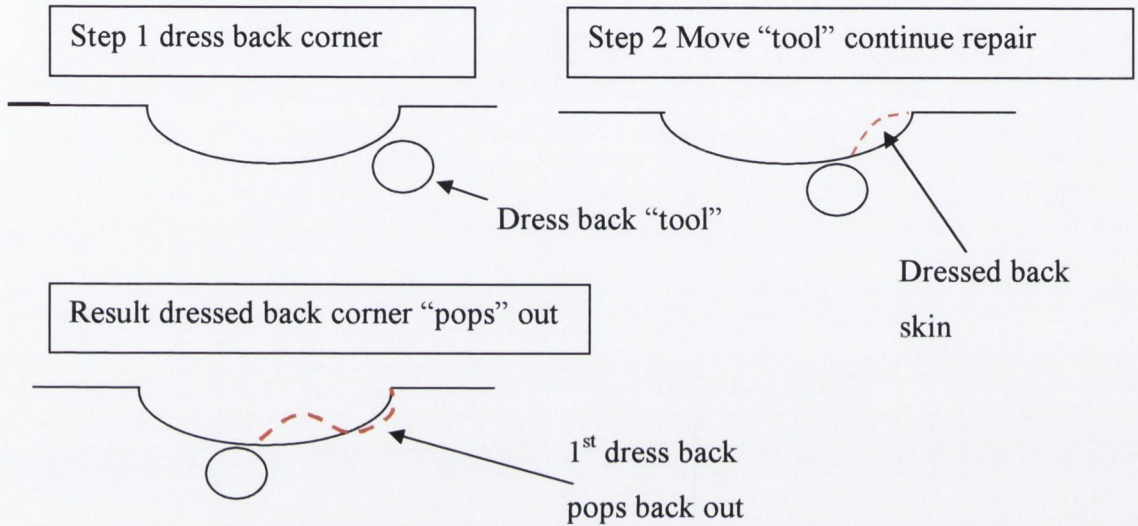


Figure 5.97 Schematic of modelling difficulties encountered in dress back

In an effort to overcome this problem using a simple modelling solution, the dress back tool was changed to a small cylindrical shape. It was hoped that the greater surface of the cylinder in contact with the skin would provide support to the skin in successive dress back “pushes” and prevent previously dressed back areas popping out. Figure 5.98 shows the finite element set up, depicting both the indenter and the dress back “tool” on either side of the panel skin.

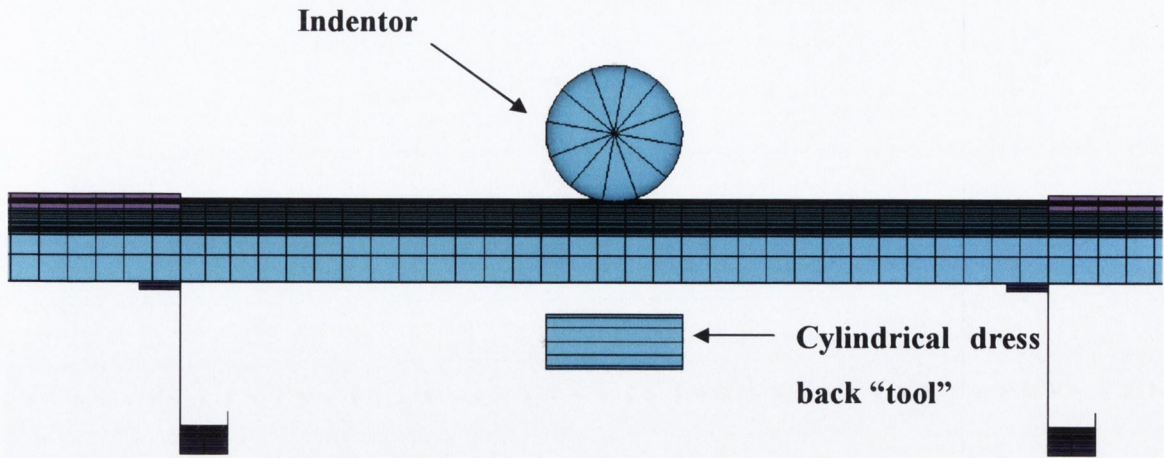


Figure 5.98 FE set up of dress back procedure

Denting was carried out in a stringer-frame bay to a maximum depth of 26mm, leaving a residual dent of 10mm to be dressed back. Figure 5.99 and Figure 5.100 plot the radial displacements for the maximum displacement and residual dent respectively.

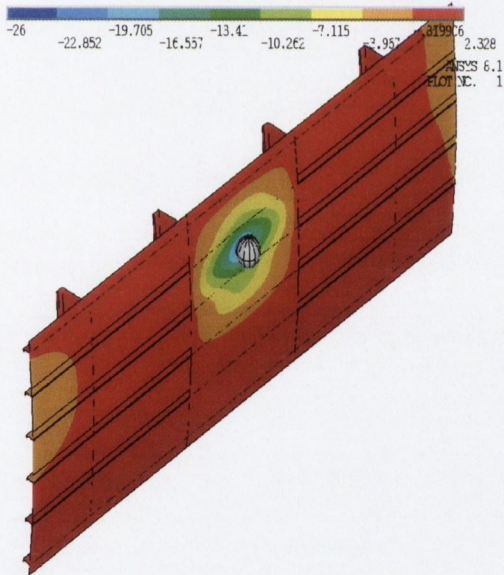


Figure 5.99 Max applied dent depth

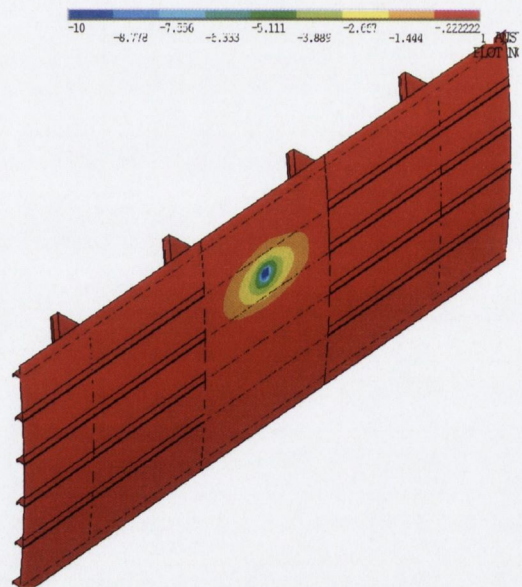


Figure 5.100 Residual dent depth

The residual dent was then dressed back using a series of incremental “pushes” with the cylinder on the inner surface of the skin. In total a series of ten pushes were necessary to dress back the centre of the dent to within 0.1mm of the original coordinate.

Figure 5.101 and Figure 5.102 show the dress back and the result of the dress back after four of the ten operations. This process resulted in an incremental recovery in the dent

depth at each pass until the centre of the dent was dressed back to within 0.1mm of the original position, as shown in Figure 5.103

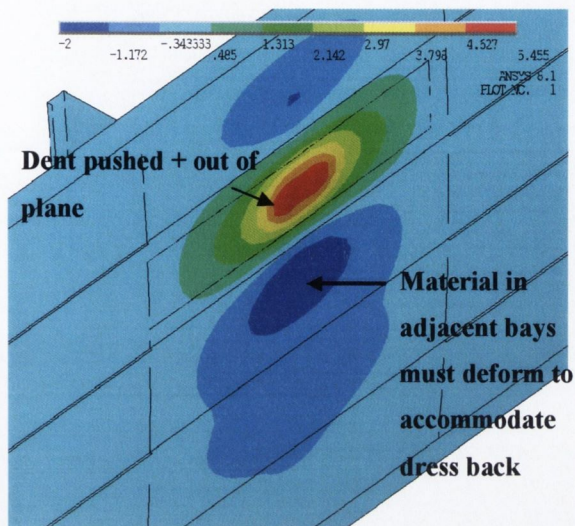


Figure 5.101 Tool displacing dent in radial direction

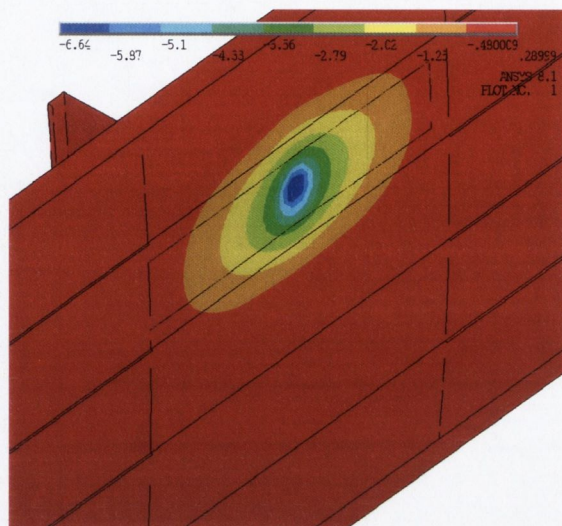


Figure 5.102 Dent recovers to 6.5mm in radial direction

From Figure 5.103, it can be seen that, due to the necessary simplification of using the cylindrical shape as the dress back tool, the areas which accumulated the highest stresses over the ten operations were at the cylinder edges. As a result, these areas were dressed back further than the centre of the dent. In addition, the material in the adjacent stringer-bays was stretched to the extent that two depressions of 1mm depth were formed. In reality the energy imparted by the hammer blows would result in the material under the hammer reaching yield point. This would result in a dressed back area consisting of numerous "little dents". As a result, the material deformation would be concentrated locally around the original dent and, it is unlikely that these large deformations of 1mm in adjacent bays would be formed. Despite these approximations in modelling, it was felt that the reworked dent surface would indicate whether there would be increases in ultimate compressive strength for an actual reworked dent.

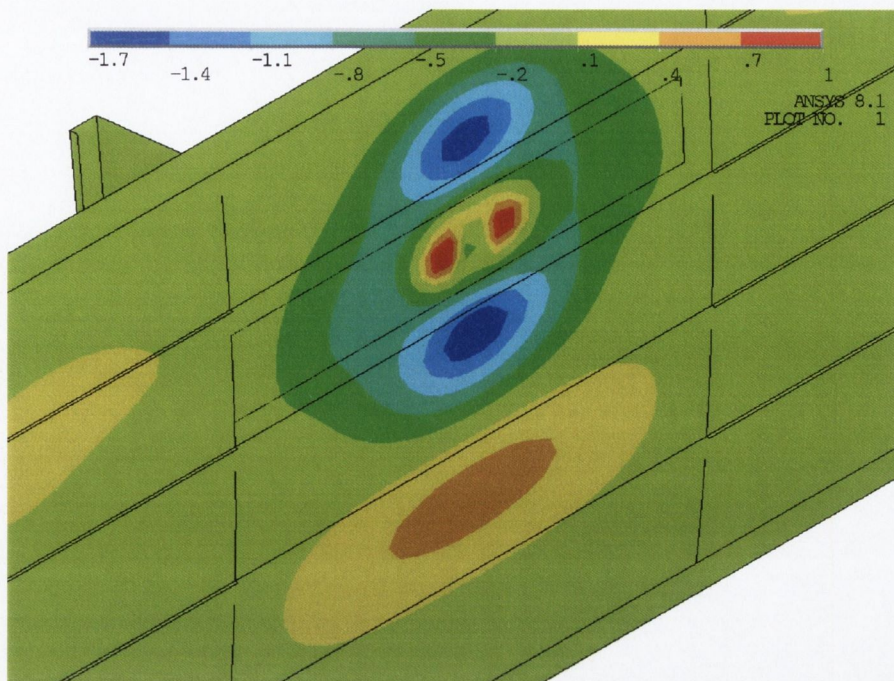


Figure 5.103 Final dressed back dent showing out-of-plane radial displacement

### 5.9.1 Compression Response of a Repaired Dented Panel

Figure 5.104 plots the compression load versus end shortening for the pristine panel, the dented panel and the repaired panel. The ultimate pristine compressive strength was 423KN and the bay dented panel ultimate compressive strength was 393KN. The dressed back or “repaired” panel performed very well under compression with an ultimate compressive load of 417KN.

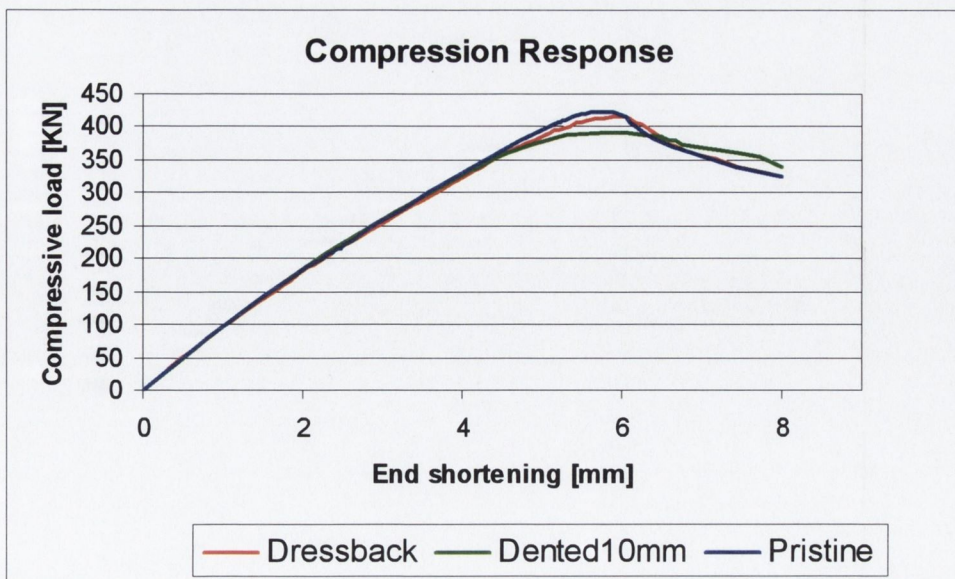


Figure 5.104 Compressive load versus end shortening for the pristine, dented and dressed back panel

From a static strength perspective, this is a very good result. The dressed back panel recovers 80% of the load reduction.

The dress back procedure does, however, result in a very different stress distribution in the panel skin. Figure 5.105 through Figure 5.112 plot the longitudinal and circumferential stress distribution in the dented and dressed back skin before compressive loading.

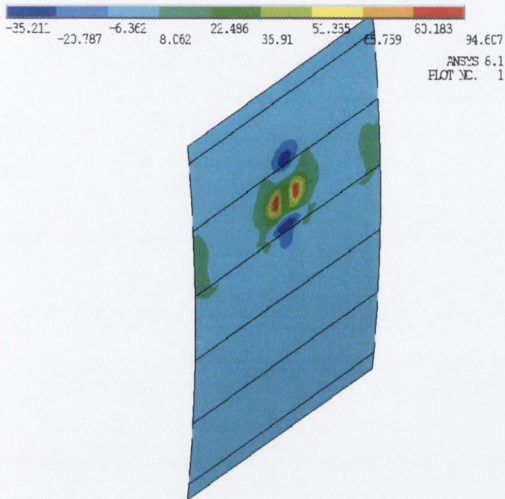


Figure 5.105 Dent longitudinal stress top surface

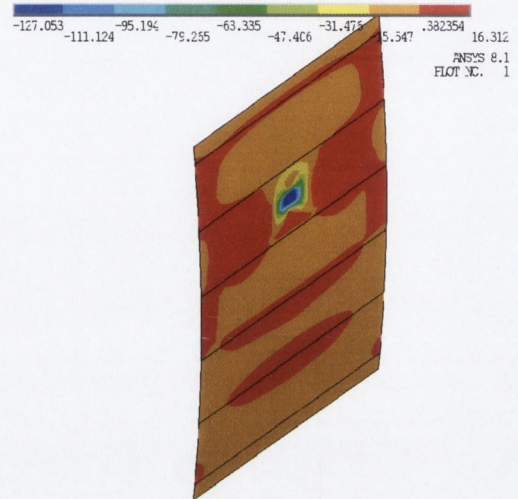


Figure 5.106 Dent longitudinal stress bottom surface

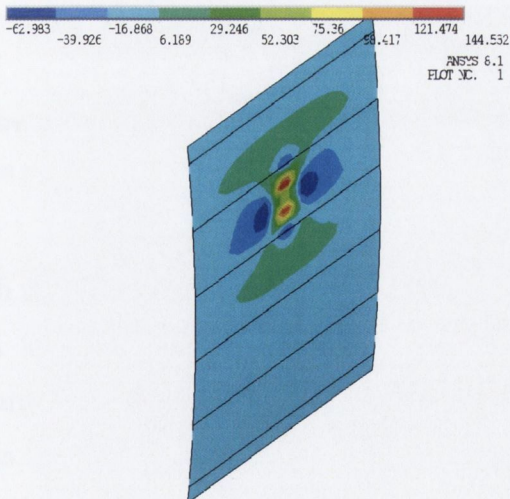


Figure 5.107 Dent circumferential stress top surface

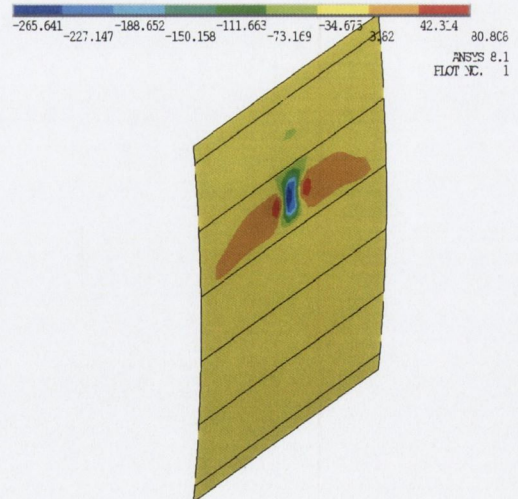
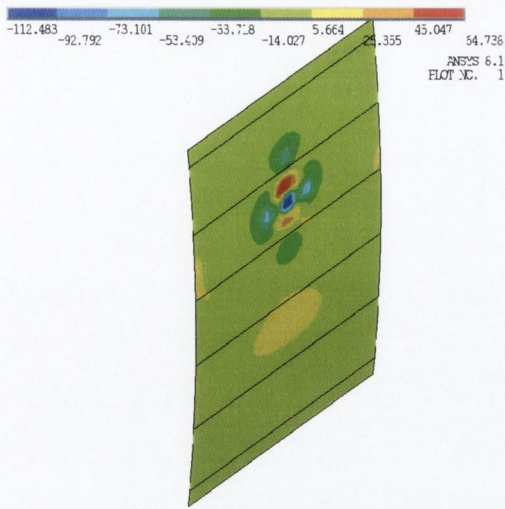
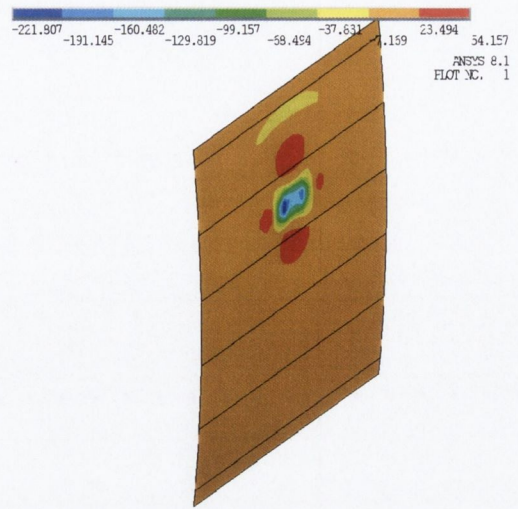


Figure 5.108 Dent circumferential stress bottom surface



**Figure 5.109 Dressed back dent longitudinal stress top surface**



**Figure 5.110 Dressed back dent longitudinal stress bottom surface**

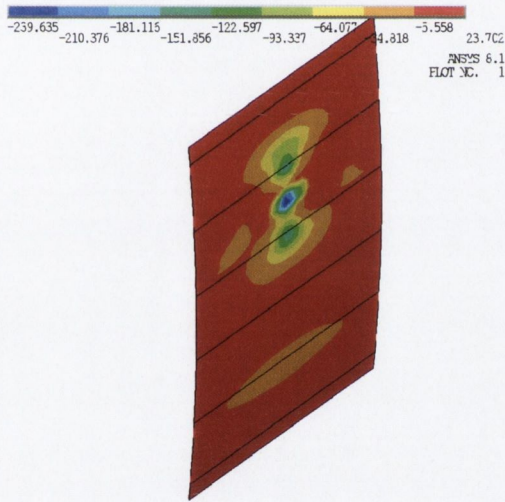


**Figure 5.111 Dressed back dent circumferential stress top surface**

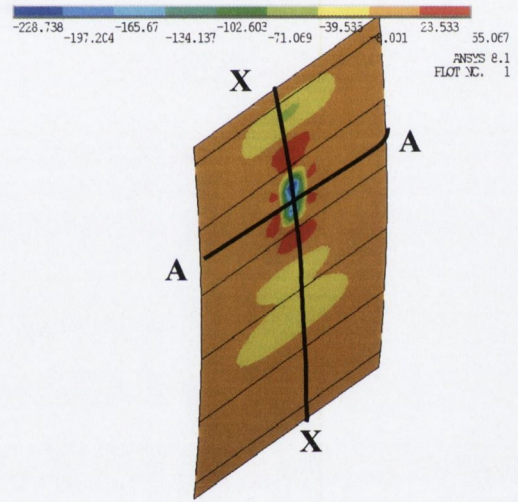


**Figure 5.112 Dressed back dent circumferential stress bottom surface**

Both the longitudinal stress along section X-X and the circumferential stress along section A-A for both the top and bottom shell surfaces are plotted in Figure 5.113 through to Figure 5.116. These plots give a clearer indication of the change in stress state due to the dress back procedure modelled. The longitudinal stress on the top surface, Figure 5.113, changes from tensile in the centre of the dent to compressive after dress back, more importantly the edges of the cylinder have resulted in two peaks of tensile stress at either edge of the dent which could be a possible source of crack growth. A similar result is present for the longitudinal stress on the bottom surface, where the edges of the dent show a growth in tensile stresses.

The circumferential top stress on the top surface along section A-A, as shown in Figure 5.115, shows a reversal in stress state at the centre of the dent from tensile to compression. On the other hand, the circumferential stresses for the bottom shell surface show a reduction in stress levels after dress back, Figure 5.116

Although the modelling method used to simulate the dress back procedure was based on a number of simplifying assumptions, the results indicate that dent dress back does restore compressive strength to the panel, largely due to the reduction in size of the damage. However, the results also indicate that from a fatigue viewpoint reworking the dent could potentially introduce very high tensile stresses. This could result in a situation where the repaired dent is more harmful than the dent itself. Although outside the scope of the research presented here, it does raise interesting questions regarding the repair of dents through dress back.

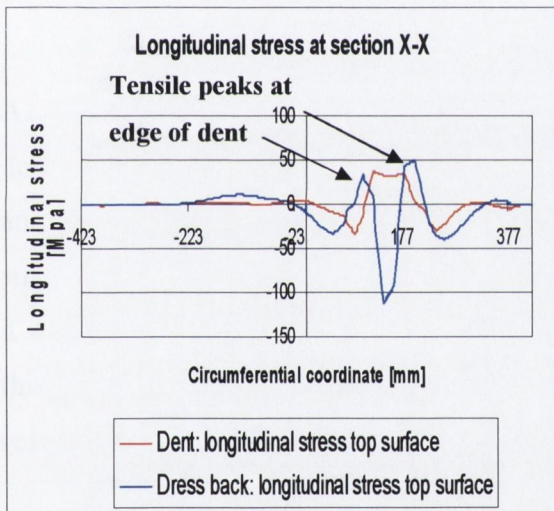


Figure 5.113 Longitudinal stress at section X-X on the shell top surface

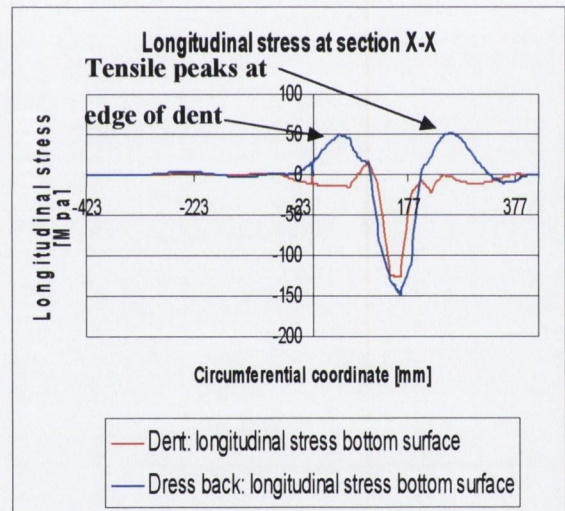
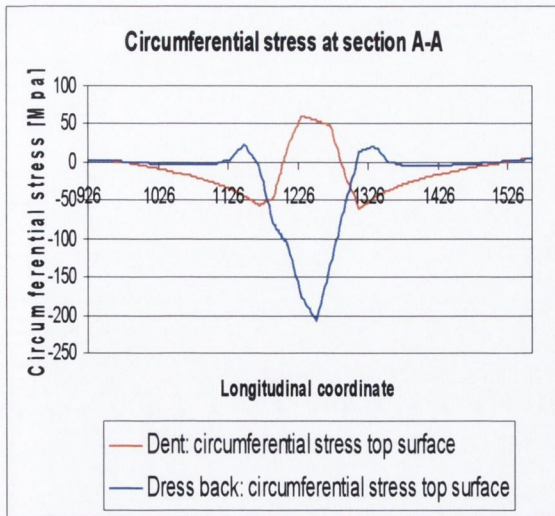
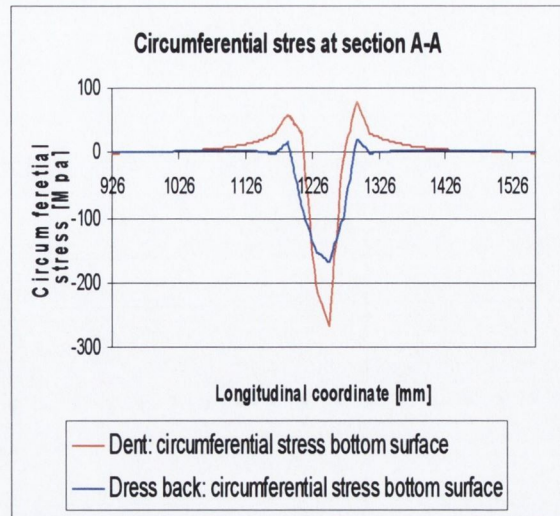


Figure 5.114 Longitudinal stress at section X-X on the shell bottom surface





**Figure 5.115** Circumferential stress at section X-X on the shell top surface



**Figure 5.116** Circumferential stress at section X-X on the shell bottom surface

## 5.10 Effect of Including Residual Stresses

As noted in the literature review, section 2.8, it has been common practice to model the dent as a geometrical idealisation without incorporating the residual stresses resulting from an actual denting process. While the model presented in this thesis improves on this simplification by modelling the indentation using a full surface-to-surface contact analysis, it was of interest to establish whether the extra computational effort required in modelling this phase was necessary, or whether a simple geometric idealisation yielded comparable results.

To investigate whether this was the case, a model was created which updated the finite element model geometry to the deformed configuration from the indentation phase without incorporating the associated stresses. This was achieved using an in-built ANSYS method which accesses the nodal displacements after a given operation and adds them to the original nodal co-ordinates.

For the FE model presented here, the geometric dent was updated from the FE geometry of an actual indentation simulation. This FE model had its nodal coordinates displaced to the deformation of a residual dent without incorporating the associated residual strains and stresses. Figure 5.117 plots the compression response for the case of a dent on a stringer

for the actual simulation of the dent as presented in section 5.3.2, and for the case where the FE geometry is updated.

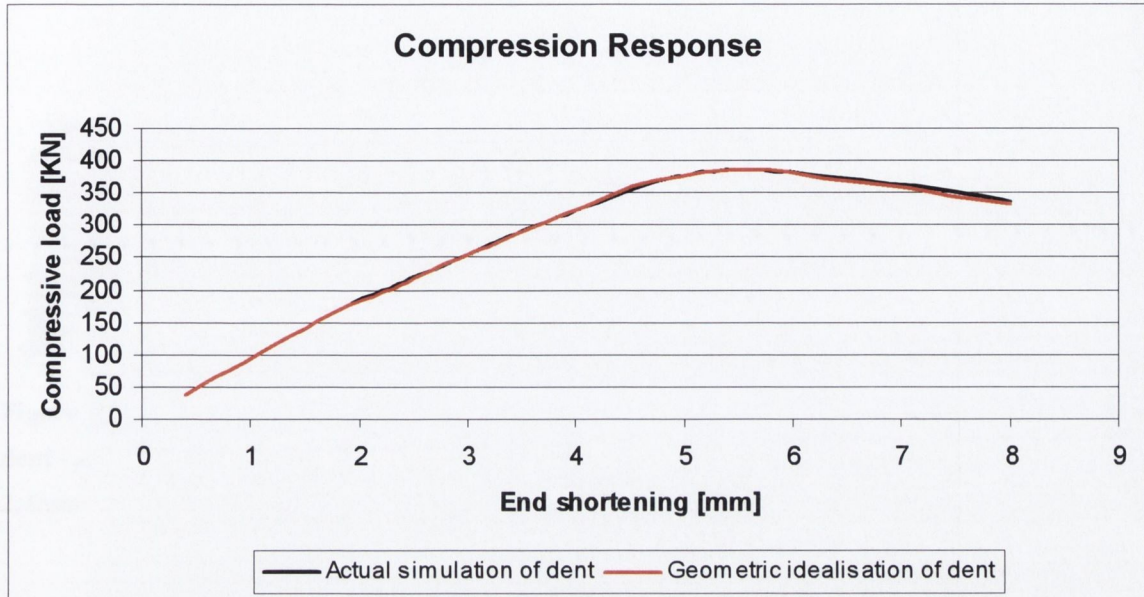


**Figure 5.117 Compression responses for a dent incorporating residual stresses and a dent based on a geometric idealisation**

It is clear that there is a very close correlation between the two models; the maximum load predicted for the geometric idealisation was 386kN versus 383kN for the actual simulation of the dent. Detailed examination shows that although the overall panel stiffness is predicted accurately without including the residual stresses and strains, the actual local deformation response and hence, local stress gradient is quite different. Figure 5.118 plots the radial displacement for the model incorporating the full dent with associated strains and stresses at an end shortening of 2.4mm, and Figure 5.119 shows the corresponding plot for the panel with the geometric idealisation of the dent. It is clear that while the “actual dent” affects both of the adjacent bays and undermines the establishment of a repetitive local buckling mode in a large area of the panel, the effects of the “geometric” dent are more localised. From Figure 5.119 it can be seen that a fully developed local skin buckling mode with five half waves in the longitudinal direction has been established in all but one bay for the model with the “geometric” dent. This contrasts with the model of the “actual” dent where local skin buckling has been completely undermined in all but two bays, Figure 5.118.

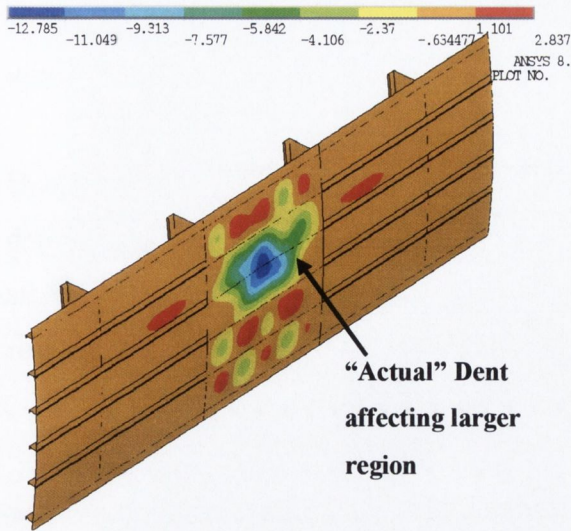


Figure 5.118 Dented panel incorporating actual dent radial displacement at an end shortening of 2.4mm

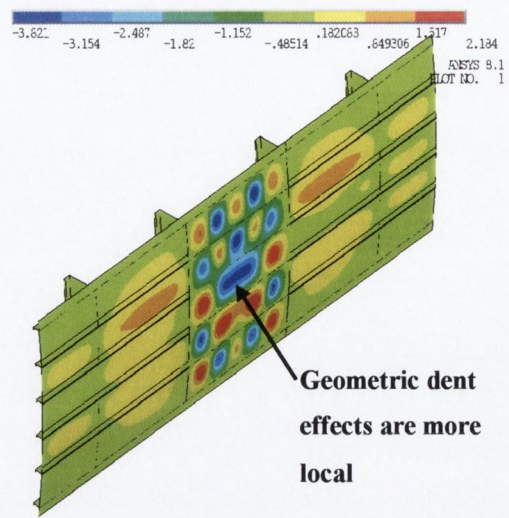


Figure 5.119 Geometric idealisation of dent radial displacement at an end shortening of 2.4mm

This change in local buckling response is maintained throughout the end-shortening, Figure 5.120 and Figure 5.122 show the progression of local skin buckling in both models due to an increased load of 275KN in both models at an end shortening of 3.3mm.

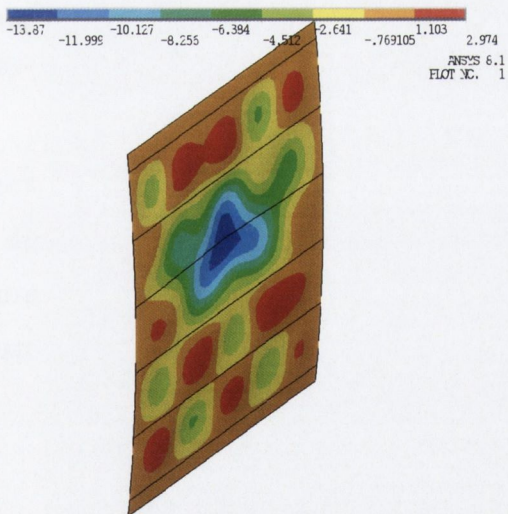


Figure 5.120 Radial displacement at an end shortening of 3.3mm for an "actual" dent

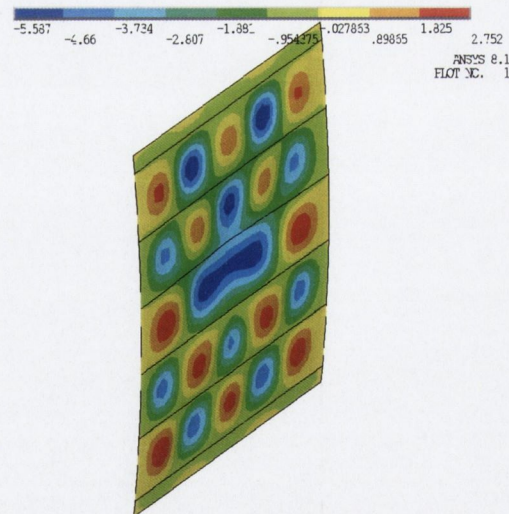


Figure 5.121 Radial displacement at an end shortening of 3.3mm for a "geometric" dent

From Figure 5.121, it can be seen that omitting the residual stresses causes the panel with the "geometric" dent to respond in a manner very similar to the pristine panel presented earlier. The panel is able to establish and maintain a fully developed skin buckling mode, with the exception of one stringer-frame bay. This contrasts with the response when the

strains and stresses are included in the dent as shown in Figure 5.120, where the dent undermines the establishment of a fully developed skin buckling pattern.

Due to the change in buckling deformation, there is a consequential change in load distribution in the panels. Figure 5.122 and Figure 5.123 plot the mid-surface longitudinal stress at cross section X-X for the actual dent and the geometric representation of the dent respectively.

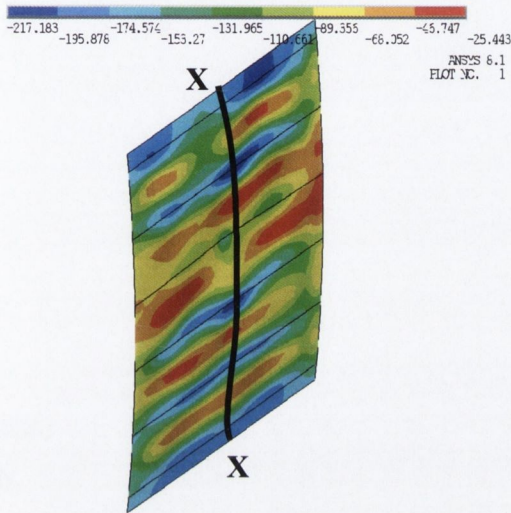


Figure 5.122 “Actual” dent longitudinal mid-surface stress at an end shortening of 3.3mm

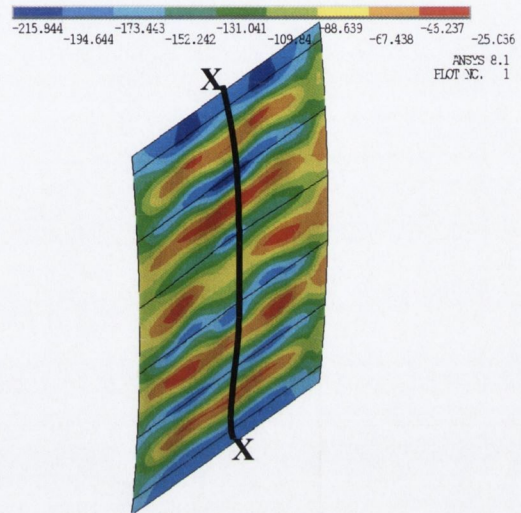


Figure 5.123 “Geometric” dent longitudinal mid-surface stress at an end shortening of 3.3mm

Figure 5.122 and Figure 5.123 show close agreement with each other with the exception of the dented stringer. The longitudinal mid-surface stress along the path X-X is plotted in Figure 5.124 and it can be seen that the model of the “geometric” dent underestimates the reduction in compressive longitudinal stress in the dented stringer.

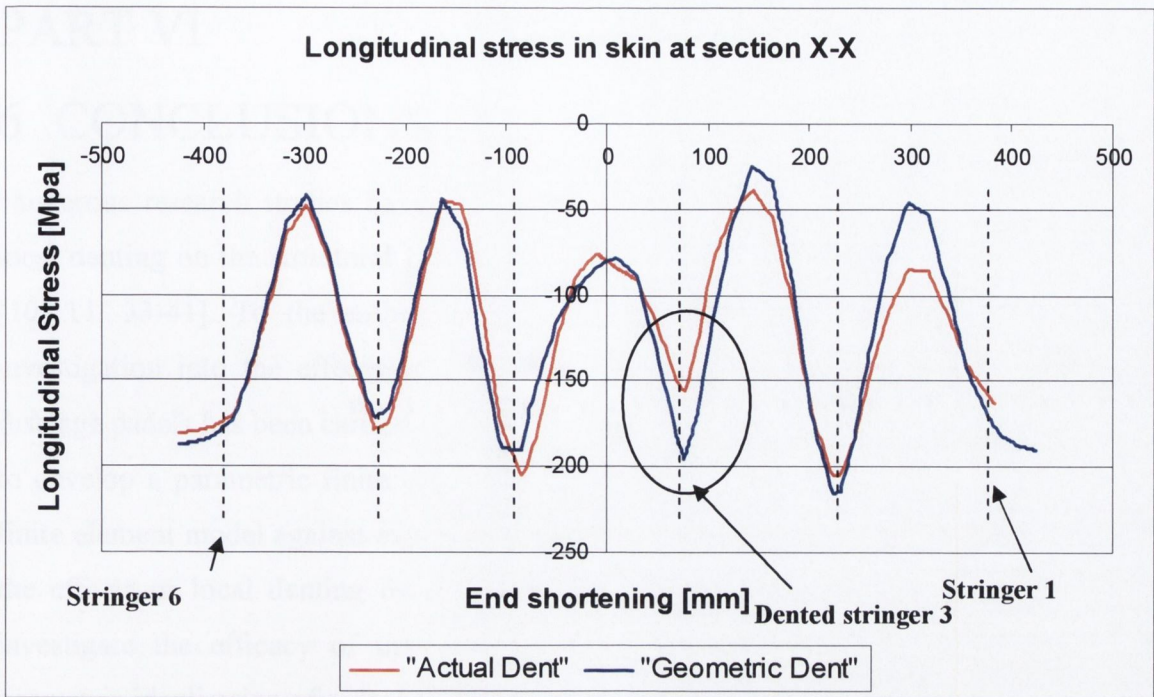


Figure 5.124 Longitudinal mid-surface stress along path X-X at end shortening of 3.3mm

While it is clear that modelling the dent as a geometric idealisation shows close agreement with the “actual” dent model for the overall prediction of ultimate compressive panel strength, it has also been shown that this method results in a very different local buckling response. This will result in inaccurate predictions of local strains and stresses; in particular, the stress gradient in the buckled region will be very different, which is of interest from a fatigue viewpoint. It can therefore be concluded that geometric idealisation of the dent is acceptable for calculating reductions in overall panel strength but that a full model of the dent, including the residual strains and stresses, is necessary if the user wishes to investigate whether local yielding has occurred in the panel or whether the resulting stresses are likely to be of concern from a fatigue viewpoint. To the author’s knowledge this has not been reported in the literature before.

## PART VI

### 6 CONCLUSIONS

Numerous research studies have numerically and experimentally examined the effect of local denting on the structural behaviour of steel cylinders and offshore tubular members [10, 11, 33-41]. To the author's knowledge, however, no numerical or experimental investigation into the effects of dents on the ultimate compressive strength of aircraft fuselage panels has been carried out previously. Therefore the objectives of this thesis were to develop a parametric finite element model to simulate this process, to benchmark the finite element model against experimental tests, to carry out parametric investigations into the effects of local denting on the ultimate compressive strength of aircraft panels, to investigate the efficacy of the dent dress back repair method and establish whether geometric idealisation of a dent is an acceptable simplification in determining the ultimate compressive strength of the panel.

Based on the results presented in this thesis, the following conclusions can be drawn:

1. The developed finite element model showed excellent correlation with the experimental results for the case of a dent on a stringer, predicting the reduction in ultimate compressive load to within 1.2% of that recorded experimentally.
2. Shallow dents were shown to result in a disproportionate reduction in load in comparison to deeper depths, suggesting the structures sensitivity to even slight impact damage.
3. Dents located mid-way between the frames had the most severe impact on the ultimate compressive strength.
4. The excellent load redistribution capabilities of the stiffened aircraft panel were demonstrated by their ability to support 80% of the undamaged ultimate compressive load when dented across several stringers to a dent depth of 15mm.
5. Reductions in stringer pitch were shown to have no significant effect on the relative reductions in ultimate compressive strength.
6. The current repair procedure of dent dress back for dents in bays was shown to have excellent benefits in terms of compressive strength recovery.
7. The procedure for modelling dents as a geometric idealisation, as reported in the literature, was shown to be an acceptable assumption for predicting the ultimate strength under compressive loading, however, it was demonstrated that the

response on a local level is not predicted accurately, which is of importance if local stress concentrations are of interest.

## PART VII

### 7 FUTURE WORK

The modelling of the dent dress back procedure in section 5.9 predicted very high residual stresses at the edges of the dressed back region which could be a cause of concern from a fatigue viewpoint. Section 5.9 details the simplifying assumptions made in developing this dress back model and there is significant scope to develop on this for a more accurate representation of the actual dress back procedure. A key component of this process is its time dependent nature due to the energy imparted by the hammer impacting the dented region. It is therefore suggested that explicit modelling of such a procedure would be the appropriate path to take and ANSYS provides this capability through the LS-DYNA solver. The parametric FE model developed in the course of this research allows for automated generation of the models which, with the addition of some code to switch from the implicit to the explicit solver and switch element types, would make it an ideal tool to carry out such a study.



## REFERENCES

- 1 AECMA, *"Facts and Figures 2001"*, European Association of Aerospace Industries, available online at <http://www.aecma.org/FactsnFigs.htm>
- 2 IARCAS RTD proposal, part B, March 2001
- 3 McGowan D.M., Ambur D.R., *"Compression Response of a Sandwich Fuselage Keel Panel With and Without Damage"*, NASA Technical Memorandum 110302, 1997
- 4 Tomblin J., Lacy T., Smith B., Hooper S., Vizzini A., Lee S., *"Review of Damage Tolerance for Composite Sandwich Airframe Structures"* U.S. Department of Transport Technical Report 1999
- 5 Hashagen F., de Borst R., *"Numerical Assessment of delamination in fibre metal laminates"*, Computer Methods in Applied Mechanics and Engineering no. 145, pages 141-159, 2000
- 6 Gerard G., Becker H., *"Handbook of Structural Stability part III Buckling of Curved Plates and Shells"*, National Advisory Committee for Aeronautics 1957
- 7 Godoy L.A., *"Stresses and pressures in thin-walled structures with damage and imperfections"*, International Journal of Thin-Walled Structures, no. 32, pages 181-206, 1998
- 8 [http://www.centennialofflight.gov/essay/Air\\_Power/Fokker/AP7.htm](http://www.centennialofflight.gov/essay/Air_Power/Fokker/AP7.htm)
- 9 Safarian P., *"Personal correspondence to K. Lacey"*, Structure Repair Group, Federal Aviation Authority (Formerly of Boeing), May 8th 2003.
- 10 Ronalds B.F., Dowling P.J., *"Damage of orthogonally stiffened shells"* Behaviour of Offshore Structures, pages 419-428, 1985
- 11 Walker A.C., Kwok M.K., *"Process of damage in thin-walled cylindrical shells"*, Advances in Marine Structures, pages 111-135, 1987
- 12 Megson T.H.G., *"Aircraft Structures for Engineering Students"*, Butterworth Heinemann, 2000
- 13 Schwarzmeier, K.O. *"Diag2-Geometric non-linear parameter calculation for diagonal tension simulation using MSC/Nastran"*, MSC conference paper, 1999
- 14 Kuhn P., Peterson J., Levin L.R., *"A Summary of Diagonal Tension Part I/II"* NACA Technical Report 2661/2662.
- 15 Bruhn E.F., *"Analysis and Design of Flight Vehicle Structures"*, Jacobs Publishing Inc. 1973

- 16 Donnell L.H., "A new theory for the buckling of thin cylinders under axial compression and bending", Transactions of the American Society of Mechanical Engineers, no. 56, pages 795-806, 1934
- 17 Lundquist E.E., "Strength tests of thin-walled duralumin cylinders in compression" Report 473, NACA 1957
- 18 Von Karman T, Dunn L.G., Tsien H-S, "The influence of curvature on the buckling characteristics of structures", Journal of the Aeronautical Sciences 1940
- 19 Singer J., Arbocz J., Weller T., "Buckling Experiments: Experimental Methods in Buckling of Thin-Walled Structures, Vol. 2, Shells, Built-up Structures, Composites and additional topics", John Wiley and sons, 2002
- 20 Brush D O and Almroth B O, "Buckling of Bars, Plates and Shells", McGraw-Hill, 1975
- 21 Timoshenko S. and Woinowsky-Krieger S., "Theory of Plates and Shells", McGraw-Hill, New York and Kogakusha, Tokyo, 1959
- 22 ECCS, European Convention for Constructional Steelwork, "Buckling of Steel Shells" European Recommendations, Fourth Edition, 1988.
- 23 Cox H.L., "The theory of flat panels buckled in compression", ARC R and M 1934
- 24 Marguerre K., "The apparent width of the plate in compression", National Advisory Committee for Aeronautics, 1937
- 25 Godoy L.A., "Thin-walled Structures with Structural Imperfections, Analysis and Behaviour", 1<sup>st</sup> Edition, Pergamon ,1996
- 26 Investigation report B 5/2001 L, "Aircraft damage in hailstorm west of Helsinki 21-07-2001" Accident Investigation Board, Finland, 2001
- 27 U.S. Department of Transportation Federal Aviation Administration, "Repair Assessment Program Order No. 8300.13", July 2003
- 28 Airbus "A340-500-600 Structural Repair Manual", July 2003
- 29 Jochem, J., "Personal correspondence to K. Lacey", Airbus ESGC1, June 21<sup>st</sup> 2004
- 30 Simmons F., Vecenia J., Wallace J., "Effects of dent removal of the design properties of fuselage skin material", American Institute of Aeronautics and Astronautics (AIAA) paper no. 2000-1467, April 2000
- 31 Murray N.W. "Introduction to the theory of thin-walled structures", Oxford Clarendon Press, 1984
- 32 Croll J.G.A., Kaleli F, Kemp K.O., Munro J., "A simplified approach to the analysis of geometrically imperfect cooling tower shells". Journal of Engineering Structures, pages 92-98, 1979

- 33 Harding J.E., Onoufriou A., "Behaviour of ring-stiffened cylindrical members damaged by local denting", Journal of Constructional Steel Research, Vol 33, pages 237-257, 1995
- 34 Ellinas C.P., Valsgard S., "Collision and damage of off-shore structures: A state of the art" Journal of Energy Resources Technology, ASME, 107(9), pages 297-314, 1985
- 35 Ronalds B.F., Dowling P.J., "Compressive strength of stiffened cylindrical shells with large imperfections", Buckling of structures: Theory and experiment, no. 1, pages 313-334, 1988
- 36 Ronalds B.F., Dowling P.J., "A denting mechanism for orthogonally stiffened cylinders", International Journal of Mechanical Sciences, Vol. 29, pages 743-759, 1987
- 37 Walker A.C., McCall S., Thorpe T.W., "Strength of damaged ring and orthogonally stiffened shells- part I: Plain ring stiffened shells", International Journal of Thin-Walled Structures, Vol. 5, pages 425-453 1987
- 38 Walker, A.C., McCall, S., Thorpe, T.W." Strength of damaged ring and orthogonally stiffened shells- part II:T-ring and orthogonally stiffened shells", International Journal of Thin-Walled Structures, Vol. 6, pages 19-50, 1988
- 39 Paik J.K., Thayamballi A.K., "Ultimate strength of dented steel plates under axial compressive loads", International Journal of Mechanical Sciences, 45, pages 433-388, 2003
- 40 Hu S.Z., Jiang L., "A finite element simulation of the test procedure of stiffened panels", Marine Structures, Vol. 11, pages 75-99, 1988
- 41 Hu S.Z., Chen Q., Jiang L., Zimmerman T.J.E., "Ultimate collapse tests of stiffened plate ship structural units", Marine Structures, pages 587-609, 1987
- 42 Hambly E.T., Calladine C.R., "Buckling experiments on damaged cylindrical shells" International Journal of Solids and Structures, Vol. 33, Issue 24, Pages 3539-3548, October 1996,
- 43 Zienkiewicz O.C., Taylor R.L., "Finite Element Method", Vol 1, 5<sup>th</sup> edition, Butterworth-Heinemann, 2000
- 44 Rao S.S., "The Finite Element Method in Engineering", 2<sup>nd</sup> Edition, Pergamon Press 1988
- 45 Bakker M.C.M, Pekoz, T, "The finite element method for thin walled structures-basic principles", International Journal of Thin-Walled Structures, Vol. 42, pages 179-189, 2003

- 46 Trueb U., "*Stability problems of elastic plastic plates and shells by finite elements*", PhD. Thesis, University of London, 1983
- 47 Bates D., "*Nonlinear finite element analysis of curved beams and shells*", PhD Thesis, University of London, 1985
- 48 Brooker D.C., "*A numerical study on the lateral indentation of continuously supported tubes*", Journal of Constructional Steel Research, Volume 60, Issue 8, Pages 1177-1192, August 2004.
- 49 Brooker D.C. "*Numerical modelling of pipeline puncture under excavator loading. Part I. Development and validation of a finite element material failure model for puncture simulation*" International Journal of Pressure Vessels and Piping, Volume 80, Issue 10, Pages 715-725, October 2003.
- 50 Brooker D.C., "*Numerical modelling of pipeline puncture under excavator loading. Part II: parametric study*" International Journal of Pressure Vessels and Piping, Volume 80, Issue 10, Pages 727-735, October 2003.
- 51 Jochem J., "*Remaining stresses after dent dress back in fuselage skin*" Airbus Technical Report, Airbus ESGC1, 2002
- 52 Lundquist E, Stowell EZ. "*Critical compressive stress for flat rectangular plates Elastically restrained*", NACA Technical Note, 1942, No. 733.
- 53 Gerard G, Becker H. "*Handbook of structural stability, Part I. Buckling of flat plates*", NACA Technical Note, 1954, No. 3781.
- 54 Bleich F., "*Buckling strength of metal structures*", New York: McGraw-Hill Book Co, 1952.
- 55 Paik J.K., Thayamballi A.K., "*Buckling strength of steel plating with elastically restrained edges*", International Journal of Thin-Walled Structures, Vol. 37, Issue 1, Pages 27-55, , May 2000
- 56 Paik J.K., Thayamballi A.K., Kim D.H., An analytical method for the ultimate compressive strength and effective plating of stiffened panels, Journal of Constructional Steel Research, 49, pages 43-68, April 1999
- 57 Oesmann, W., "*Technical Note EV11-3470/94*", Deutsche Aerospace, Airbus, 1994
- 58 Jochem J., From proceedings of Iarcas Meeting No. 3, Contract G4RD-CT2000-00401, Date, May 16th and 17th, 2002
- 59 Hashagaen F., "*Numerical analysis of failure mechanisms in fibre metal laminates*", PhD Thesis, Delft Technical University, 1998
- 60 Rust W., Schweizerhof K., "*Finite element limit load analysis of thin-walled structures by ANSYS (implicit), LS-DYNA (explicit) and in combination*",

- International Journal of Thin-Walled Structures, Vol. 41, pages 227-244, 2003
- 61 Featherston C.A., "*The use of finite element analysis in the examination of instability in flat plates and curved panels under compression and shear*", Int. Journal of Non-Linear Mechanics, vol. 35, pages 515-529, 2000
- 62 ANSYS, "*ANSYS 8.1 Help Manual*", ANSYS Inc. Canonsburg, PA. U.S.A., 2004
- 63 Buehrle R.D., Fleming G.A., Pappa R.S., Grosveld F.W., "*Finite element model development for aircraft fuselage structures*", proceedings of the 18<sup>th</sup> International Modal Analysis Conference, San Antonio, Texas, Feb, 2000
- 64 Ansys Inc., "*Basic Structural Non-linearities training manual*" Ansys Inc., Canonsburg, PA. U.S.A., 2001
- 65 Viceconti M., Bernakiewicz, M., "*Theoretical background of contact mechanics implementation in finite elements method*", extension of article entitled: "*Large-sliding contact elements accurately predict levels of bone-implant micromotion relevant to osteointegration*", Journal of Biomechanics Vol 33 pages 1611-8, 2000
- 66 Kloosterman G., "*Contact Methods in Finite Element Simulation*", PhD Thesis, University of Twente, 2002
- 67 Bathe K.J., "*Finite Element Procedures*", Prentice hall, 1996
- 68 Hinton E., "*NAFEMS: Introduction to non-linear finite element analysis*", NAFEMS Ltd. Glasgow U.K.
- 69 Ansys Inc., "*Contact Analysis with ANSYS: training manual*" Ansys Inc., Canonsburg, PA. U.S.A., 2001
- 70 Cook R.D., Malkus D.D., Plesha M.E., "*Concepts and Applications of Finite Element Analysis*", 3<sup>rd</sup> ed., John Wiley & Sons, 1989.
- 71 [http://www.padtinc.com/epubs/focus/2003/0014\\_0123/article2.htm](http://www.padtinc.com/epubs/focus/2003/0014_0123/article2.htm)
- 72 Jochem, J., "*Personal correspondence to K. Lacey*", Airbus ESGC1, Oct 12<sup>th</sup> 2004